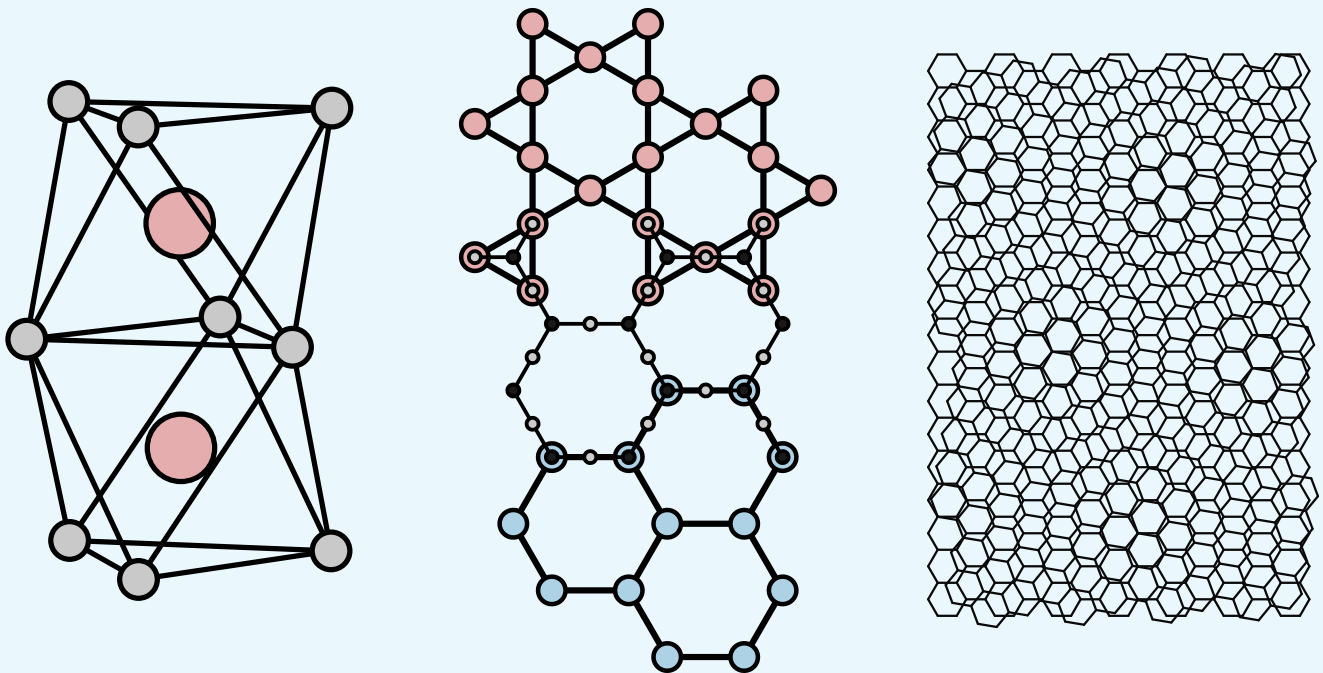
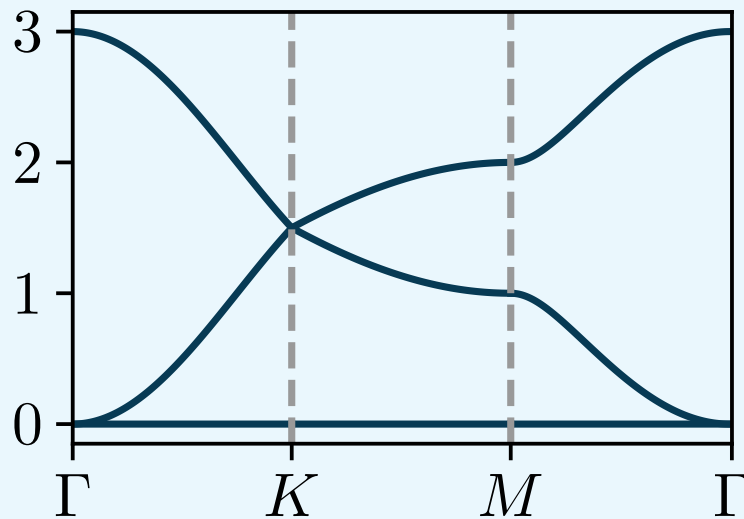


Electronic Spectra: Topology, Supersymmetry, and Statistics



Electronic Spectra: Topology, Supersymmetry, and Statistics

Inaugural-Dissertation

zur

Erlangung des Doktorgrades

der Mathematisch-Naturwissenschaftlichen Fakultät

der Universität zu Köln

vorgelegt von

Jan Attig

aus Jülich



Köln 2022

Berichterstatter:

Prof. Dr. Simon Trebst

Prof. Dr. Sebastian Diehl

Tag der mündlichen Prüfung:

3.3.2022

Die vorliegende Dissertation wurde von der Mathematisch-Naturwissenschaftlichen Fakultät der Universität zu Köln angenommen.

Abstract

The description of electronic behavior within solids is a major part of modern Condensed Matter Physics. It is well known that depending on the precise conditions, very diverse phenomena arise from the interacting electrons in the material. To make predictions, it is therefore crucial to understand the electronic structure in a material and to compute its *electronic spectrum*. This thesis discusses three different aspects of electronic spectra including their numerical solution, each highlighting a distinct approach.

In a first part, this thesis presents a numerical solution of many-electron spectra on small clusters of IrO_6 octahedra. Such clusters are relevant in the field of strongly coupled matter as they give rise to the elementary building blocks of many topological spin systems, localized $j = 1/2$ moments. Exact diagonalization of the full many-electron interaction Hamiltonian is utilized to compute multi-particle spectra with respective eigenstates. Subsequently, these eigenstates are further used for numerical calculations of resonant inelastic X-ray scattering (RIXS) amplitudes. The numerical approach is versatile enough to be applied to different examples in this thesis, covering single-site RIXS spectra as in $\text{Ba}_2\text{CeIrO}_6$, materials with local clusters like $\text{Ba}_3\text{InIr}_2\text{O}_9$ and $\text{Ba}_3\text{Ti}_{3-x}\text{Ir}_x\text{O}_9$ and Kitaev materials such as Na_2IrO_3 and $\alpha\text{-RuCl}_3$. In particular, interference effects in the RIXS amplitudes are shown to play a crucial role of determining the nature of delocalized eigenstates in these materials.

In a second part, supersymmetry is used to link the spectra of electronic lattice models with bosonic counterparts. To this endeavor, an exact lattice construction is introduced, underlying the supersymmetric identification and providing a visual representation of the supersymmetric matching. As a first instance of the supersymmetric map, it will be shown that models of complex fermions and models of complex bosons are supersymmetrically related if they reside on the two sublattices of a bipartite lattice. Another similar identification is introduced for Majorana fermions on a bipartite lattice which can be related to real boson models on one of the sublattices, allowing for the explicit construction of related mechanical models. As examples of this classical construction, the Kitaev model and a second order topological insulator with floppy corner modes are discussed. In both examples, the supersymmetrically related mechanical model is shown to exhibit the same spectral properties as its quantum mechanical analogue and even inherit topologically protected localized corner modes.

In a third part, the electronic spectra of general Moiré materials are investigated at the example of twisted bilayer graphene. This part demonstrates that statistical principles are best suited to describe the vast number of bands originating from the large Moiré unit cells. The statistical description reveals a localization mechanism in momentum space which is investigated and described. The mechanism does not only apply to all parts of the spectrum in twisted bilayer graphene but is also believed to apply to generic Moiré materials. Moreover, exceptions from this general mechanism in twisted bilayer graphene are discussed in detail which turn out to be described by harmonic oscillator states.

Kurzzusammenfassung

Die Beschreibung elektronischen Verhaltens in Materialien ist ein Kernpunkt moderner Festkörperphysik. Es ist bekannt, dass sich abhängig von den genauen Materialparametern sehr unterschiedliche qualitative Eigenschaften aus den wechselwirkenden Elektronen ergeben können. Daher ist es grundsätzlich unumgänglich, für jede Art von Vorhersage das elektronische Verhalten des Materials zu kennen und dessen sogenanntes *elektronisches Spektrum* berechnen zu können. Das Ziel dieser Arbeit ist es, in drei verschiedenen Teilen jeweils verschiedene Aspekte der Berechnung elektronischer Spektren hervorzuheben und zu diskutieren.

Im ersten Teil der Arbeit wird die numerische Lösung des gesamten Viel-Elektronen-Problems auf kleinen isolierten Clustern aus IrO_6 Oktaedern untersucht. Diese Arten von Clustern finden Anwendung im Bereich von stark korrelierten Materialien, wo sie unter anderem dafür bekannt sind, dass sie lokale $j = 1/2$ Momente hervorbringen, die sich zu effektiven Spin-Modellen kombinieren lassen. Im Rahmen dieser Arbeit wird sowohl die numerische Lösung des Wechselwirkungs-Hamiltonians mittels exakter Diagonalisierung vorgestellt, als auch die weitere Benutzung der Eigenzustände zur Berechnung von Intensitäten resonanter, inelastischer Röntgen-Streuung (RIXS). Mit diesem numerischen Werkzeug werden dann Materialien mit einzelnen IrO_6 Oktaedern, wie $\text{Ba}_2\text{CeIrO}_6$, Dimer-Materialien in denen die lokalen Cluster aus zwei IrO_6 Oktaedern bestehen, wie $\text{Ba}_3\text{InIr}_2\text{O}_9$ und $\text{Ba}_3\text{Ti}_{3-x}\text{Ir}_x\text{O}_9$, sowie sogenannte Kitaev Materialien wie Na_2IrO_3 und $\alpha\text{-RuCl}_3$ untersucht. In diesen Material-Bespielen wird insbesondere demonstriert, dass die Interferenzeffekte in RIXS Intensitäten Aufschluss über die Lokalisation der Eigenzustände geben können.

Im zweiten Teil der Arbeit wird Supersymmetrie angewandt um die Spektren elektronischer Gittermodelle mit denen bosonischer Gegenstücke zu verbinden. Zu diesem Zweck wird eine Gitterkonstruktion eingeführt, die der supersymmetrischen Verbindung zu Grunde liegt und eine visuelle Repräsentation ebendieser darstellt. Als erstes Beispiel dieser Verbindung wird gezeigt, dass Modelle komplexer Fermionen und Bosonen supersymmetrisch miteinander verbunden sind, wenn sie auf den zwei Subgittern eines bipartiten Gitters definiert sind. Ein weiteres Beispiel für eine supersymmetrische Verbindung im Rahmen dieser Arbeit ist die Identifikation von topologischen mechanischen Systemen, die auf einem der Subgitter eines verbundenen Majorana-Fermionen Systems definiert sind. Als Beispiele der mechanischen Systeme werden klassische Modelle für das bekannte Kitaev Modell sowie für einen topologischen Isolator zweiter Ordnung hergeleitet. In beiden Beispielen zeigt das supersymmetrisch verbundene mechanische Modell sowohl die spektralen Eigenschaften des Majorana Systems als auch seine topologischen Anregungen.

Im dritten und letzten Teil der Arbeit werden die elektronischen Spektren von sogenannten Moiré Materialien am Beispiel von Twisted Bilayer Graphen untersucht. Dabei handelt es sich um ein zweidimensionales Material, in dem das gegeneinander Verdrehen zweier Graphenlagen zu einer Vergrößerung der Einheitszelle und der Bildung flacher Bänder an

einem besonderen Drehwinkel führt. Dieser Teil der Arbeit befasst sich insbesondere mit der Frage, inwiefern statistische Untersuchungen der Spektren mehr Einblick über physikalische Effekte der großen Bandstrukturen geben können. Insbesondere wird gezeigt, dass die statische Beschreibung einen Lokalisationsmechanismus im Impulsraum beschreiben kann, der in allen Bereichen des Spektrums Anwendung findet. Mittels dieses Mechanismus kann beschrieben werden, wie flache Bänder allgemein in Moiré Materialien entstehen können. Zusätzlich werden auch Ausnahmen von diesem Mechanismus diskutiert, die sich schlussendlich als Zustände eines harmonischen Oszillators beschreiben lassen.

Contents

1. Introduction and outline	1
I. Numerical RIXS	5
2. Introduction	7
3. Theoretical modeling	9
3.1. Single particle physics on a single site	9
3.2. Single particle physics on many sites	16
3.3. Multi particle physics	18
3.4. Resonant inelastic X-ray scattering (RIXS)	24
3.5. Numerical implementation and RIXSCalculator.jl	31
4. Material examples	37
4.1. Single particle RIXS in $\text{Ba}_2\text{CeIrO}_6$	37
4.2. Dimer materials and RIXS variants of Young's double slit	41
4.2.1. Disorder effects in $\text{Ba}_3\text{Ti}_{3-x}\text{Ir}_x\text{O}_9$	41
4.2.2. Dimers with three holes in $\text{Ba}_3\text{InIr}_2\text{O}_9$	45
4.3. Kitaev materials	49
4.3.1. RIXS interference patterns in Na_2IrO_3	50
4.3.2. Double spin-orbit exciton in $\alpha\text{-RuCl}_3$	57
4.4. Beyond RIXS	61
5. Summary and discussion	63
II. Supersymmetry and Topology	65
6. Introduction	67
7. Lattice models	69
7.1. Lattices and unitcells	69
7.2. Bandstructures of quadratic lattice models	71
7.3. Numerics of lattice models and LatticePhysics.jl	73

8. Graph theory and supersymmetry	81
8.1. Block matrices and supersymmetry	81
8.2. Topological invariants under supersymmetry	83
8.3. Block matrices and graph theory	84
8.4. Supersymmetry as a graph correspondence	87
9. Complex fermions and complex bosons	89
9.1. Supersymmetric charge	89
9.2. Examples	91
10. Majorana fermions and topological mechanics	103
10.1. Supersymmetric charge	103
10.2. Real bosons and classical balls and springs	104
10.3. Example I: Mechanical Kitaev model	107
10.3.1. The Kitaev model and its analytical solution	107
10.3.2. Classical balls and springs model	108
10.3.3. Measuring spectra in the mechanical model	110
10.3.4. Spectral correspondences	113
10.4. Example II: Mechanical second order topological insulator	114
10.4.1. Second order topological insulator from Majorana fermions	115
10.4.2. Classical balls and springs model	115
10.4.3. Spectral correspondences	117
10.4.4. Localized corner modes	118
10.4.5. Topological invariant	120
10.5. Additional aspects	122
10.5.1. Negative spring constants	122
10.5.2. Noise	124
11. Beyond supersymmetry: Fermions and spin spirals	129
11.1. Classical spin-spiral ground states	129
11.2. Lattice construction to free fermion models	132
11.3. Lattice construction vs. supersymmetry	133
11.4. Examples	134
12. Summary and discussion	139
III. Universal Features of Moiré Bandstructures	143
13. Introduction	145
14. Modeling twisted bilayer graphene	151
14.1. Real space geometry	151
14.2. Real space hopping model	155

14.3. Momentum space continuum model	158
15. Delocalized states in twisted bilayer graphene	161
15.1. Measures of localization	161
15.2. Velocity statistics	162
15.3. Energy level statistics	166
15.4. Wavefunction statistics	169
15.5. Spectral dependence of observables	172
15.6. The three regimes of localization	178
15.7. Anomalously flat bands: Magic angle flat bands	179
15.8. Anomalously flat bands: Harmonic oscillator states	182
16. Summary and discussion	187
17. General concluding remarks	189
Bibliography	193

1. Introduction and outline

A substantial part of modern Condensed Matter Physics is devoted to describing the behavior of fast electrons in the context of a nearly static lattice of atomic nuclei. From a quantum mechanical perspective such behavior manifests itself in the formation of eigenstates with respective energies which form so-called *electronic spectra*. Although electrons are known from the standard model as elementary particles, their behavior in solids is much richer compared to free or isolated electrons, mostly due to two key ingredients. First, electrons in solids have to be considered subject to a periodic background modulation which in many forms differs from the vacuum. Second, and most importantly, in a macroscopic material there are exponentially many (interacting) electrons whose interplay allows for the emergence of fascinating complexity.

There have been many tantalizing observations of diverse electronic behavior in the past 100 years. Electronic models are found to underlie the majority of today's phenomena, starting with seemingly free particles which transport charge and heat, to ordered phases in which electronic degrees of freedom appear to be pinned to certain states even at finite temperatures. Effects of electronic correlations in a material, in particular with strong spin-orbit coupling [1, 2], can range from the formation of superconducting phases or quantum critical points, to emergent spin models exhibiting exotic phases such as spin liquids [3, 4]. Especially in recent years, the notion of topological order and fractional excitations have been in the focus of research, promising advances not only on the level of theoretical understanding but with real-world applications such as engineering a first quantum computer.

From a theoretical perspective, electronic models have especially been enriched by one particular concept, namely the notion of quasi-particles or effective degrees of freedom. This advance ultimately led to a shift in perspective, opening the possibility of *engineering* certain particles with desired properties within a solid instead of *searching* for them in the form of more exotic elementary particles in vacuum. In this process, quasi-particle descriptions not only allowed describing previously incomprehensible effects but also simplified the development of tailored materials exhibiting meticulously designed properties in their effective quasi-particle models.

Nowadays, electronic models are at the heart of many discussions in modern Condensed Matter Physics and determining their electronic spectra is a recurring essential task in describing the overall behavior of a material. This thesis is devoted to providing three different numerical perspectives on the field of electronic spectra. The three examples considered are representative for an entire family of problems, each highlighting a unique

aspect, thus elevating their solutions to be applicable in a broader context.

In **Part I** of this thesis, numerical exact diagonalization will be employed to obtain electronic spectra of the full electronic many-body problem. This discussion will be held in the context of resonant inelastic X-ray scattering (RIXS) measurements on materials exhibiting strong spin-orbit coupling and partially filled d -shells. Such materials are natural ingredients for the formation of local $j = 1/2$ moments and have therefore great relevance in the fabrication of tailored spin-models. **Chapter 2** provides a brief introduction to these materials which is followed by their theoretical description in **Chapter 3** together with the concept of numerical exact diagonalization and numerical RIXS. In **Chapter 4**, delocalized states in different materials are then investigated by calculating numerical RIXS amplitudes which are compared to experimentally obtained data. In general, such analyses fundamentally lay the basis for *topological* aspects of electronic models and the formation of respective quasi-particles. Part I is then closed with a brief summary and outlook in **Chapter 5**.

In **Part II**, the focus shifts from a full many-body description of localized states to the discussion of periodic so-called Bloch states of a single particle in a periodic lattice. In particular, this part focuses on the analysis of bandstructures with regard to *supersymmetry* (SUSY) formulated on the basis of the underlying lattice structure. Following a brief introduction in **Chapter 6** about the role of supersymmetry, **Chapter 7** gives an overview over the concept of non-interacting lattice models. This concept will be brought into correspondence with supersymmetry in **Chapter 8**, followed by several examples. The first example in **Chapter 9** concerns the connection between complex fermions and bosons which can be connected by supersymmetry if they reside on matching sublattices of a bipartite lattice. The second example in **Chapter 10** discusses the supersymmetric connection between Majorana fermions on a bipartite lattice and real bosons on one of its sublattices. In particular, connections to topological mechanics are discussed and it is shown that topological invariants can be defined for the mechanical system, which inherit the topology of the Majorana fermion system. Finally, a brief discussion of previous work regarding a correspondence of spin-spiral ground states and the Fermi surfaces of free fermion systems is presented in **Chapter 11**, before being followed by a small discussion and outlook in **Chapter 12**.

In **Part III** of this thesis, another shift of focus is performed by increasing the effective size of elementary building blocks. Here, the family of Moiré materials is highlighted which is characterized by extraordinary large unitcells stemming from the interplay of two periodic structures with slightly different periodicities. Due to the resulting electronic spectra with huge number of bands, *statistical* principles are much better suited to describe the behavior in these Moiré materials. After a brief introduction in **Chapter 13** to the family of Moiré materials, band structure calculations for twisted bilayer graphene are introduced in **Chapter 14** as a prime example for a Moiré material. **Chapter 15** then discusses the impact of the Moiré structure on the electronic spectrum, resulting in the statistical investigation of localization effects in momentum space leading to the natural formation

of flat bands. The mechanism takes place in three distinct regimes of localization which are discussed and then applied to twisted bilayer graphene. Then, a brief summary of other types of flat bands in twisted bilayer graphene is performed, followed by a general summary in **Chapter 16**, summarizing the entirety of Part III.

With these three topical parts being discussed, the thesis closes with some final concluding remarks and a brief discussion in **Chapter 17**.

Part I.
Numerical RIXS

2. Introduction

Among different properties induced by electronic behavior, materials exhibiting magnetism have always been a source of intriguing effects. Starting with the discovery of magnetism and the electromagnetic force, fascination pursued all the way to modern condensed matter physics. With the formulation of statistical physics, many microscopic models have been proposed to explain and predict thermal ordering of intrinsic magnetic moments. Whereas in the early days of statistical physics, the Ising model enabled studying ferromagnetism, nowadays more complex magnetic phases are of interest. These phases can in particular arise in frustrated systems which prevent long-range magnetic order by a particular exchange geometry so that interactions cannot be simultaneously satisfied. One particular example of such models is the Kitaev model [3] which describes spins interacting on a honeycomb lattice with bond-directional couplings. It has been shown [3] that its ground state is a long sought-after quantum spin liquid.

With the growing complexity of theoretical models, also the complexity of experimental materials grew in time. In recent years particular interest has been paid to transition metal oxides with partially filled 4d and 5d orbitals. Strong spin-orbit coupling in these materials in combination with surrounding crystal field effects gives rise to spin-orbit coupled $j = 1/2$ moments, as demonstrated in Fig. 2.1. These moments can subsequently be driven to Mott insulating phases by electronic correlations, giving rise to many exotic phases of matter [1, 2]. First experimental investigations of such materials have been performed on the example of Sr_2IrO_4 [5, 6], however work in this thesis focuses more on so-called *Iridate* materials, in which Iridium atoms are surrounded by oxygen octahedra. Typically, Ir exhibits an Ir^{4+} ($5d^5$) valence, which in combination with effects of the oxygen crystal field make these IrO_6 building blocks ideal for realizing $j = 1/2$ moments.

It was realized that the intrinsic IrO_6 building blocks can be aligned in various geometries, giving rise to different effective interactions between $j = 1/2$ moments [4, 7, 8]. Corner-sharing geometries are typically associated with Heisenberg exchange whereas edge-sharing octahedra have been found to realize bond-directional couplings [4] which are necessary for material realizations of the Kitaev model. As a natural consequence, the family of iridate materials received much attention.

One tool to probe the electronic states within these materials is resonant inelastic X-ray scattering (RIXS). In a RIXS measurement, the inelastic contribution to scattering amplitudes of resonant X-rays is observed. Since Ir is strongly absorbing neutrons, RIXS outperforms the otherwise widely used tool of neutron scattering in the Iridates. In particular combining RIXS with interferometric approaches proved a fruitful combination [9].

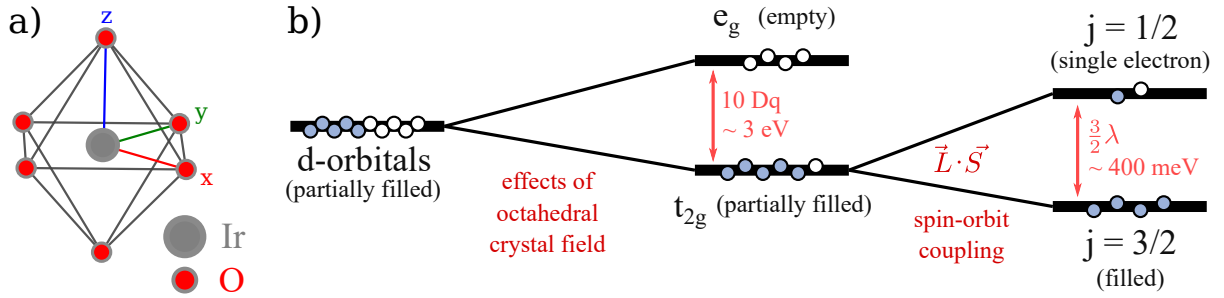


Figure 2.1.: Formation of $j = 1/2$ moments in materials with partially filled d -shells and strong spin-orbit coupling - Schematic depiction of a IrO_6 octahedron (panel a)) with intrinsic formation of $j = 1/2$ moments (panel b)) from a partially filled d -shell. Strong crystal field effects of the surrounding oxygen atoms, forming an octahedral crystal cage, split the d -orbitals into two multiplets, called e_g and t_{2g} . While the e_g states are empty, the t_{2g} states are partially filled and can be split further by additional interactions. In particular, strong spin-orbit coupling splits the t_{2g} multiplet into $j = 1/2$ and $j = 3/2$ states. For the common configuration of 5 electrons within the d -shell, the $j = 3/2$ states are completely filled and there is only a single electron, occupying the $j = 1/2$ states, forming an effective spin-1/2 degree of freedom that can subsequently interact with neighboring moments.

It could be shown that interference effects in RIXS intensities, similar to the famous double-slit experiment by Young, could resolve quasi-molecular orbitals in $\text{Ba}_3\text{CeIr}_2\text{O}_9$, providing a way for other material investigations [9].

The work in this Part I aims at providing a numerical perspective on the method of RIXS interferometry. In particular, this part covers a numerical implementation to investigate the family of iridate materials and aid in experimental interpretation of RIXS data. The entirety of code is contained in the packages `RIXSCalculator.jl` and `RIXSPlotter.jl` for the programming language Julia. The implementation is modular and allows the investigation of various cluster geometries with varying particle numbers. To illustrate the flexible implementation, this part covers many different example systems, which are partially still considered to be work-in-progress.

The part is organized as follows. First in Chapter 3, the conceptual methods of multi-particle exact diagonalization and RIXS are introduced. Then, in Chapter 4, these methods are applied to a number of example systems, ranging from a single-site system to edge-, face- and corner-sharing dimers in various iridate materials. Finally, a brief summary and conclusion of this part is drawn in Chapter 5.

3. Theoretical modeling

Let us begin by discussing the theoretical formalism to describe electronic states in systems where partially filled d shells are subject to a mix of strong spin-orbit coupling, crystal field effects as well as electronic correlations. To this endeavor, this chapter starts with a single-particle description of isolated IrO_6 octahedra in Sec. 3.1, containing a brief introduction to single-particle quantum mechanics and the necessary basis and operator definitions commonly used for such materials. From there, a generalization to many sites is carried out in Sec. 3.2, followed by another extension to multiple particles in Sec. 3.3 introducing Fock space language. After the many-particle Hamiltonian is discussed, the chapter ends by introducing the RIXS process in Sec. 3.4, followed by the implementation into the respective Julia modules in Sec. 3.5.

3.1. Single particle physics on a single site

In this first section, let us focus on describing eigenstates of a *single* particle on a *single* Iridium site. After some initial notes on general quantum mechanics, first, a description of the basis is given, then a formulation of the Hamiltonian in terms of this basis. Note that on the level of a single particle, there will not be a formal distinction in terms of holes and electrons yet, however when including more than a single particle in the next sections, this distinction will reappear.

General notes on single-particle Quantum Mechanics

Before addressing Iridates directly, let us first review some basic formalism. In principle, quantum mechanics describes the behavior of complex wavefunctions $|\psi\rangle$ by solving a fundamental differential equation known as the Schrödinger equation

$$\hat{H} |\psi\rangle = -i \frac{\partial}{\partial t} |\psi\rangle. \quad (3.1)$$

For static problems, this equation can be further simplified. Wavefunctions decompose into an oscillating part in time, $|\chi(t)\rangle$ as well as an additional time-independent part $|\phi\rangle$ which describes a static behavior in space. This time-independent wave function follows a simplified version of the Schrödinger equation which can be formulated as an eigenvalue equation

$$\hat{H} |\phi\rangle = \varepsilon_\phi |\phi\rangle. \quad (3.2)$$

3. Theoretical modeling

Here, ε_ϕ describes the energy of state $|\phi\rangle$. In principle, the physics of these static systems is therefore governed by the eigensystem of the corresponding Hamilton operators, i.e. eigenstates and corresponding eigenvalues of its matrix description.

From a technical perspective, the general formalism to describe the physics of a quantum particle is the following. One has to start by choosing a basis representation of Hilbert space, i.e. a set of states $\{|a_n\rangle\}$ for the (usually closed) system. Any given state can then be written as

$$|\psi\rangle = \sum_n \alpha_n |a_n\rangle \quad (3.3)$$

with complex prefactors $\alpha_n \in \mathbb{C}$. These prefactors can e.g. be represented as some vector $\vec{a} = (\dots, \alpha_n, \dots)^T$ if one is interested in a matrix representation of the state. Subsequently, one has to formulate the action of operators \mathcal{O} on the basis states, e.g. spin operators. This can be done by formulating the overlaps $\langle a_n | \mathcal{O} | a_m \rangle = \mathcal{O}_{m,n}$ for the operator \mathcal{O} which also allows to write a given operator as a matrix. Since the Hamiltonian is built up from these operators, it is straight forward to also obtain the matrix description of the Hamiltonian. Finally diagonalizing the Hamiltonian matrix leads to eigenvalues and eigenstates. Whereas the eigenstates can be identified with the wavefunctions of a single particle, the eigenvalues give the corresponding energies of these states. In total, this procedure would be characterized as a "solution" of the quantum problem.

Whereas many problems can be solved analytically in this regard, oftentimes a numerical solution is the only option. Numerically one has to diagonalize the Hamiltonian matrix explicitly in order to obtain eigenenergies and eigenstates. Although in principle these matrix-vector operations are implemented quite efficiently in nearly any programming language, the most challenging part is the size of the matrix. The matrix dimension is directly related to the size of the Hilbert space. For a Hilbert space with N basis states, the Hamiltonian matrix is of size $N \times N$. This is especially important as a system with n particles which can occupy one out of two states, $N = 2^n$, i.e. the Hilbert space scales exponentially. Then, diagonalizing the corresponding $2^n \times 2^n$ Hamiltonian matrix might even exceed the available numerical resources.

Coming to the systems at hand, it becomes apparent that there are some key questions which have to be answered in order to phrase the following discussion in the language of single-particle quantum mechanics. First of all, the Space of states has to be chosen. Second, respective operators acting on these states are defined which then can build up the Hamiltonian.

Choosing the right basis

Most materials have complex atomic configurations with many electrons on a vast variety of orbitals. However all materials in the following discussion share a common theme – their physics can be described in terms of electrons within the partially filled d -shell. The d -shell is a $\ell = 2$ multiplet consisting of five states that are distinguished by $m_\ell = -2, -1, 0, 1, 2$.

Due to an octahedral crystal field around the atoms at hand, the d orbitals are split into two subgroups, two e_g and three t_{2g} orbitals, as seen in Fig. 2.1. The splitting is on the order of several eV which in combination with the low filling of the d -shell means that we can concentrate on the t_{2g} subgroup from here on. Within the t_{2g} subgroup, an effective $\ell = 1$ structure emerges [10].

Since from here on, all calculations take place within the t_{2g} manifold, the explicit label of \hat{L}_{eff} will be dropped. Therefore, all subsequent references to either \hat{L} or the quantum number ℓ are referring to the *effective* orbital quantum number unless stated differently.

To parameterize the t_{2g} states one can therefore choose a basis with quantum numbers ℓ and s . Basis states have the form $|\ell, m_\ell, s, m_s\rangle_{\text{LS}} = |\ell, m_\ell\rangle \otimes |s, m_s\rangle$ with orthonormal bases $\{|\ell, m_\ell\rangle\}$ and $\{|s, m_s\rangle\}$. Note that we are focusing on the case of t_{2g} electrons, i.e. $\ell = 1$ and $s = \frac{1}{2}$. This yields six different basis states with quantum numbers $m_l = -1, 0, 1$ and $m_s = \pm 1/2$ which can be represented in the form $|m_l, m_s\rangle$ as

$$\begin{array}{lll} | -1, \uparrow \rangle & | 0, \uparrow \rangle & | +1, \uparrow \rangle \\ | -1, \downarrow \rangle & | 0, \downarrow \rangle & | +1, \downarrow \rangle \end{array} \quad (3.4)$$

An alternate parametrization of the ℓ -part of the basis uses real-space coordinates of the surrounding crystal field. Orbitals along axes α and β can be written as $|\alpha\beta\rangle$ or similarly abbreviated by the direction γ that they do not spread along, i.e. $|\alpha\beta\rangle \hat{=} |\gamma\rangle$. In total, the XYZ-basis definition reads

$$\begin{aligned} |x\rangle \hat{=} |yz\rangle &= (|1\rangle - |-1\rangle)/\sqrt{2} \\ |y\rangle \hat{=} |zx\rangle &= i(|1\rangle + |-1\rangle)/\sqrt{2} \\ |z\rangle \hat{=} |xy\rangle &= |0\rangle \end{aligned} \quad (3.5)$$

In principle, many different bases can be proposed. These can be transformed by employing projectors which are defined from the overlap $\langle a|b\rangle$ where $|a\rangle$ and $|b\rangle$ are basis states of different bases. In the remainder of this Part I special bases will be used to accommodate various forms of hopping between sites.

Operators for single particles

In order to formulate a Hamiltonian for a single particle, let us look at the elementary operators that can act on the LS basis states. Action on other bases, like the XYZ basis, can be expressed in terms of projectors. In principle, only two elementary operators with three components each are possible: \hat{L}^μ, \hat{S}^ν . Combining these operators allows for the construction of many different Hamiltonians.

Let us start with the spin operators \hat{S}^ν that can act on the spin part of the LS basis states. A widely used technique is to represent spin-operators by Pauli matrices σ_ν , i.e.

3. Theoretical modeling

$\hat{S}^\nu = \frac{1}{2}\sigma_\nu$. This is however not the preferred method here as the use of Pauli matrices implies a particular choice of basis which is deliberately left open for now. Applying the operator \hat{S}^z to a given state yields

$$\hat{S}^z |s, m_s\rangle = m_s |s, m_s\rangle \quad (3.6)$$

which reflects our choice of spin basis, i.e. the z -axis of the spin quantization frame.

Action of the other two components \hat{S}^x and \hat{S}^y can better be understood in terms of raising and lowering operators S^+ and S^- which are defined as

$$\begin{aligned} S^+ &= \hat{S}^x + i\hat{S}^y \\ S^- &= \hat{S}^x - i\hat{S}^y \end{aligned} \quad (3.7)$$

They act on the basis states as raising or lowering their respective spin projection quantum number m_s as

$$S^\pm |s, m_s\rangle = \sqrt{s(s+1) - m_s(m_s \pm 1)} |s, m_s \pm 1\rangle \quad (3.8)$$

and in return spin operator components can now be rephrased in terms of raising and lowering operators

$$\begin{aligned} \hat{S}^x &= \frac{1}{2}(S^+ + S^-) \\ \hat{S}^y &= \frac{1}{2i}(S^+ - S^-) \end{aligned} \quad (3.9)$$

The orbital momentum operator \hat{L} can be represented very similarly to the spin operator. The z -component acts as on the ℓ part of the basis as

$$\hat{L}^z |\ell, m_\ell\rangle = m_\ell |\ell, m_\ell\rangle \quad (3.10)$$

and the x and y components can be rewritten again in terms of raising and lowering operators

$$\begin{aligned} \hat{L}^x &= \frac{1}{2}(L^+ + L^-) \\ \hat{L}^y &= \frac{1}{2i}(L^+ - L^-) \end{aligned} \quad (3.11)$$

which act on the basis states as

$$L^\pm |l, m_l\rangle = \sqrt{l(l+1) - m_l(m_l \pm 1)} |l, m_l \pm 1\rangle \quad (3.12)$$

Note that in contrast to the spin quantization frame, the orbital quantization frame is tied to the surrounding crystal field axes which enables the $\ell = 1$ description in the first place.

Building blocks for single-particle Hamiltonians

Now that operators \hat{L}^μ and \hat{S}^ν have been introduced, let us turn our attention to various terms that contribute to the effective Hamiltonian of electrons within the t_{2g} orbitals. In the remainder of the RIXS chapter, especially three terms will be used, those are *magnetic field*, *spin-orbit coupling* as well as *crystal field distortion*.

The magnetic field term can be written as

$$H_B = \vec{B} \cdot \hat{S} \quad (3.13)$$

and describes the coupling of the spin moment to a local magnetic field with strength \vec{B} . It can be written in the spin basis $\{|\uparrow\rangle, |\downarrow\rangle\}$ as a matrix

$$H_B = \frac{1}{2} \begin{pmatrix} B_z & B_x - iB_y \\ B_x + iB_y & -B_z \end{pmatrix} \quad (3.14)$$

where the individual elements have been obtained by computation of overlaps, e.g.

$$\begin{aligned} H_{B,\uparrow\uparrow} &= \langle \uparrow | H_B | \uparrow \rangle \\ &= \langle \uparrow | B_x \hat{S}^x | \uparrow \rangle + \langle \uparrow | B_y \hat{S}^y | \uparrow \rangle + \langle \uparrow | B_z \hat{S}^z | \uparrow \rangle \\ &= B_x \langle \uparrow | \hat{S}^x | \uparrow \rangle + B_y \langle \uparrow | \hat{S}^y | \uparrow \rangle + B_z \langle \uparrow | \hat{S}^z | \uparrow \rangle \end{aligned} \quad (3.15)$$

where elements $\langle \alpha | \hat{S}^\nu | \beta \rangle$ can be resolved using the equations above. The Hamiltonian matrix in Eq. (3.14) has eigenvalues

$$E_{1,2} = \pm \frac{1}{2} \sqrt{B_x^2 + B_y^2 + B_z^2} = \pm \frac{1}{2} |\vec{B}| \quad (3.16)$$

which indicates that a field \vec{B} splits levels by magnitude $|\vec{B}|$ independent of its direction w.r.t. the spin quantization axis.

The spin orbit coupling term couples spin and orbital momentum as

$$H_{SO} = \lambda \hat{L} \cdot \hat{S} \quad (3.17)$$

with coupling of the scale λ . In general, it will also split levels into a $j = 1/2$ singlet and a $j = 3/2$ doublet. The Hamiltonian matrix can again be obtained by evaluating elements $\langle \alpha | H_{SO} | \beta \rangle$ which leads to overlaps of the form $\langle \alpha | \hat{L}^\mu \hat{S}^\mu | \beta \rangle$. In numerics, special attention has to be paid to those matrix elements as $\hat{L}^\mu \hat{S}^\mu$ acts on both subspaces of the LS basis simultaneously.

The last term which is frequently used in the context of t_{2g} orbitals is the crystal field distortion term. This term originates from geometric distortions of the octahedral field away from its cubic limit. Sources of the distortion often lie within the crystal structure

but also may originate from external sources like applied pressure. The correction to the Hamiltonian can be formulated in terms of the effective orbital momentum operators \hat{L}^μ as

$$H_{\text{CF}} = \Delta (\vec{n} \cdot \hat{L})^2 \quad (3.18)$$

where Δ gives the strength and \vec{n} the direction of the distortion. In practice, there are in particular two directions of distortion which are relevant, namely *trigonal* distortion, denoting $\vec{n} = [1, 1, 1]$, and *tetragonal* distortion labeling $\vec{n} = [0, 0, 1]$.

Numerically, the computation of these terms is more involved than e.g. the $\vec{B} \cdot \hat{S}$ term since it contains $\hat{L}_\mu \hat{L}_\nu$ terms which act twice on the same state. One can either write down an elaborate analytical solution by explicitly expressing all possible combinations, or one can resort to rewriting the term with an identity as

$$\langle \alpha | \hat{L}_\mu \hat{L}_\nu | \beta \rangle = \sum_\gamma \langle \alpha | \hat{L}_\mu | \gamma \rangle \langle \gamma | \hat{L}_\nu | \beta \rangle \quad (3.19)$$

in which the computation of elements is then similar to the $\vec{B} \cdot \hat{S}$ term.

Typical Hamiltonians for a single particle

Having established various terms that can contribute to the Hamiltonian of a single particle in the t_{2g} orbitals, let us now turn to discussing the eigenstates of the single-particle Hamiltonian

$$H = -\lambda \hat{L} \cdot \hat{S} - \Delta (\hat{L}^z)^2 \quad (3.20)$$

which contains both spin-orbit coupling as well as a tetragonal crystal field distortion. The analytical solution of this Hamiltonian was given by Ament et.al. in Ref. [11]. In the following, both a discussion of the relevant physics as well as a comparison of the numerics to the analytical solution is given. It is noteworthy that numerics in this context inherently builds the Hamiltonian matrix dynamically by computing elements $\langle \alpha | H | \beta \rangle$ for a given orthonormal single particle basis $|\alpha\rangle$.

The exact solution [11] for the above Hamiltonian consists of three Kramers doublets, f , g and h with energies

$$E_f = \frac{\lambda}{\sqrt{2} \tan(\theta)}, \quad E_g = -\Delta - \frac{\lambda}{2}, \quad E_h = \frac{-\lambda \tan(\theta)}{\sqrt{2}} \quad (3.21)$$

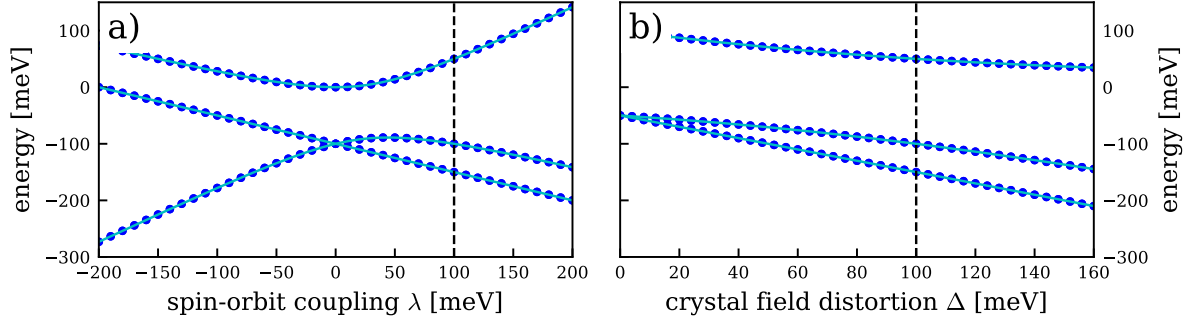


Figure 3.1.: Comparison of single-particle ED - Exact diagonalization (ED) results (blue dots) of a single hole with Hamiltonian $H = -\lambda\hat{L}\cdot\hat{S} - \Delta L_z^2$ in comparison to the exact solution by Ament et al. [11] (cyan line). Panel a) shows variation of the spin-orbit coupling strength λ whereas panel b) shows variation in crystal-field distortion, parameterized by Δ . Vertical lines denote the strength of λ and Δ in the respective other plot.

whose states can be represented in the LS basis as

$$\begin{aligned} |f, \uparrow\rangle &= \sin(\theta) |0, \uparrow\rangle - \cos(\theta) |1, \downarrow\rangle \\ |f, \downarrow\rangle &= \cos(\theta) |-1, \uparrow\rangle - \sin(\theta) |0, \downarrow\rangle \end{aligned}$$

$$\begin{aligned} |g, \uparrow\rangle &= |1, \uparrow\rangle \\ |g, \downarrow\rangle &= |-1, \downarrow\rangle \end{aligned}$$

$$\begin{aligned} |h, \uparrow\rangle &= \cos(\theta) |0, \uparrow\rangle + \sin(\theta) |1, \downarrow\rangle \\ |h, \downarrow\rangle &= \cos(\theta) |0, \downarrow\rangle + \sin(\theta) |-1, \uparrow\rangle \end{aligned}$$

with θ defined by spin orbit coupling and crystal field distortion as

$$\tan(2\theta) = \frac{2\sqrt{2}\lambda}{\lambda - 2\Delta} \quad (3.22)$$

Dependence of the eigenenergies on couplings as well as a comparison to exact diagonalization (ED) results can be seen in Fig. 3.1. For positive spin-orbit coupling, the electronic structure indicates that the hole occupies the separated (mostly $j = 1/2$) Kramers doublet $|f\rangle$ which is separated from rest of bands.

In summary, this section provided an overview over the single-particle physics of a single hole on a single Iridium site. Starting from the definition of basis states to describe the t_{2g} states, the section went on by discussing the relevant single-particle operators which are present in the following sections, Spin-Orbit coupling, Crystal field distortion effects

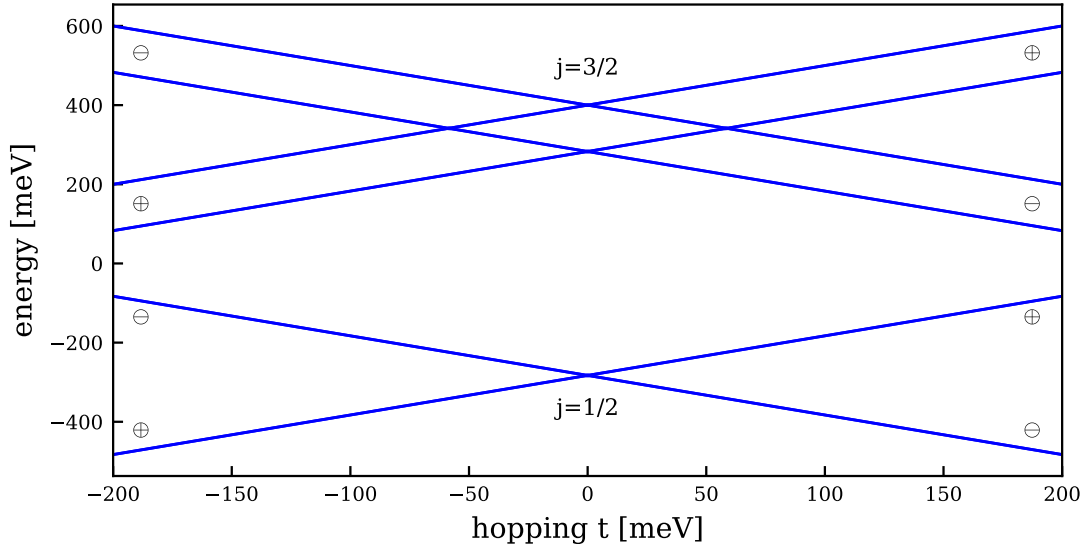


Figure 3.2.: ED of a simple hopping Hamiltonian - Exact diagonalization results of a single hole which is hopping on two sites according to the Hamiltonian given in Eq. (3.28) while still being subject to spin-orbit coupling and crystal-field distortion. The splitting between the $j = 1/2$ and $j = 3/2$ groups can be observed at zero hopping, indicated by labels in the plot. Upon increasing hopping strength t to finite values, a splitting of the single-particle levels into bonding- and antibonding pairs is observed, following the form of Eq. (3.29). The respective sign of the superposition is indicated as a label at each branch.

as well as magnetic field terms.

Upon introducing the various terms, comparisons to the analytic solution of Ament et al. [11] have been performed. These comparisons showed the correctness of numerical implementations on the one side and illustrated the physics of a single hole in the t_{2g} states on the other side. In the following sections, the single-particle description will be the basis for an extension to multiple sites and to multiple particles.

3.2. Single particle physics on many sites

In many materials, electrons within the t_{2g} orbitals are not tightly bound to their respective atomic core, but can delocalize among several sites within a given cluster. This process makes it necessary to extend the single-particle formalism developed before to more than one site. To do so, two things have to be done. First of all, the basis has to be extended to more than one site. Second, a new type of operator, the hopping operator, is introduced to enable hopping between sites of the same cluster.

Extending the already known LS and XYZ bases to more than one site is achieved by

adding a new quantum number which indicates the site. States are transforming as

$$|\alpha\rangle \mapsto |\alpha\rangle \otimes |i\rangle \hat{=} |\alpha, i\rangle \quad (3.23)$$

where $|\alpha\rangle$ describes an LS or XYZ basis state and i is a site label. Due to this additional structure, operators are local, i.e. diagonal in the new quantum number, since

$$\langle \alpha, i | \beta, j \rangle = \langle \alpha | \beta \rangle \delta_{ij} \quad (3.24)$$

which means that eigenenergies are only replicated for each site.

In contrast to the on-site single-particle operators, the hopping operator connects states on different sites. Usually it is written in Fock-space language in the form

$$H \sim \sum_{i,j} \sum_{\alpha,\beta} t_{ij}^{\alpha\beta} c_i^{\alpha\dagger} c_j^\beta \quad (3.25)$$

which takes a particle from orbital β on site j and moves it to orbital α on site i . In a single-particle description, this would result in matrix elements of the form

$$\langle \alpha, i | H_{\text{hop.}} | \beta, j \rangle = t_{ij}^{\alpha\beta} \quad (3.26)$$

or alternatively writing the hopping operator as

$$H_{\text{hop.}} = \sum_{i,j} \sum_{\alpha,\beta} t_{ij}^{\alpha\beta} |\alpha, i\rangle \langle \beta, j| \quad (3.27)$$

Generically, hopping leads to splitting the degeneracy of levels on multiple sites into so-called bonding and antibonding states. To elaborate on this, let us consider an example system with local spin-orbit coupling and crystal field distortion on two sites, i.e. local Hamiltonians in the form of Eq. (3.20), as well as hopping that preserves the eigenstate

$$\langle \alpha, 1 | H_{\text{hop.}} | \beta, 2 \rangle = t \delta_{\alpha\beta} \quad (3.28)$$

Exact diagonalization results of this example system are shown in Fig. 3.2. For finite hopping strength t , every level is split into a bonding and a antibonding combination of different energy. The corresponding wavefunctions have the form

$$\begin{aligned} |\psi_{\alpha,1}\rangle &\sim |\alpha, 1\rangle + |\alpha, 2\rangle & E_{\alpha,1} &= E_\alpha + t \\ |\psi_{\alpha,2}\rangle &\sim |\alpha, 1\rangle - |\alpha, 2\rangle & E_{\alpha,2} &= E_\alpha - t \end{aligned} \quad (3.29)$$

For the examples discussed in the context of this thesis, *effective* hopping between the Ir d -orbitals takes either place as direct Ir-Ir overlap or as indirect hopping on the Ir-O-Ir hopping paths via shared oxygen atoms in the IrO₆ crystal cages. Depending on the local IrO₆ geometry, several distinct hoppings are thus plausible [12].

3.3. Multi particle physics

In most situations, the physics of a single particle does not correctly describe all effects emerging from the local cluster of atoms, which is due to effects untreated on the single-particle level such as interactions. In the following, the language of second quantization and Fock space will be used to describe both single-particle and multi-particle operators in the context of this chapter.

Conventional many-particle wavefunctions

Describing more than one particle with conventional quantum mechanics can be facilitated by expanding the Hilbert space utilizing the Kronecker product.

$$\mathbb{H}_n = \mathbb{H}_1 \otimes \mathbb{H}_1 \otimes \cdots \otimes \mathbb{H}_1 \quad (n \text{ copies}) \quad (3.30)$$

On the level of wavefunctions this is equivalent to giving all of the many (distinguishable) particles the ability to delocalize in the single particle Hilbert space independently from any other particle. In short, wavefunctions are equipped with more coordinates to account for the growth in particle number

$$|\psi\rangle = \sum \alpha_{j_1 j_2 \dots j_n} |a_{j_1}\rangle |a_{j_2}\rangle \dots |a_{j_n}\rangle \quad (3.31)$$

The increase in Hilbert space dimension is exponential in particle number which can be seen as similar to how the possible number of states in a classical thermodynamic description is growing exponentially in particle number. However, within these many states, some might be forbidden by particle exchange statistics.

In principle, the exchange of indistinguishable particles has to leave the probability density as it is. Wavefunctions can therefore only change up to a sign

$$P_{ij}\psi = \psi e^{i\varphi} \quad (3.32)$$

This sign change in particle exchange defines the two particle classes of bosons and fermions. Bosons have a relative sign of $e^{i\varphi} = +1$ under particle exchange, the wavefunction remains the same if one exchanges two bosons $\psi(r_1, r_2) = +\psi(r_2, r_1)$. Fermions on the other hand have a negative exchange sign of $e^{i\varphi} = -1$, i.e. the wavefunction changes sign under particle exchange $\psi(r_1, r_2) = -\psi(r_2, r_1)$. Therefore, fermions cannot occupy the same state with more than one particle, a property also known as the Pauli principle.

Second quantization and Fock space

In most applications, the use of explicit wavefunctions is not feasible and one instead utilizes an effective approach known as second quantization. In this formalism, one takes

the single-particle basis $|\alpha\rangle$ of a system as a starting point and occupies each state α by many particles n_α . The relevant information of a given state is then not encoded in a Schrödinger-like wavefunction consisting of many single-particle terms but given by how many particles occupy which single-particle state. Multi-particle states can therefore be written as

$$|\psi\rangle = \sum_{n_1 n_2 \dots} c_{n_1 n_2 \dots} |n_1, n_2, \dots\rangle \quad (3.33)$$

with basis states in this new number basis

$$|n_1, n_2, n_3, \dots\rangle \in \mathcal{F} \quad (3.34)$$

which is a basis of the so called Fock space \mathcal{F}

$$\mathcal{F} = \mathcal{F}_0 \oplus \mathcal{F}_1 \oplus \mathcal{F}_2 \oplus \dots \quad (3.35)$$

Here, $\mathcal{F}_N = \mathbb{H}_N^{A/S}$ describes the Hilbert spaces for a fixed number of bosons and fermions respectively. On top of these states, an additional vacuum state $|\text{vac}\rangle$ is included as a state without particles $|\text{vac}\rangle \equiv |0, \dots, 0\rangle$. This state is not part of standard Schrödinger-like quantum mechanics but necessary for the construction of Fock space. In the present case, the particles are electrons and therefore fermions, such that the single-particle occupation numbers are restricted to $n_\alpha = 0, 1$, i.e. the well known Pauli principle holds. Last but not least, it is noteworthy that basis states in Fock space are orthonormal, i.e.

$$\langle \dots n'_\alpha \dots | \dots n_\alpha \dots \rangle = \prod_\alpha \delta(n'_\alpha, n_\alpha) \quad (3.36)$$

On top of the description of individual states, raising and lowering operators are used to connect states with different occupations. i.e. for inserting or removing particles. Their actions on general Fock states are

$$\text{for bosons: } c_i^\dagger |n_1, n_2, \dots, n_i, \dots\rangle = \sqrt{n_i + 1} |n_1, n_2, \dots, n_i + 1, \dots\rangle \quad (3.37)$$

$$\text{for fermions: } c_i^\dagger |n_1, n_2, \dots, 0, \dots\rangle = (-1)^{\sum_{j < i} n_j} |n_1, n_2, \dots, 1, \dots\rangle \quad (3.38)$$

$$c_i^\dagger |n_1, n_2, \dots, 1, \dots\rangle = 0 \quad (3.39)$$

$$\text{for bosons: } c_i |n_1, n_2, \dots, n_i, \dots\rangle = \sqrt{n_i} |n_1, n_2, \dots, n_i - 1, \dots\rangle \quad (3.40)$$

$$\text{for fermions: } c_i |n_1, n_2, \dots, 1, \dots\rangle = (-1)^{\sum_{j < i} n_j} |n_1, n_2, \dots, 0, \dots\rangle \quad (3.41)$$

$$c_i |n_1, n_2, \dots, 0, \dots\rangle = 0 \quad (3.42)$$

By utilizing this notation, a generic Fock state can thus be written as creation of particles from the vacuum

$$|n_1, n_2, \dots\rangle = \prod_i \frac{1}{\sqrt{n_i!}} (c_i^\dagger)^{n_i} |\text{vac}\rangle \quad (3.43)$$

In our context, we will discuss the creation and annihilation of electrons and holes which will be represented by the following notation: d_α^\dagger creates an electron and a_α^\dagger creates hole in state α . Annihilation is similar as d_α removes an electron and a_α removes a hole from state α . Since electron creation is the same as hole annihilation, those operators can be brought into correspondence as

$$d_\alpha^\dagger = a_\alpha, \quad d_\alpha = a_\alpha^\dagger \quad (3.44)$$

Similarly, electron occupation $n_\alpha = d_\alpha^\dagger d_\alpha$ in state α is related to the corresponding hole occupation $h_\alpha = a_\alpha^\dagger a_\alpha$ in the same state as

$$n_\alpha = 1 - h_\alpha \quad (3.45)$$

In the remainder of this chapter, calculations will be mostly carried out in the hole picture as the total number of particles will then be lower.

Single-particle operators

Having established the description of Fock space basis states, let us turn our attention to the Fock space representation of single-particle operators. In particular, it is necessary to formulate the aforementioned operators describing spin-orbit coupling, magnetic field and crystal field distortion.

As mentioned in the theory part, any single-particle operators $A^{(1)}$ has a Fock space representation A which can be written as

$$A = \sum_{\alpha,\beta} \langle \alpha | A^{(1)} | \beta \rangle a_\alpha^\dagger a_\beta. \quad (3.46)$$

Here, matrix elements $\langle \mu | A^{(1)} | \nu \rangle$ are assumed to be known, they can e.g. be computed as discussed in the single particle section.

When performing numerical exact diagonalization, it is necessary to obtain a matrix representation of these operators in Fock space. In principle, one can use the same strategy as for single-particle operators by calculating matrix elements for Fock space states μ and ν explicitly in terms of the overlap

$$\begin{aligned} A_{\mu\nu} &= \langle \mu | A | \nu \rangle = \langle \dots n_\gamma^\mu \dots | A | \dots n_\gamma^\nu \dots \rangle \\ &= \sum_{\alpha,\beta} \langle \alpha | A^{(1)} | \beta \rangle \langle \dots n_\gamma^\mu \dots | a_\alpha^\dagger a_\beta | \dots n_\gamma^\nu \dots \rangle \end{aligned} \quad (3.47)$$

To evaluate this expression, one has to be able to calculate elements of the form $\langle \mu | a_\alpha^\dagger a_\beta | \nu \rangle$ for Fock space basis states $|\mu\rangle$ and $|\nu\rangle$ which is in principle possible.

Multi-particle operators and interaction Hamiltonian

So far, particles in Fock space occupy single-particle orbitals but are non-interacting apart from the fermionic hard-core repulsion due to the Pauli principle. Interactions in many different forms naturally appear as quartic terms in the Hamiltonian. In the context of this chapter, let us focus on a specific formulation of Coulomb repulsion, suitable for discussing the t_{2g} orbitals in most of the relevant atoms.

Coulomb interaction in general is a repulsive (attractive) force between particles of the same (different) electrical charge which decays as $1/r^2$ in distance. Inherently, modeling Coulomb repulsion on the level of wavefunctions becomes a real challenge and is disregarded in this context. Instead one formulates an effective interaction Hamiltonian in second quantization which takes into account repulsion between electrons on the same site [13]. This special form of the interaction Hamiltonian is formulated in the electron picture as

$$\begin{aligned}
H_{\text{int}} &= U_1 \sum_{i,\alpha} n_{i\alpha\uparrow} n_{i\alpha\downarrow} \\
&+ \frac{1}{2} (U_2 - J_H) \sum_{i,\alpha \neq \alpha', \sigma} n_{i\alpha\sigma} n_{i\alpha'\sigma} + U_2 \sum_{i,\alpha \neq \alpha'} n_{i\alpha\uparrow} n_{i\alpha'\downarrow} \\
&+ J_H \sum_{i,\alpha \neq \alpha'} d_{i\alpha\uparrow}^\dagger d_{i\alpha\downarrow}^\dagger d_{i\alpha'\downarrow} d_{i\alpha'\uparrow} - J_H \sum_{i,\alpha \neq \alpha'} d_{i\alpha\uparrow}^\dagger d_{i\alpha\downarrow} d_{i\alpha'\downarrow}^\dagger d_{i\alpha'\uparrow}
\end{aligned} \tag{3.48}$$

explicitly distinguishing between orbitals $\alpha = x, y, z \hat{=} yz, xz, xy$ on sites i with spin $\sigma = \uparrow, \downarrow$. The interaction Hamiltonian is parameterized in terms of Hubbard interactions U_1 and U_2 , Hund's coupling J_H . It is common to make another assumption on this interaction Hamiltonian in terms of the symmetries of the surrounding crystal field. For a cubic crystal field, one has the relation

$$U_1 = U_2 + 2J_H. \tag{3.49}$$

This makes it possible to rename U_1 to U and calculate U_2 from $U = U_1$ and J_H which reduces the number of interaction parameters to two.

Concerning numerical implementations of the above Hamiltonian, one again needs to compute explicit matrix elements. In principle, the same strategy as from previous sections is employed, i.e. calculating the matrix elements explicitly as the overlap

$$H_{\text{int},\mu\nu} = \langle \mu | H_{\text{int}} | \nu \rangle = \langle \dots n_\gamma^\mu \dots | H_{\text{int}} | \dots n_\gamma^\nu \dots \rangle$$

for Fock space states μ and ν . This leads to expressions of the form

$$\langle \dots n_\gamma^\mu \dots | a_\alpha^\dagger a_\beta a_\varphi^\dagger a_\theta | \dots n_\gamma^\nu \dots \rangle \quad \text{or} \quad \langle \dots n_\gamma^\mu \dots | a_\alpha^\dagger a_\beta^\dagger a_\varphi a_\theta | \dots n_\gamma^\nu \dots \rangle$$

which one has to evaluate numerically for the respective basis representation.

To compare the numerical and analytical data, let us discuss some results found upon investigation of the interaction Hamiltonian [13]. The following energies for four to six

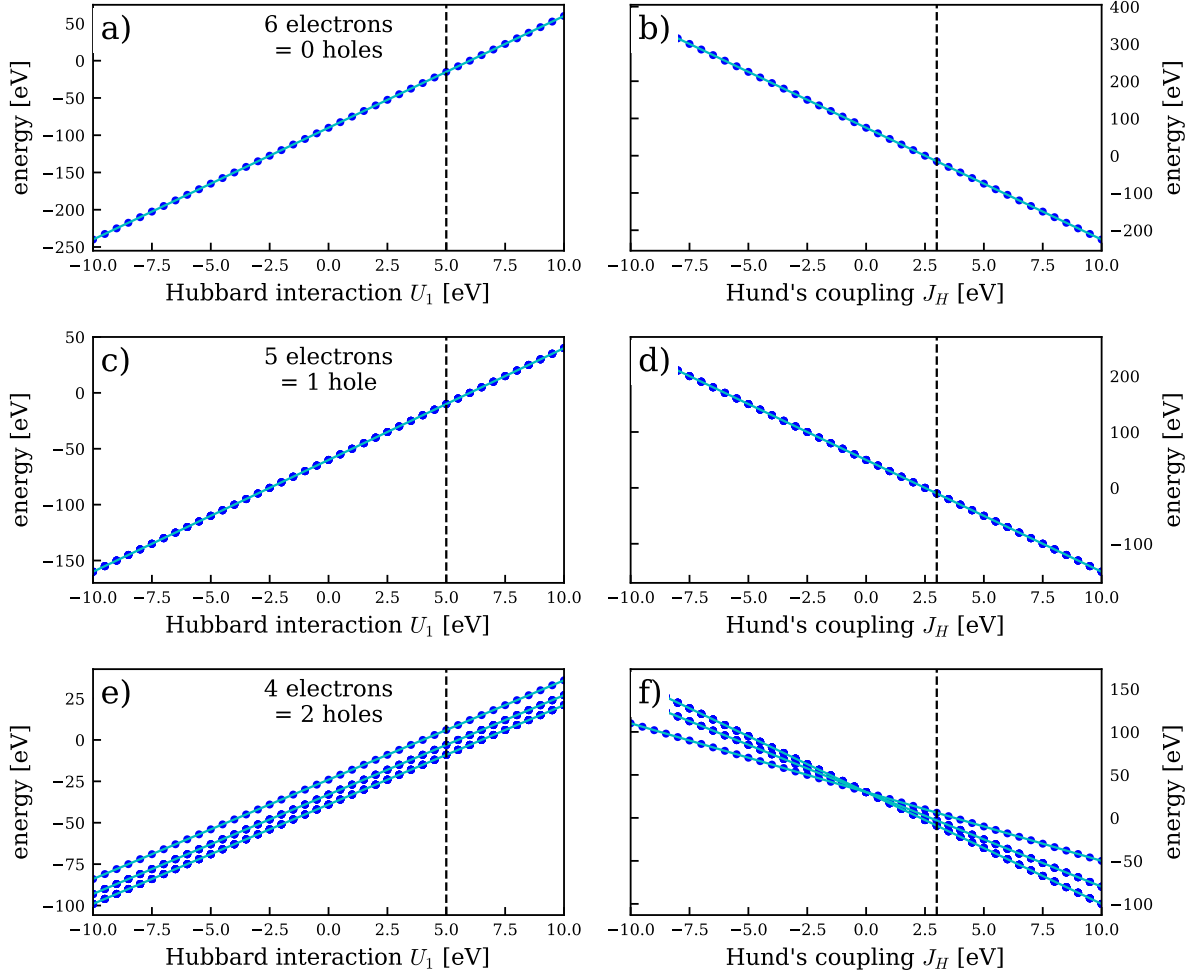


Figure 3.3.: Comparison of multi-particle ED - Exact diagonalization results of the interaction Hamiltonian given in Eq. (3.48) for varying Hubbard interaction U_1 as well as Hund's coupling J_H . ED results (blue dots) are compared to the exact solution by Perkins et al. [13] (cyan line). Vertical lines denote the strength of U_1 and J_H in the respective other plot. All calculations are carried out in the cubic limit, i.e. with parameters satisfying the relation $U_1 = U_2 + 2J_H$. Panels a) and b) show results for the full t_{2g} subspace, i.e. for zero holes, panels c) and d) for a single hole and panels e) and f) for two holes.

electrons (two to zero holes) have been found:

$$\begin{aligned}
 E_{0h} &= 15U_2 \\
 E_{1h} &= 10U_2 \\
 E_{2h}^{(1)} &= 6U_2 - J_H \\
 E_{2h}^{(0)} &= 6U_2 + J_H \\
 E_{2h}^{(00)} &= 6U_2 + 4J_H
 \end{aligned} \tag{3.50}$$

These energies are depicted with their parametric dependencies in Fig. 3.3 where they are also compared with exact diagonalization results of the same Hamiltonian.

Concerning explicit eigenstates, for zero and one hole, the situation is simple. In case of zero holes, the Hilbert space only has one dimension and there is only a single state with 6 electrons occupying the 6 possible t_{2g} states whose energy is $E_{0h} = 15U_2$ due to interaction of electrons. In the case of a single hole, one finds 6 states with 5 electrons occupying any but one of the 6 possible t_{2g} states (or alternatively 1 hole occupying any of the 6 t_{2g} states). The single energy of $E_{1h} = 10U_2$ is again originating from electron-electron interaction in the remaining orbitals. All states must however have the same energy, since viewed from the hole perspective there is only a single particle and no preferred orbitals.

For two holes within the t_{2g} states, the situation is more complex and it is worth discussing the findings of different eigenstates. In principle, there are $(6 \cdot 5)/2 = 15$ possibilities to occupy six states with two holes, i.e. 15 two-hole states in total. These states fall into the following categories:

- One symmetric state with energy $E_{2h}^{(00)}$ described by singlet pairs in the same orbitals

$$|2h, 1\rangle = \frac{1}{\sqrt{3}} \left(a_{x\downarrow}^\dagger a_{x\uparrow}^\dagger + a_{y\downarrow}^\dagger a_{y\uparrow}^\dagger + a_{z\downarrow}^\dagger a_{z\uparrow}^\dagger \right) |\text{vac}\rangle$$

- Two anti-symmetric states with energy $E_{2h}^{(0)}$ also described by singlet pairs in the same orbitals

$$|2h, 2\rangle = \frac{1}{\sqrt{2}} \left(a_{x\downarrow}^\dagger a_{x\uparrow}^\dagger - a_{y\downarrow}^\dagger a_{y\uparrow}^\dagger \right) |\text{vac}\rangle$$

$$|2h, 3\rangle = \frac{1}{\sqrt{6}} \left(a_{x\downarrow}^\dagger a_{x\uparrow}^\dagger + a_{y\downarrow}^\dagger a_{y\uparrow}^\dagger - 2a_{z\downarrow}^\dagger a_{z\uparrow}^\dagger \right) |\text{vac}\rangle$$

- Three states with energy $E_{2h}^{(0)}$ described by singlet pairs in different orbitals

$$\begin{aligned}
 |2h, 4\rangle &= \frac{1}{\sqrt{2}} (a_{x\downarrow}^\dagger a_{y\uparrow}^\dagger - a_{x\uparrow}^\dagger a_{y\downarrow}^\dagger) |\text{vac}\rangle \\
 |2h, 5\rangle &= \frac{1}{\sqrt{2}} (a_{y\downarrow}^\dagger a_{z\uparrow}^\dagger - a_{y\uparrow}^\dagger a_{z\downarrow}^\dagger) |\text{vac}\rangle \\
 |2h, 6\rangle &= \frac{1}{\sqrt{2}} (a_{z\downarrow}^\dagger a_{x\uparrow}^\dagger - a_{z\uparrow}^\dagger a_{x\downarrow}^\dagger) |\text{vac}\rangle
 \end{aligned}$$

- Nine states with energy $E_{2h}^{(1)}$ described by triplet pairs in different orbitals

$$\begin{aligned}
 |2h, 7\rangle &= \frac{1}{\sqrt{2}} (a_{x\downarrow}^\dagger a_{y\uparrow}^\dagger + a_{x\uparrow}^\dagger a_{y\downarrow}^\dagger) |\text{vac}\rangle \\
 |2h, 8\rangle &= a_{x\uparrow}^\dagger a_{y\uparrow}^\dagger |\text{vac}\rangle \\
 |2h, 9\rangle &= a_{x\downarrow}^\dagger a_{y\downarrow}^\dagger |\text{vac}\rangle \\
 |2h, 10\rangle &= \frac{1}{\sqrt{2}} (a_{y\downarrow}^\dagger a_{z\uparrow}^\dagger + a_{y\uparrow}^\dagger a_{z\downarrow}^\dagger) |\text{vac}\rangle \\
 |2h, 11\rangle &= a_{y\uparrow}^\dagger a_{z\uparrow}^\dagger |\text{vac}\rangle \\
 |2h, 12\rangle &= a_{y\downarrow}^\dagger a_{z\downarrow}^\dagger |\text{vac}\rangle \\
 |2h, 13\rangle &= \frac{1}{\sqrt{2}} (a_{z\downarrow}^\dagger a_{x\uparrow}^\dagger + a_{z\uparrow}^\dagger a_{x\downarrow}^\dagger) |\text{vac}\rangle \\
 |2h, 14\rangle &= a_{z\uparrow}^\dagger a_{x\uparrow}^\dagger |\text{vac}\rangle \\
 |2h, 15\rangle &= a_{z\downarrow}^\dagger a_{x\downarrow}^\dagger |\text{vac}\rangle
 \end{aligned}$$

All of these states, with energies shown in Fig. 3.3, can again be found in results of the numerical calculations, making the comparison to Ref. [13] an ideal test case for any numerical implementation.

3.4. Resonant inelastic X-ray scattering (RIXS)

In the following, let us discuss how to use the energies and states obtained from exact diagonalization to emulate the RIXS process and obtain RIXS spectra that can be compared to experimental data. After a brief introduction, we will first look at photon-assisted transitions in general and then concentrate more on the specific case of the RIXS process. Focus will be on the involved dipole operators and their specific form for RIXS between the Iridium $2p$ core and $5d$ t_{2g} levels. Finally, we will discuss the necessary geometry and perform a complete example calculation of how a spectrum can be computed numerically.

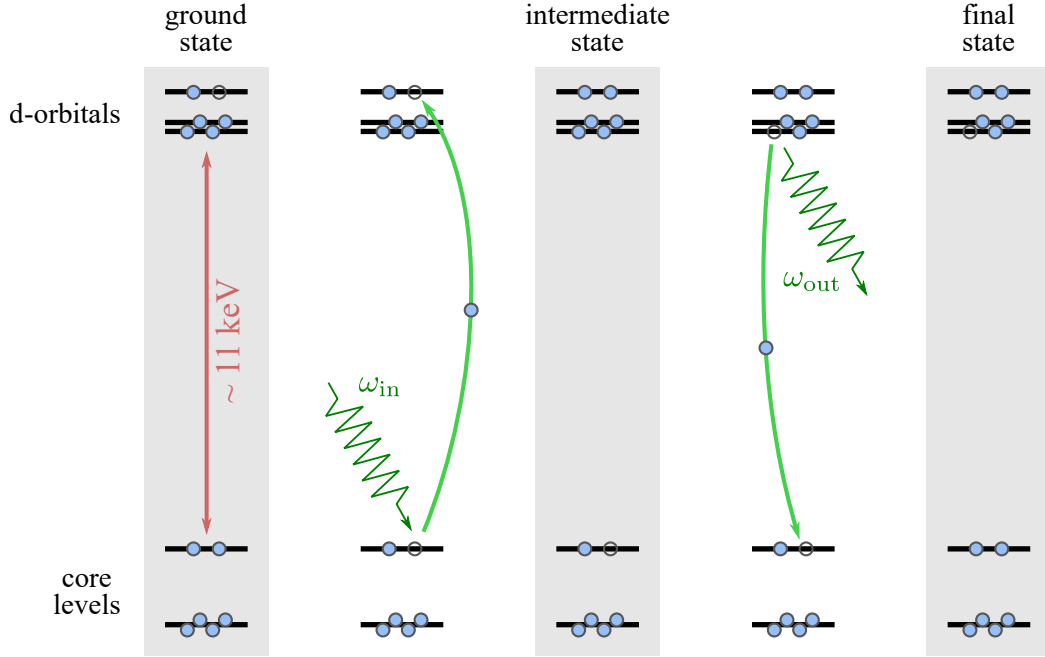


Figure 3.4.: RIXS process - Sketch illustrating the RIXS process. In the ground state, core-levels are filled and there are partially empty states within the d -levels. Exciting a core electron is achieved by resonant absorption of incoming X-rays of frequency ω_{in} , leading to an intermediate state with a vacancy in the core-levels. This core hole is then subsequently filled by de-exciting another electron from the d -levels, in the process emitting X-rays with frequency ω_{out} . In total, the process yields a transition within the d -levels which can be resolved by comparing incoming and outgoing X-ray frequencies as $\Delta E = \omega_{out} - \omega_{in}$.

The RIXS technique

Resonant inelastic X-ray scattering (RIXS) is a spectroscopy technique utilizing X-rays which are absorbed and re-emitted by the material. Filtering incoming or outgoing X-ray photons depending on their polarization, energy and momentum allows to determine the excitation structure of a material to great detail. In the study of strongly correlated materials, RIXS is a highly used technique, enriching the toolkit of available spectroscopy flavors. In the context of this thesis, the recent extension of RIXS interferometry [9] is discussed and employed to identify quasi-molecular excitations.

The entire RIXS process, depicted in Fig. 3.4, can be formulated as follows. First, a core electron is resonantly excited to a vacancy in an excited state by absorbing an incident X-ray photon. Following this transition, another electron falls down to the core vacancy by emitting another X-ray photon. The discrepancy in incoming and outgoing energies of these photons will then correspond to the difference in energies of these respective states. From a broad perspective, the RIXS process can therefore also be understood in making an

internal excitation between states which does not involve the core states. In the examples here, the excited states are the t_{2g} states whereas the core-levels are typically Ir $2p$ states.

Photon-assisted transition amplitudes

Let us start the discussion of RIXS transitions from the broader perspective of a generic quantum system described by some Hamiltonian H . Under perturbation of another operator H' , transitions between states α will occur. The rates of these transitions can be described by Fermi's golden rule as

$$\Gamma(i \rightarrow f) = \langle f | \hat{H}' | i \rangle \quad (3.51)$$

where $\Gamma(i \rightarrow f)$ describes the rate to go from $|i\rangle$ to $|f\rangle$.

In the special case of RIXS, the first part of a transition occurs by exciting a $2p$ core electron to the $5d$ t_{2g} levels by absorbing a resonant X-ray photon. The amplitude that this process occurs under absorption of an X-ray photon of frequency ω therefore is

$$A(i \rightarrow f, \omega) = \langle f | \hat{D} | i \rangle \delta(\omega, E_f - E_i) \quad (3.52)$$

where the perturbation to the Hamiltonian is now given in terms of the dipole operator \hat{D} .

For a given photon of momentum \vec{q} and polarization $\vec{\epsilon}$, the dipole operator \hat{D} can be given explicitly as

$$\hat{D} = \vec{\epsilon} \cdot \hat{r} e^{i\vec{q} \cdot \vec{R}} \quad (3.53)$$

where \hat{r} is the position operator and \vec{R} is the position at which the transition occurs. For the RIXS process discussed in the context of this thesis, further simplifications can be made [11]. If an electron is excited from the core p shell to the d shell t_{2g} orbitals, the dipole operator can be defined as

$$\hat{r} \cdot \vec{\epsilon} = \sum_{\alpha, \beta, \sigma} \langle 5d_{\alpha} | \hat{r} | 2p_{\beta} \rangle \cdot \vec{\epsilon} d_{\alpha, \sigma}^{\dagger} p_{\beta, \sigma} \quad (3.54)$$

since both core and t_{2g} states are described by the same angular momentum. In this expression, the only non-zero elements are

$$\begin{aligned} \langle x | \hat{y} | z \rangle &= \langle z | \hat{y} | x \rangle = 1 \\ \langle y | \hat{z} | x \rangle &= \langle x | \hat{z} | y \rangle = 1 \\ \langle z | \hat{x} | y \rangle &= \langle y | \hat{x} | z \rangle = 1 \end{aligned} \quad (3.55)$$

which allow for the calculation of an explicit matrix representation of $\hat{r} \cdot \vec{\epsilon}$ and \hat{D} .

RIXS transition amplitudes for a single hole on a single site

The entire RIXS transition can be formulated by combining two of the core- t_{2g} transitions described before to bring an electron from the core to the t_{2g} states and another one back to the core. The net transition in this case is then only within the t_{2g} states and can be detected by a mismatch in absorbed and emitted X-ray frequency, i.e. the weight of inelastic scattering processes.

Let us focus first on materials in a d^5 configuration which allow for a much easier description. In these materials, the t_{2g} levels are partially filled with electrons leaving only a single vacancy. Thus they can alternatively be written as occupied by a single hole, allowing a single-particle description. During the RIXS process, this hole is excited into the core levels and falls back to any of the t_{2g} levels.

For a single hole within the t_{2g} states, the transition amplitude of this entire process therefore can be written as

$$A(i \rightarrow f) = \sum_p \langle f | \hat{D}_{\text{out}} | p \rangle \langle p | \hat{D}_{\text{in}} | i \rangle \quad (3.56)$$

where $|i\rangle$ and $|f\rangle$ now describe t_{2g} states and p enumerates all available core p levels.

It is important to distinguish between *all* core levels and the *available* core levels in this case since strong spin-orbit coupling within the core splits the p levels into $j = 1/2$ and $j = 3/2$ multiplets which are so far apart in energy that they can be addressed individually by the incoming X-ray beams. The projection of the hole on the core multiplet is called *core-hole projection* and the two RIXS processes, one utilizing the $j = 1/2$ and the other utilizing the $j = 3/2$ multiplet, are called L_2 -edge and L_3 -edge RIXS.

RIXS transition amplitudes for many particles on larger clusters

In principle, most materials have clusters with more than a single hole on a single site which is involved in the RIXS process. Let us therefore discuss the influence of either more sites or more holes during the process, starting with more holes, i.e. more particles. Since exciting a hole to the core levels is non-adiabatically changing the quantum state, relaxation effects for this non-equilibrium state have to be generally accounted for if more than a single hole is occupying the t_{2g} states, i.e. for 4 electrons or less. These relaxation effects will take place once the excitation takes place and will alter the state to which the single hole drops back from the core.

For simplicity and because many of the investigated systems have only a single particle per site, the effects of the intermediate state are neglected in this case. One can argue that this corresponds to a *fast excitation approximation* in which the lifetime of the intermediate state is assumed to be smaller than the relaxation time of the system.

Within the fast excitation approximation, it is straight forward to generalize the dipole

transition operator to the framework of many particles. First, both of the excitation and following de-excitation as well as the core-hole projection are grouped into a single single-particle operator, called simply \hat{D}^L for the edge L (either L_2 or L_3), written as

$$\hat{D}^L = \sum_{p \in L} \hat{D}_{\text{out}} |p\rangle \langle p| \hat{D}_{\text{in}} \quad (3.57)$$

Then, a suitable many-particle dipole operator in second quantization can be defined as

$$\hat{D}^L = \sum_{\alpha, \beta} \hat{D}_{\alpha\beta}^L a_{\beta}^{\dagger} a_{\alpha} \quad (3.58)$$

which can be implemented numerically like other operators discussed before.

In case the cluster has more than a single site, additional dipole operators have to be constructed on each site since a transition can in principle occur on any of these sites. The final dipole operator can then be written as the sum of individual dipole operators on all sites j of the cluster

$$\hat{D}^L = \sum_j \hat{D}_j^L \quad (3.59)$$

where positions \vec{R}_j within the transition amplitudes have to represent the position of sites j in the cluster.

Transition intensities and calculation of experimental spectra

Replicating an experimental measurement means not to compare transition amplitudes but rather *intensities* $I(\Delta E)$. They take the form

$$I(\Delta E) = \sum_{i, f} p_i |A(i \rightarrow f)|^2 \delta(\Delta E - (E_f - E_i)) \quad (3.60)$$

and thereby sum over different transition amplitudes between various t_{2g} states $|i\rangle$ and $|f\rangle$ at energies E_i and E_f . The intensity is dependent on the difference in incoming and outgoing X-ray energy $\Delta E = \hbar(\omega_{\text{out}} - \omega_{\text{in}})$ which has to match the difference in eigenenergies.

In the expression for the transition intensities, another variable p_i appears which describes the probability that the system is in state $|i\rangle$. Usually one would consider thermal occupation for the p_i , however in the following examples the temperatures will be very low so that one can consider the system to be in its ground state, i.e. $p_i = 0$ for all states higher in energy.

Also, despite assuming a sharp δ -like response in deposited energy, the true transition sensitivity has a finite line width and shape. There are two possible reasons for a finite width in general. First, the intrinsic lifetime of the excitation corresponds to a finite width in energy. Second, the detector only has a finite resolution in energy. Since in current RIXS

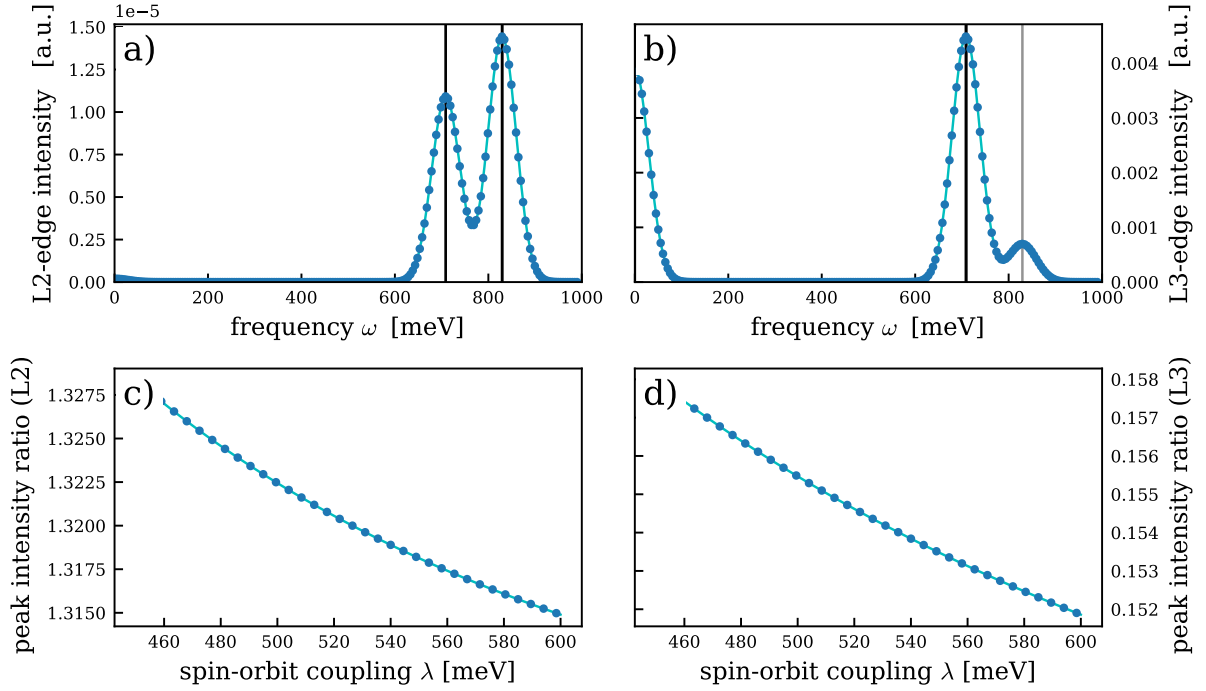


Figure 3.5.: Single hole numerical RIXS spectra - Calculated RIXS spectra from dipole transition amplitudes at both the L2 and the L3 edge for one hole with spin orbit coupling and crystal field distortion. Panels a) and b) show the bare spectra, whereas panels c) and d) show relative intensities of the two peaks. All plots compare numerical results (blue dots) to the analytical solution by Ament et al. [11] (solid cyan line).

experiments, the precision is still much larger than the intrinsic width effect, the detector is actually the main source of line shape. Thus in the following, let us use a Gaussian line shape with around 25 meV of broadening corresponding to the experimental resolution.

Altogether, this allows to numerically compute RIXS spectra. These spectra are graphs which display intensity as function of deposited X-ray energy ΔE , sometimes written as a loss-frequency ω .

Example calculations

To illustrate the process of RIXS spectrum calculations, let us consider an example system of a single hole. In the following, the RIXS spectrum of this system is calculated and compared to the analytical solution by Ament et al. [11]. Note that here we focus purely on the transitions as the exact eigenstates and energies for a single hole in the t_{2g} states have already been discussed in a previous section.

Performing the steps outlined before yields spectra shown in Fig. 3.5. The calculated in-

tensity is shown for both the L2 as well as L3 edges. Apart from the agreement between numerical solution and analytical formulas, one can make some qualitative observations. Both spectra show two transition peaks which are clearly resolved. They describe transitions from $j = 1/2$ into the two $j = 3/2$ states, which are split by crystal field distortion. Such transitions are also called spin-orbit excitons and play an important role later on in the chapter.

Comparing the L2 to the L3 edge, one can observe that the L2 edge carries only a fraction of the total weight compared to the L3 edge. This stems from the ground state largely being a $j = 1/2$ state which suppresses transitions to the core- $j = 1/2$.

For the sake of comparison one can even go a step further and compare relative peak heights of the two spin-orbit excitations. Fig. 3.5 also shows such relative peak heights in dependence of the Hamiltonian parameters spin-orbit coupling λ and crystal field distortion Δ .

Concerning the process of how the spectra are calculated, there are clear distinctions between the numerical and analytical approach. From an analytical perspective, the transition amplitudes can be written down exactly, simplified by the fact that both core and t_{2g} levels can be written as $L = 1$ states. In their paper [11], Ament et al. give transition amplitudes within t_{2g} states as $B_{\sigma_i\sigma_f}^{\alpha_i\alpha_f}$ with $\alpha_i = f, g, h$ describing the orbital and $\sigma_i = \uparrow, \downarrow$ describing the remaining Kramers degeneracy. Then for both the L2 and L3 edge, Ament et al. give exact relations of how amplitudes B depend on both Hamiltonian parameters λ and Δ as well as the polarization characteristics of incoming and outgoing X-rays.

In the numerical solution, elements are more modular. Whereas the analytical solution required individual derivations for the transitions, in the numerics all of them are treated on an equal footing. Most of the formulas are explicitly executed within the code and therefore do not rely on upfront derivations.

Dependency of spectra on geometry

As already hinted before, the experimental spectra are very sensitive to the experimental geometry and the alignment of X-ray beams. In principle, the geometry enters the dipole operators in form of the polarization which is always perpendicular to the beam momentum. Furthermore, for systems with two or more sites, the transferred momentum direction also plays a role as it can lead to interference effects discussed at length in this chapter.

Some basic effects of different sample orientations relative to the beam can be found in Fig. 3.6 for both the L2 and L3 edges. There, the numerically calculated spectra are compared for tilting the sample along various principle axes in the lab frame. It can be seen that rotations of the sample not only change relative heights of the transition peaks but can also lead to a complete suppression of the transition as well.

It is important to keep in mind the effects depicted in Fig. 3.6, since in the following

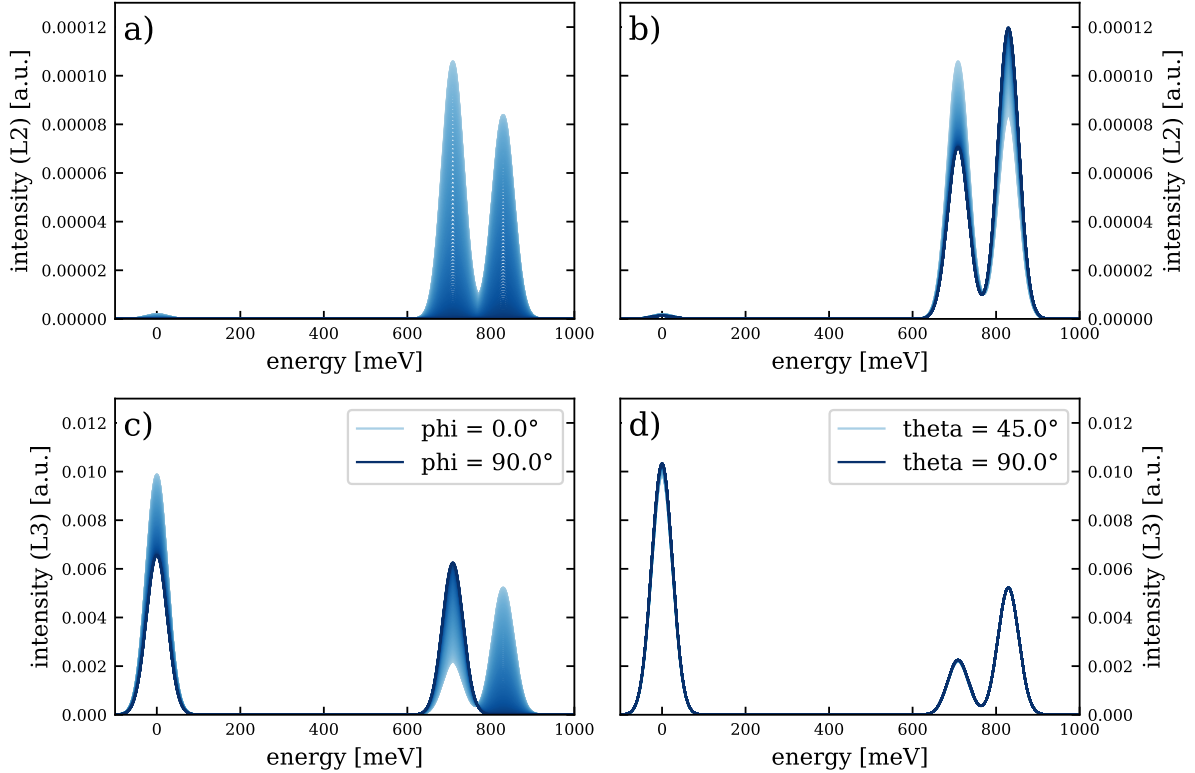


Figure 3.6.: Geometric influence on numerical RIXS spectra - Calculated RIXS spectra from dipole transition amplitudes at the L2 edge, shown in panels a) and b), and the L3 edge, shown in panels c) and d), for a single hole with spin orbit coupling and crystal field distortion. Plots show the dependence of spectra on geometry of sample and beam. In panels a) and c), the sample is rotated around the x axis of the lab frame, whereas panels b) and d) show a rotation around the y axis respectively.

chapters these effects will be convoluted with additional interference effects coming from delocalized states across multiple sites. The example of transitions on a single octahedra are therefore a relevant starting point to discuss the impact of geometric factors on the spectra.

3.5. Numerical implementation and RIXSCalculator.jl

Finally, let us switch gears in the following section and discuss the numerical implementation of RIXS and exact diagonalization. Both have been unified in a code framework that has been uploaded to github under the name of `RIXSCalculator.jl` [S1] with a plotting part outsourced to a package called `RIXSPlotter.jl` [S2]. In combination, these two packages allow performing exact diagonalization of the entire cluster Hamiltonian as well

as computing RIXS spectra of these states. The code is developed in close proximity to the experiments and features many design-elements inspired by the experimental counterparts.

The following section is structured as follows. We will start by reviewing how to represent the Fock basis numerically, followed by the basic geometry needed for the RIXS process. Then the packages `RIXSCalculator.jl` and `RIXSPlotter.jl` are reviewed briefly. Finally, some more technical discussion is performed on how to deal with degenerate levels within the ED calculations.

Representation of Fock space basis

Among the different set of bases used in any code that performs exact diagonalization, the Fock space basis deserves some additional comments on its specific implementation. Generally speaking, a basis of Fock space can be represented in many different ways. As notation so far suggested, Fock space basis states can be represented by a list of occupation numbers which is as long as there are single-particle states. States can also be written as a string of creation operators on the vacuum. Yet another representation takes the string of these creation operators and only stores their orbitals in a list as long as there are particles in the state.

$$|0\dots 01_\alpha 0\dots 01_\beta 0\dots 0\rangle \sim a_\alpha^\dagger a_\beta^\dagger |\text{vac}\rangle \sim |'\alpha\beta'\rangle$$

In the context of cluster calculations of this thesis, the last representation yields a much shorter list of numbers which might be preferable in a numerical context.

One downside of a short basis representation however is the absence of normal ordering. While it is convention to normal order creation operators, the application of an operator to one of these states might yield a non-normal ordered state. This case has to be treated in general as for $\alpha \neq \beta$

$$a_\alpha^\dagger a_\beta^\dagger |\text{vac}\rangle = -a_\beta^\dagger a_\alpha^\dagger |\text{vac}\rangle \quad (3.61)$$

and therefore overlaps in short hand notation change sign as well

$$\langle '\beta\alpha' | '\alpha\beta' \rangle = -\langle '\alpha\beta' | '\alpha\beta' \rangle. \quad (3.62)$$

This means that normal ordering is very important when computing overlaps in the abbreviated form, in contrast to the full Fock space representation which has the ordering directly built in.

Geometry

In principle, the equations so far cover the entire calculation of transition intensities and RIXS spectra alike. In practice however, there is a lot more to consider when calculating transition amplitudes, since a lot of parameters have to be represented during the calculation. Although merely an engineering challenge in the numerical implementation, let us

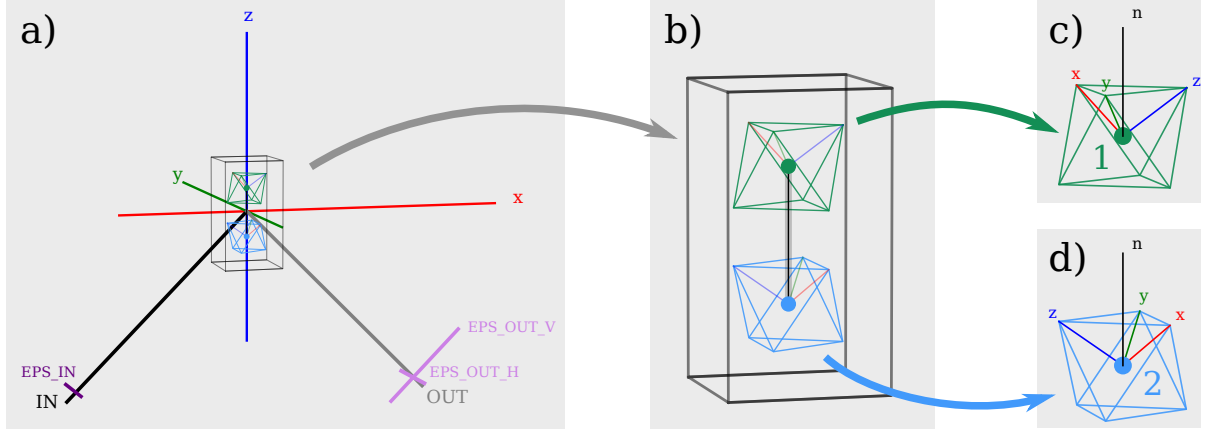


Figure 3.7.: Overview of RIXS geometry - Different levels of geometry involved in the RIXS process and its calculation. On a global (or laboratory) level depicted in panel a), the sample orientation is set relative to the incoming and X-ray beam as well as to the outgoing direction into the detector. Photon polarizations are set perpendicular to these directions. Within the sample, depicted in panel b), individual clusters of Ir atoms and their surrounding oxygen cages are arranged relative to each other. The example in this figure shows a face-sharing geometry. Within each oxygen octahedron, depicted in panels c) and d), local orbital quantization axes are spanning an internal coordinate frame in which the crystal field distortion direction \vec{n} is given.

discuss for completeness the different levels of coordinate frames one has to consider when representing a system numerically.

As seen in Fig. 3.7, geometrical information on the system can be displayed in a hierarchical form. Information is collected on various levels, ranging from the lab system frame via the sample all the way down to individual sites. Every of these levels considers a certain subset of parameters and differs by a coordinate transformation from the ones above and below. It is important to hand information up and down through the different levels as certain parameters are easier to specify in some frame than in another. Although the following discussion seems rather conceptual, the individual levels are all represented as individual objects with corresponding dependencies in the numerical implementation later on.

Let us start with the global lab frame. This frame means to represent the laboratory in which the RIXS experiment is performed. Pictorially, this frame contains the sample, as well as incoming and outgoing X-ray beams and their polarization. Note that for experimental reasons, the experiments mentioned later in Chapter 4 do not measure outgoing polarization. Therefore to reproduce such data, one has to take both horizontal and vertical components into account.

The sample containing the Ir clusters is contained within the lab frame with some relative rotation. It contains one cluster of Ir sites, arranged in their respective geometrical ori-

entation. On the level of the sample it is easiest to specify the exact directions of crystal field distortion as well as specify the hopping Hamiltonian.

The individual sites form the lowest level. They contain all local information, e.g. spin-orbit coupling, Hubbard interaction and dipole operators. Although most of these parameters can be specified internally by only considering sites themselves, some information is better passed down the levels. In particular, the orientation of X-ray beams can easily be specified in the lab frame, being then transformed to the coordinate frames of individual sites where the dipole operators are built.

RIXSCalculator.jl and RIXSPlotter.jl

Having introduced basis representation and geometry, let us now discuss the code implementation covered in `RIXSCalculator.jl` [S1] and `RIXSPlotter.jl` [S2]. This part should not be understood as an extensive manual or documentation, but rather as outlining some of the design principles behind the implementation. More information can be found in the respective github projects.

The implementation of `RIXSCalculator.jl` and `RIXSPlotter.jl` has been designed both for user friendliness as well as for performance. Scripts from these packages should be able to run fast in a live session or jupyter notebook while still executing large-scale diagonalizations.

To improve performance as well as readability, a hierarchical type structure has been implemented which utilizes the powerful tools of just-in-time compilation (JIT) and multiple dispatch that the programming language Julia has to offer. Further improvements to performance are the utilization of buffers to not recalculate all parts of matrices when only certain parameters change.

To improve user accessibility, the type structure is supplemented by many convenience functions that allow for a very readable code. Furthermore, many objects have a custom output that show their internal stages in a meaningful way. For more complex data structures, plotting is implemented so that e.g. geometrical relations can simply be plotted for adjustment and debugging.

On the matter of types, let us discuss the basic type structure in the code. The first object created in any project is the basis of the Hilbert space. Each basis is represented as an object of corresponding type `Basis`, containing objects of type `BasisState` which describe the individual basis states. In fact, the type tree surrounding basis and states is much more complex with a hierarchy between single and multi particle basis as well as individual implementations for every t_{2g} basis state. This plethora of objects allows to define projection matrices and overlaps of basis states.

Operators are represented as their own type `Operator`. Again, operators form a rich type tree with many dependencies and their types already includes the type of the respective

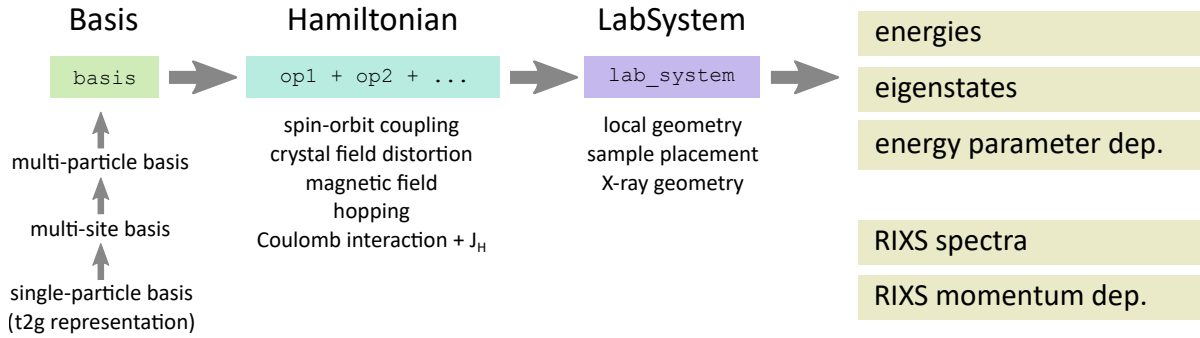


Figure 3.8.: Workflow in RIXSCalculator.jl - Workflow in the package RIXSCalculator.jl [S1] is structured similar for every example. First, a basis representation is obtained by generalizing a certain representation of the t_{2g} states to more sites and particles. In a second step, this basis serves as the foundation of newly added operators, which can be of many different types. Summing these operators with the basis "+" operation yields another operators which can serve as the Hamiltonian. The third step is to construct a so-called LabSystem object, which encapsulates the local cluster and scattering geometry. With these objects, a series of functions is implemented to provide exact diagonalization of the Hamiltonian, plots for the dependency of energies on parameters, as well as functions for the calculation of RIXS amplitudes and spectra.

basis on which the operator is defined. This way, an operator is tight to a certain basis and various tools regarding the operator can be tailored to its representation. One noticeable feature is that operators come with an interface, which implements setting and getting of internal parameters, as well as meta-operators that implement mathematical operations. Together, this allows for readable code in the form of e.g. `ham = op1 + op2` when constructing a Hamiltonian.

On top of the operators, the geometry discussed before is implemented into its own type called `LabSystem`. Objects of this type contain the plethora of basis transformations needed to transform lab coordinates into the local coordinates of the respective sites. A `LabSystem` is always based on an operator describing the Hamiltonian, thus giving a meaningful representation of the entire RIXS setup. Within the `LabSystem`, also dipole operators are defined. They enable the computation of spectra which can be directly obtained from the `LabSystem`.

All together, the code forms a self-contained framework of functions, revolving around bases, operators and the lab system. When used, one has to create these objects consecutively, starting with the basis and operator and ending with the scattering geometry contained in the lab system. During calculations, the lab system can be used as an interface to adjust parameters of the Hamiltonian as well as the scattering geometry. Meaningful outputs and plotting capabilities complement the user interface of the `LabSystem` and allow for direct visual representation of internal geometry with output as in Fig. 3.7 which

was directly produced with the code. An overall representation of the typical build-up and workflow can be seen in Fig. 3.8.

Numerical analysis of degenerate eigenstates

In this next part, let us deviate from the precise code implementation but instead discuss a frequent generic problem in numerical exact diagonalization, which is how to deal with degenerate levels. In case that there is a degenerate subspace within the eigenstates of the Hamiltonian, a numeric solver will necessarily pick just any basis. This basis is however in most cases not easy to read and one would like to find a rotated basis in which eigenstates take a much more readable form. More formally, in this case the Hamiltonian operator \hat{H} commutes with a symmetry \hat{G} as $[\hat{H}, \hat{G}] = 0$, i.e. it is possible to find a basis which is both eigenbasis to \hat{H} as well as eigenbasis to \hat{G} . This is equivalent to demanding eigenstates of \hat{H} to be written in the eigenbasis of \hat{G} . In principle, there are two strategies to do so. The naive method tries lifting the degeneracy in a controlled manner, whereas another more elaborate way uses additional analysis to separate the levels in a post-processing step.

The first naive possibility of obtaining a nicer state representation is adding a term to the Hamiltonian of the form

$$\hat{H} \rightarrow \hat{H} + \alpha \hat{G} \quad (3.63)$$

where α is a small, random number. The eigenvalues of this new operator are only of $\mathcal{O}(\alpha)$ different to the ones of the old Hamiltonian. However, this small split is already enough to lift the degeneracy. In practice, this is often applied with a magnetic field to lift e.g. the spin degeneracy within the eigenstates.

A second possibility to obtain a more readable eigenbasis is to construct an overlap matrix of the symmetry operation

$$M_{ij} = \langle i | \hat{G} | j \rangle \quad (3.64)$$

within the degenerate subspace of the eigenbasis $\{|j\rangle\}$ of \mathcal{H} . The eigenvectors of M will form a new basis which is simultaneous eigenbasis of \hat{H} and \hat{G} . The states are eigenbasis of \hat{G} as they originate from diagonalizing M and they are eigenstates of \hat{H} because they are built as a linear superposition of states that come from the eigenbasis of \hat{H} initially. The advantage of this two step procedure is that one also gains new quantum numbers which distinguish between the new basis states in terms of symmetry.

Note that both methods however require additional knowledge in terms of the symmetry operator \hat{G} which enables the degeneracy in the first place.

4. Material examples

Having discussed the theoretical and numerical framework at length, let us turn our attention to material examples in this chapter. To start with, Sec. 4.1 aims at providing an example for a system where RIXS can give insight into the physics of a *single* Ir site, namely within the double-perovskite material of $\text{Ba}_2\text{CeIrO}_6$. This section is mostly based on work in Ref. [P1].

Following the examples of a single site, Sec. 4.2 enhances the discussion of the RIXS amplitudes by the aspect of interferometry. Starting with this section, interference effects originating from quasi-molecular orbitals are the dominant feature which can be compared to experimental data. The first example in this section concerns $\text{Ba}_3\text{Ti}_{3-x}\text{Ir}_x\text{O}_9$ in which disorder effects can be shown to produce dimers and single sites in a disordered mix. The RIXS calculations in this section aim at complementing experimental data in a current work-in-progress project [14]. The second example of Sec. 4.2 discusses $\text{Ba}_3\text{InIr}_2\text{O}_9$, a dimer material with three holes on the dimer. Most of this work is still in a preliminary state and contributes to yet another work-in-progress project [P2].

In the third section of this chapter, Sec. 4.3, the concepts of RIXS interferometry are applied to two examples of the so-called Kitaev materials. The first example concerns RIXS interference patterns in Na_2IrO_3 , which can be shown to illustrate the underlying bond-directional character of couplings typically associated with the Kitaev model. Overall, calculations show a remarkable similarity to experimental data from Ref. [15]. In a second subsection, the local structure of $\alpha\text{-RuCl}_3$ is discussed. In particular, this includes calculations underlying Ref. [P3], illustrating the observation of a double spin-orbit exciton in the optical spectra of this material.

The chapter finally closes with a few remarks on the applicability of the numerical toolbox beyond RIXS, illustrating in particular the possibility of calculating optical conductivities in Sec. 4.4.

4.1. Single particle RIXS in $\text{Ba}_2\text{CeIrO}_6$

In the light of recent interest into strongly coupled spin-orbit entangled Mott insulators [2] with partially filled 4d and 5d orbitals, much attention is paid to materials with intrinsic $j = 1/2$ moments [1]. Particular iridate systems in which Iridium atoms are situated in oxygen octahedra fit this category perfectly as strong spin-orbit coupling naturally enhances a spin-orbit coupled character of eigenstates. Additionally, the possibilities of realizing different

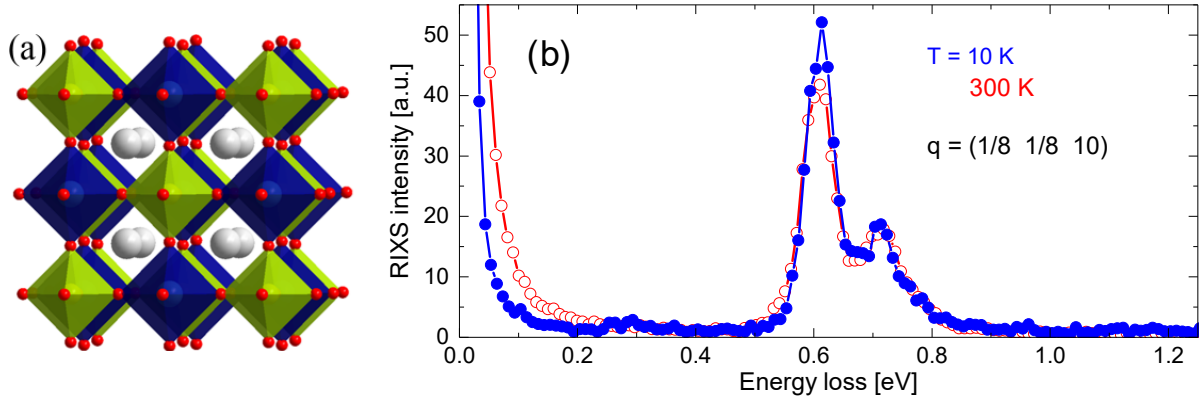


Figure 4.1.: Crystal structure and experimental RIXS data for $\text{Ba}_2\text{CeIrO}_6$ - Panel a) shows an overview over the crystal structure of $\text{Ba}_2\text{CeIrO}_6$ which is a double-perovskite material with interlacing fcc lattices, each occupied by oxygen octahedra filled with either a Ir or a Ce atom. Panel b) shows the experimental RIXS data for both $T = 10\text{K}$ and $T = 300\text{K}$, exhibiting a clearly visible double-peak structure indicating a crystal-field split spin-orbit exciton. Figures adapted from Fig. 1 and Fig. 3 of Ref. [P1].

effective interactions by various alignment geometries between IrO_6 octahedra [4, 7, 8] make these materials a perfect playground for the realization of exotic magnetic materials.

In the search for a perfect local $j = 1/2$ moment, $\text{Ba}_2\text{CeIrO}_6$ is reported to be particularly close to an ideal $j = 1/2$ ground state [P1]. Structurally, this material realizes a cubic double perovskite structure of two interlacing fcc lattices, visualized in panel a) of Fig. 4.1. On the vertices of these fcc lattices, corner-sharing oxygen octahedra are situated, hosting both Ir as well as Ce atoms respectively. X-ray structure analysis confirms that the crystal structure is indeed cubic [P1]. However, RIXS data of the same compound reveals a double-peak structure for the spin-orbit excitation, shown in panel b) of Fig. 4.1. This feature is indicative of crystal field distortions which can split the $j = 1/2 \rightarrow j = 3/2$ excitation contradicting the findings of structure analysis at first sight.

From an even broader perspective, it is a regularly posed question in these types of materials if there is a pure $j = 1/2$ ground state or if distortions to the surrounding oxygen octahedra mix too much $j = 3/2$ contributions to the ground state. In this section, numerical calculations in the framework of the present thesis are used to supplement experimental RIXS data in order to determine the nature of the ground state.

Numerical ED and RIXS

Employing numerical exact diagonalization for the system at hand is straight forward in the scheme developed so far. The Ir atoms on one of the fcc lattices in $\text{Ba}_2\text{CeIrO}_6$ are in a $5d^5$ configuration, yielding exactly one hole occupying the t_{2g} states.

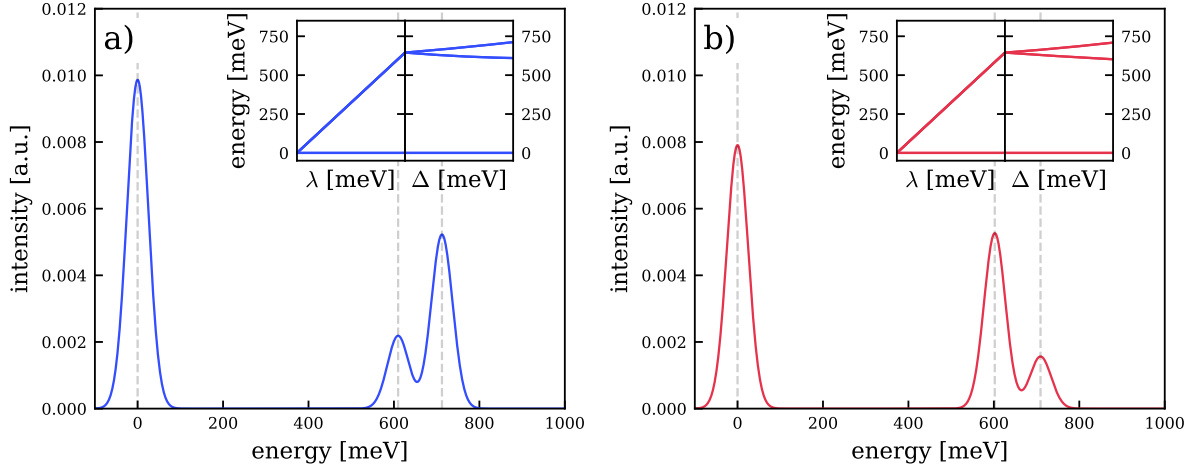


Figure 4.2.: ED and RIXS calculations for Ba₂CeIrO₆ - Experimental RIXS intensity peak data from Ba₂CeIrO₆ is consistent with two different sets of parameters, $\lambda = 430\text{meV}$, $\Delta = 170\text{meV}$ shown in panel a) as well as $\lambda = 430\text{meV}$, $\Delta = -150\text{meV}$ shown in panel b). Panels themselves show the calculated RIXS spectra in numerics. Additionally, each panel shows the evolution of ED energies upon increasing parameters from 0 to their respective values. It can be traced how the splitting evolves.

The code framework of `RIXSCalculator.jl` allows for the modeling of an effective single-particle problem on an isolated Iridium site. This yields a local Hamiltonian for a single hole of the form

$$H = \lambda \hat{L} \cdot \hat{S} + \Delta L_z^2 \quad (4.1)$$

i.e. containing both the effect of spin-orbit coupling as well as crystal field distortions. For a given set of parameters, one is able to numerically diagonalize the resulting Hamiltonian matrix and obtain energies as well as wavefunctions of the eigenstates. The differences between energies can then be compared to experimental excitation energies in RIXS.

As already seen earlier in Fig. 3.1, applying both spin-orbit coupling and crystal field distortion splits the t_{2g} levels into three distinct states. The differences between the lowest lying states and the two higher ones can be compared to the experimental double-peak structure, more precisely to respective excitation energies therein. One can find agreement for two different sets of parameters

$$\begin{aligned} \lambda = 430 \text{ meV} \quad \text{and} \quad \Delta = 170 \text{ meV} \\ \text{or} \quad \lambda = 430 \text{ meV} \quad \text{and} \quad \Delta = -150 \text{ meV} \end{aligned} \quad (4.2)$$

which correspond to elongation or compression of the oxygen cage surrounding the Iridium. A graphical representation of both numerical RIXS spectra as well as the energies obtained by ED can be seen in Fig. 4.2 for both sets of parameters.

Further investigation of the eigenstates shows that the ground state wavefunction is

$$\begin{aligned}
 |0\rangle &= 0.991 \left| \frac{1}{2}, \frac{1}{2} \right\rangle - 0.133 \left| \frac{3}{2}, \frac{1}{2} \right\rangle \quad (\text{elongation}) \\
 \text{and} \quad |0\rangle &= 0.995 \left| \frac{1}{2}, \frac{1}{2} \right\rangle - 0.1 \left| \frac{3}{2}, \frac{1}{2} \right\rangle \quad (\text{compression}),
 \end{aligned} \tag{4.3}$$

which looks largely like a $j = 1/2$ ground state. In fact, the $j = 1/2$ contribution in the ground state amounts for 99% of the total weight, only 1% of the weight can be attributed to an admixture of $j = 3/2$. This holds for both elongation and compression and is a clear evidence for a $j = 1/2$ ground state.

The $j = 1/2$ nature of the ground state has to be put also into the context of large crystal field distortion. Despite a significant value of $\Delta \sim \frac{1}{3}\lambda$, the ground state showed little to no $j = 3/2$ contributions. From yet another perspective, such a large value of Δ is even more surprising. Structure analysis utilizing X-rays found the crystalline structure to be nearly perfectly cubic [P1]. This is however not reflected in the large value of Δ which is in good agreement with RIXS. A possible explanation might be the presence of local disorder which is not seen by the global structure analysis or other effects.

Final notes / Outlook

As seen by numerical calculations, the local $j = 1/2$ picture is still realized to a high degree, despite the presence of structural distortions in the form of a finite crystal field splitting. The origin of this crystal field splitting might be disorder in the octahedra as the cubic structure was only confirmed to be realized on average, whereas RIXS is an intrinsically local probe.

Having established the local $j = 1/2$ character of the electronic states, Ref. [P1] uses the local moments to construct an effective spin model. This model turns out to include both nearest and next-nearest neighbor Heisenberg coupling between $j = 1/2$ moments, as well as anisotropic, bond-directional Kitaev exchange. Both Luttinger-Tisza calculations of the classical limit as well as FRG calculations of the quantum model reveal a rich phase diagram, including ordered phases as well as a quantum spin liquid phase. This spin liquid appears to be destabilized by finite Kitaev couplings [P1], contradictory to the common knowledge of Kitaev couplings inducing frustration and therefore stabilizing spin liquid phases. Using the experimentally relevant parameters, $\text{Ba}_2\text{CeIrO}_6$ can indeed be found to sit tantalizingly close to the boundary of the spin-liquid phase.

All in all, the example of $\text{Ba}_2\text{CeIrO}_6$ shows the importance of numerical calculations for confirming local spin-orbit moments in comparison to RIXS data.

4.2. Dimer materials and RIXS variants of Young's double slit

In the journey across more $j = 1/2$ spin-orbit entangled materials, the following section concerns materials with IrO_6 octahedra arranged in dimers. In principle, there are numerous examples of such systems, here however we are in particular concerned with $\text{Ba}_3\text{Ti}_{3-x}\text{Ir}_x\text{O}_9$ and $\text{Ba}_3\text{InIr}_2\text{O}_9$, both of which are from the family of $\text{Ba}_3M\text{Ir}_2\text{O}_9$ with M being a metal. Since claims of spin-liquid behavior in the family of $\text{Ba}_3M\text{Ir}_2\text{O}_9$, the entire family got much attention especially since the role of M could be occupied by materials with different valence [16, 17].

Structurally, IrO_6 octahedra form dimers with a shared face between two octahedra in these materials. Dimers are then arranged in triangular layers, with each dimer having 12 neighbors. Since the metal M in these materials can change in valence, the effective particle number on the dimer can be adjusted. In this spirit, $\text{Ba}_3\text{CeIr}_2\text{O}_9$ ($M = \text{Ce}$), a system with two holes per dimer, showed traces of quasi-molecular orbitals built from local $j = 1/2$ states [9], $\text{Ba}_3\text{InIr}_2\text{O}_9$ ($M = \text{In}$), a system with three holes per dimer, showed persistent spin dynamics down to 20mK and no sign of magnetic ordering [18] and $\text{Ba}_3\text{ZnIr}_2\text{O}_9$ ($M = \text{Zn}$), a system with four holes per dimer, was reported to show spin-orbital liquid behavior [19, 20].

From the perspective of RIXS, dimer systems offer a previously unexplored possibility, namely the presence of RIXS interference. On the example of $\text{Ba}_3\text{CeIr}_2\text{O}_9$, it was shown that interference effects in the RIXS intensity can be used to trace down quasi-molecular orbitals [9]. This can in principle be understood from the following: If the RIXS process applies to a delocalized state on the entire dimer, the two localized transitions from the individual atoms can interfere destructively depending on the transferred momentum along the dimer axis. This is generally similar to Young's double slit experiment for light.

The present section of this thesis aims at providing theoretical groundwork for supporting RIXS experiments [14] on the material family $\text{Ba}_3M\text{Ir}_2\text{O}_9$. At first, the material $\text{Ba}_3\text{Ti}_{3-x}\text{Ir}_x\text{O}_9$ is introduced in which an increase in the concentration of Ir was found to suppress magnetism. The second part of this section highlights some calculations for the material $\text{Ba}_3\text{InIr}_2\text{O}_9$ which is an example for a dimer system with three holes.

4.2.1. Disorder effects in $\text{Ba}_3\text{Ti}_{3-x}\text{Ir}_x\text{O}_9$

One missing piece of the puzzle in the family of $\text{Ba}_3M\text{Ir}_2\text{O}_9$ has been the role of disorder. In particular, the structural disorder of Ir and M atoms exchanging locations in the crystal structure has not been sufficiently explored. Especially for Ti as an atom with radius similar to the Iridium atomic radius [17], disorder effects are expected to occur in $\text{Ba}_3\text{Ti}_{3-x}\text{Ir}_x\text{O}_9$ for different concentrations x of Iridium.

To investigate disorder effects in this material, RIXS interferometry can be employed.

Since structurally, misplaced Ti hinder the formation of electronic dimers, the amount of site disorder directly relates to the RIXS response. Similarly, for small concentrations of Ir, only single IrO₆ octahedra are expected to be observed whereas for large concentrations x , dimer formation and therefore a suppression of magnetism is expected. Similar to the identification of quasi-molecular orbitals in Ba₃CeIr₂O₉ by interference patterns in RIXS intensities, electronically delocalized dimer states can be expected to show a respective momentum signature in their RIXS intensities.

In the following, this part of the thesis therefore aims at providing a theoretical and numerical description of the relevant Ir clusters in Ba₃Ti_{3- x} Ir _{x} O₉ as well as their RIXS spectra. By comparing to experimental RIXS data, this can in principle be used to assign cluster formation to observed RIXS features. Although this project is still considered work-in-progress, some preliminary results are already discussed.

Model Hamiltonian for Ba₃Ti_{3- x} Ir _{x} O₉

Ba₃Ti_{3- x} Ir _{x} O₉ generally has a layered structure with alternating layers of vertical face-sharing oxygen octahedra and single octahedra, connected corner-sharing. The octahedra can either host a Ir or a Ti atom. Since only the Ir exhibits magnetism and the Ti is non-magnetic, the following calculation focuses only on Ir sites. Disorder between Ti and Ir can in principle lead to three different Ir clusters. Apart from an isolated IrO₆ octahedron, one can either encounter a dimer within one layer, characterized by face-sharing geometry, or a dimer between the two different layers which then forms in a corner-sharing geometry. Since in principle a statistical mixture gives rise to the behavior, clusters with more than two Ir are expected to be unlikely for moderate concentrations of Ir.

To model the electronic structure in Ba₃Ti_{3- x} Ir _{x} O₉, one therefore needs a total of three separate calculations, one for each type of cluster. Each of those calculations consists of exactly diagonalizing the electronic Hamiltonian for the respective cluster as well as calculating the Iridium L₃ edge RIXS spectrum for its excitations. In detail, these calculations differ both in number of sites and particles as well as in the exact geometry. One cluster is simply a single Ir site within an oxygen octahedron whereas the other two clusters are both dimers, although with different hopping geometries. In the end, a statistical mixture of the three clusters should give rise to the experimentally observed spectrum, i.e. it should contain measurable traces of all three clusters.

Let us start the discussion of the cluster Hamiltonian with a focus on the core ingredient, i.e. the local Hamiltonian on the Iridium sites. On every such site, the local Hamiltonian takes the form

$$H = \lambda \hat{L} \cdot \hat{S} + \Delta (\vec{n} \cdot \hat{L})^2 + H_{\text{int}}. \quad (4.4)$$

which consists of spin-orbit coupling and distortions to the oxygen crystal field as well as interactions between electrons modeled by the interaction Hamiltonian H_{int} shown in Eq. (3.48).

In practice, interactions between electrons only come into play when the d^5 Iridium ions are part of a dimer, otherwise only a single hole can be present on one site. The combination of spin-orbit coupling and crystal field distortion has been discussed before. The only new nuance here is the introduction of a distortion direction \vec{n} on every Ir site, which is parallel to the lattice vector \vec{c} in $\text{Ba}_3\text{Ti}_{3-x}\text{Ir}_x\text{O}_9$. In the numerical representation, \vec{c} is used as the sample z axis, corresponding to the local $[111]$ direction in every octahedron.

Whereas the cluster of just a single site is isolated and does not host any hopping between its constituents, the two dimer clusters do have hopping contributions to their total Hamiltonians. The cluster consisting of the corner-sharing dimer uses a hopping formulation within the xyz basis which can be written as

$$H_{\text{hop.}} = \sum_{\nu} t c_{1,\nu}^{\dagger} c_{2,\nu} + \text{h.c.} \quad (4.5)$$

where ν runs over all states $|x, \uparrow\rangle$, etc on the two Ir ions. As a simplification for reduced parameter complexity, every hopping element has the same amplitude t .

The hopping on the second cluster consisting of a face-sharing dimer uses a description within the a_{1g} basis which is the proper eigenbasis for trigonal crystal field distortion. The hopping is again diagonal in these orbitals with amplitude t for every hopping element, so the Hamiltonian can be written as

$$H_{\text{hop.}} = \sum_{\alpha} t c_{1,\alpha}^{\dagger} c_{2,\alpha} + \text{h.c.} \quad (4.6)$$

where α runs over all states $|a_{1g}^+, \uparrow\rangle$, etc. Note that in this case, one has to take care of tilted spin quantization axes. A hopping process $|\alpha, \sigma\rangle \rightarrow |\alpha, \sigma\rangle$ will implicitly tilt the spin σ when transitioning from one site to the other since the spin-up direction on both sites is tied to the orbital z -direction which is tilted between sites. To resolve this tilt between spin-quantization axes, one can either reformulate the hopping or tilt the spin-quantization axes on both Ir sites relative to the orbital quantization axes so that they align globally.

ED and RIXS for $\text{Ba}_3\text{Ti}_{3-x}\text{Ir}_x\text{O}_9$

With the Hamiltonian defined, exact diagonalization and calculation of RIXS spectra for the Ir L3-edge can be performed for all clusters separately. The results of these calculations can be found in Fig. 4.3. Parameters for the individual clusters are set to

$$\begin{aligned} \lambda &= 400 \text{ meV} \\ \Delta &= 250 \text{ meV} \\ U &= 2300 \text{ meV} \\ J_H &= 250 \text{ meV} \\ t &= 200 \text{ meV} \end{aligned} \quad (4.7)$$

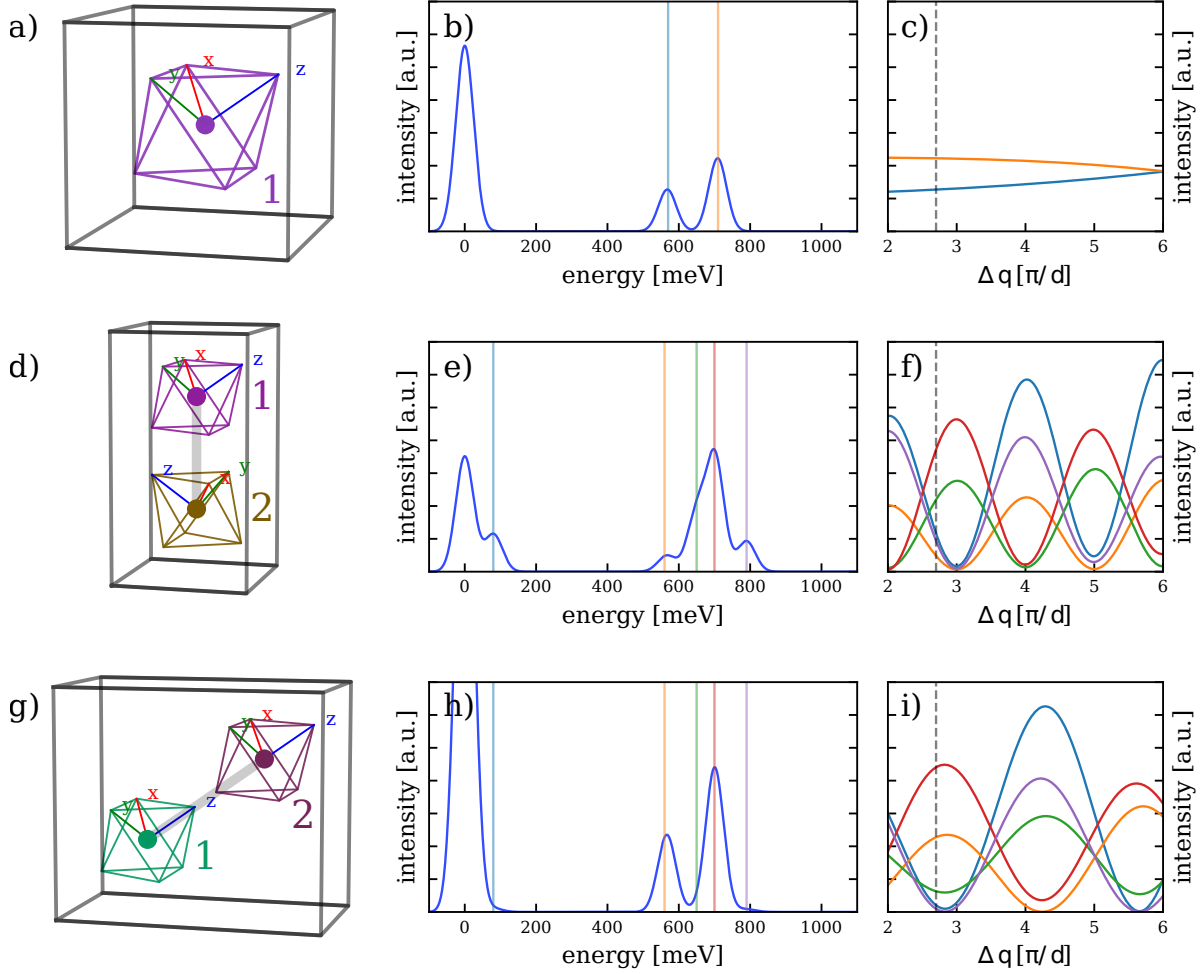


Figure 4.3.: ED and RIXS calculations for elementary Iridium clusters in $\text{Ba}_3\text{Ti}_{3-x}\text{Ir}_x\text{O}_9$ - Rows show elementary clusters in the disordered material $\text{Ba}_3\text{Ti}_{3-x}\text{Ir}_x\text{O}_9$ which contribute separately to the overall RIXS intensities. Clusters are single sites, displayed in panels a)-c), face-sharing dimers, displayed in panels d)-f) as well as corner-sharing dimers, displayed in panels g)-i). Panels a),d) and g) show illustrations of the clusters, directly obtained from RIXSCalculator.jl. Panels b),e) and h) show a typical numerical RIXS spectrum. Peaks from this spectrum are analyzed regarding their momentum space interference patterns with results depicted in panels c),f) and i). Colors of the lines in these panels match the color of vertical lines in panels b),e) and h) denoting the peak positions. Note that the single site only shows an overall geometric effect due to tilting of incoming and outgoing X-ray beams. Both dimer configurations however show signs of interference effects as the peaks are modulated periodically. The frequency of this modulation is proportional to the site distance along the deposited momentum direction that is different for both dimers.

and the dimer length in real space is set to unity. This enables to measure the transferred momentum directly in integer multiples of π .

In general, the results show different kind of behavior for the three elementary clusters. In the case of a single site, plots in Fig. 4.3 show a similar picture to the results discussed before for the single site system in Fig. 4.2. Note, that no periodic modulation of the RIXS intensities in transferred momentum is expected to be observed since there is only a single hole located on a the single site.

For both dimer systems, one can in contrast observe a modulation of RIXS intensity in transferred momentum demonstrated in Fig. 4.3. This modulation is a clear sign of a delocalization of wavefunctions between the two sites of the cluster, leading to interference effects in the outgoing X-ray beams. If one considers the exact modulation frequency in terms of transferred momentum for the two different dimers, one can find a mismatch of frequency. This mismatch stems from the mismatch in projected dimer length along the axis of transferred momentum. Here, the dimer length is the same in both cases but the second dimer has a shorter projected distance of sites along the direction of deposited momentum, resulting in a longer period in transferred momentum.

Concluding Remarks

Summarizing the resulting behavior, one can conclude that indeed all three clusters exhibited unique behaviors in the numerical RIXS spectra. The single isolated octahedron did not show any interference patterns in RIXS intensity (as expected), but only geometric contributions from the changes to incoming and outgoing polarization when varying the transferred momentum. In contrast, calculations for both dimer yielded a clearly modulated RIXS intensity in transferred momentum, both with unique periods.

The numerical RIXS intensity data suggests that this system is well suited for comparison to experimental data. Individual features in experimental spectra can be investigated regarding their dependence on transferred momentum and then be compared to the numerical analysis carried out in this section. In principle, such a comparison might be able to quantitatively determine how disorder locally plays out in $\text{Ba}_3\text{Ti}_{3-x}\text{Ir}_x\text{O}_9$ for different Iridium concentrations x .

4.2.2. Dimers with three holes in $\text{Ba}_3\text{InIr}_2\text{O}_9$

Let us turn our attention to the next material in the $\text{Ba}_3M\text{Ir}_2\text{O}_9$ family, $\text{Ba}_3\text{InIr}_2\text{O}_9$, which is a dimer material with three holes per dimer. Experimental data suggests spin-liquid behavior in this material so naturally it is a good candidate for numerical investigations. In the following, the possibilities of numerical ED and RIXS will be demonstrated and prepared for further analysis. Note that this work is currently work-in-progress [P2] and therefore does not constitute a finalized project yet.

Exact diagonalization of $\text{Ba}_3\text{InIr}_2\text{O}_9$

Setting up exact diagonalization calculations for $\text{Ba}_3\text{InIr}_2\text{O}_9$ is straightforward. Clusters in this material are face-sharing dimers similarly to $\text{Ba}_3\text{Ti}_{3-x}\text{Ir}_x\text{O}_9$ with the same cluster Hamiltonian, consisting of spin-orbit coupling, crystal field distortion, a_{1g} -hopping and Hubbard interactions.

A first comparison to experimental RIXS peak data reveals the following parameter estimates

$$\begin{aligned}
 \lambda &= 430 \text{ meV} \\
 \Delta &= 75 \text{ meV} \\
 U &= 1250 \text{ meV} \\
 J_H &= 330 \text{ meV} \\
 t_{a_{1g}} &= 510 \text{ meV} \\
 t_{e_g^\pi} &= 280 \text{ meV}
 \end{aligned}
 \tag{4.8}$$

where λ and J_H can be estimated from other Ir compounds and the rest of parameters are fitted to the RIXS data.

The actual exact diagonalization calculation can then be performed and is displayed as a consecutive increase in parameters in Fig. 4.4. First, the increase in U splits states into $t_{2g}^4 t_{2g}^5$ and $t_{2g}^3 t_{2g}^6$ multiplets, i.e. it raises triple hole-occupancies to higher energies. Then, spin-orbit coupling λ splits the $j = 1/2$ and $j = 3/2$ states, leading to four different combinations for the three holes. Hund's coupling J_H brings down one state with $j = 3/2$ contribution towards the ground state whereas hopping t mixes states further, inducing $j = 3/2$ contribution into the ground state. Note that there are also states unaffected by hopping. Overall, eigenenergies depend on hoppings approximately linear in t .

Further investigations require additional implementation of symmetries into the numerics as the nature of the states so far is best expressed in those.

RIXS calculations for $\text{Ba}_3\text{InIr}_2\text{O}_9$

Based on the exact diagonalization results, calculations of RIXS intensities can be performed. For a general setup similar to the experiment, with momentum transfer along the dimer axis, typical spectra can be found in Fig. 4.5. Note that all four spectra are for four different values of transferred momentum, measured in units of π/d where d is the dimer length. Overall, the excitations are separated into single- and double-spin-orbit-exciton groups, as already suggested by the exact diagonalization data.

Beyond a clearly visible impact from geometric changes in the scattering geometry, periodic momentum dependencies of the peaks can be observed. This is a clear signature of delocalized orbitals across the dimer which lead to a periodic behavior in transferred

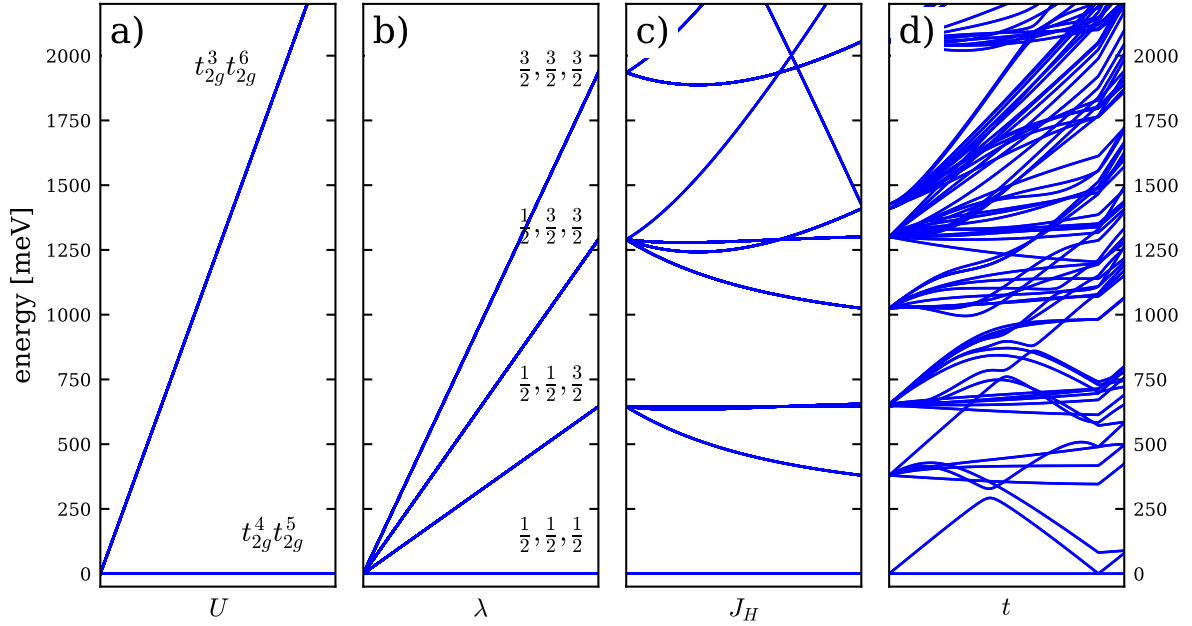


Figure 4.4.: Exact diagonalization for $\text{Ba}_3\text{InIr}_2\text{O}_9$ - Numerical exact diagonalization data shown for consecutive increase of parameters in $\text{Ba}_3\text{InIr}_2\text{O}_9$ which is described by local dimers with 3 holes. Following states across the diagram reveals that the first splitting, induced by Hubbard interaction U , raises the states which included triple occupied sites high up in energy compared to the rest. A further increase in spin-orbit coupling λ separates all states by how much $j = 3/2$ moments they include, leaving a ground state which is purely $j = 1/2$. This state is then mixed with $j = 3/2$ states from higher energies as Hund's coupling J_H and hopping t bring states down from higher energies.

momentum similar to previous discussion. However, with the Hilbert space reaching a large size, clear statements about the exact nature of individual states are challenging. In particular, additional information about inherent symmetries would be greatly impactful in the interpretation of this data.

Concluding Remarks

In summary, the numerical implementation could successfully be applied to modeling $\text{Ba}_3\text{InIr}_2\text{O}_9$. Comparing exact diagonalization data to the peaks of experimental RIXS data suggest that the parametrical description from this section is consistent with previously obtained literature values and that in principle, numerical calculations of the eigenspectrum are beneficial for the understanding of experimental data.

Furthermore, numerical RIXS intensity data from $\text{Ba}_3\text{InIr}_2\text{O}_9$ can now readily be compared to experimental data. This comparison is currently ongoing (during the writing of this

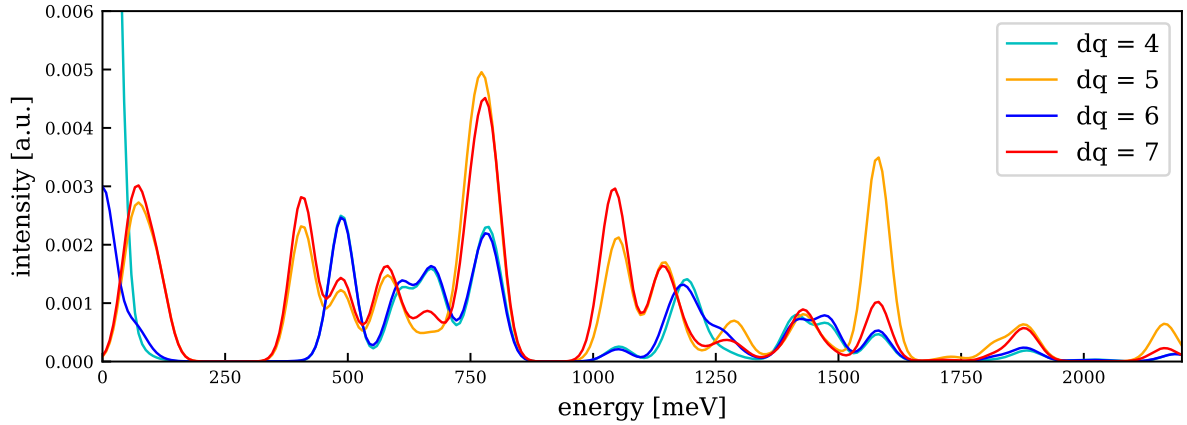


Figure 4.5.: Numerical RIXS spectrum for $\text{Ba}_3\text{InIr}_2\text{O}_9$ - Numerical spectra for different transferred momenta dq in units of π/d where d is the dimer length. Peaks show a clear signature of momentum modulation, demonstrating the quasi-molecular character of states.

thesis) and will be part of an upcoming publication [P2]. Particular focus is set on the qualitative comparison between momentum space periodicities in peak intensity data. A quantitative comparison will be challenging to obtain in this case as, since the fast collision approximation, leading to the form of RIXS amplitudes used in the numerics, is much likely not valid in the context of $\text{Ba}_3\text{InIr}_2\text{O}_9$. It remains to be seen how much this influences the agreement of spectral data.

4.3. Kitaev materials

Along the quest for possible magnetic models, the search for an experimental confirmation of the Kitaev spin liquid [3] has raised much attention. This elusive state of matter forms in a model of bond-directional Ising interaction on a honeycomb lattice and raised much attention as the first ever analytically solvable spin liquid ground state. Since the proposal by Jackeli and Khaliullin [4] that such bond-directional exchange can be realized between $j = 1/2$ moments in edge-sharing octahedra, there has been a lot of interest in the materials Na_2IrO_3 and $\alpha\text{-RuCl}_3$ which both are layered materials of edge-sharing octahedra. Inside these octahedra, the Ir in Na_2IrO_3 or the Ru in $\alpha\text{-RuCl}_3$, are expected to provide the necessary $j = 1/2$ moments which then can interact within layers of the respective materials.

The low-temperature behavior of both materials has been studied extensively. Both materials seem to order magnetically at very low temperatures [1, 21–24] which indicates that a pure Kitaev spin-liquid can be ruled out. However it was found that in $\alpha\text{-RuCl}_3$ inelastic neutron scattering, THz spectroscopy and Raman scattering all show signs of dominant Kitaev interactions in the form of a magnetic continuum [25–32]. The continuum has fermionic character [29, 32] and only shows signs of dynamical spin-spin correlations between nearest neighbors [26]. Most recently, it was also discovered that $\alpha\text{-RuCl}_3$ exhibits a half-quantized thermal Hall effect in strong magnetic fields [33], substantiating the classification of $\alpha\text{-RuCl}_3$ as a proximate Kitaev spin-liquid.

Similar experimental evidence for Na_2IrO_3 is still sparse. Neutron scattering on Na_2IrO_3 proves to be difficult since Ir absorbs neutrons very well. Magnetic excitations are in principle available in RIXS like in other materials, however the edge-sharing geometry leads to lower energies, therefore bringing the excitation energies down to the experimental resolution of 24 meV [34, 35]. However, it was demonstrated that RIXS interferometry can be used to overcome experimental resolution and show a momentum space interference pattern consistent with expected Kitaev behavior [15].

This section aims at providing a numerical perspective to the question how the elementary building blocks in the materials of Na_2IrO_3 and $\alpha\text{-RuCl}_3$ show signs of dominant Kitaev interactions. It should be noted that this section does not feature an extensive overview over the analytical solution of the Kitaev model itself, which rather is delayed to Sec. 10.3 in the context of lattice models, but is rather concerned with the physics of its atomic constituents. In the following, this analysis is based on two assumptions. First of all, since the interference pattern in RIXS data of Na_2IrO_3 only shows signs of nearest-neighbor correlations [15], it is possible to model the RIXS data by only taking into account disconnected individual bonds in `RIXSCalculator.jl`. Modeling these RIXS experiments on an electronic level including the magnetic excitations is laid out in the first part of this section. In the second part, the low-energy behavior of $\alpha\text{-RuCl}_3$ is investigated, based on calculations for Ref. [P3]. This investigation reveals a double spin orbit excitation, which can be seen in both RIXS and Raman data.

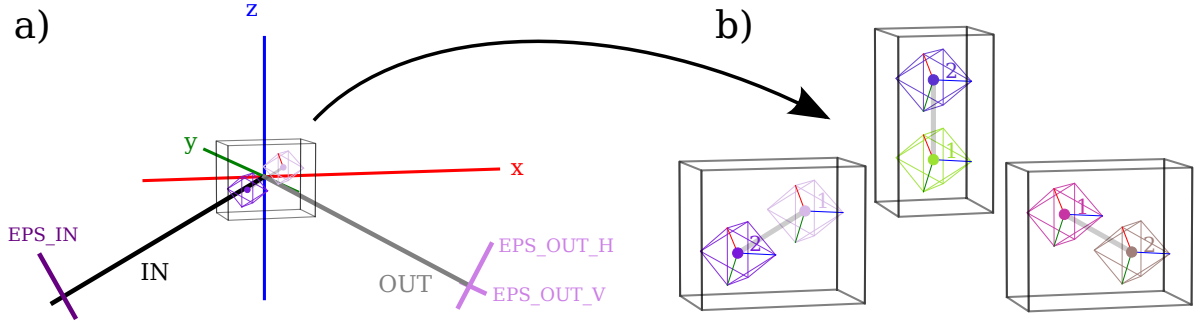


Figure 4.6.: Numerical implementation of Na_2IrO_3 - The RIXS setup in Na_2IrO_3 is modeled after experiments performed in Ref. [15], which examines momentum transfer within the honeycomb planes of Na_2IrO_3 , as depicted in panel a). Locally, Na_2IrO_3 is modeled by the individual bonds (x,y,z) in the honeycomb plane which are built up from two IrO_6 octahedra each, sharing a common edge. To model these elementary bonds, three separate lab systems are implemented, shown in panel b). The local Hamiltonian of these two-site clusters consists of spin-orbit coupling, crystal field distortion perpendicular to the honeycomb planes, Hubbard interaction and Hund coupling as well as hopping between the octahedra.

4.3.1. RIXS interference patterns in Na_2IrO_3

Let us start by discussing how to probe Kitaev physics with RIXS in the material Na_2IrO_3 , i.e. as done in the paper [15]. Although ab initio calculations suggest that Na_2IrO_3 is closer to a pure Kitaev model than $\alpha\text{-RuCl}_3$ [24], it has a magnetic ordering transition at around $T_N = 15\text{K}$ below which a zigzag order is built up [1, 24, 36–39]. Dominating Kitaev terms were already suggested by RIXS [40], however it was only recently that fingerprints of Kitaev physics were observed [15].

In this part we will discuss these recent RIXS observations from a numerical standpoint. We will start by introducing a suitable model Hamiltonian for Na_2IrO_3 after which exact diagonalization and RIXS simulations are carried out. After having discussed their results, a brief comparison to experimental data is drawn.

Modeling Na_2IrO_3

To model Na_2IrO_3 in numerics, let us make some general assumptions. First of all experimental data only finds correlations on nearest-neighbor scales, therefore it is reasonable to only take into account individual bonds. In terms of code this means having three independent samples consisting only of a single bond, whose spectra are summed up finally. Together, these three bonds span the lattice plane whose normal can be related to the experimental sample c -direction.

Each bond consists of two Ir-octahedra with Ir being in a d^5 configuration, meaning a

single hole within the t_{2g} states. The two octahedra of every bond are sharing a common edge which leads to a peculiar form of hopping. The shared edge differs between all three bonds s.t. the hopping is also different for each bond. For the common edge within the xy plane of the octahedra, hopping takes the form

$$H_{\text{hop.}} = \sum_{\sigma=\uparrow\downarrow} t_K (a_{1x\sigma}^\dagger a_{2y\sigma} + a_{1y\sigma}^\dagger a_{2x\sigma}) + t_J (a_{1z\sigma}^\dagger a_{2z\sigma}) + \text{h.c.} \quad (4.9)$$

with parameters t_K and t_J describing the off-diagonal (Kitaev) and diagonal (Heisenberg) part of the hopping. The remaining two bonds with their common edge in another plane have respective cyclic permutations of this hopping Hamiltonian. Apart from hopping between sites, the usual local operators describe the on-site physics of each octahedron, including spin-orbit coupling, Hubbard interaction as well as crystal field distortions. Parameters that are reasonable to describe Na_2IrO_3 are e.g.

$$\begin{aligned} \lambda &= 430 \text{ meV} \\ \Delta &= 0 \text{ meV} \\ U &= 1300 \text{ meV} \\ J_H &= 250 \text{ meV} \\ t_J &= 350 \text{ meV} \\ t_K &= 350 \text{ meV} \end{aligned} \quad (4.10)$$

which will be used through though the entire section.

Concerning the RIXS geometry, one is interested in particular in momentum transfer which is either parallel or anti-parallel to one of the bonds while still lying in the lattice plane. This particular scattering geometry allows to select interference contributions from the different bonds. From a practical perspective, this geometry can be achieved by rotating the sample within the lab frame relative to the axis of momentum transfer. In the following, let us use the convention that the lattice plane is parallel to the plane of incoming and outgoing X-rays and will only be rotated around its normal vector.

Exact diagonalization of Na_2IrO_3

Having a complete Hamiltonian for each bond allows numerical exact diagonalization to be performed. Since the basis contains 66 states in total, the Hamiltonian is of size 66×66 and gives 66 eigenvalues. Particular interest lies on the lowest eigenvalues, denoting not only the ground state but also the excitations visible in RIXS.

To gain insight in the nature of the different eigenstates, Fig. 4.7 shows the consecutive evolution of eigenenergies when raising each individual Hamiltonian parameter to its experimental value. As seen in the figure, U separates states with different number of particles per site, i.e. the states that remain at low energies now only have one hole per site. Next,

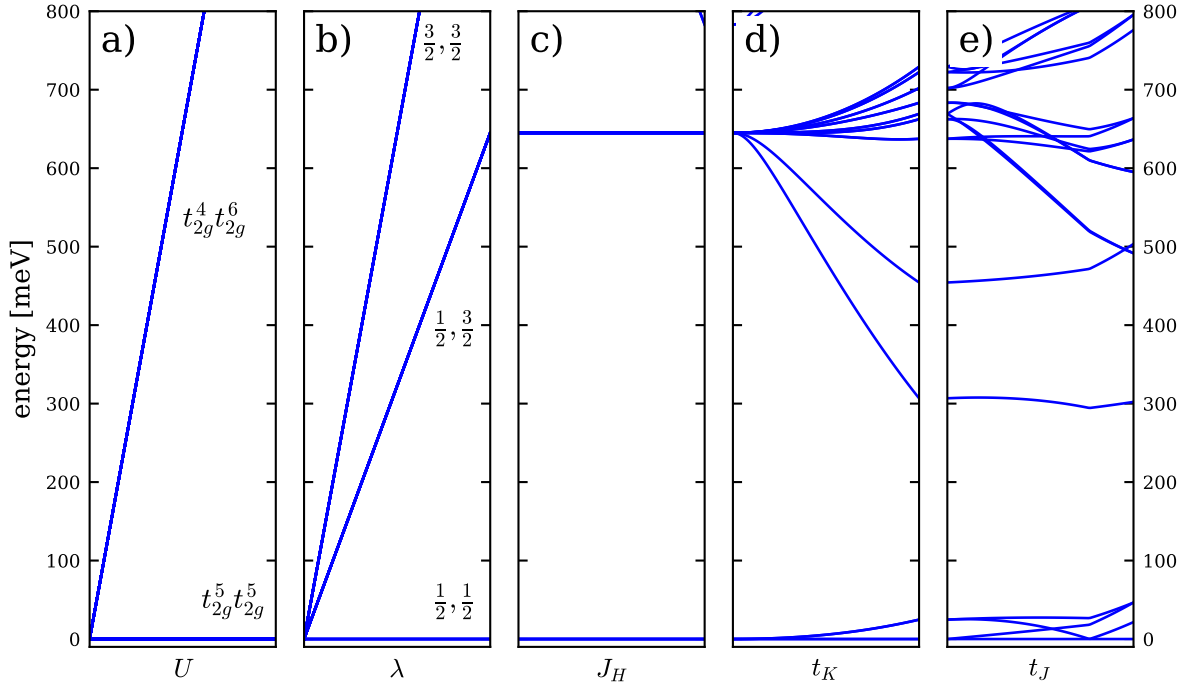


Figure 4.7.: Exact diagonalization of Na_2IrO_3 - Eigenenergies as function of consecutively increased parameters in the model Hamiltonian for Na_2IrO_3 . Following the different interactions increase reveals that the low-energy states for finite parameters consists of mostly $j = 1/2$ states.

λ splits the $j = 1/2$ and $j = 3/2$ states on both sites, leaving three combinatorial solutions for the combined 2-particle state. The ground state consists of states with both holes in a $j = 1/2$ state. Applying Hund's coupling J_H changes nothing within the low energy states since particles here are on different sites and therefore do not interact with J_H . Finally, hopping t_K and t_J mixes states as the two holes on different sites delocalize due to hopping. One can however observe that for the low energies, more mixing arises from t_K compared to t_J .

Having described these low energy states, one can make some noteworthy observations. First, the low energy multiplet consists only of states with $j = 1/2$ for both holes, with both holes being on different sites. Excitations within this multiplet will therefore only transition between these states. Second, the first different state is brought down towards low energies by t_K and can be identified as a state having one hole in the $j = 3/2$ while the other hole is still within $j = 1/2$. An excitation from the ground state to this state would correspond to a spin-orbit excitation.

Having investigated the rich energy spectrum arising from exact diagonalization, let us now turn towards calculations of the RIXS process.

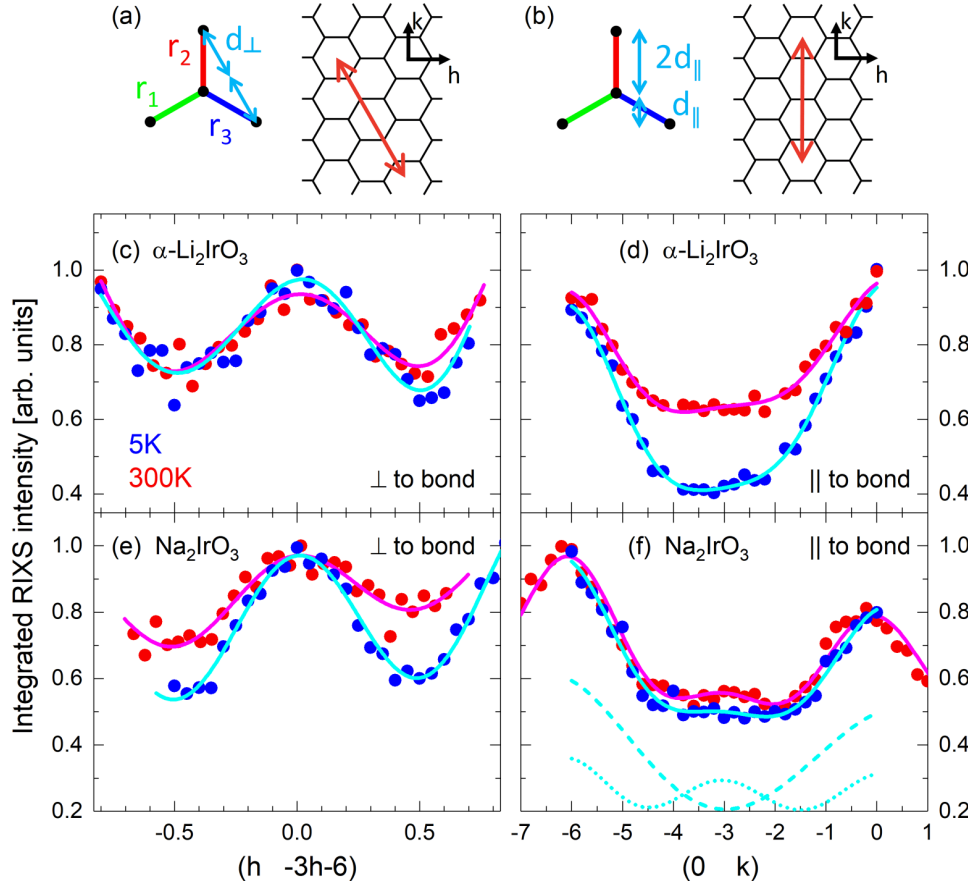


Figure 4.8.: Experimental RIXS results on Na_2IrO_3 - Momentum dependence of experimental RIXS data on Na_2IrO_3 and the related compound $\alpha\text{-Li}_2\text{IrO}_3$ shows signs of periodic modulation. Depending on the scattering geometry (displayed above the data), either a single or two cosine functions can be observed, which is in good agreement with theoretical predictions. Figure taken from Ref. [15].

Interference effects in Na_2IrO_3

The RIXS transitions which can occur in Na_2IrO_3 take place between the ground state and states of higher energy. Experimentally, one is interested in the region of energies below 400 meV, which corresponds to the lowest four excitations. Once again it is worth noting that the spectra of all bonds are calculated separately and only summed up in the end.

The numerical results for the RIXS intensities can be found in Fig. 4.9 and Fig. 4.10. Both datasets show the RIXS intensities as function of transferred momentum and deposited energy for the two relevant geometries, transferred momentum perpendicular to one bond (Fig. 4.9) and parallel to one bond (Fig. 4.10). Each dashed red line denotes a cut at a certain energy, corresponding to the numerical transition energy. These cuts can be found below the panel. Similarly, each cyan line corresponds to a constant momentum cut, i.e. a

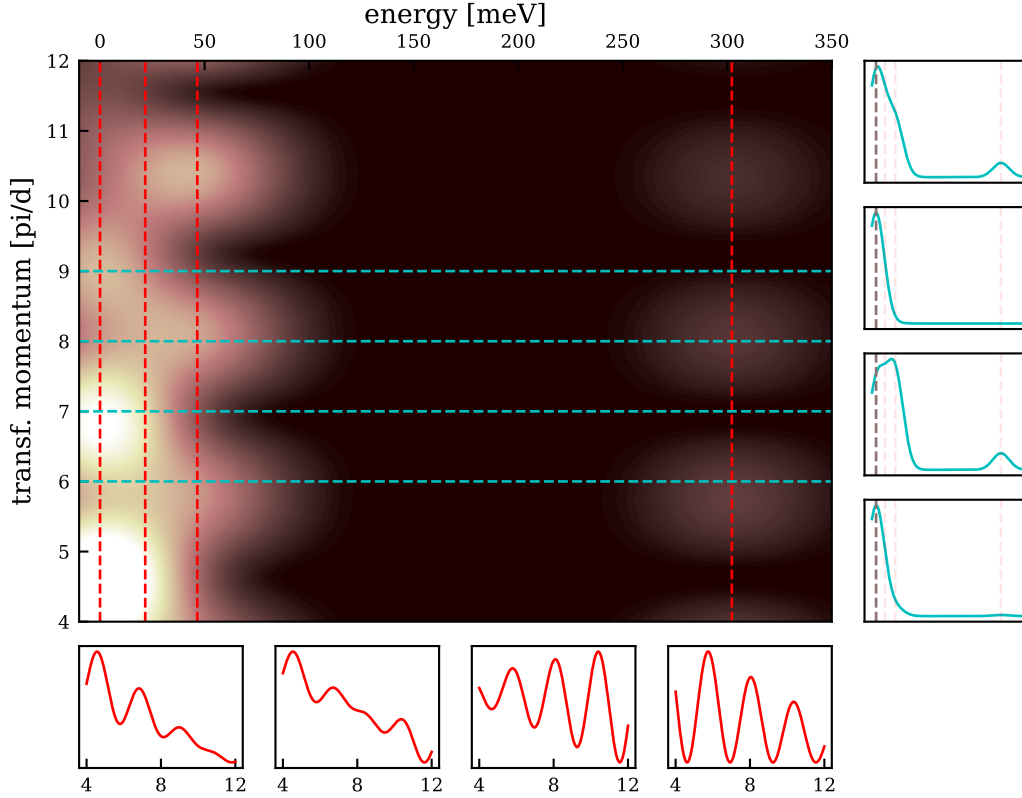


Figure 4.9.: Momentum dependent RIXS intensities in Na_2IrO_3 , perpendicular geometry - Maps of the numerically calculated RIXS intensities for the perpendicular geometry in Na_2IrO_3 showing dependencies of intensities on transferred momentum and deposited energy. All intensity data was calculated by averaging the x, y and z bond data. Data is calculated for momentum transfer perpendicular to the z bond. Momentum space map includes vertical (red) and horizontal (cyan) cuts, along which intensities are displayed below and beside the map respectively. Data shows a clear periodic modulation in momentum space, owing its existence to the delocalized nature of orbitals along the bonds. In total, the data can be described by a single momentum space period compatible with interference from the x and y bonds. The z -bond cannot lead to any interference behavior in this geometry since its projected length along the momentum transfer is 0. Behavior can be compared with experimental data in panels c) and e) of Fig. 4.8.

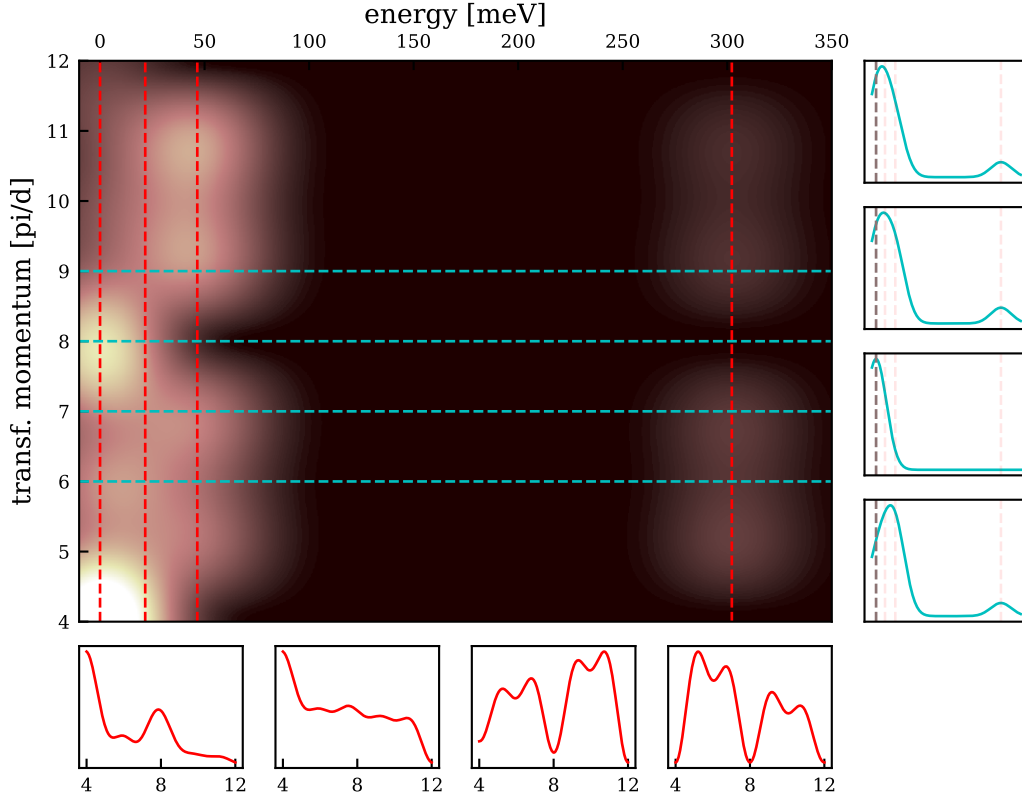


Figure 4.10.: Momentum dependent RIXS intensities in Na_2IrO_3 , parallel geometry - Maps of the numerically calculated RIXS intensities for the parallel geometry in Na_2IrO_3 showing dependencies of intensities on transferred momentum and deposited energy. All intensity data was calculated by averaging the x, y and z bond data. Data is calculated for momentum transfer along the z bond. Momentum space map includes vertical (red) and horizontal (cyan) cuts, along which intensities are displayed below and beside the map respectively. Data shows a clear periodic modulation in momentum space, owing its existence to the delocalized nature of orbitals along the bonds. In total, the data can be described by two momentum space sine/cosine functions, compatible with interference from all three bonds. Since the x and y bonds have a different projected length along the momentum transfer, compared to the z -bond, modulation frequencies differ. Behavior can be compared with experimental data in panels d) and f) of Fig. 4.8.

regular RIXS spectrum for a fixed geometry. Those spectra are shown in cyan on the right hand side of the main panel.

Generally one can observe the elastic line at zero energy as well as two transition peaks for transitions within the $j = 1/2$ subspace. At around 300 meV, one can observe the first spin-orbit excitation, i.e. the transition from the $j = 1/2$ ground state to the $j = 3/2$ state.

There is a qualitative difference between the two sample orientations. For transferred momentum perpendicular to one bond, momentum dependence only shows a periodic behavior which can be described by a single cosine function. In contrast, if the momentum transfer is parallel to one bond, the periodic behavior shows the superposition of two cosine functions of different frequency. This behavior can be directly related to the scattering geometry. If the momentum transfer is perpendicular to one bond, this bond will not show an interference pattern as its projected length along the momentum transfer is zero. However, for the parallel geometry, it will give a contribution along with the other two bonds which have a different projected length along the momentum transfer axis.

Comparing to experimental data can also be done. In the experiments [15], the RIXS intensity is integrated for low energies and high energies. These two regions are defined by a threshold of around 30 meV, up to which everything is counted as *low energy* and above which signals contribute to *high energy* data.

Concluding Remarks

In summary, this section provided an overview over numerical RIXS calculations in the Kitaev material Na_2IrO_3 . Both exact diagonalization as well as RIXS intensity calculations have been carried out on three separate clusters, each consisting out of two IrO_6 octahedra with a shared edge. Relative to the scattering geometry, these clusters have been arranged to resemble the three elementary x -, y - and z -bonds in the honeycomb layers of Na_2IrO_3 .

With parameters in correspondence with experimental data, the low-energy states in Na_2IrO_3 form a manifold of $j = 1/2$ states which can be probed by numerical RIXS intensity calculations. Employing this technique leads to the two different interference diagrams of Fig. 4.9 and Fig. 4.10 which agreed qualitatively very well to experimental RIXS data published in Ref. [15], shown in Fig. 4.8.

This level of agreement suggests that RIXS responses in Na_2IrO_3 can very well be modeled by the present numerical implementation. On one side, this is relevant for future experimental investigations which might probe large regions of momentum space to reveal the bond-directional character of Na_2IrO_3 even more strikingly. On the other side, this agreement is already a striking sign for dominant Kitaev couplings in Na_2IrO_3 .

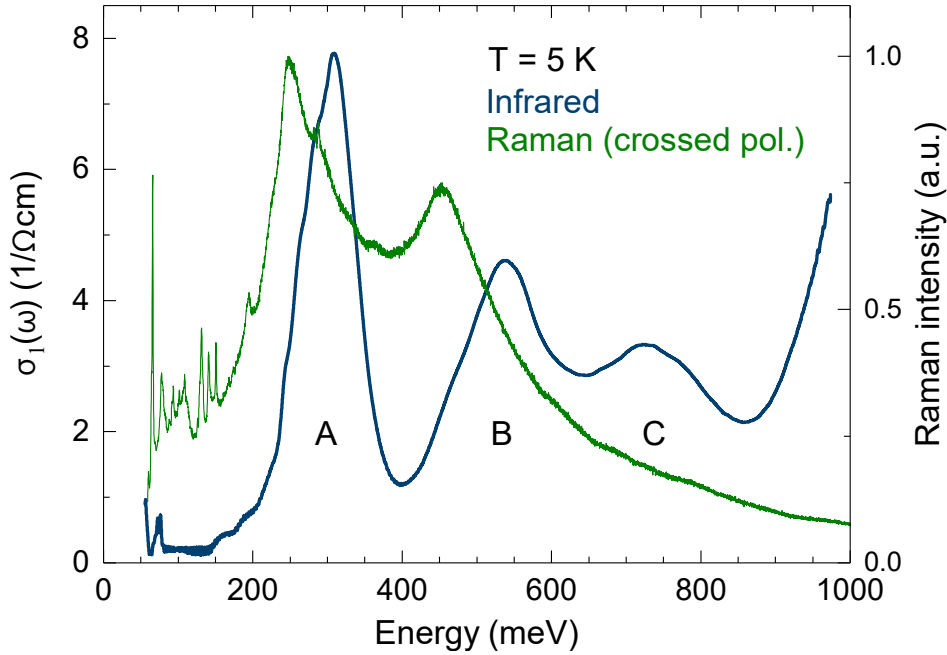


Figure 4.11.: Experimental RIXS results on α -RuCl₃ - Experimental infrared absorption and Raman scattering data for α -RuCl₃ showing a multi-peak structure. Peaks A and B are visible both in Raman and Infrared whereas peak C is only seen in infrared absorption data. Peaks between the two datasets are shifted by phonon modes. Figure taken from Ref. [P3].

4.3.2. Double spin-orbit exciton in α -RuCl₃

Let us shift focus to the most prominent Kitaev material in recent years, α -RuCl₃. Although also α -RuCl₃ shows signs of magnetic ordering at low temperatures, owing its existence to interactions beside Kitaev terms [21–23], it has been commonly appreciated that α -RuCl₃ realizes a proximate Kitaev spin-liquid. A magnetic continuum with fermionic character can be observed in inelastic neutron scattering, THz spectroscopy and Raman scattering [25–32] which only shows signs of dynamical spin-spin correlations between nearest neighbors [26]. Most stunning is the recent discovery of a half-quantized thermal Hall effect [33].

Although the Kitaev character of α -RuCl₃ has been investigated to a large extent, the low energy excitation spectrum of the spin-orbit coupled moments still is not clear. Partially, this is due to great challenges for RIXS at the Ru *L* and *M* edges [41, 42]. Whereas RIXS could confirm the $j = 1/2$ character of related iridate materials [P1, 43–46] by measuring the spin-orbit exciton, i.e. the excitation to the $j = 3/2$ state, in α -RuCl₃ there is no clear picture of attributing low-energy features to certain excitations, but only many conflicting proposals so far.

In this spirit, inelastic neutron scattering and Ru *M* edge RIXS proposed values as spread

out as 145, 195 and 231 meV for the spin-orbit exciton [25, 42, 47]. Similarly, infrared absorption finds absorption bands at 0.3, 0.53, 0.75 eV [47–53] with unclear origin. Those peaks have been proposed to be due to a Mott gap or excitations to e_g states [47, 49, 50], however this is unlikely as it would be in contrast to quantum chemistry calculations [54, 55].

This part of the thesis uses calculations underlying Ref. [P3] to provide an alternative and consistent picture for the low-energy excitations in α -RuCl₃. By combining infrared absorption and Raman scattering data, it was proposed in Ref. [P3] that the peaks are single-, double- and triple-spin-orbit exciton excitations. The data from Ref. [P3] is also displayed in Fig. 4.11. In this section, we want to discuss the numerical calculations supporting this picture.

Model Hamiltonian for α -RuCl₃

Modeling α -RuCl₃ within the numerics works very similar to how Na₂IrO₃ was treated in the last part. Again, the sample is divided into individual bonds which are simulated separately. Moreover, since in this case we are only interested in the exact diagonalization, we can neglect all but one bond.

The single remaining bond consists of two Ir-octahedra with Ir atoms being in a d^5 configuration. The octahedra at the ends of the bond are sharing a common edge lying within the xy plane, ultimately yielding the off-diagonal form of hopping already present in Na₂IrO₃. In total, α -RuCl₃ is described by the same Hamiltonian as Na₂IrO₃, however parameter values differ slightly as

$$\begin{aligned}
 \lambda &= 160 \text{ meV} \\
 \Delta &= 60 \text{ meV} \\
 U &= 2000 \text{ meV} \\
 J_H &= 400 \text{ meV} \\
 t_J &= 0 \text{ meV} \\
 t_K &= 160 \text{ meV} =: t_{xy}
 \end{aligned}
 \tag{4.11}$$

is used for α -RuCl₃.

Exact diagonalization for α -RuCl₃ and the double-spin-orbit exciton

Fig. 4.12 shows the results from exactly diagonalizing the α -RuCl₃ Hamiltonian numerically. Again, eigenenergies are displayed upon consecutive increase of model parameters. An initial increase of λ separates the $j = 1/2$ states from $j = 3/2$ states. Since the two holes can either be both in $j = 1/2$ (lowest energy), one in $j = 1/2$ and one in $j = 3/2$ or both be in $j = 3/2$, there are in total three branches developing. Increasing Δ splits the $j = 3/2$ further, therefore the three levels get split differently depending on how much

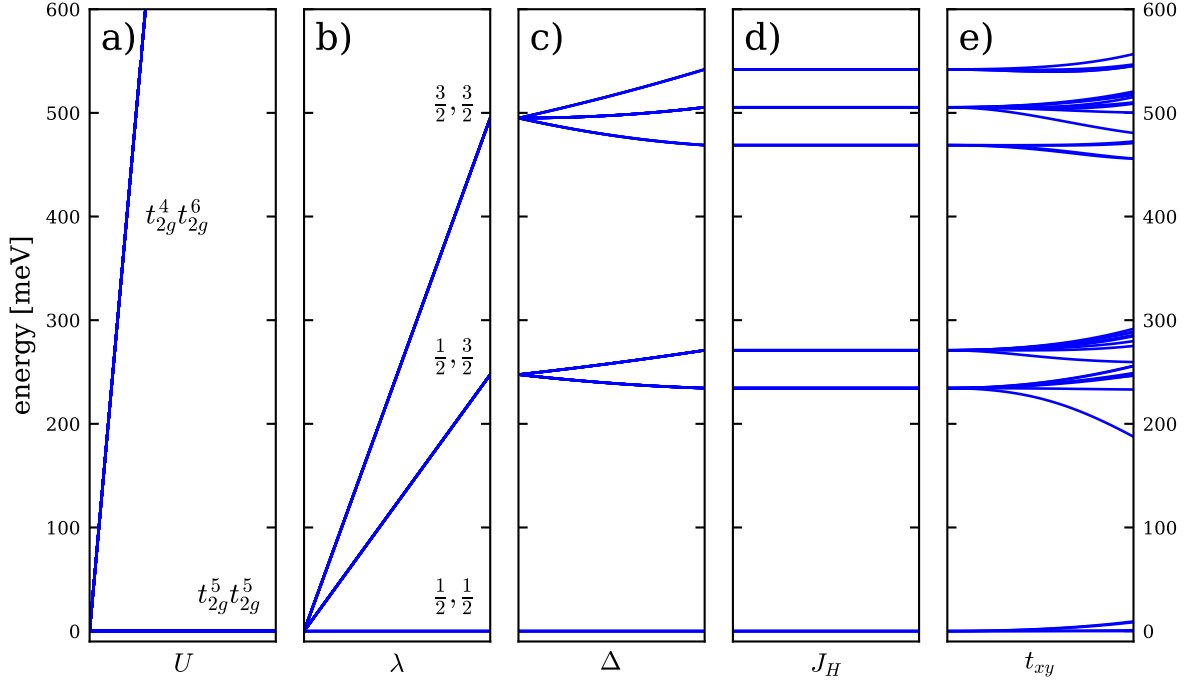


Figure 4.12.: ED for low energy states of α -RuCl₃ - Evolution of 2-hole eigenenergies in α -RuCl₃ when increasing couplings one after another to their experimental values. Following the states to the experimental parameters (dashed line) shows that the three groups correspond to $(j = 1/2, j = 1/2)$ states, $(j = 1/2, j = 3/2)$ and $(j = 3/2, j = 3/2)$ states for the two particles respectively. Corresponding excitations would be described as single- and double-spin orbit excitons respectively and fit nicely to experimental Raman and infrared absorption data [P3]. Experimental data is also depicted for illustration purposes in Fig. 4.11.

$j = 3/2$ they contain. Increasing Hubbard interaction U will drastically lift the energies of all states in which the two particles are on the same site. From hereon, the ground state only contains states with one particle per site. Hund's coupling J_H only affects the states with particles on the same site, which are at this point high in energy, therefore leaving the low-energy levels unchanged. Finally, hopping t_{xy} splits/mixes levels as it induces delocalization between sites.

Regarding the final states under experimental parameters, one can make some observations. In total, there are roughly three groups of states for energies below 600 meV. The lowest lying states contain only two-particle states with both holes being in the $j = 1/2$ manifold. The next group contains only states with one hole being in the $j = 1/2$ and one hole being in the $j = 3/2$. Excitations from the ground state to this group therefore correspond to a spin-orbit excitation. The third group further up in energy corresponds to states where both holes are in the $j = 3/2$ manifold. Therefore excitations to this manifold correspond

to performing a double spin-orbit excitation.

Concluding Remarks

In this part, numerical calculations of the eigenspectrum in α -RuCl₃ have been performed. Motivated by the previous success in modeling a Kitaev material locally with individual bonds only, the numerics focused on two edge-sharing IrO₆ octahedra with parameters adapted to fit α -RuCl₃.

All in all, calculations of eigenenergies showed a remarkable agreement with peaks in the Raman and infrared data presented in [P3]. This agreement indicates that the low-energy structure of α -RuCl₃ can indeed be understood from the perspective of single- and double-spin-orbit excitons, unifying many conflicting approaches.

4.4. Beyond RIXS

So far, the numerical implementation allowed only for the computation of eigenstates in Ir clusters and their respective excitation spectra in terms of L2 and L3 edge RIXS processes. Although it is able to handle a variable number of holes and sites within the clusters, the numerical implementation is tailored to tackle this specific situation. A general question one might naturally have is how the code handles beyond these specific problems. This will be addressed in the present section. More precisely two extensions or changes will be discussed. First, the RIXS process will be substituted by measurement of optical conductivities and second, a temperature dependent state occupation with Boltzmann weights is introduced.

Let us start with discussing the optical conductivity. It essentially describes the ability of electrons to flow through the cluster upon interaction with light. On a technical level, transitions from initial states $|i\rangle$ to other eigenstates $|f\rangle$ are introduced in a similar formalism to the dipole amplitudes, one only replaces the dipole operator by the hopping operator. Since at this point it is a purely conceptual discussion, only qualitative features of the optical conductivity are of interest, so that it can be written as

$$\sigma(\omega) = \sum_f \langle f | H_{\text{hop}} | i \rangle \delta(\omega, E_f - E_i) \quad (4.12)$$

for some number of eigenstates.

As a second change, eigenstates of the system are thermally distributed, i.e. have an occupation probability given by their eigenenergy

$$p_i = \frac{1}{Z} e^{\beta E_i} \quad (4.13)$$

with Z given by

$$Z = \sum_i e^{\beta E_i}. \quad (4.14)$$

This in principle allows for excitations from any state to any other state.

For illustration purposes, let us consider the following example system containing two sites connected by hopping as well as some local Hamiltonians on each site. Results for the optical conductivity as defined above can be seen in Fig. 4.13. In principle, the code is able to show basic features of this optical conductivity and even changes in peak intensities for varying temperatures. In a subsequent step, this data can be compared to experimental data as well.

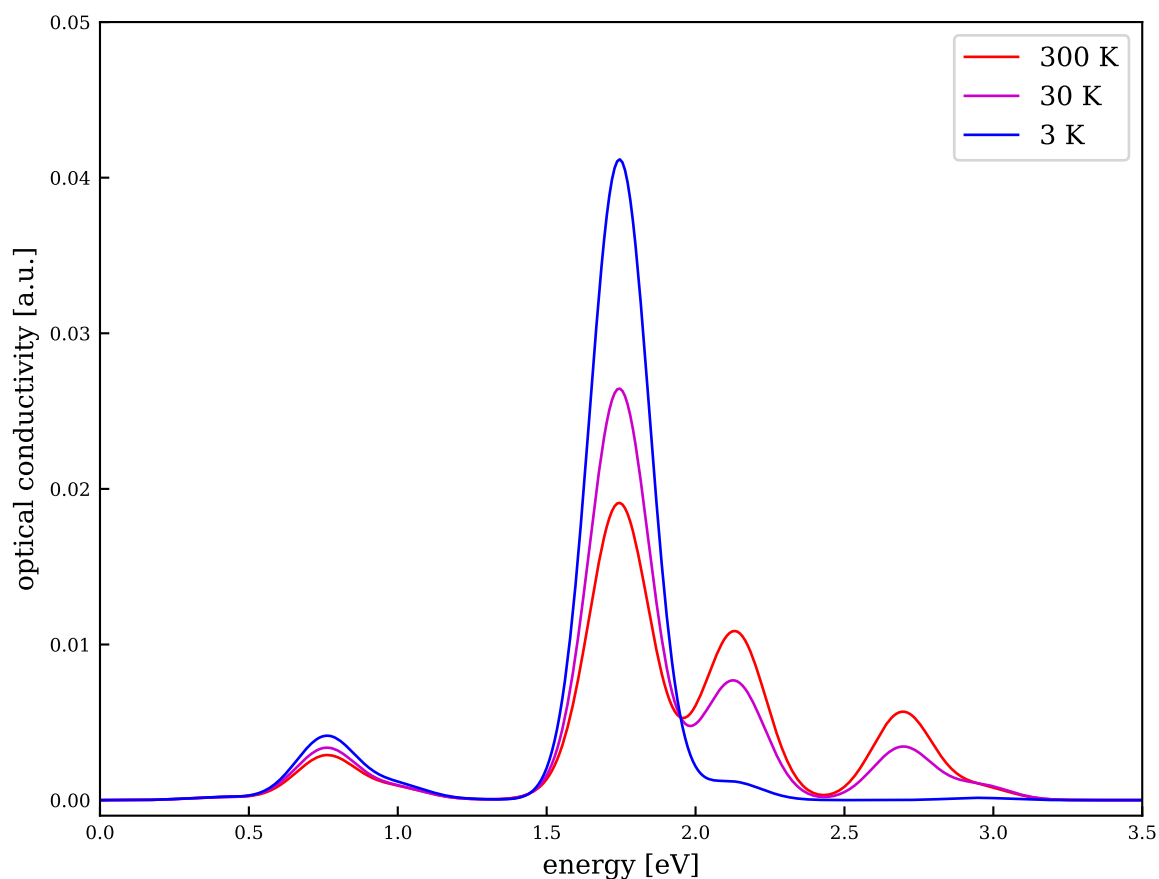


Figure 4.13.: Optical Conductivity from ED - Temperature dependence of optical conductivity in a system modeling a fictitious 2-hole dimer. The system includes spin-orbit coupling, crystal field distortion effects, Hubbard interaction and hopping between two corner-sharing IrO_6 octahedra. Calculations of the optical conductivity have been performed by computing transition amplitudes while replacing the dipole operator by the hopping operator according to Eq. (4.12). Temperature dependence has been modeled by including thermal occupation of quantum states.

5. Summary and discussion

In this Part I, a numerical toolbox called `RIXSCalculator.jl` [S1] has been developed for computing exact diagonalization and RIXS calculations in a variety of iridate (cluster) materials. Overall, the implementation allows flexibility in choosing applications with the only limitation being a description in terms of $\ell = 1$ states. This requirement was met as all examples in Chapter 4 focused on the t_{2g} subspace of the $5d$ shell in various iridate materials. Between examples, not only the relevant interactions were changed, but also the geometry and number of particles. Numerically, the full many-body Hamiltonian for a variable number of holes or electrons can be computed, including interactions such as spin-orbit coupling, crystal field distortions, external magnetic fields, hopping, Hund's coupling and Hubbard interaction.

Concerning physical examples, this chapter focused mostly on iridate materials in which the local geometry was described by IrO_6 octahedra. It was seen that "real" dimer materials, where pairs of IrO_6 octahedra were structurally isolated from other pairs, could be described similarly well as extended Kitaev systems that only took a single bond into considerations.

Generally, materials with more than a single IrO_6 octahedron allowed for the application of RIXS interferometry, i.e. the search for interference patterns in the RIXS intensities. Such periodicities are thought of as signatures of quasi-molecular orbitals which describe states that are delocalized across (parts of) the cluster.

The physical motivation for investigating such materials lies within the formation of magnetic models. All of the materials investigated show the formation of local $j = 1/2$ moments which subsequently can interact across the material in different forms, yielding a variety of effective spin models. Whereas the resulting spin models were not the main focus of this part, the interest was mainly about the intrinsic electronic structure forming these magnetic moments.

The discussion of example systems started with the material $\text{Ba}_2\text{CeIrO}_6$, a double-perovskite material in which local $j = 1/2$ moments form inside the IrO_6 octahedra on one of the fcc sublattices. Whereas structure analysis confirmed the extraordinary purity of cubic symmetry, RIXS data revealed that the character of local moments still includes $j = 3/2$ mixtures originating from finite crystal field distortions away from the cubic limit. In particular numerical calculations of this chapter could confirm the components of local wavefunctions when comparing excitation energies to measured RIXS data.

In a subsequent section, the family of $\text{Ba}_3M\text{Ir}_2\text{O}_9$ materials with face-sharing Ir-dimers was investigated. Particular interest has been paid to $\text{Ba}_3\text{Ti}_{3-x}\text{Ir}_x\text{O}_9$, in which an increase of Ir

concentration was experimentally found to suppress magnetism, an observation which was counterintuitive at first. Calculations however support another view on this observation as the increase in Ir concentration facilitates the formation of dimers which are non-magnetic, yielding different momentum space signatures in RIXS intensities. This work allows comparison with experimental RIXS data, which is currently work-in-progress. Yet another work-in-progress project in the family of $\text{Ba}_3\text{M}\text{Ir}_2\text{O}_9$ is the work on $\text{Ba}_3\text{InIr}_2\text{O}_9$ which featured a dimer with 3 holes. First results of exact diagonalization and RIXS calculations have been shown, however most of the comparison and discussion on the ground state is still work-in-progress.

As a last class of example systems, the famous Kitaev materials Na_2IrO_3 and $\alpha\text{-RuCl}_3$ have been investigated. Although these materials do not form isolated dimers, RIXS intensity measurements suggested that correlations only persist up to nearest neighbors, facilitating a local cluster picture yet again. In Na_2IrO_3 was on the precise form of momentum space interference effects [15], which could be verified to show signs of dominant Kitaev exchange up to high temperatures. Currently there is again more work-in-progress. In $\alpha\text{-RuCl}_3$, calculations focused more on the precise form of low-energy excitations confirming the existence of a double-spin orbit exciton [P3]. Here, calculations could be brought into correspondence with both Raman and infrared absorption data.

A small and final section demonstrated that in principle the code in `RIXSCalculator.jl` is not limited to RIXS. Here, also a principle form of optical conductivity was calculated to demonstrate once again the versatility that this full diagonalization approach can achieve.

Currently, work on the code focuses mostly on adding symmetries into the numerical implementation. Symmetries allow generally for a reduction of Hilbert space and access to larger clusters of IrO_6 octahedra. Another benefit of implementing symmetries is the improvement in interpretability of the output. Particularly, the interpretation of output for larger systems has proven to be challenging and thus could greatly benefit from this additional information.

Part II.

Supersymmetry and Topology

6. Introduction

A substantial part of modern condensed matter physics can be expressed as the study of correlated electrons in the periodic arrangement of atoms. As the study of the full quantum-many body problem of correlated electrons is too extensive, a necessary first step is to discuss the free electronic problem first, i.e. the single particle description. Although being very simplistic, these free electronic models describe many phenomena to a surprising accuracy.

Within the field of electronic models, it has long been appreciated that symmetries play a major role in characterizing the behavior of a system. Besides crystalline symmetries of the underlying lattice, especially the behavior of a model under internal symmetries such as time-reversal symmetry, particle-hole symmetry or chiral symmetry, was shown to determine if and which topological phases are possible to realize in a system [56].

Yet another symmetry is supersymmetry. This symmetry, originally introduced in high-energy physics [57–59] to explain physics beyond the standard model [60], relates the electronic (fermionic) degrees of freedom to other bosonic particles. In contrast to other conventional symmetries it therefore does not map states within a given system, but rather provides a link to other related models which behave similarly. Although the concept was introduced in high-energy physics, supersymmetry can also be relevant for a non-relativistic context, e.g. in the study of random phenomena and quantum chaos in mesoscopic systems [61].

A similar concept of relating two models with identical properties has been explored in the field of topological mechanics. Here, mechanical models are constructed that contain the (topological) properties of electronic models [62]. Exploiting this correspondence lead to fascinating incarnations of electronic features in mechanical systems such as the realization of floppy boundary modes in isostatic lattices which can be identified with topologically protected boundary modes in topological insulators [63, 64].

Conventionally, topological mechanical systems can be constructed by defining a classical system with Newtonian equation of motion $\ddot{x} = -\mathbf{D}x$ where the dynamical matrix \mathbf{D} comes from the Schrödinger equation

$$i\frac{\partial}{\partial t} \begin{pmatrix} \sqrt{\mathbf{D}}^T x \\ i\dot{x} \end{pmatrix} = \begin{pmatrix} 0 & \sqrt{\mathbf{D}}^T \\ \sqrt{\mathbf{D}} & 0 \end{pmatrix} \begin{pmatrix} \sqrt{\mathbf{D}}^T x \\ i\dot{x} \end{pmatrix}, \quad (6.1)$$

of a corresponding quantum problem. It has already been noted [62, 63] that such Hamiltonian matrices as in Eq. (6.1) correspond to symmetry class BDI [56] and therefore gener-

ically exhibit a supersymmetric form [61]. Moreover, connecting the two concepts of SUSY and topological mechanics can even be done explicitly [65], which hints at a supersymmetric formulation of topological mechanics.

Usually, supersymmetry is performed on the level of identifying operators and Hamiltonians between subsystems. In this thesis however, a different approach is proposed which instead relies on the underlying lattice graph structure. By interpreting interaction matrices as adjacency matrices one can then obtain supersymmetric relations formulated on the level of lattice graphs.

Overall, the part is organized as follows. First, Chapter 7 provides a brief introduction to quadratic lattice models and their numerical solution, as they are the building blocks of the upcoming discussion. Then in Chapter 8, the concept of supersymmetry is introduced and it is shown how graph theoretical language of lattice graphs can help in defining supersymmetric relations. With these technical details discussed, a series of different applications are demonstrated. First, complex fermions are mapped to complex bosons with a sublattice-to-sublattice mapping in Chapter 9. Then, Majorana fermions are demonstrated to be the natural counterpart of topological mechanical systems in Chapter 10. In this chapter, the isospectrality between mechanical and Majorana models is explicitly shown at two examples. Finally, some discussion of additional correspondences is given in Chapter 11 before finishing with a summary and outlook in Chapter 12.

In principle, the arguments in this part are basis for a work-in-progress manuscript [P4], which is currently in preparation. However, details on the Majorana fermion correspondence have already been published in Ref. [P5].

7. Lattice models

Let us start the discussion of graph theoretical supersymmetry by first introducing the basic concept of lattice models. We will first discuss the notion of lattices, unitcells and graphs and then extending it by adding quadratic Hamiltonians. These physical models yield bandstructures whose numerical computation will be discussed at the end of the section.

7.1. Lattices and unitcells

In condensed matter physics, any crystalline lattice structure can be written as being composed of two parts, a *Bravais lattice* and a *basis*. The Bravais lattice defines the translations under which the crystalline structure is invariant. For d spatial dimensions, there are at most d of such independent translations, which are also referred to as Bravais lattice vectors $\vec{a}_1, \dots, \vec{a}_d$.

The basis contains the atomic positions of the crystal, which are shifted by translations of the Bravais lattice. Because of these translations it does not need infinitely many of such positions but typically only a few so called basis sites \vec{r}_i with $i \in [1, N]$, which are then subsequently periodically arranged.

Combining the two concepts of Bravais lattice and basis, any atomic position in a crystal lattice can be written as

$$\vec{R} = \vec{r}_i + \sum_{j=1}^d n_j \vec{a}_j, \quad (7.1)$$

with integer prefactors $n_j \in \mathbb{Z}$. The combination of Bravais lattice and basis is also referred to as *unitcell* of the lattice. Examples of such unitcells and lattices are shown in Fig. 7.1. Here, atomic positions are also connected by so-called *bonds* which are edges between sites of minimal distance. Later, bonds will play a role when defining interactions between degrees of freedom situated on the individual sites.

When solving a model on a periodic lattice, one often performs a Fourier transformation into momentum space, as will be demonstrated later. This is a beneficial operation, since a Bravais lattice in real space, always has a momentum space partner which is a Bravais lattice as well. This so-called *reciprocal lattice* is spanned by reciprocal lattice vectors $\vec{b}_1, \dots, \vec{b}_d$ which fulfill the condition

$$\vec{a}_i \cdot \vec{b}_j = 2\pi \delta_{ij}, \quad (7.2)$$

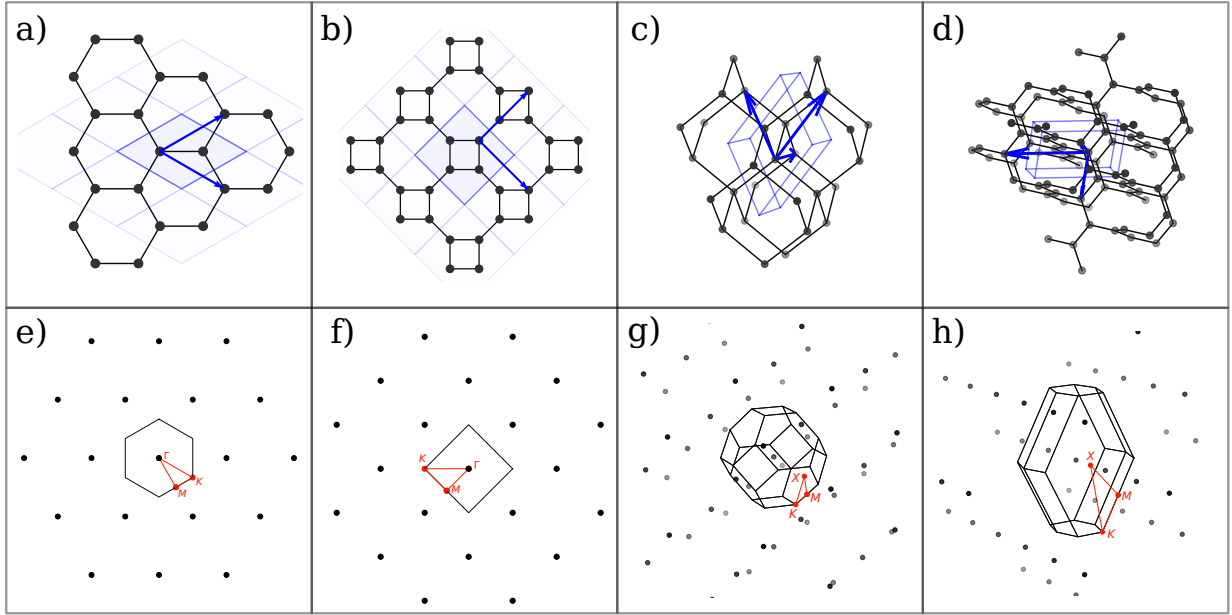


Figure 7.1.: Unitcells in 2d / 3d with corresponding Brillouin zones - Exemplary illustrations of unitcells for the honeycomb, square-octagon, diamond and hyperkagome lattices, shown in panels a) - d). Each lattice can be constructed from a Bravais lattice and a basis, whereas lattice vectors of the Bravais lattice are shown as blue arrows and the basis consists of sites within the unitcell (blue region). The corresponding reciprocal lattices, including a respective illustration of the Brillouin zone, are shown in panels e) - h).

where \vec{a}_i refers to the Bravais lattice vectors of the lattice in real space.

Furthermore, in reciprocal space, the concept of a basis is replaced by the concept of a (first) *Brillouin zone*. The first Brillouin zone is the *Wigner-Seitz cell* of the reciprocal lattice and thus is defined as the set of points which is closer to the origin than to any other point of the lattice. This allows a rewriting of any momentum \vec{q} as

$$\vec{q} = \vec{k} + \sum_{i=1}^d \tilde{n}_i \vec{b}_i, \quad (7.3)$$

with integer prefactors $\tilde{n}_i \in \mathbb{Z}$ and a \vec{k} within the first Brillouin zone. Fig. 7.1 contains also the reciprocal lattices and Brillouin zones for each of the 2d and 3d examples shown before.

7.2. Bandstructures of quadratic lattice models

Now let us focus on models defined on lattices, specifically on one special family of models only including quadratic interaction terms. Such quadratic models are also often called free models because they describe non-interacting particles. Although at first glance seeming quite restrictive, many materials are very well described by these free models as the assumption of non-interacting particles is well justified within the quasi-particle picture. In the following, one can imagine particles occupying localized orbitals and hopping from site to site. In fact, these models are also a generic solution in periodic structures due to Bloch's theorem. In total, all of these models allow a generic solution, which will be discussed in the following.

Let us start with a generic free model of the form

$$\mathcal{H} = \sum_{\mu\nu} \mathbf{a}_\mu^\dagger \mathbf{M}_{\mu\nu} \mathbf{a}_\nu \quad (7.4)$$

describing particles created and annihilated by operators \mathbf{a}_μ defined on sites μ of an infinite lattice. Particles can hop from site μ to ν with amplitudes $\mathbf{M}_{\mu\nu}$ following the same translational invariance as the underlying lattice. In principle, there can be multiple orbitals on each lattice site, which would result in \mathbf{a}_μ having \tilde{d} components as well as the interaction being described by a $\tilde{d} \times \tilde{d}$ matrix \mathbf{M} .

The periodic lattice structure allows utilizing a Fourier transform of this generic model which will finally bring it in a block-diagonal form. Let us start by formalizing the lattice structure, i.e. defining that lattice points μ are located at positions

$$\vec{r}_\mu = \vec{R}_\alpha + \vec{r}_i \quad (7.5)$$

where \vec{R}_α is the corresponding Bravais lattice site and \vec{r}_i the position of the basis site within the unitcell. With this definition, we can split the summation and rewrite the model to

$$\mathcal{H} = \sum_{\alpha\beta} \sum_{ij} \mathbf{a}_{\alpha i}^\dagger \mathbf{M}_{\alpha\beta ij} \mathbf{a}_{\beta j}. \quad (7.6)$$

The next step is to define the actual Fourier transform. Let us use the convention

$$\begin{aligned} \mathbf{a}_{\alpha i}^\dagger &= \frac{1}{\sqrt{N}} \sum_{\vec{k}} \mathbf{a}_{ki}^\dagger e^{+i\vec{k} \cdot (\vec{R}_\alpha + \vec{r}_i)} \\ \mathbf{a}_{\beta j} &= \frac{1}{\sqrt{N}} \sum_{\vec{k}'} \mathbf{a}_{k'j} e^{-i\vec{k}' \cdot (\vec{R}_\beta + \vec{r}_j)} \end{aligned} \quad (7.7)$$

where N describes the total number of Bravais lattice sites and \vec{k} and \vec{k}' label momenta within its first Brillouin zone. For any finite lattice, these momenta are discretely spaced resulting in N different momentum values for a Bravais lattice of N sites.

Inserting the Fourier transform into Eq. (7.6) results in

$$\mathcal{H} = \frac{1}{N} \sum_{\alpha\beta} \sum_{ij} \sum_{\vec{k}\vec{k}'} \mathbf{a}_{\vec{k}i}^\dagger e^{+i\vec{k}\cdot(\vec{R}_\alpha+\vec{r}_i)} \mathbf{M}_{\alpha\beta ij} \mathbf{a}_{\vec{k}'j} e^{-i\vec{k}'\cdot(\vec{R}_\beta+\vec{r}_j)} \quad (7.8)$$

$$= \frac{1}{N} \sum_{\alpha\beta} \sum_{ij} \sum_{\vec{k}\vec{k}'} \mathbf{a}_{\vec{k}i}^\dagger \mathbf{M}_{\alpha\beta ij} \mathbf{a}_{\vec{k}'j} e^{i(\vec{k}\cdot\vec{r}_i-\vec{k}'\cdot\vec{r}_j)} e^{i(\vec{k}\cdot\vec{R}_\alpha-\vec{k}'\cdot\vec{R}_\beta)} \quad (7.9)$$

which can now be further simplified by the use of lattice periodicity. To do so, note that many elements of \mathbf{M} are actually zero. The only non-zero elements are those given by hopping processes from site μ to ν , i.e. from Bravais lattice site α to β . For those elements, let us write

$$\vec{R}_\beta = \vec{R}_\alpha + \vec{\delta}_{\alpha\beta} \quad (7.10)$$

i.e. explicitly introducing the distance in terms of Bravais lattice vectors $\vec{\delta}_{\alpha\beta}$. Inserting this into the Hamiltonian removes the sum over β and simplifies further to

$$\mathcal{H} = \frac{1}{N} \sum_{\alpha} \sum_{ij} \sum_{\vec{k}\vec{k}'} \mathbf{a}_{\vec{k}i}^\dagger \mathbf{M}_{\alpha\beta ij} \mathbf{a}_{\vec{k}'j} e^{i(\vec{k}\cdot\vec{r}_i-\vec{k}'\cdot(\vec{r}_j+\vec{\delta}_{\alpha\beta}))} e^{i(\vec{k}-\vec{k}')\cdot\vec{R}_\alpha}. \quad (7.11)$$

Lattice periodicity of the Bravais lattice allows to use the identity

$$\frac{1}{N} \sum_{\alpha} e^{i(\vec{k}-\vec{k}')\cdot\vec{R}_\alpha} = \delta(\vec{k}-\vec{k}') \quad (7.12)$$

which is partially already contained in the previous expression. Therefore, also the summations over α and \vec{k}' can be resolved and one obtains

$$\mathcal{H} = \sum_{\vec{k}} \sum_{ij} \mathbf{a}_{\vec{k}i}^\dagger \mathbf{M}_{ij} \mathbf{a}_{\vec{k}j} e^{i\vec{k}\cdot\vec{\Delta}_{ij}} \quad (7.13)$$

where the hopping spans real space distances of $\vec{\Delta}_{ij} = \vec{r}_i - (\vec{r}_j + \vec{\delta}_{\alpha\beta})$.

In total, the simplification steps yielded a block-diagonalized Hamiltonian matrix. Each individual of the in total N blocks is of size $\tilde{d}b \times \tilde{d}b$ where \tilde{d} is the number of orbitals on every lattice point and b the basis size of the lattice. Each momentum \vec{k} thus describes $\tilde{d} \cdot b$ eigenstates that are intrinsically periodic with period \vec{k} . A common theme is to follow the eigenenergies upon variation of \vec{k} . Plotted along a high-symmetry path, this form of diagram is called a *bandstructure* and can be used to extract information about the model in a pictorial way.

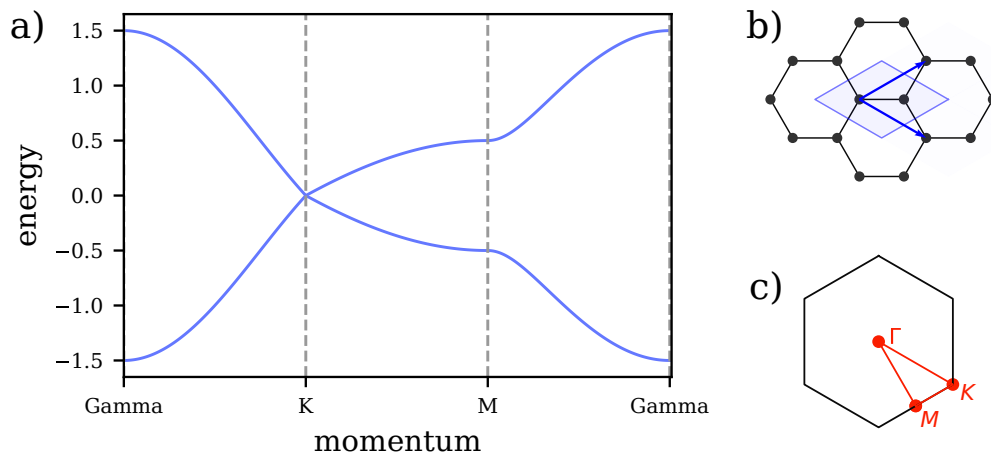


Figure 7.2.: Honeycomb bandstructure - Numerically calculated bandstructure (c.f. panel a)) for a model of nearest-neighbor hopping on the honeycomb lattice, which is shown in panel b). The bandstructure is calculated along a path in reciprocal space depicted in panel c).

7.3. Numerics of lattice models and LatticePhysics.jl

Having established the general formalism of quadratic models on lattices, let us discuss how to solve the models and extract spectral properties in practice. The core element of the bandstructure calculation is the construction and diagonalization of the momentum space interaction matrix $\mathbf{M}_{ij}(\vec{k}) = \mathbf{M}_{ij} \exp(i\vec{k} \cdot \vec{\Delta}_{ij})$. Of course, for models with only a few degrees of freedom or small bases one can write down the momentum space interaction matrix explicitly and diagonalize it analytically. This process however works in practice only for matrices which are at most 2×2 or 3×3 and one would usually employ some form of numerical diagonalization for bigger matrices.

Numerical diagonalization itself comes in many shapes and forms. There are different approaches and partial software solutions existing. These solutions range from programs like Mathematica, in which one can obtain analytical eigenvalues for \vec{k} -dependent matrices of larger sizes by using computer assisted linear algebra, all the way to numerical packages as MKL, offering C-routines to quickly diagonalize complex matrices. One common feature of all of these software solutions is that the diagonalization itself is already implemented, however one has to construct the appropriate form of matrix explicitly beforehand.

Constructing the interaction matrix can again be simply implemented in many forms. The simplest one being a hard-coded function within the code to return the appropriate matrix for a passed value of \vec{k} . Although being a valid approach, the scope of the current chapter is taking a different perspective. First of all, there are many different lattice examples in the current chapter, which all would need their own function. Second, most of the work in this

chapter builds upon the underlying lattice graph and transformations thereof. Both these aspects show the necessity for a code-package that builds a suitable interaction matrix for an underlying lattice graph. This graph can then be visually debugged and modified between the following examples while still retaining a suitable interaction matrix.

During the work behind the following sections, all lattice graph related routines have been grouped together and developed as a single package for the programming language Julia, called `LatticePhysics.jl` [S3]. This package provides the underlying lattice graph structure as well as bandstructure calculation and plotting capabilities for it. In the following, let us quickly discuss the extent of automation possible with such a package and how certain aspects of bandstructure calculations can be automated with `LatticePhysics.jl`. This section however should not be misunderstood for an extensive documentation, which instead can be found on github [S3].

Unitcells and Lattices

The central object which needs a code representation is the lattice graph underlying the system. Generally speaking, such a lattice graph consists of *sites* and *bonds*, which are edges connecting different sites, as well as some form of periodicity. Whereas sites are directly inferred from the Bravais lattice and basis sites of the physical lattice, bonds have no direct physical counterpart. However it is useful in the following to identify every bond with exactly one hopping or interaction term \mathbf{M}_{ij} in the Hamiltonian.

Sites of a lattice are represented in `LatticePhysics.jl` as their own type `Site` which contains a label as well as a real space position. Similarly, bonds are represented as objects of type `Bond`, containing indices of connected sites, a label and information on wrapping periodic boundary conditions, if applicable. Since bonds are only defined in the context of either a finite lattice graph or a unitcell, giving dependent information such as indices or periodic boundary is reasonable.

From a physical perspective, any lattice can be represented as a Bravais lattice plus a basis, which together form the *unitcell* of such lattice. In `LatticePhysics.jl`, unitcells have their own type `Unitcell` which contain both basis sites and bonds as well as the `lattice vectors` of the underlying Bravais lattice. Unitcells are the basis of later calculations in momentum space since they represent exactly the needed combination of basis site positions and Bravais lattice periodicity.

A *finite lattice graph* can be constructed. These objects are called `Lattice` in the code context of `LatticePhysics.jl` and contain the same information as a `Unitcell` object with the addition of the unitcell that the lattice was built from. `Lattice` objects can be used whenever a finite representation of a lattice is needed, e.g. in the context of plotting and visualizing or for codes on finite lattices like Monte Carlo methods. The use of unitcells and lattices within `LatticePhysics.jl` is also briefly highlighted in Fig. 7.3.

Momentum space

Since many of the upcoming bandstructure calculations are carried out in momentum space, it is worth automating the process of generating contextual momentum space data for a given unitcell within `LatticePhysics.jl`. More precisely, the focus will be on creating reciprocal unitcells and lattices as well as meaningful representations of the first Brillouin zone for any unitcell. A final helpful tool will be to automatically find high-symmetry points within the Brillouin zone and generate paths through momentum space that navigate from point to point.

Most of the momentum space calculations are based around *reciprocal unitcells*. `LatticePhysics.jl` provides functionality to directly obtain such a reciprocal unitcell for any real-space unitcell. A reciprocal unitcell contains reciprocal lattice vectors satisfying perpendicularity relations with the real-space lattice vectors.

A *Brillouin zone* can be computed automatically for any 2d or 3d unitcell object by constructing the reciprocal lattice and its first Wigner-Seitz cell respectively. Corners, edges and faces of the Brillouin zone are saved in an object of type `BrillouinZone` which can then be used for plotting or further computation. Additionally, there are functions provided which check if a passed momentum point is within the first Brillouin zone or which fold a passed momentum point into the first Brillouin zone by shifting it along the reciprocal lattice.

Finally, the `BrillouinZone` object can implicitly be used to quickly define high-symmetry points in momentum space for a passed unitcell. These points can then be chained together to form a `ReciprocalPath` in momentum space, which can be plotted or also used for further computation. In Fig. 7.3, these momentum space objects are constructed and plotted after the real space unitcell and lattice construction has taken place.

Hamiltonians

Having the ability to generate any geometric lattice graph in code allows to further define Hamiltonians based on these lattices. To stay within the scope of this chapter, let us concentrate on how to represent models that are quadratic, i.e. that have exactly two interacting objects on two different sites. These are models of the form

$$\mathcal{H} = \sum_{\mu\nu} \mathbf{a}_\mu^\dagger \mathbf{M}_{\mu\nu} \mathbf{a}_\nu \quad (7.14)$$

with objects \vec{a}_μ defined on sites μ as well as interaction between sites μ and ν . This interaction can e.g. be some form of hopping as described above or a spin interaction.

In principle, one can distinguish two different approaches to solve these models, one being exact calculations on finite graphs in real space, the other one being in momentum space utilizing the periodicity of the Bravais lattice, as laid out in section 7.2. Both approaches

have in common that two ingredients have to be known:

1. The *connectivity* of the underlying lattice graph, represented by the sum $\sum_{\mu\nu}$ which sums over interaction terms
2. The *parametrical values* of couplings or hoppings, represented by the interaction matrix elements $\mathbf{M}_{\mu\nu}$.

The connectivity information is already encapsulated in either a `Unitcell` or `Lattice` object as a list of bonds and thus readily available within the code. Note again that the convention of representing every pairwise interaction as a single bond is used. To also supply parametrical values to the individual bonds, i.e. give a value on how strong a certain interaction is, a new object of type `BondHamiltonian` is provided in `LatticePhysics.jl`. A `BondHamiltonian` translates any bond to a complex number denoting the interaction strength. If there is more than a single orbital per site or more than one spin component, the `BondHamiltonian` can also return an entire $\tilde{d} \times \tilde{d}$ matrix.

It is further possible to group the `BondHamiltonian` and `Unitcell` together into a `Hamiltonian` object to contain all information of a quadratic Hamiltonian in a single object. A `Hamiltonian` object also already contains all information necessary to build up the momentum interaction space matrix $\mathbf{M}_{ij}(\vec{k}) = \mathbf{M}_{ij} \exp(i\vec{k} \cdot \vec{\Delta}_{ij})$, thus a respective function is also provided to quickly compute such a matrix.

Bandstructures and momentum space manifolds

With the definition of Hamiltonians complete, let us turn our attention towards the goal of the numerical implementation, the automated calculation of bandstructure data for models only specified by a unitcell. As mentioned before, the `Hamiltonian` object already contains everything necessary for building the momentum interaction space matrix $\mathbf{M}_{ij}(\vec{k}) = \mathbf{M}_{ij} \exp(i\vec{k} \cdot \vec{\Delta}_{ij})$. Thus it can be combined with a `ReciprocalPath` allowing the matrix creation along a path.

In `LatticePhysics.jl`, functions are already implemented to automatically create and diagonalize the interaction matrix along a given path, yielding a `Bandstructure` object containing eigenvalues of eigenstates along the path. These energies can either be used for further computation or simply be displayed. Formatting a plotted bandstructure can be done automatically as well since the reciprocal path describing the x-axis is also stored within the `Bandstructure` object.

Instead of calculating the bandstructure as a function of momentum, one is also often interested in finding the set of momenta that have an eigenstate at a certain energy E_0 like e.g. the Fermi surface. These momentum space manifolds are implemented as objects of type `EnergyManifold`. Functions that compute them perform a mixture of Newton's method and minimization to find sample momenta satisfying $E(\vec{k}) - E_0 = 0$. An additional

search constructs high-symmetry points and lines from the Brillouin zone and adds any relative high-symmetry points with eigenstates of energy E_0 to the list as well.

Example workflow

All of these definitions provide a versatile framework with lattice related functions based on abstract specification and without a detailed individual implementation for every case. A brief highlight showing the versatility of the workflow can be found in Fig. 7.3. Here, subplots have been made with functions provided in the scope of `LatticePhysics.jl` and the relevant code snippet generating the plots has been provided as well.

Final notes on implementation

All in all, `LatticePhysics.jl` [S3] provides an efficient implementation for lattice-based calculations. It defines the lattice and unitcell functionality that can be used in further codes as well as a complete workflow for bandstructure calculations. During its development, both speed and user accessibility have been equally prioritized.

One example for the accessibility of bandstructure calculations is the conciseness of the overall workflow. One can obtain a custom bandstructure in as little as four steps:

1. Define geometry in terms of a unitcell. Some unitcells are already included and thus do not have to be defined manually.
2. Define parameters for the interaction, i.e. a `BondHamiltonian`. Again, some very common parametrical models have already been implemented. Together with the unitcell from step 1, this defines the `Hamiltonian` object.
3. Define a path in momentum space, either explicitly by using coordinates or by passing labels of high-symmetry points.
4. Calculate and plot the bandstructure along the path. Construction of the interaction matrix, diagonalization and extraction of eigenvalues are automated along the path and can readily be used.

However, the code is not only accessible but also fast. The speed comes mainly from the utilized programming language, Julia. It features a just-in-time compilation (JIT) which compiles every function when it is called instead of interpreting it every time. The initial costs of compilation are outweighed by far, especially in a large project where functions are called repeatedly.

To fully utilize JIT, functions have to be type-stable, which is facilitated by a large type-tree in `LatticePhysics.jl`, in which object types already contain vital information on what objects are supposed to do. The type tree goes hand-in-hand with another Julia feature called multiple dispatch. This allows Julia to dispatch a function call to individual

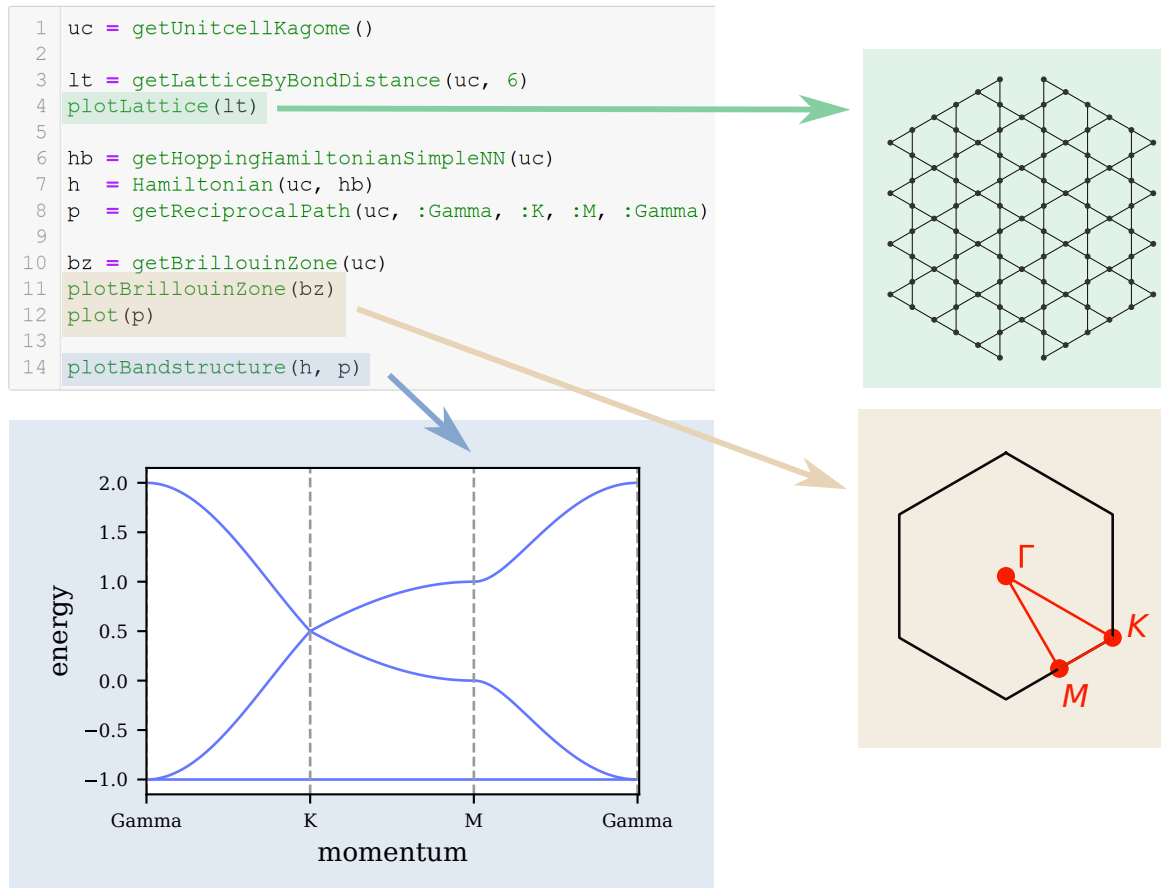


Figure 7.3.: Example workflow of `LatticePhysics.jl` - Code snippet shows an exemplary workflow for obtaining bandstructure data from `LatticePhysics.jl`. First, in line 1, a unitcell is specified from the set of pre-implemented unitcells. Lines 2 and 3 construct a finite lattice, which extends at most 6 bonds beyond the first basis site in the central unitcell, and plot it. In the subsequent lines 6-8, the electronic hopping model and reciprocal space information is gathered. Line 6 specifies a pre-implemented hopping term which weights all bonds with hopping 1.0. The reciprocal path in line 8 is then used for bandstructure calculation. Lines 11 and 12 visualize the path as well as the Brillouin zone obtained in line 10. Line 14 finally calculates and visualizes the bandstructure. All subplots have been directly obtained from `LatticePhysics.jl`.

methods based on the type structure of the input parameters, in principle similar to C++'s overloading principle. In the context of JIT however, multiple dispatch allows the respective functions to be type stable since they are only defined for the respective input types.

With these features, julia itself can reach performances like C code. In the context of `LatticePhysics.jl` this is particularly important when it comes to the runtime of bandstructure calculations. The bottleneck in a bandstructure calculation is the diagonalization of interaction matrices, which scales as $\mathcal{O}(N^3)$ where N is the linear dimension of the matrix. However, interaction matrices are usually sparse and only contain $\mathcal{O}(N)$ elements, i.e. every site can interact with a finite number of surrounding sites. A good rule of thumb is therefore that the runtime of the matrix creation should not be larger than the runtime of matrix diagonalization. Since matrix diagonalization is utilizing an internal C library like MKL or OpenBLAS, one has to essentially write fast code as well.

Through the rest of the thesis, `LatticePhysics.jl` will play a major role as the numerical backbone of calculations. In the current chapter, all bandstructure calculations have been performed with this code. Furthermore, the majority of figures is directly obtained from plotting functions within the library. Last but not least, the geometry information from finite lattices has been crucial in constructing matching boson and fermion lattices in the rest of this chapter, in particular in section 10 when calculating spectra of classical lattice models.

In the next chapter about Moiré materials, `LatticePhysics.jl` is used to generate the huge Moiré cells needed for describing twisted bilayer graphene. Since the code itself is already optimized it is then sufficient to generate the unitcells, since the matrix creation and bandstructure calculation are automated already.

Even beyond the scope of this thesis, `LatticePhysics.jl` provides a good starting ground for numerical codes. The connectivity data of lattices and unitcells is also particularly important for codes such as Monte Carlo methods. In such codes a huge hurdle for a fast and readable implementation is the definition of the lattice geometry, which can be outsourced to this library now.

8. Graph theory and supersymmetry

Having addressed lattice models and their solution, let us turn our attention now towards supersymmetry. In order to understand supersymmetry from the perspective of graph theory, let us start by examining a basic property of block matrices. It is generally known that squaring a hermitian matrix of the form

$$\mathbf{H} = \begin{pmatrix} & \mathbf{R} \\ \mathbf{R}^\dagger & \end{pmatrix}, \quad (8.1)$$

yields a block-diagonal matrix with two blocks on the diagonal

$$\mathbf{H}^2 = \begin{pmatrix} \mathbf{R}\mathbf{R}^\dagger & \\ & \mathbf{R}^\dagger\mathbf{R} \end{pmatrix} \quad (8.2)$$

in which the two blocks $\mathbf{R}\mathbf{R}^\dagger$ and $\mathbf{R}^\dagger\mathbf{R}$ have the same eigenvalues except for zero values which result from the dimension mismatch between the kernels of \mathbf{R} and \mathbf{R}^\dagger .

Although quite well-known, this property will be at the core of the following correspondence. This chapter aims at providing an overview of how the identification of $\mathbf{R}\mathbf{R}^\dagger$ and $\mathbf{R}^\dagger\mathbf{R}$ as supersymmetrically linked boson and fermion lattice models can be understood already at the level of interaction graphs or lattices. The section starts by reviewing the matrix property from the perspective of supersymmetry. Then, the matrix property is once again analyzed from the context of graph theory. Finally, both perspectives are unified. The next sections will then present numerous and extensive examples for this kind of view.

8.1. Block matrices and supersymmetry

Let us start by examining the matrix property from the perspective of supersymmetry. The central part of the matrix property is the isospectrality of sub-blocks under squaring. Similarly, supersymmetry is also about matching spectra between bosonic and fermionic models. In fact, the entire formalism of supersymmetry has great similarities to the matrix property identification. Here, let us recount some basic aspects of SUSY which are necessary for the later discussion. For simplicity, let us specialize on models of non-interacting fermions and bosons which still describe a variety of condensed matter systems like Fermi liquids and exotic phases of matter such as superconducting phases and Bose gases.

Let us consider a system containing both fermionic (c , c^\dagger) and bosonic (b , b^\dagger) degrees of

freedom. The central object of interest in supersymmetry is the (*fermion-odd*) *supersymmetric charge operator* \mathcal{Q} that identifies fermions with bosons

$$\mathcal{Q} = c^\dagger \mathbf{R} b. \quad (8.3)$$

Its definition uses some matrix \mathbf{R} which can be square or rectangular depending on the number of the fermionic and bosonic degrees of freedom in the system. Note however that there are different implications on the spectra of partner models generated by \mathcal{Q} depending on the mismatch between fermion and boson number. Written as a matrix, \mathcal{Q} can be identified with the matrix \mathbf{H} in Eq. (8.1).

With the SUSY charge operator defined above, the SUSY Hamiltonian can be constructed by

$$\mathcal{H}_{\text{SUSY}} = \{\mathcal{Q}, \mathcal{Q}^\dagger\} = c^\dagger \mathbf{R} \mathbf{R}^\dagger c + b^\dagger \mathbf{R}^\dagger \mathbf{R} b \equiv \mathcal{H}_F + \mathcal{H}_B. \quad (8.4)$$

As one can see, the entire Hamiltonian decomposes into two non-interacting parts which describe the fermionic and bosonic Hamiltonians, respectively. These are given by the two matrices, $\mathbf{R} \mathbf{R}^\dagger$ and $\mathbf{R}^\dagger \mathbf{R}$, which can be identified with the two diagonal blocks of \mathbf{H}^2 in Eq. (8.2).

As already argued in the matrix property, the eigenvalues (or even momentum dependent spectra) of \mathcal{H}_F and \mathcal{H}_B agree and the respective eigenstates can be explicitly related by \mathcal{Q} . This allows a one-to-one identification of bosonic states $|v\rangle$ and fermionic states $|u\rangle$ as

$$|u\rangle = \frac{\mathbf{R}}{\sqrt{\omega}} |v\rangle \quad \text{and} \quad |v\rangle = \frac{\mathbf{R}^\dagger}{\sqrt{\omega}} |u\rangle, \quad (8.5)$$

which will have far-reaching consequences as demonstrated later on.

A final note can be made on the appearance of zero modes in the spectra of either bosons or fermions. For a square matrix \mathbf{R} , \mathcal{H}_F and \mathcal{H}_B are entirely isospectral, even including any present zero modes. This comes from the fact that $\mathbf{R} \mathbf{R}^\dagger$ and $\mathbf{R}^\dagger \mathbf{R}$ have the same eigenvalues and dimension, leaving no additional kernel to compensate any occurring zero modes. However, for a rectangular matrix \mathbf{R} , this is no longer the case. As a result, one system will have more zero-energy eigenmodes than the other, as outlined before. In supersymmetry, such a mismatch is characterized by the Witten index

$$\begin{aligned} \nu &= \dim(\text{kernel}[\mathbf{R}]) - \dim(\text{kernel}[\mathbf{R}^\dagger]) \\ &= \text{col}[\mathbf{R}] - \text{row}[\mathbf{R}]. \end{aligned} \quad (8.6)$$

which is the topological invariant of a SUSY theory. A finite Witten index $\nu \neq 0$ indicates the appearance of flat bands in the band structure of either \mathcal{H}_F and \mathcal{H}_B .

8.2. Topological invariants under supersymmetry

With a notion of supersymmetry introduced, one might think about how topology can be related between the two SUSY partner Hamiltonians. Whereas the identification of possible topological phases in fermionic systems has been understood to a great extent, owing its existence to the classification of fermion symmetries, the corresponding boson side has long been neglected. In the following, let us discuss first, how symmetries on both the bosonic and fermionic side are related by supersymmetry. Then, the relation of topological invariants at the example of Berry phases is discussed.

First, let us talk about symmetries in fermionic band structures in general and how they transform under supersymmetry. As the topology in the fermion system is dictated by symmetries, one might naturally wonder about their existence in the boson system. In general, the following set of symmetries in a fermion Hamiltonian is important: Time-reversal symmetry (\mathcal{T}), particle-hole symmetry (\mathcal{P}), and chiral/sublattice symmetry ($\mathcal{C} = \mathcal{PT}$). Both \mathcal{T} and \mathcal{P} are anti-unitary symmetries, whereas \mathcal{C} is a unitary symmetry. \mathcal{T} generally commutes with the Hamiltonian, with a set of symmetry-eigenvalues $\mathcal{T}^2 = \pm 1$. \mathcal{P} and \mathcal{C} anti-commute with the Hamiltonian with respective symmetry eigenvalues $\mathcal{P}^2 = \pm 1, \mathcal{C}^2 = 0, 1$. These lead to a total of ten distinct combinations forming the ten distinct topological classes of Hamiltonians describing any non-interacting electronic system [56].

In mapping the fermionic states to their bosonic counterparts via SUSY as displayed in Eq. (8.5), the aforementioned anti-unitary and unitary symmetries prevail to retain the topological properties of the band structures. Each symmetry comes therefore as a natural analogue on the boson side. In this spirit, e.g. the time-reversal symmetry in a fermionic system \mathcal{T}_F translates to its partner bosonic system via SUSY as $\mathcal{T}_B = \mathbf{R}^{-1}\mathcal{T}_F\mathbf{R}$. In a later section, this process will be demonstrated in greater detail for an example.

Since symmetries can be related from one SUSY-partner to the other, one might wonder how topological invariants map in the same process. In the following discussion, let us focus on the Berry phase as a prime example of such an invariant. The Berry phase has provided a useful way to characterize band topology in generic electronic systems. In lattice models specifically, the conventional form of the Berry phase can be computed from Bloch eigenfunctions of the Hamiltonians $\mathbf{R}\mathbf{R}^\dagger$ and $\mathbf{R}^\dagger\mathbf{R}$ but may differ substantially depending on what type of lattices they describe. In general, the closed-orbit Berry phase for an eigenfunction of $\mathbf{R}\mathbf{R}^\dagger$ is given by

$$\theta_B^{\mathbf{R}\mathbf{R}^\dagger} = i \oint \langle u(\mathbf{k}) | \partial_{\mathbf{k}} u(\mathbf{k}) \rangle \cdot d\mathbf{k}, \quad (8.7)$$

whereas similarly an eigenfunction of $\mathbf{R}^\dagger\mathbf{R}$ at the same energy has Berry phase

$$\begin{aligned}\theta_B^{\mathbf{R}^\dagger\mathbf{R}} &= i \oint \langle v(\mathbf{k}) | \partial_{\mathbf{k}} v(\mathbf{k}) \rangle \cdot d\mathbf{k} \\ &= \theta_B^{\mathbf{R}\mathbf{R}^\dagger} + i \oint \frac{\Im(\langle u(\mathbf{k}) | (\partial_{\mathbf{k}}\mathbf{R}) | v(\mathbf{k}) \rangle)}{\sqrt{\omega_n(\mathbf{k})}} \cdot d\mathbf{k},\end{aligned}\tag{8.8}$$

where the additional term in the last line can be seen as a consequence of the identification in Eq. (8.5). For integrands in this term which can be written as $\partial_{\mathbf{k}}\mathcal{F}(\mathbf{k})$ for some function $\mathcal{F}(\mathbf{k})$, the conventional Berry phases θ_B of the partner systems will be equal.

In general, the relation in Eq. (8.8) shows that supersymmetry can be used to deduce one Berry phase from the other. Furthermore, it is possible to define two supersymmetric Berry phases

$$\begin{aligned}\theta_{\text{SUSY}}^{\mathbf{R}\mathbf{R}^\dagger} &\equiv \theta_B^{\mathbf{R}\mathbf{R}^\dagger} + i \oint \frac{\Im(\langle v(\mathbf{k}) | \mathbf{R}^\dagger (\partial_{\mathbf{k}}\mathbf{R}) | v(\mathbf{k}) \rangle)}{\omega(\mathbf{k})} \cdot d\mathbf{k}, \\ \theta_{\text{SUSY}}^{\mathbf{R}^\dagger\mathbf{R}} &\equiv \theta_B^{\mathbf{R}^\dagger\mathbf{R}} - i \oint \frac{\Im(\langle u(\mathbf{k}) | (\partial_{\mathbf{k}}\mathbf{R}) \mathbf{R}^\dagger | u(\mathbf{k}) \rangle)}{\omega(\mathbf{k})} \cdot d\mathbf{k},\end{aligned}\tag{8.9}$$

in which the additional terms can be regarded as covariant corrections induced by supersymmetry.

8.3. Block matrices and graph theory

In condensed matter physics, matrices are often appearing as *interaction* or *hopping* matrices in a lattice system. These matrices generally describe the relation between degrees of freedom which are defined on some underlying lattice, yielding a graph structure. In graph theory, such matrices would therefore also be called *weighted adjacency matrices* as they are based on the adjacency of the underlying graph structure. More generally, an *adjacency* matrix \mathbf{A} for a graph with vertices $\{v_i\}$ is defined as

$$\mathbf{A}_{ij} = \begin{cases} 1 & v_i \text{ connected to } v_j \\ 0 & \text{otherwise} \end{cases}\tag{8.10}$$

and can be extended to a *weighted adjacency* matrix by including a label l_{ij} for every non-zero element of \mathbf{A}_{ij} .

For the special case of block-off-diagonal matrices in Eq. (8.1), the matrix \mathbf{H} can be seen as the adjacency matrix of a graph with vertices that fall into two distinct categories $\{v_i^A\}$ and $\{v_i^B\}$. Vertices in one set are exclusively connected to vertices in the other set, i.e. not to the ones in their own set. This property defines a *bipartite* graph. In condensed matter theory, lattices with this property are also called *bipartite* lattices and often times exhibit

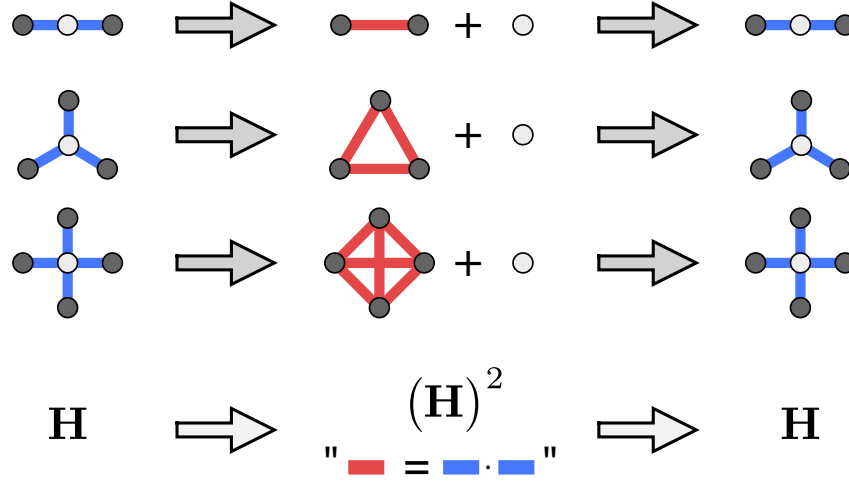


Figure 8.1.: Square and Square-root of adjacency matrices - Graphical representation of squaring and taking the square-root of an adjacency matrix describing a bipartite lattice. Different rows show elementary z -coordinated sites with increasing coordination z . Each site transforms under squaring to a fully-connected plaquette (clique) consisting of z sites which are all-to-all connected. Due to this mapping, a square-root can be being the inverse process, i.e. replacing fully-connected plaquettes by respectively coordinated sites.

a sublattice symmetry.

Matrix squares – Let us turn our attention to the process of squaring an adjacency matrix \mathbf{A} and in particular how this process changes the underlying graph. For a generic adjacency matrix \mathbf{A} , elements of the squared matrix can be computed as

$$(\mathbf{A}^2)_{ij} = \sum_k \mathbf{A}_{ik} \mathbf{A}_{kj}. \quad (8.11)$$

This can be interpreted as a new adjacency matrix, describing a different adjacency on the same vertices. Whereas \mathbf{A} connected vertices v_i and v_j with weight A_{ij} , \mathbf{A}^2 now chains two of those connections together, thus connecting next-nearest neighbor vertices v_i and v_j separated by an additional vertex v_k in between. On a pictorial level one can therefore understand squaring an adjacency matrix by taking next-nearest neighbors in the graph.

Coming back to the matrix property of Eq. (8.1) and Eq. (8.2), let us focus on the case of \mathbf{A} describing the adjacency of a bipartite graph. In this case, next-nearest neighbors of vertices in set A are necessarily also in set A (as there is an additional vertex of set B in between). Therefore, a bipartite graph necessarily decomposes into its two distinct subgraphs under squaring. These subgraphs are not connected any more. In total, this result could already be predicted from the special form of Eq. (8.2), since interpreting this equation as an adjacency matrix would yield two disconnected graphs. Summarizing the

whole procedure of squaring a bipartite adjacency matrix is also depicted in Fig. 8.1.

Moreover, the aforementioned mismatch of rank leading to a nonzero kernel dimension and resulting appearance of zero modes also has a pictorial representation in graph language. As the number of rows and columns of \mathbf{R} is determined by the number of elements in sets A and B respectively, a graph with different numbers of A sites and B sites will necessarily lead to an adjacency matrix with zero modes. In the context of lattices, the number of elements in set A is proportional to the number of basis sites in sublattice A within the unitcell which means that a mismatch in number of basis sites results in the appearance of zero modes.

Matrix square-roots – Similar to how squaring an adjacency matrix can be interpreted as taking next-nearest neighbors, one can also ask about the inverse direction, i.e. taking the square-root of an adjacency matrix. Note that for a generic matrix, the square-root cannot be defined uniquely, but only up to unitary transformations. For the graph theoretical view however, let us focus on finding a square-root that has a meaning in another graph. From a technical side, this can be understood in finding a matrix \mathbf{H} for a given matrix \mathbf{M} s.t. $\mathbf{H}^2 = \mathbf{M}$ or alternatively $\mathbf{H} = \sqrt{\mathbf{M}}$.

As seen previously, squaring the adjacency matrix of a bipartite graph yielded two disconnected subgraphs. One approach to find a square root is therefore to invert this process and propose a new second subgraph for a given graph so that both together can form a bipartite square-root graph. This would naturally decompose into the original graph under squaring, separating off the additionally defined second subgraph.

The construction of such a second subgraph can in principle be facilitated by an algorithm which builds on a simple observation. As seen in Fig. 8.1, z -coordinated sites in a bipartite graph will produce *fully connected plaquettes* with z vertices under squaring. Such fully connected plaquettes are also called *cliques* in graph theory. An algorithm to find the square-rooted graph for a given graph would therefore naturally replace all such fully-connected plaquettes by respectively coordinated sites that are newly introduced. These new sites form the second sublattice of the bipartite graph.

Although the algorithm itself can be described broadly speaking by the replacement of cliques, let us focus on some minor details, which go along with this process. First of all, in most cases the graphs will be labeled graphs yielding weighted adjacency matrices. These labels have to fulfill Eq. (8.11) under squaring, which might pose a problem in itself, especially at boundaries. Second, every z clique contains cliques of order $z - 1$. Therefore an efficient algorithm should start by replacing plaquettes in descending order. Third, it is known in computer science that finding all maximal cliques in a graph (which is relevant for the algorithm to work) is an NP-hard problem. However in a physics situation this can usually be circumvented as one encounters unitcells which put an upper limit on how large cliques can become.

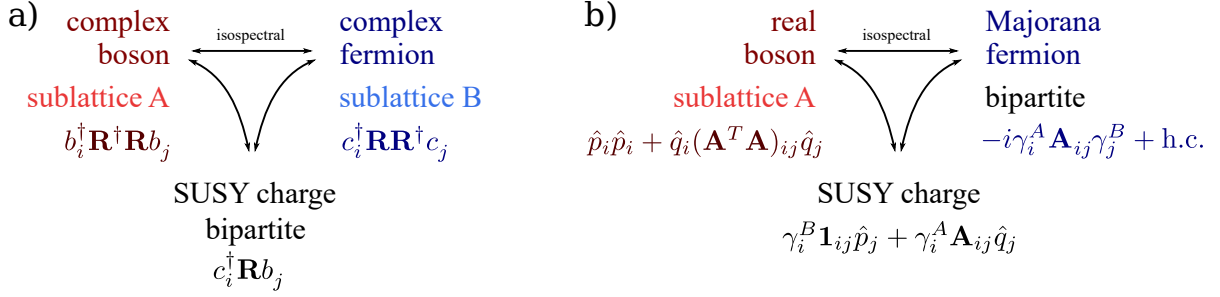


Figure 8.2.: Different SUSY mappings with corresponding graph language - Sketch of the correspondence between graph language and supersymmetry. Panel a) shows the schematic relation between complex bosons and fermions which can be connected by a SUSY charge defined on a bipartite lattice. In this case, both models are residing on its respective A and B sublattices. In panel b), the same correspondence is demonstrated for real bosons and Majorana fermions. Here, the real bosons reside on the sublattice of the bipartite Majorana fermion lattice. In total, graph language can help in quickly identifying geometric structures within the corresponding models, however each class of models has to be studied in detail.

8.4. Supersymmetry as a graph correspondence

It is the central idea of the SUSY-lattice graph identification, that the two supersymmetric partner systems can be viewed as the two subgraphs in a bipartite graph. Similar to how under squaring the graph its two sublattices become decoupled, the SUSY charge yields two distinct Hamiltonians under squaring which do not interact. Therefore, the procedure of generating matching boson and fermion Hamiltonians can be simplified from the view of generating matching sublattices of a bipartite lattice.

Similar to how the bare graph correspondence was illuminated from different angles, also the implications of a graph language on supersymmetry can be investigated from many directions. As a first and direct consequence, it is helpful to associate the SUSY charge with a bipartite lattice whose A sites describe fermions and whose B sites describe bosons. Such a graphical correspondence already implies a graphical understanding of the two subsystems which was not hitherto unexplored without additional investigations.

Nevertheless, from a practical perspective one usually does not start with the supersymmetric charge. Instead, supersymmetry is often used to find a matching counterpart for either a bosonic or fermionic system. However, constructing such a SUSY partner, i.e. finding $\mathbf{R} \mathbf{R}^\dagger$ for $\mathbf{R}^\dagger \mathbf{R}$ is in general fairly complicated since the matrix square-root $\mathbf{R}^\dagger \mathbf{R} \rightarrow \mathbf{R}$ does not have a unique solution. Moreover, general methods such as a Cholesky decomposition yield non-local results \mathbf{R} which physically do not seem to match a local $\mathbf{R}^\dagger \mathbf{R}$.

To preserve locality, the graph square-root algorithm comes into play. As demonstrated

before, a graph square-root can be obtained by a replacement of cliques with newly added sites. This procedure generically produces a bipartite lattice capable of yielding the original lattice under squaring. When interpreting the newly added sites as particles of the other type (i.e. bosons or fermions for a given fermion or boson model respectively), the process of finding a SUSY charge can be recasted as substituting interaction-cliques in the given problem with newly added operators.

All in all, the consequences of identifying supersymmetry with a graph correspondence are quite substantial. The following part of this thesis is devoted to showing two particular examples in which the graph-language greatly simplifies the analysis, schematically depicted in Fig. 8.2. The first example discusses SUSY implications for complex fermions and bosons which turns out to be a correspondence between sublattices of a bipartite lattice.

The second example turns to the role of supersymmetry in Majorana fermion systems which turn out to be connected to real boson systems. In this example, the real bosons are defined on one of the sublattices of the bipartite Majorana fermion lattice, leading again to a "lattice-to-sublattice" correspondence, albeit in a different form compared to the complex boson case.

9. Complex fermions and complex bosons

In this chapter, let us turn our attention towards the first practical example of how supersymmetry can be assisted by graph theory. To this endeavor, we will discuss how a system of well-known complex fermions can be equipped with a matching system of complex bosons which are isospectral to the fermion system. This supersymmetric matching goes along a special form of supersymmetric charge in these systems as well as an extensive list of examples.

Overall, this chapter aims to provide an introductory example to how supersymmetry can be expressed by graph theory. It is by no means an extensive overview, since a lot of the contents are still work in progress.

9.1. Supersymmetric charge

For some matrix \mathbf{R} , consider the SUSY charge

$$\mathcal{Q} = c_i^\dagger \mathbf{R} b_j \tag{9.1}$$

which defines bosons b_j and fermions c_i linked by a matrix \mathbf{R} . All degrees of freedom can be understood in graph language as being defined on the sublattices of a bipartite graph whose adjacency between sublattices can be described in terms of \mathbf{R} .

From the SUSY charge, partner Hamiltonians H_F and H_B can be calculated which describe free fermion and boson models, respectively. The partner Hamiltonians are derived by

utilizing the anti-commutator of the SUSY charge operator, i.e. $\{\mathcal{Q}, \mathcal{Q}^\dagger\}$, which leads to

$$\begin{aligned}
 H_{\text{SUSY}} &= \{\mathcal{Q}, \mathcal{Q}^\dagger\} \\
 &= \sum_{ijkl} R_{ij} R_{lk}^* \{c_i^\dagger b_j, b_k^\dagger c_l\} \\
 &= \sum_{ijkl} R_{ij} R_{lk}^* \{b_k^\dagger c_l, c_i^\dagger b_j\} \\
 &= \sum_{ijkl} R_{ij} R_{lk}^* \left(b_k^\dagger \{c_l, c_i^\dagger\} b_j - c_i^\dagger [b_k^\dagger, b_j] c_l - [b_k^\dagger, c_i^\dagger] c_l b_j - c_i^\dagger b_k^\dagger [c_l, b_j] \right) \\
 &= \sum_{ijkl} R_{ij} R_{lk}^* \left(b_k^\dagger \delta_{li} b_j - c_i^\dagger (-\delta_{kj}) c_l \right) \\
 &= \sum_{ijk} R_{ij} R_{ik}^* b_k^\dagger b_j + \sum_{ijl} R_{ij} R_{lj}^* c_i^\dagger c_l \\
 &= \sum_{ij} b_i^\dagger (\mathbf{R}^\dagger \mathbf{R})_{ij} b_j + \sum_{ij} c_i^\dagger (\mathbf{R} \mathbf{R}^\dagger)_{ij} c_j
 \end{aligned}$$

where the identity

$$\{AB, CD\} = A\{B, C\}D - C[A, D]B - [A, C]BD - CA[B, D] \quad (9.2)$$

has been used, along with the commutation / anti-commutation relations

$$\begin{aligned}
 \{c_i, c_j^\dagger\} &= \delta_{ij} && \text{Fermionic anti-commutation} \\
 [b_i, b_j^\dagger] &= \delta_{ij} && \text{Bosonic commutation} \\
 [c_i, b_j] &= 0 && \text{Bosons and Fermions commute} \\
 [c_i^\dagger, b_j^\dagger] &= 0 && \text{Bosons and Fermions commute}
 \end{aligned}$$

Finally, the two partner Hamiltonians can be read off as

$$H_{\text{F}} = c_i^\dagger \mathbf{R} \mathbf{R}^\dagger c_j \quad (9.3)$$

$$H_{\text{B}} = b_i^\dagger \mathbf{R}^\dagger \mathbf{R} b_j \quad (9.4)$$

which again resemble the blocks of matrix \mathbf{R}^2 in Eq. (8.2). From a graph perspective, the two Hamiltonians are defined on the sublattices of the bipartite SUSY charge graph since $\mathbf{R} \mathbf{R}^\dagger$ and $\mathbf{R}^\dagger \mathbf{R}$ describe next-nearest neighbor processes in terms of adjacencies.

Note that this identification between a bosonic and fermionic model works explicitly both in real and momentum space as long as one can define a suitable matrix \mathbf{R} . In real space, \mathbf{R} can be directly obtained from the hopping matrix, describing the interaction adjacency, whereas in momentum space additional phase factors may come into play depending on the gauge used to perform the Fourier transform.

In the following, many explicit examples of isospectral boson / fermion models will be discussed. Although they should certainly do not represent a complete set of models, they show the vast applicability of the supersymmetric relation between lattice models of bosons and fermions.

9.2. Examples

In this section, let us look at some examples of isospectral boson and fermion models which can be linked by the supersymmetric charge defined in Eq. (9.1). All models are understood as nearest-neighbor hopping models on the respective lattice graphs with hopping constants being derived from the respective SUSY charge graph (details on this follow in the individual examples).

Technically, all calculations and plots have been performed by utilizing `LatticePhysics.jl`. This comes in particularly handy since the matching unitcells of boson and fermion models have been constructed algorithmically within the scripts, following the processes outlined in the graph constructions before, without any manual interaction. To do so, most of the following examples start from the perspective of the SUSY charge lattice, however there are also a substantial amount of examples which start from the fermion or boson lattices, respectively.

Results of the models include sketches and spectra of the boson and fermion model respectively, as well as the SUSY charge. Before showing results, it is worth noting that there are some key features which one should pay attention to:

- **Subgraphs** – The boson and fermion models are defined on the subgraphs of the SUSY charge lattice as laid out before
- **isospectrality** – The spectra between bosonic and fermionic models are guaranteed to be isospectral due to the supersymmetric connection
- **Flat bands for non-zero Witten index** – For a mismatch between the number of bosonic and fermionic degrees of freedom, the model with more degrees of freedom will inherently include flat bands at the bottom of the spectra. In the language of supersymmetry, the number of flat bands is given by the Witten index, describing the mismatch in the number of DOFs.

In the following, examples are discussed with figures showing both lattices and spectra.

To pay more attention to individual features, let us now go briefly through all examples one by one. Examples will be given as pairs *sublattice A*, *sublattice B*, *bipartite lattice*, reflecting the isospectrality between sublattices. The respective figures are also organized in a unified way, showing the graph correspondence above the spectral correspondence.

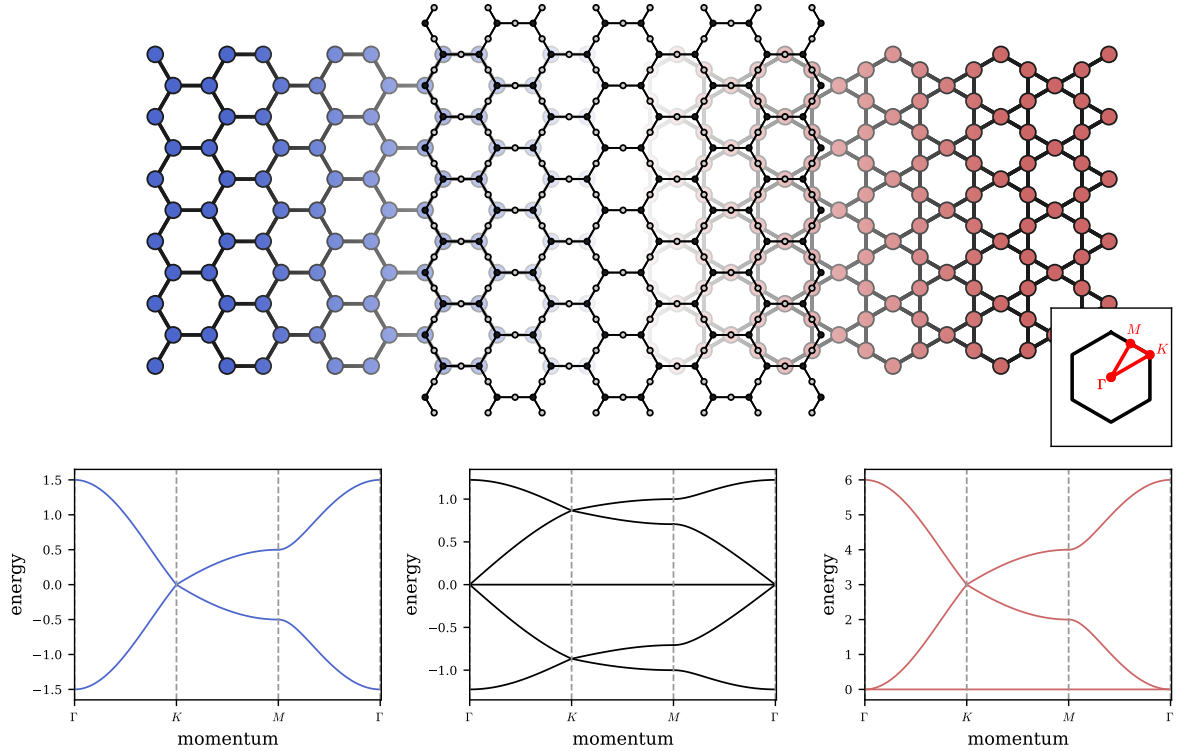


Figure 9.1.: SUSY corresponding Honeycomb and Kagome lattices - Complex fermions (blue, left) on the honeycomb lattice can be shown to be supersymmetrically linked to complex bosons (red, right) on the Kagome lattice. The mapping can be established with a SUSY charge which can be interpreted as the adjacency matrix of a honeycomb-X lattice, i.e. a honeycomb lattice with additional sites on every bond whose two sublattices are the honeycomb and Kagome lattices respectively. Plots have been directly obtained from LatticePhysics.jl.

Honeycomb, Kagome, Honeycomb-X – The first example concerns fermions on the honeycomb lattice connected to bosons on the Kagome lattice, displayed in Fig. 9.1. Both the honeycomb as well as the Kagome lattice are two-dimensional lattices with hexagonal unitcells. Whereas the honeycomb contains two sites per unitcell, the Kagome lattice has a unitcell consisting out of three sites. Concerning experimental realizations, especially the honeycomb lattice is famous for being the underlying lattice beneath graphene, the first truly two-dimensional material [66, 67].

When studying the spectra of the nearest-neighbor hopping models on the honeycomb and Kagome lattices, one can see the close resemblance of their bandstructures. The celebrated Dirac cone in the honeycomb spectrum at the K point of the Brillouin zone is matched with a similar structure at the same place in the Kagome spectrum. Similarly, the band extremes are located at the same places and spectra agree also quantitatively.

From the perspective of supersymmetry, this resemblance of spectra is no coincidence. As the honeycomb and Kagome lattices form the two sublattices of the honeycomb-X lattice, their nearest-neighbor hopping models are guaranteed to be isospectral. Moreover, the honeycomb-X as the graph underlying the supersymmetric charge, can be recovered from both individual models. Replacing either all bonds (2-cliques) in the honeycomb or triangles (3-cliques) in the Kagome lattice yields the honeycomb-X lattice.

In the context of supersymmetry, the flat band in the Kagome spectrum also has a meaning. Since the number of basis sites differs between honeycomb and Kagome lattice, the Witten index in the supersymmetric connection has to be finite and equal to the respective difference, in this case $\nu = 1$. Since a finite Witten index goes along with a finite number of zero-energy modes, the flat band in the Kagome can be viewed as the necessary consequence of the difference in number of basis sites to its superpartner, the honeycomb.

Finally note that the flat band from the Kagome spectrum also is repeated in the spectrum of the SUSY charge (which has no physical meaning but can be computed nevertheless). Here, the flat band is situated exactly in the center of bands at zero energy. This can be understood as the Kagome sublattice emerges under a square operation, bringing all negative eigenvalues to above zero, therefore transforming the bottom flat band to a mid-spectrum flat band in the reverse direction.

Triangular, Triangular, Honeycomb – For the second example, let us stick to the honeycomb lattice, however alter its context. Let us discuss what happens when the honeycomb lattice is used as the supersymmetric charge graph. In this case, its two sublattices are the two models which can be related, which are free bosons and fermions on the triangular lattice as displayed in Fig. 9.2. Both models have single-band dispersions and matching spectra.

From the point of SUSY construction, the honeycomb lattice can be constructed from the triangular lattice by replacing triangles until all bonds interactions are substituted. Here it is necessary to specify which triangles are substituted, since an interaction edge in the lattice graph always is part of an up- and a down-triangle. Replacing either up or down triangles in the entire lattice yields the honeycomb lattice.

Note that similar to how the Kagome bottom flat band was repeated as the central flat band in the spectrum of the SUSY charge, the honeycomb SUSY charge can give insight into the low-energy features of the triangular lattice model. In this spirit, the Dirac cone at the K point yields a quadratic band minimum under squaring, visible at the K point within the triangular lattice spectrum.

Last but not least it can be noted that the Witten index for this particular example is zero, since both sublattices have the same number of sites per unitcell. Therefore, no flat bands are expected at the bottom of the triangular lattice spectrum.

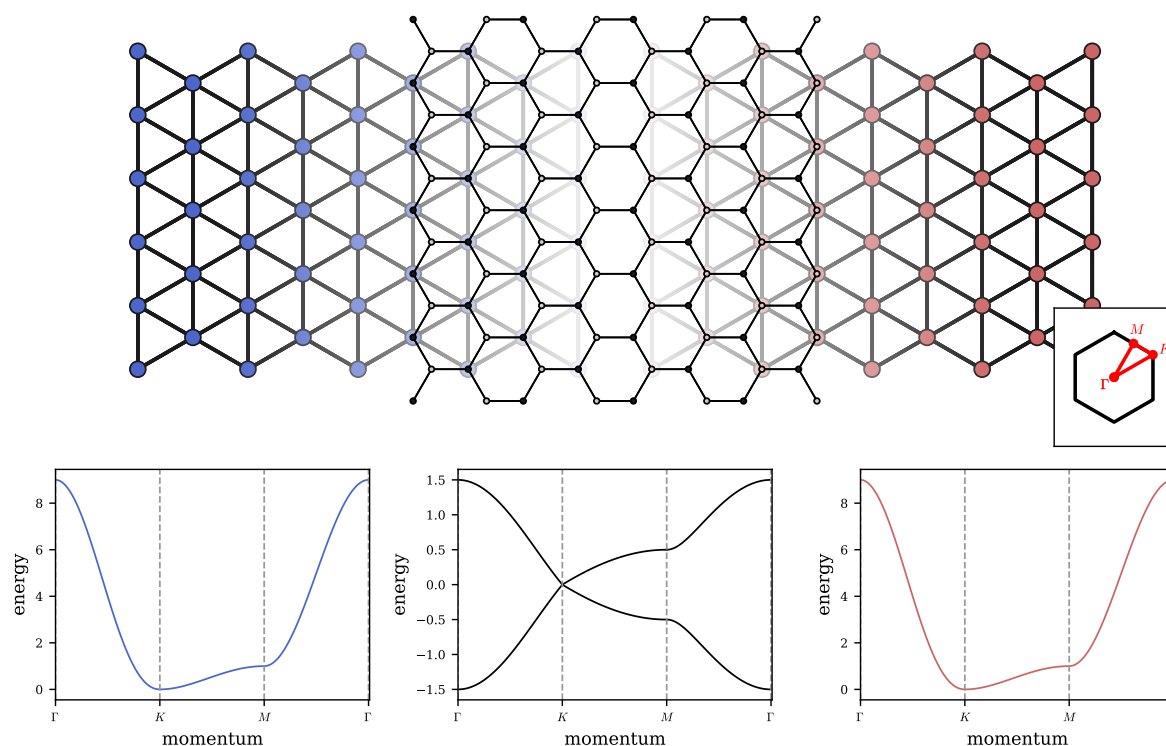


Figure 9.2.: SUSY corresponding triangular lattices - Complex fermions (blue, left) on a triangular lattice can be shown to be supersymmetrically linked to complex bosons (red, right) on the same triangular lattice. The mapping can be established with a SUSY charge which can be interpreted as the adjacency matrix of a honeycomb lattice whose two sublattices are the triangular lattices respectively. Plots have been directly obtained from LatticePhysics.jl.

Square, Checkerboard, Square-X – The next example changes the two-dimensional geometry to a square unitcell. As depicted in Fig. 9.3, the nearest-neighbor models on the square and checkerboard lattices are isospectral. This correspondence can be once again understood in terms of the graph correspondence since both the square lattice and the checkerboard lattice form the sublattices of the square-X lattice.

Although there are remarkable similarities to previous examples – general isospectrality, observation of a flat band in the checkerboard spectrum due to a finite Witten index, which again can be observed in the spectrum of the SUSY charge – there is one aspect which was previously unexplored, namely the precise form of interaction geometry.

Investigating the square-X lattice, one would conventionally conclude that its two sublattices are square lattices. Here however, the focus lies more on the interaction graph in terms of connectivities than in terms of geometrical placement. It is true that the B

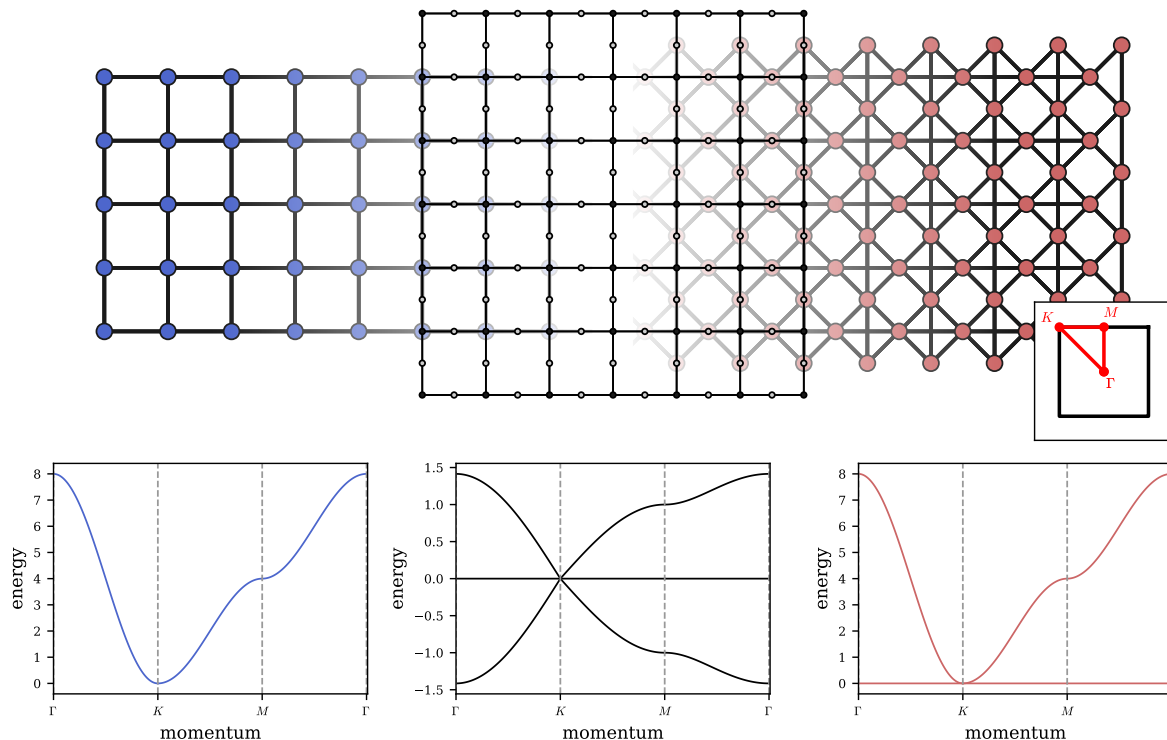


Figure 9.3.: SUSY corresponding square and checkerboard lattices - Complex fermions (blue, left) on the square lattice can be shown to be supersymmetrically linked to complex bosons (red, right) on the checkerboard lattice. The mapping can be established with a SUSY charge which can be interpreted as the adjacency matrix of a square-X lattice (center plot), i.e. a square lattice with additional sites on every bond whose two sublattices are the square and checkerboard lattices respectively. Plots have been directly obtained from `LatticePhysics.jl`.

sublattice has sites placed at positions compatible with a square lattice. However, taking next-nearest neighbors explicitly when going from the square-X to the boson problem reveals that the interactions are not those of a pure square lattice but resemble a checkerboard lattice in which each other square plaquette receives additional interactions across the plaquette diagonal.

Note also that the same construction mechanism implies that the diagonal hoppings across the square plaquettes in the checkerboard lattice have the same hopping strength as the square hoppings. This constraint is also crucial when constructing the square-X lattice from the checkerboard. Here, one would replace all 4-cliques, which are the fully connected square-plaquettes, with a new site, which is only possible for fine-tuned hoppings.

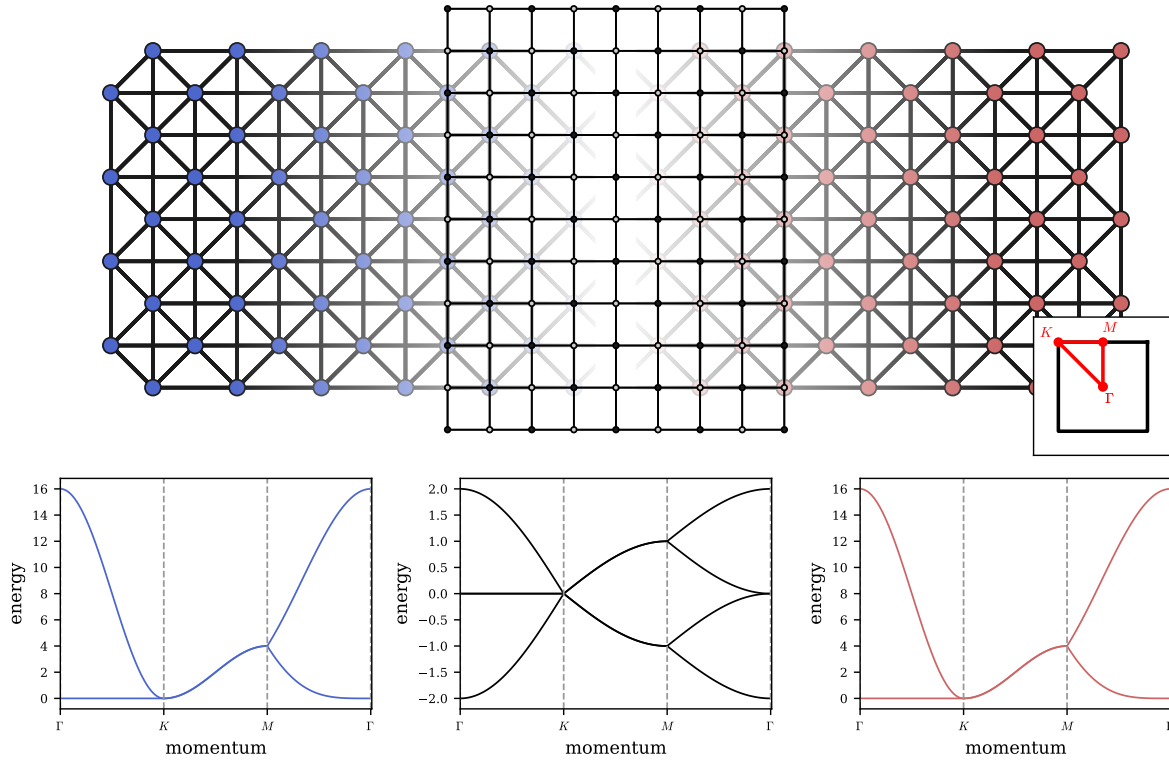


Figure 9.4.: SUSY corresponding fully connected square lattices - Complex fermions (blue, left) on the square lattice with full connectivity can be shown to be supersymmetrically linked to complex bosons (red, right) on the same fully connected square lattice. The mapping can be established with a SUSY charge which can be interpreted as the adjacency matrix of a square lattice (center plot) whose two sublattices are the fully connected square lattices respectively. Plots have been directly obtained from LatticePhysics.jl.

Fully connected Square ($\times 2$), Square – The next example stays with the square geometry, however investigates what happens when using the square lattice as the SUSY charge graph. To incorporate the bipartite nature into the graph, one has to enlarge the unitcell which is done in Fig. 9.4 to a four-site cell. Its two sublattices are again square-lattices, however with a next-nearest neighbor connectivity that is beyond nearest neighbor in the sublattices.

Again, both sub-models are isospectral and have no additional flat bands across the entire spectrum, the result of a vanishing Witten index. Apart from these features induced by supersymmetry, this example is mainly of interest because it shows that the SUSY charge lattice must be investigated in the correct unitcell to make statements on the sublattices. In this example, a single-site unitcell would not allow for a bipartite representation of sublattices and therefore not yield the respective sub-models graphically.

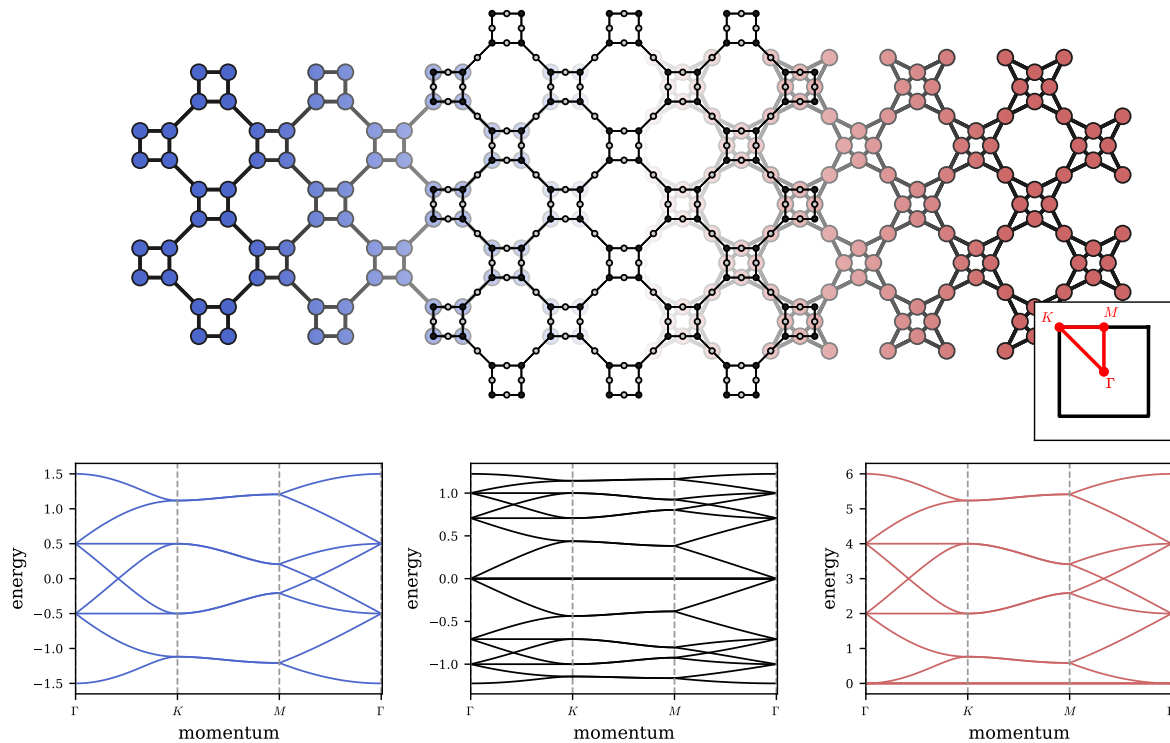


Figure 9.5.: SUSY corresponding square-octagon and Squagome lattices - Complex fermions (blue, left) on the square-octagon lattice can be shown to be supersymmetrically linked to complex bosons (red, right) on the Squagome lattice. The mapping can be established with a SUSY charge which can be interpreted as the adjacency matrix of a square-octagon-X lattice (center plot), which is a square-octagon lattice with additional sites on every bond, whose two sublattices are the square-octagon and Squagome lattices respectively. Plots have been directly obtained from LatticePhysics.jl.

Also, similar to the last square example, the hoppings within the fully connected square lattices are fixed in strength by the SUSY map. The ratio of short (diagonal) to long (vertical / horizontal across plaquettes) hoppings is $2 : 1$ as there different numbers of next-nearest neighbor hopping paths in the SUSY charge graph yielding the respective hoppings. From the inverse perspective, this means that the fully-connected square lattice model (or more often called t_1 - t_2 square lattice model) can only be mapped to the pure square lattice SUSY charge for $t_1 = t_2/2$.

Square-octagon, Squagome, Square-octagon-X – For the last two examples in two spatial dimensions, let us stick with a square geometry but increase the unitcell. To be precise, the first example concerns fermions on the square-octagon lattice and bosons on the Squagome lattice, as depicted in Fig. 9.5.

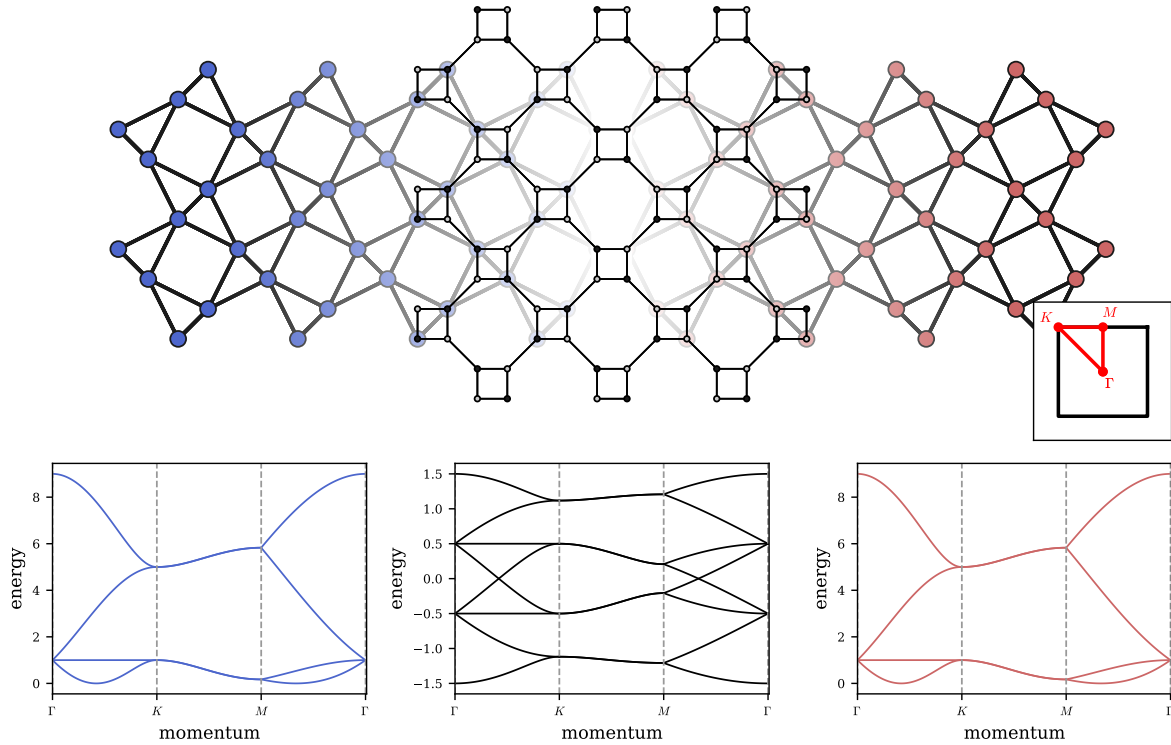


Figure 9.6.: SUSY corresponding Shastry-Sutherland lattices - Complex fermions (blue, left) on Shastry-Sutherland lattice can be shown to be supersymmetrically linked to complex bosons (red, right) on the same lattice. The mapping can be established with a SUSY charge which can be interpreted as the adjacency matrix of a square-octagon lattice (center plot) whose two sublattices are the Shastry-Sutherland lattices respectively. Plots have been directly obtained from LatticePhysics.jl.

Both models are isospectral apart from additional zero-energy modes at the bottom of the Squagome spectrum. As the squagome lattice has four basis sites more than the square-octagon lattice, the Witten index in this case is $\nu = 4$, resulting in four zero-energy bands at the bottom of the Squagome spectrum.

Concerning the construction between lattices, this example works similar to the ones before. Both square-octagon and Squagome lattices can be obtained by taking next-nearest neighbors of the square-octagon-X lattice, which is a square-octagon lattice with additional sites on every bond. These additional sites form the Squagome lattice which already hints at the construction from fermions to SUSY charge, i.e. replacing all bonds in the square-octagon with newly added sites. Similar to the example of the Kagome lattice correspondence, the Squagome can be transformed to the square-octagon-X by replacing all triangles with newly added sites.

Shastry-Sutherland ($\times 2$), Square-octagon – In the last example, let us discuss what fermion and boson models one obtains for a SUSY charge defined on the graph of a square-octagon lattice. Its two sublattices are known as Shastry-Sutherland lattices. Although identical in terms of connectivity, sublattices A and B are related by a mirror symmetry. The total relation can be seen in Fig. 9.6.

Similar to the last examples, the spectra of the two sub-models, i.e. bosons and fermions on the Shastry-Sutherland lattices, are isospectral with no zero modes. The absence of zero modes on either side can be understood from the vanishing Witten index due to identical unitcells in the two sublattices.

Concerning the lattice graph construction to reconstruct the SUSY charge graph from one of the models, one can see that replacing all triangles in the Shastry-Sutherland lattice with newly added 3-coordinated sites yields the square-octagon SUSY charge graph.

Diamond, Pyrochlore, Diamond-X – In the first 3D example, let us discuss fermions on the diamond lattice. This model is well known for exhibiting a nodal line at the square-surfaces of its Brillouin zone, depicted as points K and X' in Fig. 9.7.

Performing the SUSY mapping and replacing all 2-cliques (bonds) with newly added sites, one arrives at the diamond-X lattice as a SUSY charge graph, i.e. a diamond lattice with additional sites on every bond. Taking the next-nearest neighbors and decomposing this graph into its two sublattices, one finds bosons on the pyrochlore lattice as the second model.

Comparing the fermion and boson spectra, one finds a spectral agreement with the two models apart from two flat bands at the bottom of the pyrochlore spectrum. Similar to the two two-dimensional cases, these two flat bands are caused by the finite Witten index $\nu = 2$, coming from the larger basis of the pyrochlore which contains two sites more than the basis of the diamond lattice.

As a final note, one can also construct the diamond-X lattice from the pyrochlore. This is done by replacing all tetrahedra which are the largest fully-connected plaquettes (cliques) in the pyrochlore lattice.

Family of models from (10,3)b lattice – As a second example in three dimensions, let us discuss the family of models obtained from the (10,3)b lattice, depicted in Fig. 9.8. The (10,3)b lattice appears in modern literature mostly in the context of Kitaev spin liquids as it is realized in the materials α -Li₂IrO₃ where $j = 1/2$ moments are shown to interact with bond directional couplings possibly realizing Kitaev spin liquids. Geometrically, the lattice (10,3)b, also known as hyperhoneycomb lattice, is a tricoordinated lattice with minimal loop length 10.

A fermion model on the (10,3)b lattice can be mapped to a boson model on a lattice

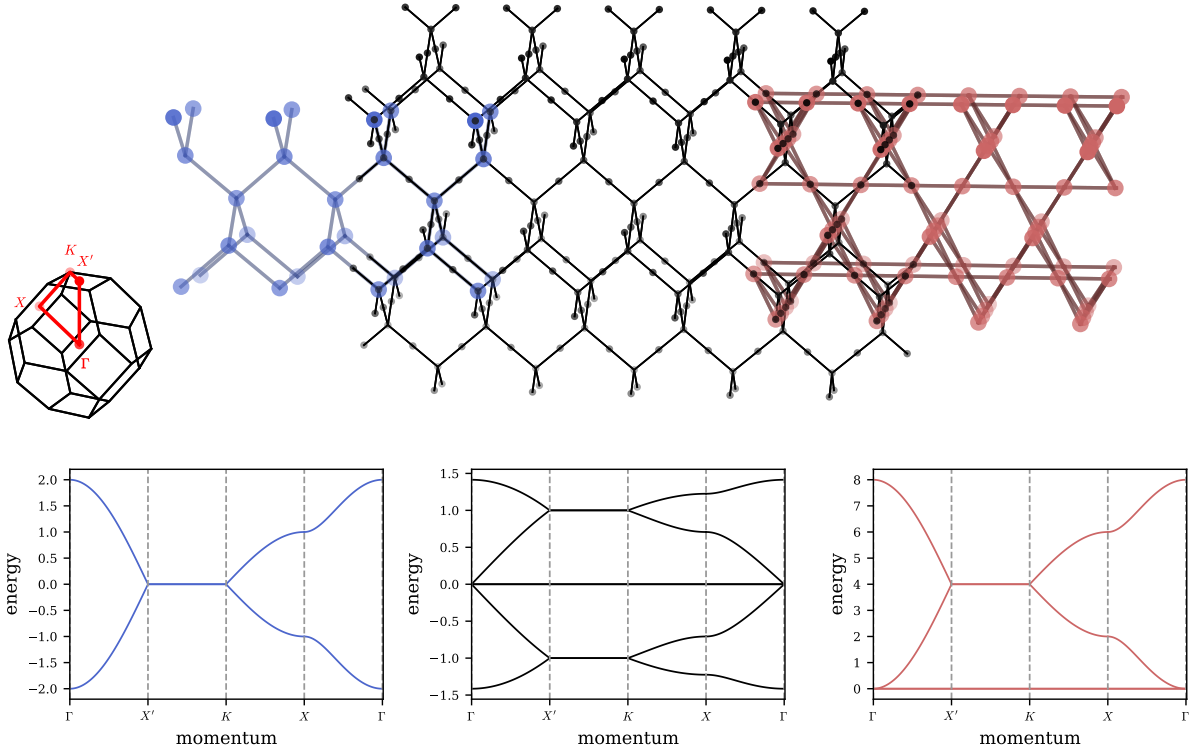


Figure 9.7.: SUSY corresponding diamond and pyrochlore lattices - Complex fermions (blue, left) on the diamond lattice can be shown to be supersymmetrically linked to complex bosons (red, right) on the pyrochlore lattice. The mapping can be established with a SUSY charge which can be interpreted as the adjacency matrix of a diamond-X lattice (center plot) which is a diamond lattice with additional sites on every bond and whose two sublattices are the diamond and pyrochlore lattices respectively. Plots have been directly obtained from `LatticePhysics.jl`.

in which the tri-coordinated sites of the hyperhoneycomb are replaced by corner-sharing triangles. Although having remarkable similarity to the hyperkagome, this is in fact not it. The relevant SUSY charge graph is on the hyperhoneycomb-X lattice and leads to a finite Witten index reflected in the flat band at the bottom of the boson model.

From the point of this chapter, the remarkable aspect is that the well-known feature of the nodal line in the fermion model is mapped to the boson model as well, leading to yet another model with a nodal line structure.

Taking the lattice (10,3)b as a graph for a SUSY charge transforms the nodal line in a different way. Its two sublattices, hosting fermion and boson model respectively, show the nodal line as a line of minimal energy states. The mapping here involves the next-nearest neighbor lattice of the hyperhoneycomb which consists of many triangular planes

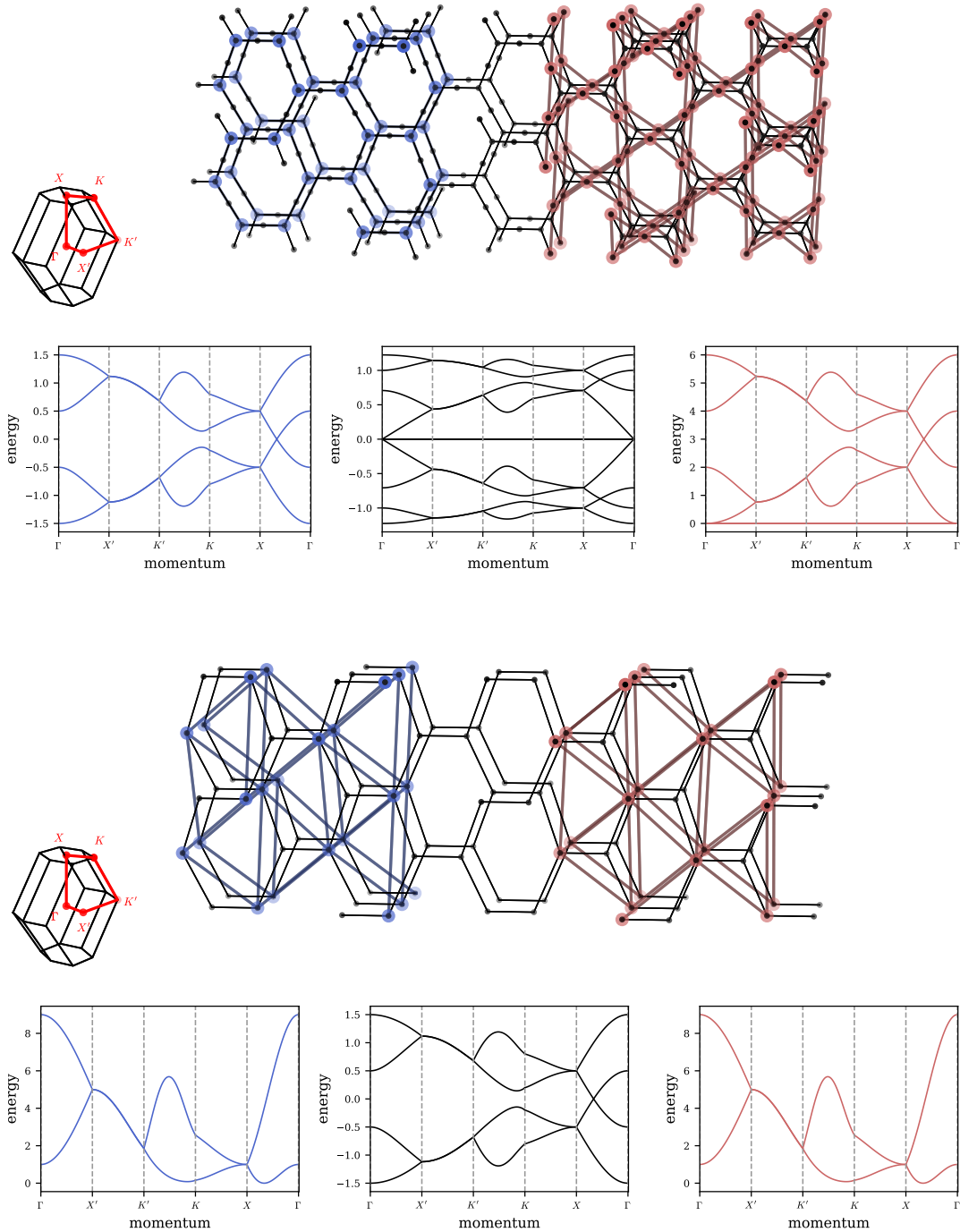


Figure 9.8.: Further 3D examples for SUSY corresponding lattices - Fermion, SUSY charge and boson lattices shown with corresponding bandstructures for examples from the family of tricoordinated lattices. Plots directly obtained from LatticePhysics.jl.

interwoven at a unique way.

All in all, the many examples of isospectral complex boson and fermion models demonstrated in this section show the ubiquitous applicability of the supersymmetric graph mapping.

10. Majorana fermions and topological mechanics

Having established a rigorous supersymmetry connection between complex fermions and complex bosons, let us turn our attention towards another flavor of particle, namely *Majorana fermions*. These fermions are real versions of the conventional (complex) fermions with the additional feature of being their own antiparticle.

The following chapter aims at providing a cohesive introduction to supersymmetry for Majorana fermions and why their models can be linked to topological mechanics. Most of the work presented in this section is based on paper [P5].

10.1. Supersymmetric charge

Let us start by defining a supersymmetry charge for Majorana fermions. Naturally, Majorana fermions, as they are real fermions, will link to real bosons. Specifically for Majorana fermions on bipartite lattices, one can define a SUSY charge of the form

$$\mathcal{Q}_{\text{MF}} = \gamma_i^B \mathbb{1}_{ij} \hat{p}_j + \gamma_i^A \mathbf{A}_{ij} \hat{q}_j \quad (10.1)$$

which corresponds to a rigidity matrix

$$\mathbf{R} = \begin{pmatrix} \mathbb{1} & 0 \\ 0 & \mathbf{A} \end{pmatrix} \quad (10.2)$$

utilizing the previous notation of $\mathcal{Q} = \vec{\gamma} \mathbf{R} \vec{b}$. This supersymmetric charge divides the Majorana fermions into two flavors which are both defined on the respective sublattices of the bipartite lattice. They are connected to two flavors of real bosons, \hat{p}_j and \hat{q}_j , which are both defined only on the B-sublattice. Bosons and fermions are connected both directly on the B sites as well as through the connectivity matrix \mathbf{A} which describes how sites from the A sublattice connect to sites of the B sublattice within the bipartite lattice.

To calculate the respective partner Hamiltonians, one has to again calculate $H_{\text{SUSY}} = \{\mathcal{Q}, \mathcal{Q}^\dagger\}$ which will result in four terms when using the identity

$$\{AB, CD\} = A\{B, C\}D - C[A, D]B - [A, C]BD - CA[B, D] \quad (10.3)$$

which was already used in the complex boson case. These four terms can then be resolved with the commutation relations of the bosons

$$[\hat{x}_i, \hat{p}_j] = i\delta_{ij} \quad (10.4)$$

$$[\hat{x}_i, \hat{x}_j] = 0 = [\hat{p}_i, \hat{p}_j], \quad (10.5)$$

and Majorana fermions

$$\{\gamma_i^A, \gamma_j^A\} = 2\delta_{ij} = \{\gamma_i^B, \gamma_j^B\} \quad (10.6)$$

$$\{\gamma_i^A, \gamma_j^B\} = 0. \quad (10.7)$$

Resolving all terms results in a SUSY Hamiltonian that decomposes into two distinct parts

$$H_{\text{fermion}} = i\gamma_j^B \mathbf{A}_{jk}^T \gamma_k^A - i\gamma_j^A \mathbf{A}_{jk} \gamma_k^B \quad (10.8)$$

$$H_{\text{boson}} = \hat{p}_i \hat{p}_i + \hat{q}_i (\mathbf{A}^T \mathbf{A})_{ij} \hat{q}_j \quad (10.9)$$

describing hopping of Majorana fermions on the initial bipartite lattice, as specified by the connectivity matrix \mathbf{A} , and boson interaction on one of its sublattices. The boson part takes a form that is very reminiscent of a classical Hamiltonian like coupled balls and springs, including both a quadratic momentum term as well as interactions that are quadratic in position.

10.2. Real bosons and classical balls and springs

Before investigating the implications of the SUSY link to real bosons, let us first discuss a much more well known context of real bosons, namely canonical quantization. Since real bosons are the particles that are naturally introduced by canonical quantization, let us start with a detour on how classical mechanics first transitioned into quantum mechanics.

Canonical quantization: From classical to quantum mechanics

In classical mechanics, particles are described by their phase space trajectories (x_i, p_i) as function of time. The shape of these trajectories can be determined by solving the particle's equation of motion, which is a differential equation setting derivatives of position and momentum into context.

One possibility to obtain such equations of motion is from Newton's axiom

$$m\ddot{x}_i = F_i \quad (10.10)$$

where F_i describes a force acting on particle i . In general, the force will again depend on

position and momentum, yielding a differential equation upon insertion.

For systems with energy conservation, another more modern route to the equation of motion can be chosen. In this formalism, a new Hamilton function $H = H(x_i, p_i)$ is introduced which describes the system's energy as function of particle position and momenta. Subsequently, equations of motion can be obtained from the Hamilton function by use of Hamilton equations

$$\dot{x}_i = \frac{\partial H}{\partial p_i}, \quad \dot{p}_i = -\frac{\partial H}{\partial x_i}. \quad (10.11)$$

Even more generalized, the Hamilton equations can be derived from Poisson brackets $\{f, g\}$ which are defined as

$$\{f, g\} = \sum_i \left(\frac{\partial f}{\partial x_i} \frac{\partial g}{\partial p_i} - \frac{\partial f}{\partial p_i} \frac{\partial g}{\partial x_i} \right) \quad (10.12)$$

and allow for obtaining the total time derivative of any function f in a Hamiltonian system by calculating

$$\frac{d}{dt}f = \{f, H\} + \frac{\partial}{\partial t}f. \quad (10.13)$$

Inserting $f = x$ and $f = p$ allows recovering the Hamilton equations. It is worth noting that the coordinates themselves have Poisson brackets

$$\{x_i, p_j\} = \delta_{i,j} \quad (10.14)$$

$$\{x_i, x_j\} = 0 = \{p_i, p_j\} \quad (10.15)$$

The historic route from classical to quantum mechanics, known as canonical quantization, is to replace all classical coordinates x_i and p_i by operators \hat{x}_i and \hat{p}_i which measure the respective quantities. To implement dynamics, Poisson brackets $\{f, g\}$ are replaced by commutators $[\hat{f}, \hat{g}]$ with an additional factor of i . This replacement first and foremost completely changes the formalism. Where in classical mechanics, particles had a well-defined position and momentum, now in quantum mechanics their position and momentum are subject to measurement. Measurement probabilities can be computed from the square of a new object $\psi(x_i, t)$, called wavefunction,

$$\rho(x_i, t) = |\psi(x_i, t)|^2. \quad (10.16)$$

whose dynamical behavior can be captured by the Schrödinger equation

$$\hat{H}(\hat{x}_i, \hat{p}_i) |\psi(x_i, t)\rangle = -i \frac{\partial}{\partial t} |\psi(x_i, t)\rangle. \quad (10.17)$$

To bridge the gap to the supersymmetric charge at hand, it is worth noting that these elementary operators \hat{x}_i and \hat{p}_i are exactly what was previously introduced as real bosons,

e.g. seen in their commutators

$$[\hat{x}_i, \hat{p}_j] = i\delta_{i,j} \quad (10.18)$$

$$[\hat{x}_i, \hat{x}_j] = 0 = [\hat{p}_i, \hat{p}_j] \quad (10.19)$$

which can be retrieved from their previously mentioned classical Poisson brackets. It is thus only naturally to identify any real boson model with a classical mechanical origin.

Real boson models from classical balls and springs

Since real bosons occur naturally upon replacing classical variables by quantum mechanical operators, let us now do the opposite: replace real boson operators in the SUSY connection with classical variables. The real boson model can thus be written as a mechanical model with the following Hamilton function

$$H = p_i^2 + q_i(\mathbf{A}^T \mathbf{A})_{ij} q_j \quad (10.20)$$

with momenta p_i of classical coordinates q_i .

A possible realization of this mechanical model is the one-dimensional movement of coupled balls or masses. Since in principle the lattice structure of the boson model is reproduced in the classical model, the one-dimensional movement can e.g. be modeled in the out-of-plane direction of the 2D lattice or just any direction in higher lattice dimension. The coupling can be facilitated by springs which have a potential energy of $V(q_i - q_j) = k_{ij}(q_i - q_j)^2$. Having only the momenta and springs leads to a Hamiltonian of the form

$$\begin{aligned} H &= \sum_i \frac{p_i^2}{2m} + \sum_{ij} \frac{k_{ij}}{2} (q_i - q_j)^2 + \sum_i \frac{\kappa_i}{2} q_i^2 \\ &\sim \sum_i p_i^2 + \sum_{ij} q_i \mathbf{D}_{ij} q_j \end{aligned} \quad (10.21)$$

in which spring constants can be computed from comparison of the dynamical matrix \mathbf{D} with Eq. (10.20) s.t.

$$k_{ij} = -2 \sum_{a \in A} \mathbf{A}_{ia}^T \mathbf{A}_{aj} \quad (10.22)$$

$$\kappa_i = 2 \sum_{a \in A} \mathbf{A}_{ai}^2 - \sum_{b \in B} k_{ib}. \quad (10.23)$$

In principle, two types of springs occur. One type of springs is coupling the masses among each other with spring constants k_{ij} . The second type of springs is coupling the masses on-site to an offset position, e.g. the lattice plane.

At this point, supersymmetry has enabled a consecutive link of any Majorana fermion Hamiltonian on a bipartite lattice to a classical balls-and-springs model with the additional

step in between of a real boson model. To underline the impact of this kind of map, let us in the following discuss two examples of well-studied Majorana fermion models which now have a classical counterpart that inherits their topological properties, yielding a topological mechanical model.

10.3. Example I: Mechanical Kitaev model

Let us start the discussion of examples by constructing a mechanical realization of the famous Kitaev model [3]. Although introduced as a quantum spin model to describe the formation of quantum spin liquids, and also being discussed in this context earlier in this thesis, it is also well known for featuring Majorana fermions as part of its analytical solution. Because it features Majorana fermions on a bipartite honeycomb lattice, it is suitable for the supersymmetric map to a classical model demonstrated in this chapter.

The example is laid out as follows. First, a brief introduction to the Kitaev model and its analytical solution is presented. Then, the mapping to its mechanical SUSY counterpart is described and analyzed. Attention is paid especially to the classical time evolution and the comparison of mechanical to Majorana fermion spectra.

10.3.1. The Kitaev model and its analytical solution

The Kitaev model has been introduced in 2006 by A. Kitaev [3] as an analytically solvable model suitable for describing quantum spin liquids. These exotic states of matter evade the conventional ordering of magnetic moments at finite temperatures by fluctuating between degenerate ground states even at zero temperature. In 2009, G. Jackeli and G. Khaliullin [4] showed that the Kitaev model can be realized in the spin-orbit coupled iridates, leading to a rush in experimental advances. This experimental realization is also part of the main focus in chapter I, where the so-called Kitaev materials and their experimental investigation play a crucial role.

To not repeat the same discussion as in chapter I, let us here focus on the technical aspects of the Kitaev model and its analytical solution. The model itself can be written as spins interacting on a honeycomb lattice with interactions

$$H = \sum_{\nu, ij} J_{\nu} \sigma_i^{\nu} \sigma_j^{\nu}, \quad (10.24)$$

where bonds are labeled in three classes, $\nu = x, y, z$ and interactions are Ising couplings of neighboring spins with components given by the bond. These competing interactions cannot be simultaneously satisfied, i.e. the system is highly frustrated.

Already upon introduction of his model, A. Kitaev demonstrated an analytical solution [3], revolving around recasting the spin operators in terms of Majorana fermions. On each site

j , four Majorana fermions $\gamma_j^x, \gamma_j^y, \gamma_j^z, \gamma_j$ are introduced such that the spin components σ_j^ν on these sites can be rewritten as

$$\sigma_j^\nu = i\gamma_j^\nu \gamma_j. \quad (10.25)$$

This reformulation of spin operators leaves the underlying spin algebra intact but allows for a drastic simplification of the spin model.

The bond-directional coupling of spin components γ_j^ν allows them to pair along such bonds, to so called bond operators

$$\hat{u}_{ij}^\nu = i\gamma_j^\nu \gamma_i^\nu, \quad (10.26)$$

which commute with both themselves as well as the Hamiltonian. Since the bond operators commute with the Hamiltonian, they are an effective (gauge) symmetry of the Hamiltonian and the Hilbert space separates into blocks which are characterized by the respective bond operator eigenvalues u_{ij}^ν .

In principle, the bond operators implemented a static background flux field in which the rest of the problem resides. The remainder of the spin model only consists of the fourth, unbound Majorana fermion on each site which can now interact along all bonds as

$$H_{\text{MF}} = i \sum_{\nu, ij} J_\nu u_{ij}^\nu \gamma_i \gamma_j \quad (10.27)$$

i.e. describing an effective free Majorana fermion hopping problem on the underlying honeycomb lattice.

A full solution to the Kitaev model therefore consists of both a solution to the background flux (gauge) field as well as solving the quadratic Majorana model in this flux configuration. At low temperatures, the flux field will be in its ground state given by Lieb theorem, however at finite temperature more flux configurations are accessible.

For the remainder of this chapter, we will focus more on the remaining Majorana problem. Since it is a quadratic hopping model on a bipartite lattice, it readily fulfills the criteria for the supersymmetric mapping and therefore can be in principle implemented in a balls and springs model.

10.3.2. Classical balls and springs model

The Majorana fermion SUSY procedure can be readily applied to the Majorana form of the Kitaev model. Here, let us incorporate both the spin coupling J_μ as well as the eigenvalues of bond operators u_{ij} into a bond dependent hopping amplitude t_μ s.t. the model reads

$$H_{\text{MF}} = i \sum_{\mu, ij} t_\mu \gamma_i \gamma_j \quad (10.28)$$

where sites i and j of course reside on the honeycomb lattice.

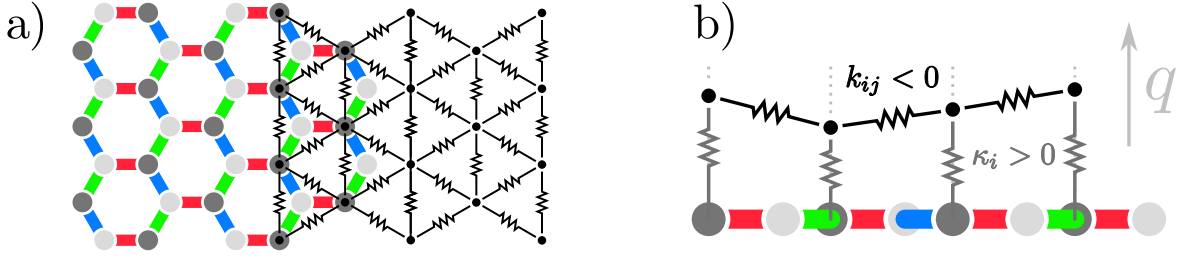


Figure 10.1.: Mechanical Kitaev model - Sketch of the mechanical version of the Kitaev model defined by masses on the triangular lattice, c.f. panel a). Masses on adjacent sites are connected by intersite springs of coupling constant k_{ij} . Additionally, masses are also connected to the lattice plane by springs with constants κ_i (c.f. panel b)). Figure adapted from [P5].

Applying the outcome from the SUSY procedure, i.e. in particular Eq. (10.9), to the Majorana model on the honeycomb lattice, leads to a real boson model on one of the two sublattices of the honeycomb lattice which is a triangular lattice. This real boson model can be further identified with a classical balls and springs model, c.f., which describes masses on sites of the triangular lattice with movement constraint to the direction perpendicular to the lattice plane and coupled by springs with spring constants given by Eq. (10.23) (coupling to the lattice plane) and Eq. (10.22) (coupling between masses). More explicitly, the spring constants in the bulk can be written as

$$k_{ij}^\sigma = -2t_\mu t_\nu \quad (10.29)$$

$$\kappa_i = 2(t_x^2 + t_y^2 + t_z^2) + 2(t_x t_y + t_y t_z + t_x t_z), \quad (10.30)$$

with σ, μ, ν describing a cyclic permutation of x, y, z .

In principle one would expect the bulk spring constants to be repeated periodically through the lattice up to the boundary at which springs are cut away by open boundary conditions. However, since the spring couplings are derived from supersymmetry, one has to be more careful. The intersite spring constants k_{ij} defined in Eq. (10.22) take into account only fermion hopping from i to j which will not change at the boundary. However, the on-site spring constants κ_i defined in Eq. (10.23) take into account both the fermionic as well as the bosonic neighborhood of the respective sites and therefore have to be adapted based on both fermion and boson boundary conditions.

Another exception from the bulk spring constants occurs in different flux sectors of the Kitaev model. In principle, any flux sector can be implemented as a certain sign configuration u_{ij} on the bonds of the honeycomb lattice. This sign configuration translates to a distribution of hopping constants t_μ which again translates to new spring constants. Especially the excitation of a single vison in a large finite lattice, i.e. by changing the flux configuration only by a small amount, spring constants have to be adapted locally.

In principle, a vison excitation in the Majorana model can be implemented as a sign-flip which translates to a similar sign-flip of spring constants in the mechanical model as well as some change of on-site spring constants.

However, with these exceptions carried out, any finite sized honeycomb lattice hosting a Majorana description of the Kitaev model can be directly translated to a corresponding balls-and-springs model on the triangular lattice. Let us use the remainder of this example to analyze these resulting mechanical models in greater detail.

10.3.3. Measuring spectra in the mechanical model

Before discussing a detailed comparison between the Majorana form of the Kitaev model and the mechanical model derived in the previous part, let us first consider *what exactly* we want to compare. In principle, supersymmetry guarantees isospectrality between the Majorana fermion Kitaev model in Eq. (10.28) and the corresponding real boson model on the triangular lattice defined by Eq. (10.9). Moreover, any fermion state can be mapped under supersymmetry to a corresponding boson state, thus not leaving any room for new physics only in the real boson model.

In contrast to the exact SUSY relation of the real boson model to the Majorana system, the *classical* balls-and-springs model is not exactly related. In general it is widely unclear to what extent a classical model inherits properties from its quantum origin, with the hope of course being that any classical version arises from an $\hbar \rightarrow 0$ limit of the quantum model. In the example at hand, we will nevertheless see, that single-particle wavefunctions in the Majorana model correspond to amplitude patterns in the classical model.

Such an identification in principle lays out a route to compare any classical property, that can be computed directly from one of the arising matrices, to a fermionic analogue. Therefore to test isospectrality between the classical and the Majorana model, a practical approach is applied. In principle, a classical eigenspectrum can be obtained by *probing* a finite path of the classical model. This involves exciting the model with some periodic force and then investigating the developing wave patterns in momentum space. Let us investigate these steps one by one in the following.

Constructing a finite lattice of classical balls and springs can be done explicitly by using a lattice library like LatticePhysics.jl. Such a library provides both the real-space positions of individual lattice sites as well as their graph connectivity. On top of this underlying lattice structure, the equations of motion of individual masses including forces between the masses can be implemented. Here, the framework of DifferentialEquations.jl [68] is used. In principle, all that is left now is to provide initial conditions and external forces or drive to simulate the time evolution of the classical mechanical model.

To mimic an experimentally realizable excitation to the model, the following force profile

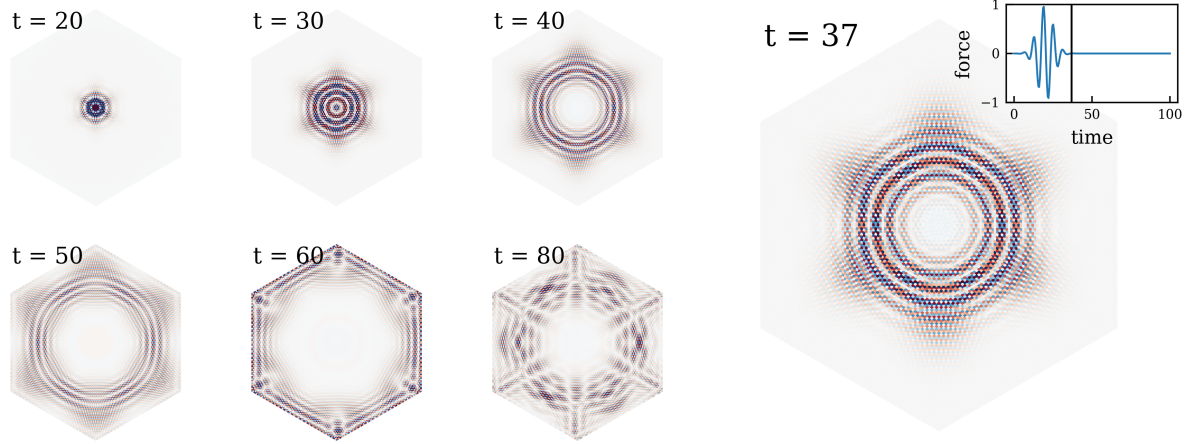


Figure 10.2.: Classical time evolution under applied force - Classical balls and spring model of the Kitaev model under applied force. Force has a frequency of $f = 1$ and is applied with a Gaussian envelope, time dependence of profile can be seen at the top right. Panels show amplitude snapshots for various times where red denotes amplitudes in the plane and blue denotes amplitudes out-of-plane. One can see that upon exertion of force, a spherical wave spreads outward through the material and reflects at the boundaries.

is used:

$$F(t) \sim \sin(f \cdot t) \exp\left(\left(\frac{t - t_0}{\Delta t}\right)^2\right). \quad (10.31)$$

It describes a periodically oscillating force with driving frequency f which occurs at time t_0 and roughly lasts Δt . In principle one could also use an infinitely oscillating profile or move the respective site directly instead of applying a force F .

Now let us investigate the resulting time-evolution of the classical model when applying the aforementioned force profile to the center site, depicted in different snapshots in Fig. 10.2. One can see that upon exerting the force profile to the model, a spherical wave packet is initiated around the center, as one would have naively expected. The spherical symmetry is not perfect but still accounts for the underlying honeycomb lattice symmetries and the wave packet bears a lot of substructure. After long times, boundary effects start to occur when the wave packet is reflected from the open boundary of the finite lattice and interferes with itself. Note that in order to resolve the boundary correctly, one has to build a finite fermion lattice and map it to the respective balls-and-springs model instead of simply replicating the balls-and-springs unitcell.

In principle, the developing wave patterns will depend on the driving frequency f both in real and momentum space. Results for different driving frequencies are depicted in Fig. 10.3. One can see that especially the local structure of the wave packet, i.e. the correlations between neighboring sites, is varying. These local discrepancies for different driving

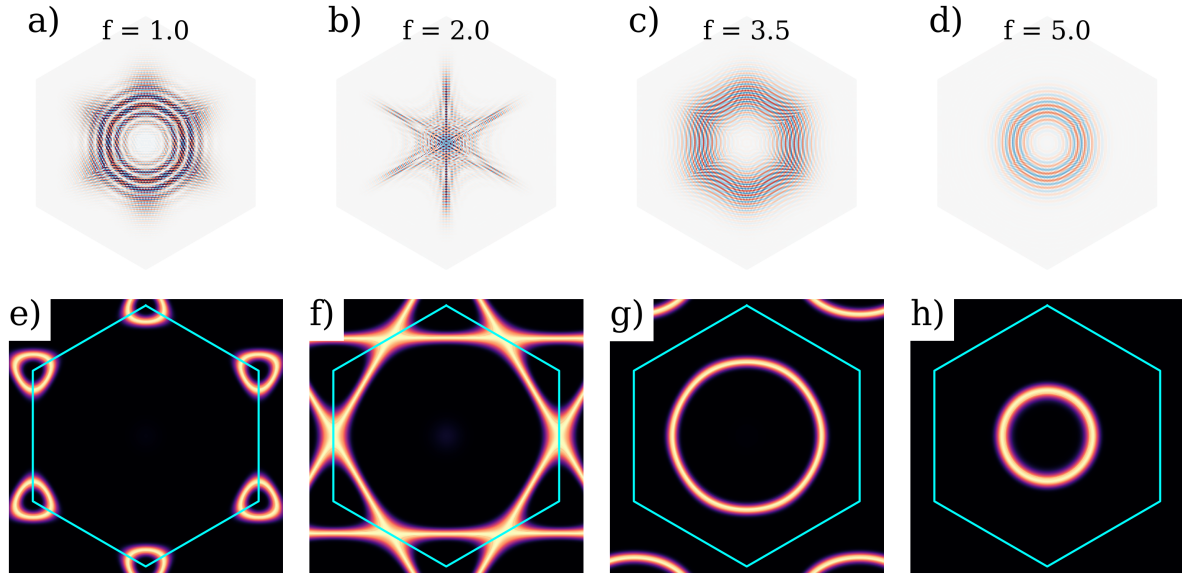


Figure 10.3.: Frequency dependence of wave patterns in real and momentum space - Snapshots of the evolving wave pattern for drives of different frequencies. Top row (panels a)-d)) shows wave pattern in real space, bottom row (panels e)-h)) shows the corresponding Fourier transform, averaged over a time interval. Additionally, the Brillouin zone of the honeycomb lattice is indicated in the bottom panels with a cyan outline. One can see that drives of different frequencies produce wavepatterns with qualitatively different momentum space characteristics.

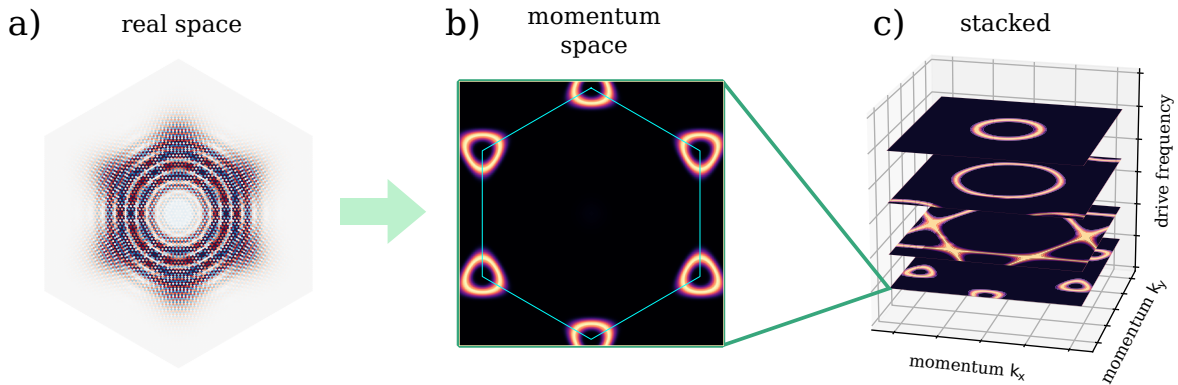


Figure 10.4.: Measurement of mechanical spectrum - Stacking Fourier transformed wave patterns by driving frequency as depicted in panel c) allows for the measurement of a mechanical spectrum. Each frequency cut corresponds to an individual simulation with the respective drive frequency. To obtain a spectrum, the real space configurations, c.f. panel a), are Fourier transformed to momentum space, c.f. panel b), and finally stacked, c.f. panel c). Taking a cut through this stack along a momentum space path reveals the band structure of the classical mechanical model in close analogy to the fermion equivalent.

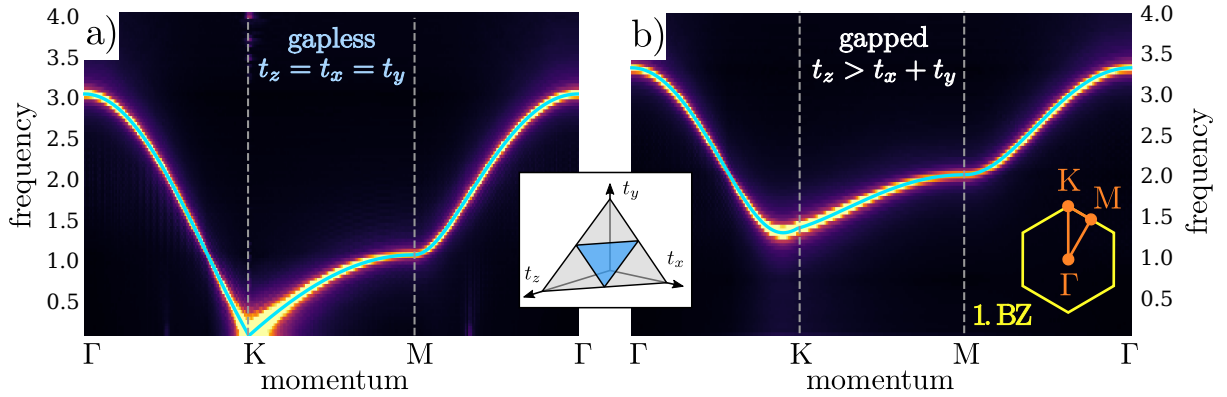


Figure 10.5.: Spectra of mechanical Kitaev model - Panels show the extracted mechanical spectra of the balls and springs model constructed from the Majorana fermion Kitaev model in comparison to the analytical bandstructure of the Majorana fermions. Mechanical spectra have been calculated by exciting a finite system with a certain frequency and then Fourier transforming the resulting wave patterns, finally showing the time-averaged Fourier weight as color coded in the driving frequency - momentum plane. Analytical spectra are calculated by diagonalizing the momentum-dependent interaction matrix and its eigenvalues are displayed as cyan lines. Both the gapless as well as the gapped phase analytical Majorana spectrum can be reproduced perfectly by the mechanical model, including the excitation gap which denotes a region in driving frequencies for which the mechanical model can not be excited by stimulus. Figure adapted from Ref. [P5].

frequencies translate to qualitative differences in momentum space, where the respective Fourier transforms show vastly different images.

Finally, a classical spectrum can be extracted from this sort of data by stacking the Fourier transforms for different driving frequencies as seen in Fig. 10.4. Plotting the Fourier intensities along specific cuts of momentum space provides plots that can be compared to fermion bandstructures. As we will see in the following, these classical excitation spectra, which are obtained in a completely experimental way, reproduce the corresponding fermion spectrum quite well in all cases.

10.3.4. Spectral correspondences

Let us discuss the mechanical spectra in the following. For this purpose, mechanical spectra of the two relevant regions of the Kitaev model have been obtained with the method laid out before. In Fig. 10.5, these spectra for the gapped and gapless region are compared to their counterparts in the analytical Majorana fermion solution.

As one can see, the mechanical spectra in Fig. 10.5 agree stunningly with their analytical analogues for both parameter cases. An agreement between the real boson model and the

Majorana fermion model was enforced by supersymmetry, however the agreement of the classical mechanical model to the Majorana fermion model had to be confirmed explicitly.

Note that this spectral correspondence is including some important details. First of all, the mechanical spectra include zero modes at the Dirac points of the Brillouin zone. These correspond to states which can be excited without an investment of energy. Furthermore, these points have been found stable across the entire gapless phase, showing a linear dispersion also seen in the mechanical model.

Upon reaching the boundary of the gapless phase, the Dirac points in the Majorana model merge and gap out the spectrum. This behavior is reproduced in the classical model, including the gap which can be observed. One naively might expect this gap to be prohibited and a Goldstone mode to form in its place, however Goldstone modes are suppressed because translational symmetry in the mechanical model along the movement direction is explicitly broken by the on-site springs. Therefore, no Goldstone mode can form and a gap is possible.

A similar gap can also be observed for high frequencies which also show no signs of excitation response. The lack of response for certain frequencies lets the material behave like an acoustic band-pass filter.

All in all, the data in Fig. 10.5 shows that mechanical spectra of the Kitaev model generically inherit the behavior of their quantum analogues, leading to mechanical behavior previously only achieved by fine-tuning. Here however, the mechanical behavior originates from a well-understood electronic system, in which tuning becomes natural.

10.4. Example II: Mechanical second order topological insulator

Let us turn our attention towards the second example in building mechanical Majorana models with supersymmetry. In this example, a mechanical second order topological insulator (SOTI) is constructed from the famous quadrupolar insulator by Bernevig and Hughes [69, 70]. In contrast to the previous example, the mechanical SOTI inherits a topologically protected zero-energy mode from its Majorana fermion counterpart which can be probed by mechanical means.

The section is organized as follows. First, a brief introduction to the quadrupolar insulator and its mapping to a mechanical model is given. Then, the mechanical model is investigated with respect to spectra. Finally, a discussion of the corner mode and the connected topological invariant is added.

10.4.1. Second order topological insulator from Majorana fermions

The *octupolar insulator* of Bernevig and Hughes [69, 70] is a prime example for a second order topological insulator (SOTI) with gapless protected corner modes. SOTIs are a special cases of so-called higher-order topological insulators which are generalizations of the conventional topological insulators but with protected hinge or corner modes instead of the conventional protected boundary modes [71].

Experimentally, SOTIs have recently been discussed in the context of engineered phononic insulators [72], microwave systems [73] and electrical circuits [74]. Also, it has been shown that elementary bismuth behaves like a SOTI with protected hinge modes along the crystal hinges [75]. From a theoretical perspective, SOTIs have also been discussed in the context of frustrated quantum magnetism [76].

In the context of this thesis, let us focus on two particular features of the quadrupolar insulator. First of all, it can be formulated as a nearest-neighbor hopping problem for fermions on a square lattice (which is bipartite). Second, it exhibits a localized corner mode which originates from a finite topological polarization.

Since mostly spectral properties of the model as well as explicit eigenstates are of interest, it can be formulated in Majorana fermions alike. In total, the model then describes Majorana fermions on a square lattice with an extended four-site unitcell. Hopping is staggered between different plaquettes with alternating hoppings. Hoppings within the unitcell have amplitude t_γ and hoppings across unitcells have amplitude t_δ as depicted in Fig. 10.6. Additionally, a π -flux is introduced into every plaquette which can be implemented into the model by flipping the signs on some bonds (drawn dashed in Fig. 10.6).

Depending on the relative strength of hoppings t_γ and t_δ , the model is either gapless ($t_\gamma = t_\delta$) or gapped ($t_\gamma \neq t_\delta$). The two gapless phases can be classified as trivial ($t_\gamma > t_\delta$) and topological ($t_\gamma < t_\delta$). The original model also exhibits localized cornermodes in the topological phase whose wavefunctions are localized in the corners of a finite system and therefore are distinct from any other state.

With these features, the Majorana SOTI is a prime candidate for yielding a rich mechanical model, featuring both isospectrality to the Majorana SOTI and localized mechanical modes at zero frequency, both of which are laid out in the following.

10.4.2. Classical balls and springs model

Constructing a classical balls and springs model out of the SOTI can be done by employing the procedure from section 10.2. This process will first generate a model of real bosonic operators and consecutively a classical balls and springs implementation of the real boson model. The entire mapping process can be seen in Fig. 10.6.

Following the construction algorithm produces a model with real boson operators on the B sublattice of the initial square lattice. On each site, one finds a momentum and a position

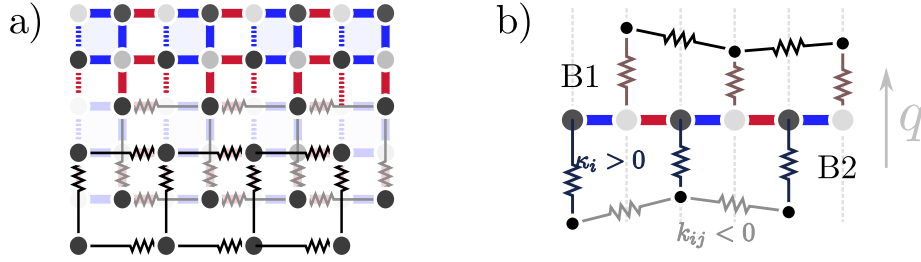


Figure 10.6.: Second order topological insulator and its mechanical analogue - Model describes hopping on a square lattice with staggered hopping amplitudes. Blue and red lines denote hopping of different strength while dashed lines signal a negative hopping sign. These hopping signs implement a π -flux through every square plaquette. When constructing the classical spring model, negative signs from π -fluxes lead to annihilation of different hopping paths across square plaquettes, thus resulting in two decoupled mechanical models. Figure adapted from [P5].

operator \hat{q}_i and \hat{p}_i , interacting with neighboring sites in the B sublattice.

Going further, the real boson model can be identified with a classical balls and springs model, describing masses on the B sublattice sites moving out of the lattice plane, as well as springs connecting masses and masses to the lattice plane. Spring couplings can be derived using Eq. (10.23) (springs coupled to the lattice plane) and Eq. (10.22) (springs between masses). More explicitly, one can extract bulk spring constants

$$k_{ij}^{\alpha} = \begin{cases} -4t_{\alpha}^2 & (\text{B1} \leftrightarrow \text{B2}, 0\text{-flux}) (\alpha = \gamma, \delta) \\ 0 & (\text{B1} \leftrightarrow \text{B2}, \pi\text{-flux}) \\ -2t_{\gamma}t_{\delta} & (\text{B1} \leftrightarrow \text{B1}, \text{B2} \leftrightarrow \text{B2}) \end{cases} \quad (10.32)$$

$$\kappa_i = \begin{cases} 4(t_{\gamma}^2 + t_{\delta}^2) + 8(t_{\gamma}^2 + t_{\delta}^2 + t_{\gamma}t_{\delta}) & (0\text{-flux}) \\ 4(t_{\gamma}^2 + t_{\delta}^2) & (\pi\text{-flux}), \end{cases} \quad (10.33)$$

which depend on both the flux within the square plaquettes as well as which sublattices of the square B-sublattice they connect. Since the square B sublattice is a square lattice as well, it contains two sublattices, B1 and B2, which are again square lattices. From Eq. (10.32) it is apparent that a π -flux decouples the B1 and B2 sublattices as all spring constants between them vanish. This decoupling originates from the relative minus signs of interfering hopping paths across the square plaquettes when squaring the hopping matrix, as being visible in Fig. 10.6.

Having gone through the entire process of mapping the π -flux SOTI, one is left with a mechanical SOTI that is described by two decoupled balls and springs models. Each model is defined on one sublattice of the B sublattice respectively and features masses moving perpendicular to the lattice plane coupled by springs. Let us turn our attention

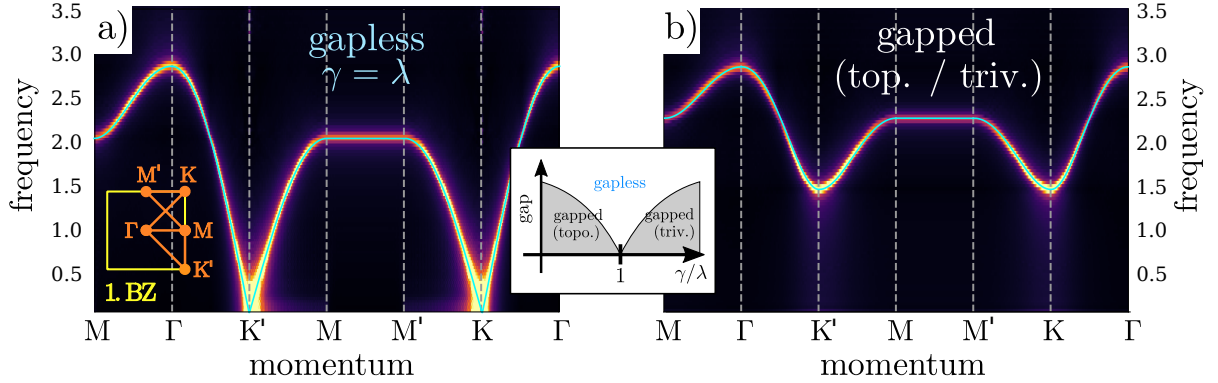


Figure 10.7.: Spectra of mechanical SOTI - Panels show the extracted mechanical spectra of the balls and springs model constructed from the Majorana fermion SOTI. Spectra have been calculated by exciting a finite system with a certain frequency and then Fourier transforming the resulting wave patterns. Spectra show the time-averaged Fourier weight as a color in the driving frequency - momentum plane. Both the gapless as well as the gapped phase spectrum can be reproduced perfectly by the classical model, including the excitation gap which denotes a region in driving frequencies for which the mechanical model can not be excited by stimulus. Figure adapted from Ref. [P5].

now to investigating this mechanical model in a similar way to investigations of the Kitaev model beforehand in the search for isospectral properties and topological features such as the celebrated zero-energy corner model.

10.4.3. Spectral correspondences

Having derived a mechanical analogue of the SOTI model, one can now start examining this classical model. Let us first focus on results for the energy spectra of the mechanical SOTI. In principle, spectral properties can be extracted in the same way as with the mechanical Kitaev model, i.e. constructing a finite patch of the mechanical system, exciting it with different driving frequencies and Fourier transforming the resulting wave patterns.

Results for such classical spectra can be found in Fig. 10.7. Here, both the gapless as well the gapped phase have been investigated. Overall the results agree very well with the Majorana fermion spectra, once again confirming the isospectrality of the two models.

Note that similarly to the Kitaev model, the mechanical SOTI also reproduces the gapped spectrum perfectly. This might be particularly surprising since it includes a region in driving frequency where the mechanical model is immune to external stimulus and cannot be excited. Thus the gap in mechanical SOTI implements a mechanical band-pass filter for a certain frequency range. The gap itself is only possible because of the on-site springs connecting the masses to the lattice plane. These springs explicitly break the continuous translational invariance of the masses and therefore preventing a Goldstone mode.

Note also that depending on the values of t_γ and t_δ , two gapless regions are possible, namely $t_\gamma < t_\delta$ and $t_\gamma > t_\delta$. For the bulk spectra, there is however no difference between the two regions since $t_\gamma < t_\delta$ is the same as $t_\gamma > t_\delta$ where labels γ and δ have been changed on each bond as well as the whole lattice being shifted by half a unitcell. The only difference in these two regions will appear once boundary effects are taken into account. Then the transformation of exchanging $\gamma \leftrightarrow \delta$ cannot be compensated by a shift in lattice anymore, resulting in a different boundary behavior for the two cases as we will discuss in the next section.

10.4.4. Localized corner modes

Having established a general spectral correspondence between the mechanical SOTI and its Majorana fermion origin, let us turn our attention now towards the topological mode which is part of the fermion model. In the Majorana fermion model, this topologically protected mode has an energy of 0 and is localized on the corners of any open-boundary square lattice. More precisely, the Majorana model hosts 4 modes, one for each corner. In the mechanical SOTI, only one sublattice is available which again decomposes into two independent models, thus hinting at only being able to observe a single cornermode for any applied excitation.

Exciting the cornermode in the mechanical model requires additional considerations. Previously, any bulk mode could be probed by applying a periodically oscillating force to the bulk, however the corner mode is 1) at the limit of zero drive frequency and 2) located at the corner. Therefore, the necessary excitation one can perform is to apply a force $F(t) = \text{const.}$ which is constant in time. In practical terms, this form of drive can also be understood as attaching a weight to the corner. The resulting motion that is expected from a zero-energy mode would be that of a free fall.

The observed motion of the mechanical SOTI in the topological phase under static force is shown in Fig. 10.8. Especially the trajectories of individual masses give great insight in the nature of the cornermode. In the logarithmic plot of Fig. 10.8 the elongations of individual masses are shown to be parallel lines with slope 2. Thus as $\log(A) \sim 2 \log(t)$, one can infer that $A \sim t^2$ which indicates a free-fall motion of individual masses as expected for a zero-energy mode. Furthermore, the lines being parallel indicates an exponential decay of amplitude from one site to the other which in combination with the colorcode of the figure or the other panel confirms the exponential localization to the corner.

At this point, it is worth noting that the cornermode is not generically inhabiting the corner of the model. For the trivial phase of the mechanical SOTI, no such mode can be observed. Also, if the excitation by constant force is not localized at the corner mode, the mode will still be excited at the particular corner, however under a time-delay that is necessary for the perturbation to reach the respective corner.

There is yet another aspect of the cornermode which can be probed in the mechanical SOTI.

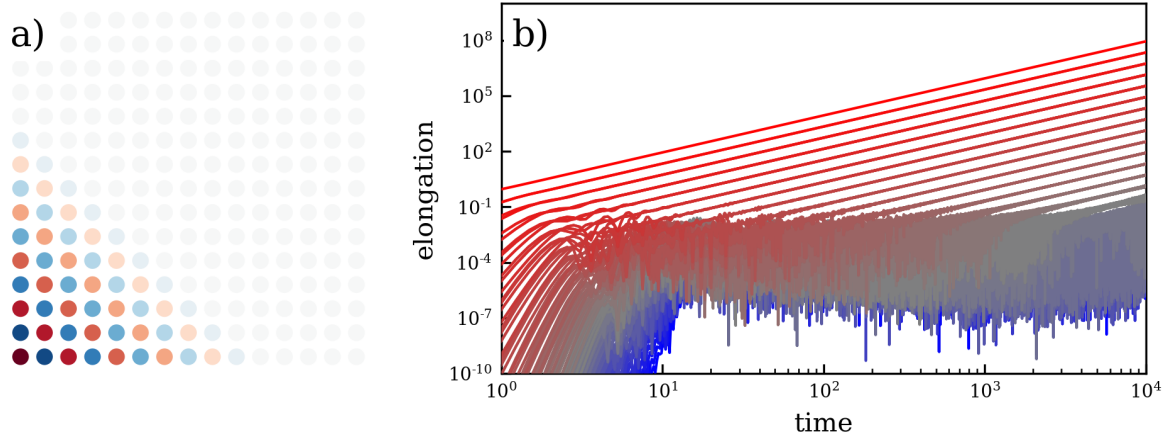


Figure 10.8.: Topologically protected cornermode in mechanical SOTI - Visualization on the emergence of a topologically protected cornermode in the mechanical SOTI model under constant force applied to the corner. Panel a) shows a real space plot with amplitudes color coded logarithmically to demonstrate the localized nature of the mode. Red and blue dots denote masses located below and above the lattice plane respectively. Panel b) shows individual trajectories in time where colors denote the distance from the excited corner with red corresponding to the excited corner itself and blue to the opposite corner. Parallel equal-spaced lines in the log-log plot indicate exponential localization in space, whereas the slope agrees with a free-fall motion $x \sim t^2$ which is expected for a zero-energy mode under constant force.

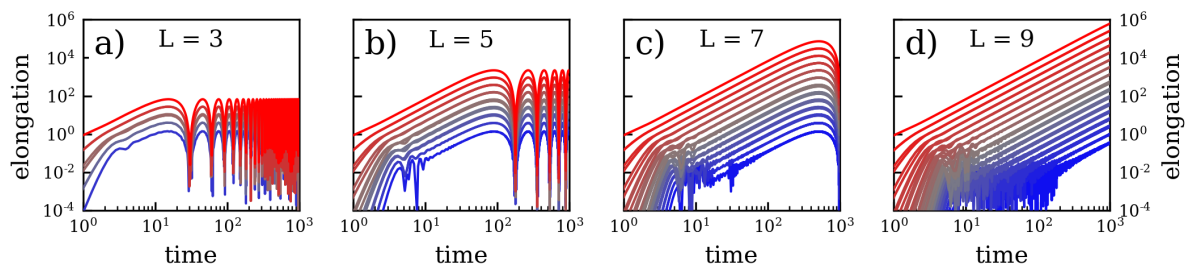


Figure 10.9.: Influence of system size on cornermode in mechanical SOTI - Individual panels show trajectories of sites upon excitation of the cornermode in systems of different linear system size L . One can see that for small system sizes, the mode exhibits a periodicity in time which indicates a finite but very small frequency of the mode. Increasing the system size reduces this effect until at $L = 9$ no traces of a finite periodicity can be seen on time scales shown in the plot.

From the fermion model of the octupolar insulator, it is known that the cornermodes are not strictly at zero energy but exhibit a small finite energy which vanishes with increasing system size. This behavior can also be found in the mechanical model as seen in 10.9 where cornermodes in systems of different linear size L are shown. For small system sizes, the trajectories do not show free fall behavior for all times but instead oscillate periodically in time. This oscillation frequency decreases as the system size is increased until the effect can no longer be observed even for medium sized systems, thus proving a direct analogue to the finite energy of the fermion mode.

Looking more closely on the time evolution of the mechanical model, one can even observe a qualitative explanation for the finite frequency of the corner mode. In principle, one can observe the free-fall motion to end when the mass on the opposite corner reaches an amplitude of $\mathcal{O}(1)$. Therefore, the time period of the mode is given by the time it takes to excite the opposite corner to $A \sim \mathcal{O}(1)$. This time depends on the exact ratio of couplings (and therefore the size of the bulk gap), as well as the system size. In particular, one can see that the increase in system size exponentially suppresses the mode's frequency. This comes from delaying an $\mathcal{O}(1)$ amplitude in the opposite corner by exponentially suppressing amplitudes away from the driven corner.

10.4.5. Topological invariant

Having observed the formation of the localized corner mode in the mechanical SOTI model, let us discuss the occurrence of a non-zero topological invariant in the bosonic model, indicating its presence in the first place. In fermionic models it has been long established, that non-trivial topology is accompanied by a finite topological charge. Such a charge can then be used as a probe to infer on non-trivial topology. In the case of the second order topological insulator, the respective topological charge is the Berry phase. Since it is calculated directly from eigenstates of the fermion bandstructure, supersymmetry allows to map it consequently to the bosonic side, where it naturally yields a corresponding bosonic observable indicating the bosonic topology. This following discussion aims at providing more insight in this mapping and argues similarly to the respective section in Ref. [P5].

Let us start by considering a general SUSY pair of fermion and boson models. In the fermion model, the Berry connection can be defined as

$$\mathcal{A} = \langle u_m(\mathbf{k}) | i \nabla_{\mathbf{k}} | u_n(\mathbf{k}) \rangle , \quad (10.34)$$

where $|u_m(\mathbf{k})\rangle$ denotes eigenvectors of the fermion Hamiltonian. Employing supersymmetry, fermion eigenstates can of course be mapped to boson eigenstates $|v_m(\mathbf{k})\rangle$ by employing the SUSY charge, or more specifically the rigidity matrix on which it is built. Ultimately,

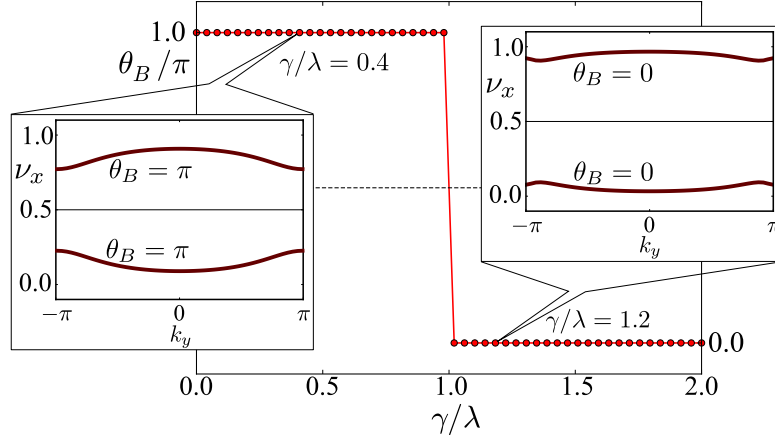


Figure 10.10.: Bosonic topological invariants in mechanical SOTI - The Berry phase θ_B/π of the mechanical SOTI model as calculated from the supersymmetric Berry curvature (10.36) depending on the staggered hopping γ/λ . Inset panels display eigenvalues ν_x of the edge Hamiltonian $\mathcal{H}_{x,\mathbf{k}}$ plotted against k_y in the topological ($\gamma/\lambda < 1$) and trivial ($\gamma/\lambda > 1$) phase. In each phase, the two bands acquire distinct Berry phases of $\theta_B = \pi$ or $\theta_B = 0$, respectively. Figure adapted from Ref. [P5].

bosonic equivalents of the fermion states read

$$|u_m(\mathbf{k})\rangle = \frac{\mathbf{R}(\mathbf{k})}{\sqrt{|\omega_m(\mathbf{k})|}} |v_m(\mathbf{k})\rangle \equiv \tilde{\mathbf{R}}(\mathbf{k}) |v_m(\mathbf{k})\rangle, \quad (10.35)$$

where a prefactor of $1/\sqrt{|\omega_m(\mathbf{k})|}$ is added to fulfill symplectic normalization in the real boson problem.

By inserting the SUSY mapping into Eq. (10.34) one can rewrite the fermionic Berry phase with bosonic states, thus defining a bosonic invariant with the same properties as the fermionic invariant.

$$\begin{aligned} \mathcal{A}_{SUSY} &= \langle v_m(\mathbf{k}) | i\tilde{\mathbf{R}}^\dagger \nabla_k (\tilde{\mathbf{R}} |v_n(\mathbf{k})\rangle) \\ &= \langle v_m(\mathbf{k}) | i\sigma_2 (\nabla_k + \sigma_2 \tilde{\mathbf{R}}^\dagger \nabla_k \tilde{\mathbf{R}}) |v_n(\mathbf{k})\rangle. \end{aligned} \quad (10.36)$$

In contrast to the conventional fermionic Berry curvature, this bosonic variant is extended by an additional covariant derivative term coming from the SUSY mapping. This additional term ensures that bosonic eigenstates which were found to be trivial under a conventional investigation can now have a non-trivial charge due to this additional term in the augmented definition.

Let us now turn towards applying this general formalism to the mechanical second order topological insulator at hand. Revealing the topology on the boson side can be done by constructing bosonic Wilson loop operators, which are defined from their fermionic

equivalents using the formalism of Eq. (10.36). These Wilson loop operators $\mathcal{W}_{x,\mathbf{k}}$ and $\mathcal{W}_{y,\mathbf{k}}$, defined along the k_x and k_y -directions respectively, define edge Hamiltonians $\mathcal{H}_{x,\mathbf{k}}$ and $\mathcal{H}_{y,\mathbf{k}}$ which also can be connected adiabatically to the effective edge Hamiltonian of the respective edges in the mechanical model.

As seen in the results depicted in Fig. 10.10, eigenfunctions in the phase $t_\gamma/t_\lambda < 1$ acquire a Berry phase of π , demonstrating that this phase is indeed the topological phase, proposed earlier by the existence of localized corner modes. In the other phase of $t_\gamma/t_\lambda > 1$, eigenfunctions of the edge Hamiltonians $\mathcal{H}_{x/y,\mathbf{k}}$ are found to possess a vanishing Berry phase, indicating that this is the trivial phase of the model. In total, the bosonic Berry phase can successfully demonstrate the existence of two topologically distinct phases in the mechanical model.

Note that a much more thorough discussion of the topological invariant with focus on the second order topological insulator can be found in the supplementary material of Ref. [P5], also discussing the formation of individual Wilson loop operators in depth. Here however, the bare possibility to define a topological charge through supersymmetry, revealing the non-trivial topology of the bosonic states, can be regarded as a proof of concept and possibility for further research.

10.5. Additional aspects

Having established a rigorous SUSY connection between a Majorana fermion model and a real boson model with a direct connection to classical topological mechanics, let us finally turn our attention to some last aspects that should be mentioned in this context. In the following part, both the negativity of the appearing spring constants as well as the influence of noise on the SUSY connection is discussed. Most of this discussion is according to the supplementary material of [P5], however enriched with additional figures.

10.5.1. Negative spring constants

Let us start by discussing the sign of spring constants in the topological mechanical model. As shown in Eq. (10.22) and Eq. (10.23), the spring constants are calculated from products and sums of fermionic hopping constants. Although in principle both on-site and intersite couplings are subject to sign changes, in particular the intersite springs come with an inherent additional minus sign $k_{ij} - t_{ij}t_{jk} < 0$. Especially in the example of the mechanical Kitaev model, one can show that there is no combination of signs on the hoppings t_μ such that there are no negative sign springs k_{ij} . All that goes to show that in principle one cannot hope to avoid negative sign springs in the mechanical models derived from the SUSY connection.

Springs with negative spring constants are however problematic in general. The potential energy of a spring is $V(l) \sim k(l - l_0)^2$ where l_0 is the rest length of the spring and l its

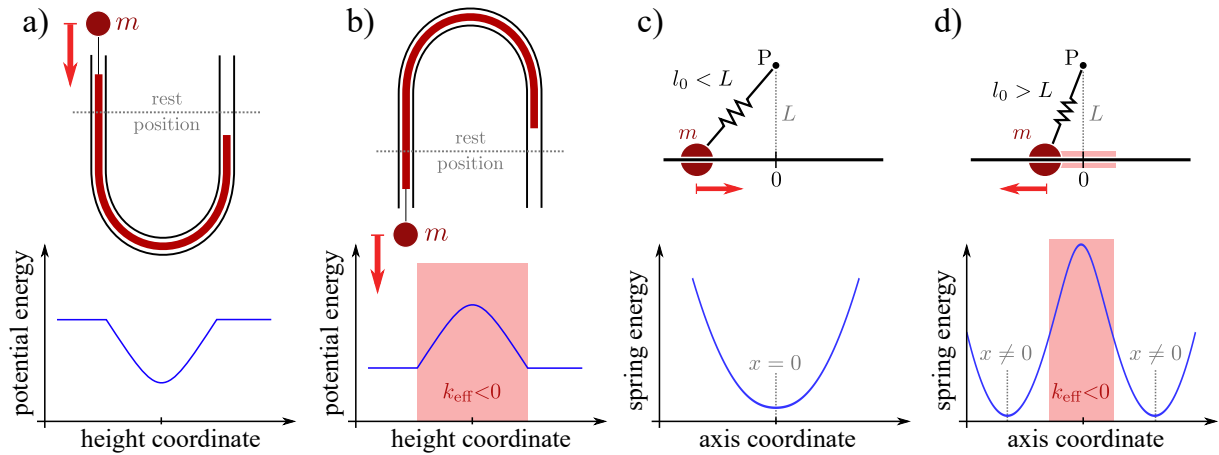


Figure 10.11.: Realizations of springs with negative spring constant - Two propositions on how to realize springs with a negative spring constant approximately, one using gravity (panels a,b) and one using conventional springs (panels c,d). Figures taken from supplementary material of [P5].

current length. For a positive k , this energy grows quadratic with l and therefore indicates that energy has to be invested to stretch the spring. However for a negative value of k , elongation of the spring gains energy indefinitely and accelerates the elongation even more the longer the spring is. This behavior for $k < 0$ is of course unphysical.

Since such unphysical negative sign springs cannot be found in nature, one has to engineer systems which behave like these negative sign springs *approximately*. Two of such examples will be laid out in the remainder of this part.

One possible realization of a negative spring constant uses gravity and is depicted in Fig. 10.11 a)+b). Here, a belt with some mass M is connected to the sample mass m and fed inside a U-shaped pipe. In the rest position of equal lengths of belt in the left and right part of the U-pipe, there is no force acting on the test mass m , however an imbalance between the belt segments creates a force on m . The orientation of the U-pipe, facing up or down, can now determine if this imbalance relaxes back or accelerates itself. Thus a downward facing U-pipe emulates the behavior of a negative sign spring constant for elongations that are comparable with the total belt length.

Another realization of a negative spring constant uses conventional springs and constraints, depicted in Fig. 10.11 c)+d). Here, a conventional spring with rest length l_0 is connected to the sample mass m and some point P . The sample mass can only move along a one-dimensional rod which is mounted in distance L to the point P . For a distance $L > l_0$, the overall force on the mass will point towards the shortest distance of the rod and P . However for a distance $L < l_0$, two energy minima emerge in equal distance to the now unstable rest position. Around this unstable point, the effective forces along the rod again emulate a spring with negative spring constant.

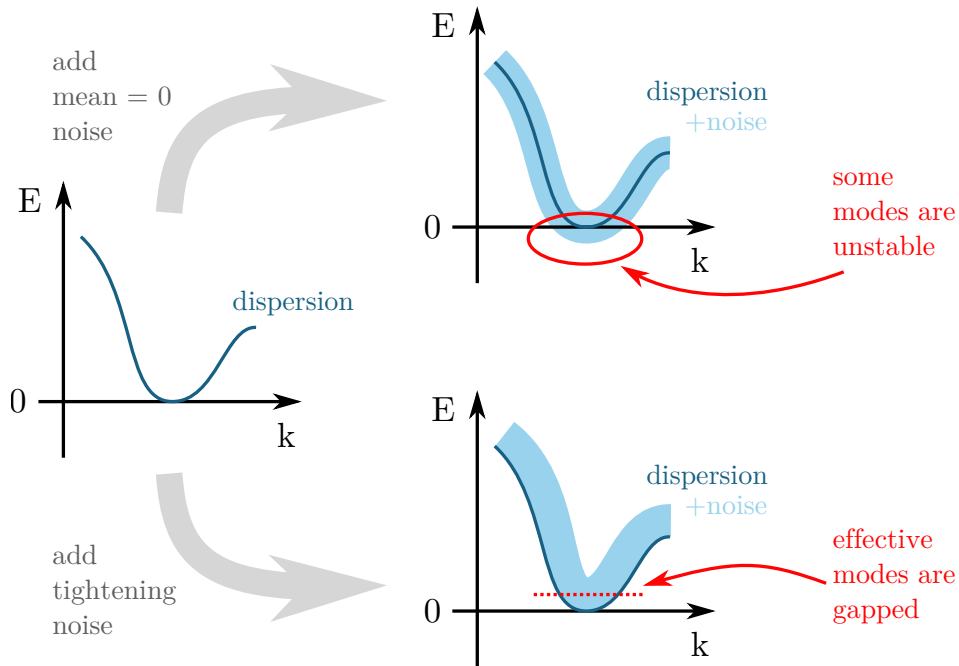


Figure 10.12.: Noise in SUSY mechanical model - General considerations regarding noise in the SUSY process. For any classical model, adding noise will randomize the energies of eigenmodes around the original dispersion. For a mode with zero energy and depending on the precise form of noise, this can either lead to the mode becoming unstable or the mode effectively gapping out to finite energy. Figure taken from supplementary material of [P5].

In principle, both approximations demonstrated in Fig. 10.11 have their own drawbacks and limitations. However, even the existence of such examples indicates that building such negative sign springs is in principle possible and remains to be solved in the respective practical implementations.

10.5.2. Noise

Another aspect worth discussing is the relevance of noise in the SUSY connection. In general, any topological feature is per definition robust to noise in the model. More precisely, topological gapless modes are protected against noise as long as the bulk gap does not close. Let us therefore not discuss the fermion side of noise but instead how noise enters the mechanical model and how it affects its dynamics and topology. Particular interest will be directed towards the topologically protected cornermode in the example of the mechanical SOTI.

In general, noise can enter the SUSY connection from different sources. Noise in the fermion model is well understood and can be translated by the SUSY connection directly

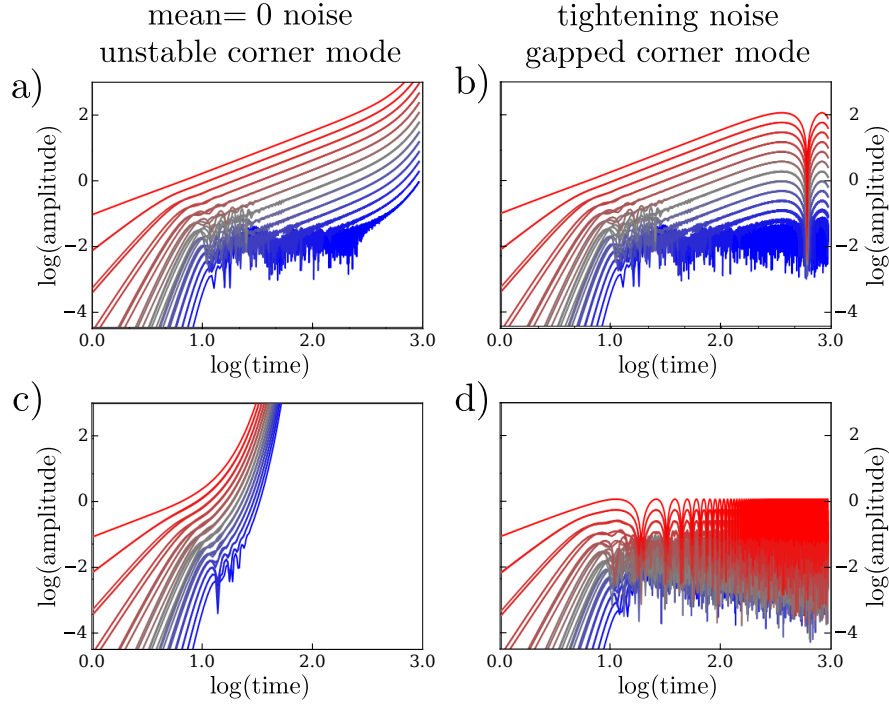


Figure 10.13.: Impact of noise in mechanical SOTI - Following the general considerations regarding noise in the SUSY process depicted in Fig. 10.12, two distinct forms of noise are implemented into the spring couplings of the mechanical SOTI. For noise which leaves the mean dispersion intact, depicted in panels a) and c), the corner mode is rendered unstable. For a form of noise which simultaneously lifts the mean dispersion away from zero energy, depicted in panels b) and d), this instability is not observed, however a finite periodicity of the mode can be observed, corresponding to a finite energy. Figure taken from supplementary material of [P5].

to a noise pattern of the bosonic and consequently of the mechanical model. Since SUSY is exact, as long as the fermion model retains its topology the boson and mechanical model will be topological as well.

Due to the way spring constants are inferred from the fermion model, any fermionic noise will result in noise fine-tuning on the mechanical side. Fine-tuned noise cannot be implemented experimentally, as springs will have natural errors in their constants which do not depend on each other. Therefore, the relevant question to investigate is: *What happens to the mechanical model, when there is noise that breaks SUSY?*

In any mechanical model, noise will broaden the spectrum of eigenmodes in energy, with details depending on the exact form of noise. This has minor consequences for anything at finite energy, however for modes at zero energy, there are direct consequences. Depending on the form of noise, the energies of eigenmodes can be altered in two different ways, depicted in Fig. 10.12. Noise can either lift the mean value of the dispersion which gives a

finite frequency to some previous zero-frequency modes or it can drive some of the modes to negative energies which will render them unstable.

Which of the two scenarios is implemented into a model depends on the choice of springs. If the spring constants only fluctuate with a certain amount, an instability cannot be avoided. If springs are also tightened so that they are less negative the spectrum can be gapped. Both scenarios can be implemented numerically into the classical mechanical simulations of the Kitaev model and SOTI alike.

In Fig. 10.14, the time evolution of the mechanical Kitaev model is shown under the influence of additional noise. One can observe that the tightened noise gaps out the zero-energy modes at the Dirac points whereas naively fluctuating spring constants lead to an unstable zero-energy mode that grows in amplitude indefinitely. Still, as Fig. 10.15 demonstrates, the spectrum itself is largely unaffected by the noise.

Similar results can also be obtained for the topologically protected cornermode in the mechanical SOTI. Results for the time evolution of the cornermode are shown in Fig. 10.12. They demonstrate once again that the cornermode does form in the SUSY-broken case of noisy springs independent of the form of noise. However, since noise in general will change the dynamics of the mechanical model in general, the cornermode is either rendered unstable or to a finite frequency.

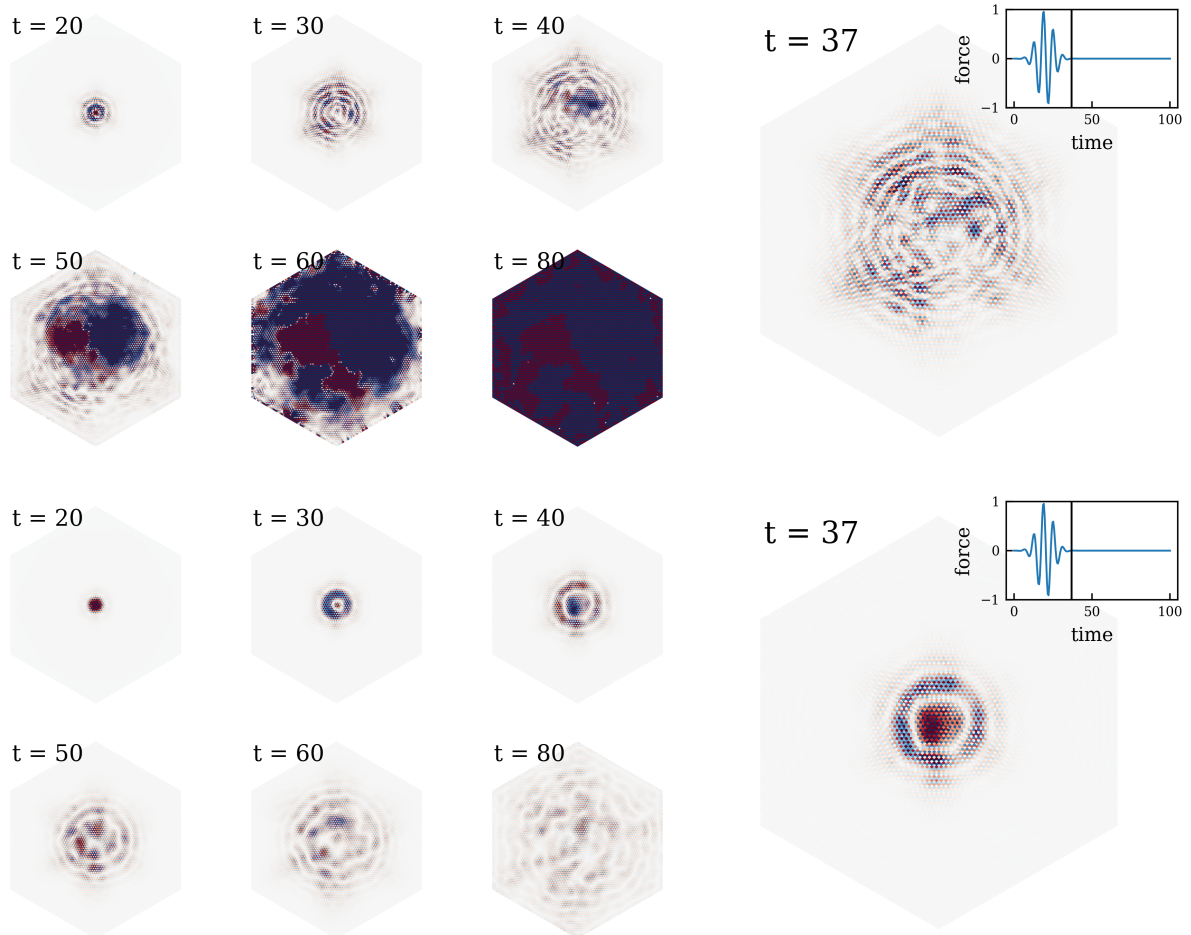


Figure 10.14.: Time evolution under noise in Classical Kitaev model - Snapshots at various times for a classical simulation of the balls-and-springs Kitaev model. Noise is included in all type of springs. Data shown here compares between random noise (upper panel) and tightening noise (lower panel) which drive the system unstable around the zero mode as well as gap the spectrum out respectively. Data can in principle be compared to the time evolution shown in Fig. 10.2.

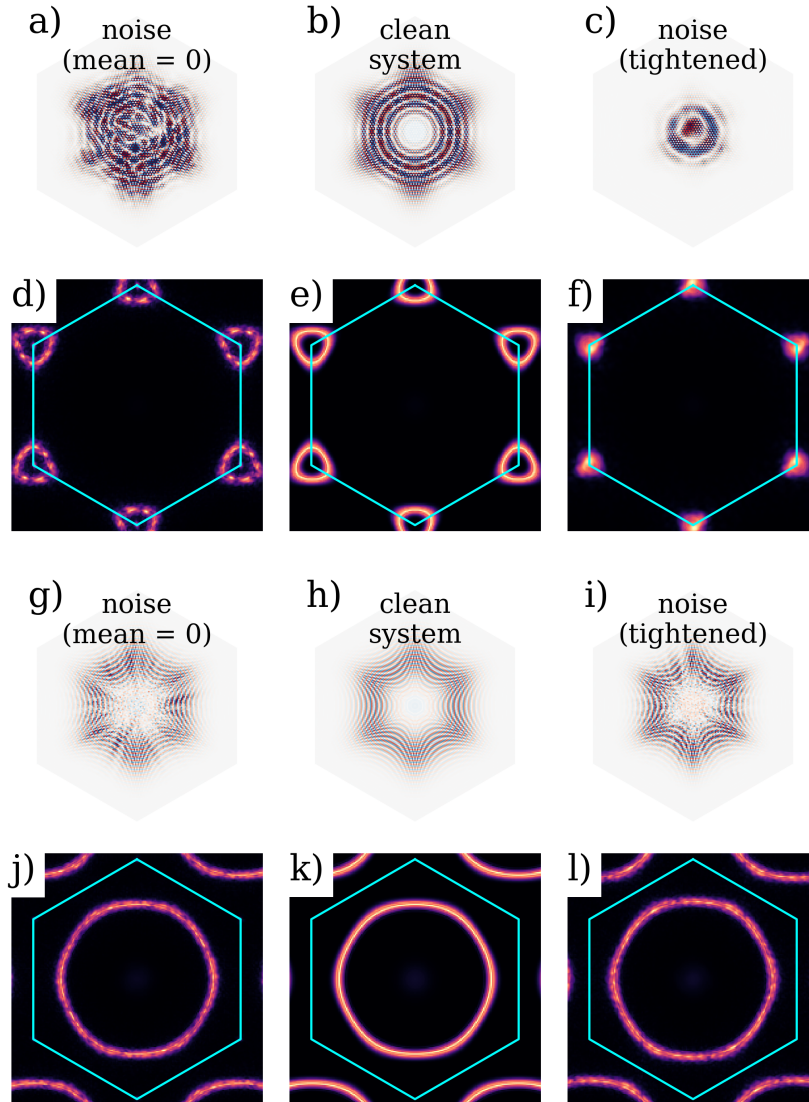


Figure 10.15.: Frequency dependent impact of noise in Classical Kitaev model - Snapshots after finite time evolution for classical simulation of the balls-and-springs Kitaev model under drives of different frequencies. Noise is included in all type of springs. Data shown here compares between random noise with zero mean (left column, panels a),d),g),j)), clean system with no noise (center column, panels b),e),h),k)) and tightening noise (right column, panels c),f),i),l)). Frequency changes between top panels a)-f) ($f = 1$) and bottom panels g)-l) ($f = 3$). Gapping out and increasing weight on the zero mode (around the K point) can be observed in the Fourier transforms. For higher frequencies, the differences between the noise profiles vanish as noise has less effect on these regions of the spectrum.

11. Beyond supersymmetry: Fermions and spin spirals

In this chapter, let us discuss some earlier work from Ref. [P6] which utilizes a different form of linking to bring a classical spin model into correspondence with a quantum fermion model. Although this work is not directly formulated as supersymmetry, its lattice identification laid the groundwork for the supersymmetric identification in later papers [P4, P5].

The chapter is organized as follows. First, classical spin models are reviewed from the perspective of Luttinger Tisza calculations which offer a method of obtaining classical ground states similar to bandstructure calculations. Then, Luttinger Tisza is actually brought into correspondence with bandstructure calculations by choosing suitable models linked by a lattice construction. This allows constructing models of matching ground states. Finally, some examples are given and the link to the supersymmetric language of this part is emphasized.

11.1. Classical spin-spiral ground states

Classical spin models often are the first steps in the search for exotic phases of quantum spin systems. Although these classical counterparts do not contain all of the quantum behavior, they can be a good starting point for many investigations and rule out certain parameter regions entirely. In principle, there are different types of classical spins, however here let us concentrate on the so called *Heisenberg spins* which can be described by 3-component vectors $\vec{S} = (S^x, S^y, S^z)$. According Hamiltonians are of the form

$$H_{\text{Heisenberg}} = \sum_{ij} M_{ij} \vec{S}_i \cdot \vec{S}_j \quad (11.1)$$

and in particular their ground states are of interest for further analyses. Although many classical Heisenberg models only have one unique ground state, there are others exhibiting (macroscopically) degenerate ground states. Specifically these extensive degenerate states are good candidates in a consecutive search for quantum spin liquids and exotic states of matter.

Only few Heisenberg models bare an analytic estimate on their ground state, so often a (partial) numerical solution has to be performed. There are many methods available,

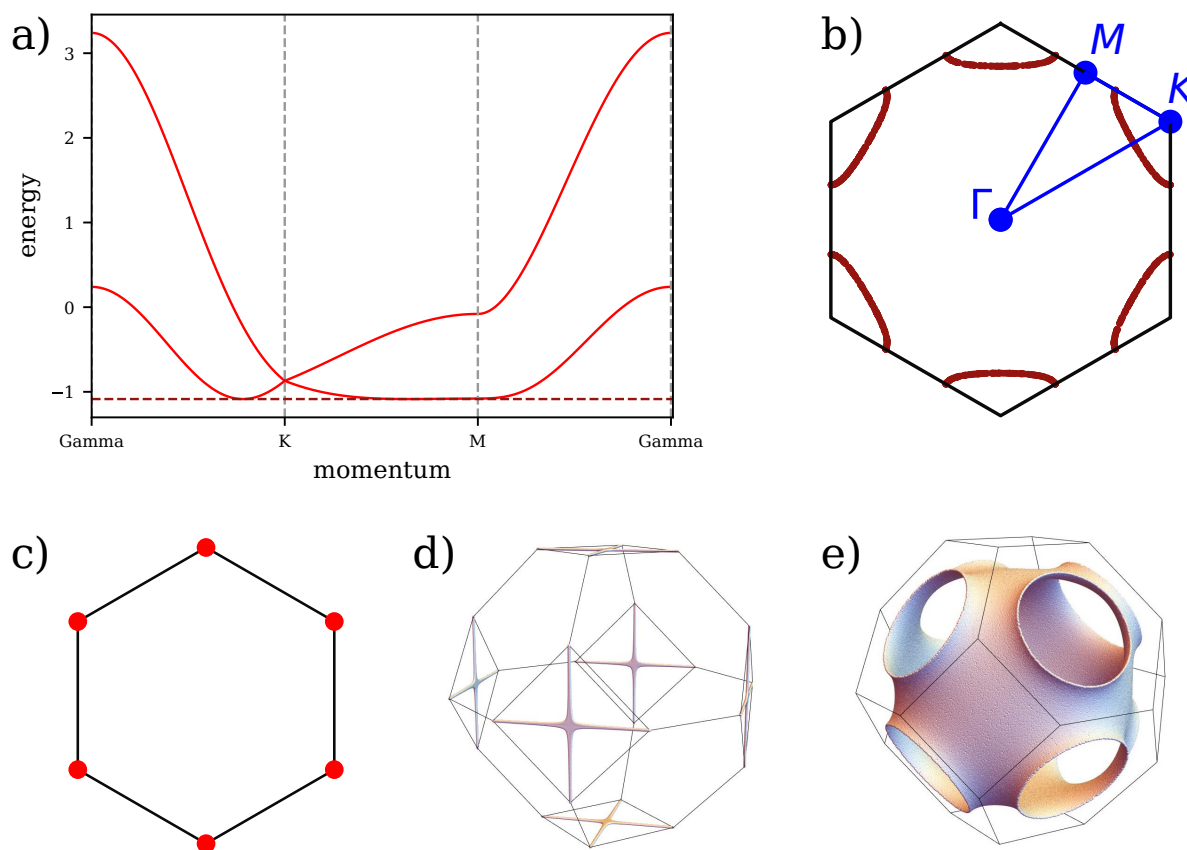


Figure 11.1.: Ground state manifolds of spin spiral models – Panels a) and b) illustrate the Luttinger Tisza method. Conceptually, a bandstructure of the spin system is calculated, c.f. panel a), and its minima are then investigated within the first Brillouin zone, c.f. panel b). Similar results can also be obtained from other methods which investigate the spin spiral states directly. Panels c)-e) show the ground state manifolds of spin spirals in different lattice geometries. Panel c) shows the 120° order on the triangular lattice, panel d) shows ground state spiral surfaces on the fcc lattice which form one-dimensional lines, panel e) shows the spin-spiral surfaces on the diamond lattice. Plots a) and b) are directly obtained from LatticePhysics.jl, panels c)-e) are reproduced from Ref. [P6].

working on finite systems with different boundary conditions however here, let us focus on the Luttinger Tisza method. This particular method bears great resemblance to a band structure calculation. The Luttinger Tisza method is based around the assumption that the ground state can be written as a coplanar spin spiral with the same unitcell as the underlying lattice. Note that of course not all classical spin ground states can be characterized in this way, however Heisenberg models have a tendency to form these coplanar spiral states in their ground state.

To emphasize the similarities of the Luttinger Tisza method with ordinary band structure calculations, let us briefly discuss its main steps. Starting with the Heisenberg Hamiltonian of Eq. (11.1), one first performs a Fourier transform to momentum space. This transforms the Hamiltonian as

$$\sum_{ij} M_{ij} \vec{S}_i \cdot \vec{S}_j \quad \rightarrow \quad \sum_{\vec{k}} \sum_{ij} \tilde{M}_{ij} \vec{S}_{\vec{k},i} \cdot \vec{S}_{\vec{k},j} e^{i\vec{k} \cdot \vec{\delta}_{ij}} \quad (11.2)$$

where \tilde{M}_{ij} now only describes the connectivity within a single unitcell. Summation over \vec{k} indicates that the Fourier transform decomposed the Hamiltonian into a block structure in which individual blocks for separate \vec{k} can be treated separately. The minimal energy of the model, which is needed as the ground state, can be found by consecutively diagonalizing the interaction matrices

$$\mathbf{M}(\vec{k}) = e^{i\vec{k} \cdot \vec{\delta}_{ij}} \tilde{M}_{ij} \quad (11.3)$$

in every block and looking for minimal eigenvalues both within the block as well as across different \vec{k} . Conceptually, Fig. 11.1 a)-b) illustrates the process of constructing a bandstructure and resulting spin-spirals surface. Having found a minimal energy eigenvalue, one can construct a coplanar spin spiral solution. The wavevector of this spin spiral is given by the momentum \vec{k} of the minimal energy eigenstate. The phases of individual spins within the basis are then given by the components of the eigenstate itself. Conceptually, Fig. 11.1 a)-b) illustrates the process of constructing a bandstructure and resulting spin-spirals surface.

Note that a solution found in this way is only valid as long as the so-called *hard spin constraint* is fulfilled. This constraint demands spins on each site having equal length. In many cases, this constraint will select a subset of states found by the minimization, however in some systems like Heisenberg models on Bravais lattices the constraint is also generically fulfilled. Note also that spin-spiral solutions are not unique to the context of Heisenberg models or Luttinger Tisza calculations, but can similarly be found in systems exhibiting spin-interactions of higher order [P7].

11.2. Lattice construction to free fermion models

In principle the diagonalization of $\mathbf{M}(\vec{k})$ yields a band structure similar to electronic band structures when shown in dependence on \vec{k} . Furthermore, the search for a specific (minimal) energy resembles the search for a Fermi energy and the corresponding states resemble the Fermi surface in electronic models, as seen in panels c)-e) of Fig. 11.1. These similarities might facilitate the idea of linking both calculations and being able to construct corresponding models with respective ground state manifolds or Fermi surfaces alike.

Linking Luttinger Tisza and ordinary band structure calculations revolves around linking the elementary interaction matrices in momentum space. Where the core of band structure calculation is to find eigenvalues of the momentum space hopping Hamiltonian $\mathbf{H}(\vec{k}) = \tilde{t}_{ij} e^{i\vec{k}\cdot\vec{\delta}_{ij}}$, Luttinger Tisza searches for eigenvalues of the spin interaction matrix $\mathbf{M}(\vec{k}) = \tilde{M}_{ij} e^{i\vec{k}\cdot\vec{\delta}_{ij}}$. The striking visual similarity of the two might tempt one to simply associate a spin-interaction M_{ij} with every hopping t_{ij} , however the correspondence is more subtle. In principle, the energies of interest in the two methods are vastly different. Whereas Luttinger Tisza is searching for *minimal* eigenvalues, ordinary electronic calculations search for eigenvalues in the middle of the spectrum, which can be shifted by the Fermi energy to be at $E = 0$.

The conceptual main idea is now to *square* the hopping matrix which moves all states to positive energies and makes the $E = 0$ Fermi surface states the lowest energy states of the matrix. The resulting squared matrix can now be compared to the spin interaction matrix. Similarly, the square-root of the spin interaction matrix yields a fitting matrix whose mid-energy states are given by the former ground state and can thus can yield a suitable hopping model.

On the level of underlying models, the process of squaring or taking the square-root can be understood in terms of the lattice connectivity. Squaring of the hopping matrix corresponds to chained hoppings, i.e. the next-nearest neighbors in terms of the graph connectivity. Similarly, going the other way from a spin to a fermion system, revolves around inserting new sites such that the next-nearest neighbor connectivity matches that of the original spin system.

In Ref. [P6], most of these steps have already been conceptualized for bipartite fermion systems. In such lattices, hopping only between different sublattices ensures a decomposition into independent systems when taking next-nearest neighbors which becomes an important aspect when constructing a lattice-based algorithm to ensure the inverse direction. In Ref. [P6], it was proposed to substitute the fully connected plaquettes of a spin lattice by newly added z -coordinated sites to go to a corresponding fermion lattice. This construction naturally added the missing sublattice of the bipartite fermion lattice and ensured a systematic procedure that generates corresponding systems of matching Fermi surface and spin spiral ground state manifold.

11.3. Lattice construction vs. supersymmetry

Of course having discussed the supersymmetry construction of this part at length, the key features in the spin-fermion correspondence, i.e. squaring of matrices, next-nearest neighbor lattices, bipartite systems decomposing into two independent subsystems, bare a striking resemblance to supersymmetry. In fact, much of the graph-based algorithms of this entire SUSY part as well as in Ref. [P4, P5] have been influenced by the lattice construction outlined in Ref. [P6]. However, let us look in greater detail at some aspects of how supersymmetry enters the spin-fermion correspondence.

The essence of supersymmetry is to link a fermion system to an isospectral boson system with the help of a new object called supersymmetric charge which essentially is squared to decompose into the respective boson and fermion systems. This triagonal relation between two systems and the SUSY charge is also reflected in the spin-fermion correspondence, where two individual spin systems are connected to a bipartite fermion system which decomposes into the two spin systems upon squaring. Especially the supersymmetric examples in section 9 about complex fermions and bosons look very similar to the spin-fermion examples outlined in Ref. [P6]. This resemblance of lattices is not coincidental as both the supersymmetric charge for complex bosons as well as the fermion model in the spin-fermion correspondence are represented as bipartite graphs. These bipartite graphs decompose into boson-/fermion-subsystems and two spin subsystems under squaring, i.e. taking the next nearest neighbors.

The concept of next-nearest neighbors also enters section 10 about Majorana fermions in which one of the sublattices of a bipartite Majorana fermion system hosts real bosons. Here, squaring is required by the particular form of supersymmetric charge, which again uses a bipartite graph to connect bosonic and fermionic degrees of freedom on different sublattices.

Finally, the concept of flat bands in the occurring systems is of great interest for many reasons. In supersymmetry, flat bands can naturally occur due to a non-zero Witten index which is graphically reflected in a mismatch between number of sites in the boson and fermion sublattices of the bipartite SUSY charge graph. Such flat bands will always emerge at the band bottom of one of the two systems. In the spin-fermion correspondence, flat bands also emerge for the individual spin systems due to similar reasons. However, in Luttinger Tisza calculations, such bands are often found to violate the hard-spin constraint, i.e. they do not contribute meaningful spin spiral states. It is only in some examples like the Kagome antiferromagnet where these bands do carry physical states and contribute an extensive ground state degeneracy.

All in all, the spin-fermion correspondence bares great resemblance to the graph-based supersymmetry connections outlined in this chapter. Although the spin-fermion correspondence is focusing on relating ground states whereas the supersymmetry construction aims at providing isospectrality, the underlying motifs agree to a large extent. Especially the process of squaring and taking next-nearest neighbors are rooted deep in the graph

language of interaction matrices and thus will reappear in different situations.

11.4. Examples

Let us also discuss some examples of the spin-fermion correspondence for better illustration. In principle, Ref. [P6] contains an extensive list of different examples which will be also briefly summarized in the following. Generically, every example comes with either a well-known spin or fermion system which will be linked to a lesser known system of the other kind.

The most prominent example of the spin-fermion correspondence is probably linking the Dirac points in graphene to the 120° order in triangular Heisenberg antiferromagnets [P6]. Here, the bipartite fermion system is a model of free electrons (or even spinless fermions) hopping on the honeycomb lattice. It is well-known that this simple hopping system exhibits two Dirac points, i.e. a Fermi surface which is zero-dimensional, and has a linear band dispersion around it. Squaring this model in the context of the spin-fermion correspondence links it to Heisenberg spins on one of its two triangular sublattices. These triangular lattice antiferromagnets have been studied independently as well. It was found that the ground state can be characterized by a series of spin-spiral states in which neighboring spins enclose an angle of 120° , hence the name 120° order. This order can be seen in Fig. 11.2 a). The wavevectors of these 120° spin spirals coincide exactly with the Dirac points in the honeycomb dispersion, as it is expected from the spin-fermion correspondence, thus linking the two systems. Even beyond the limit of isotropic couplings, a rigorous connection between spin-spiral states and Dirac cones can be drawn. Panels b)-d) of Fig. 11.2 therefore show the evolution of spin-spiral states from isotropic coupling to the limit of Dirac cones merging. This limit corresponds to the onset of Neel-order in the antiferromagnet.

Even beyond the pure ground state correspondence between the triangular antiferromagnet and the fermions on the honeycomb lattice, the spectral properties between the models can be compared. Where the honeycomb dispersion shows linear behavior in the vicinity of the Dirac points, the Luttinger Tisza spectrum shows a quadratic band behavior near its minimum. Although remarkable, this is however unphysical. Since the Luttinger Tisza spectrum describes spin spiral states, it is unsuited for describing the actual thermal excitations that occur in antiferromagnets as those are described by single spin reorientations or flips. Nevertheless, the spectral correspondence once again underlines the origin of the spin-fermion mapping.

Another interesting example of the spin-fermion correspondence concerns the formation of flat bands when squaring a fermion system with differently sized sublattices. In this regard, Heisenberg spins on the honeycomb lattice can be mapped to free fermions on the honeycomb-X lattice [P6], which is a honeycomb lattice with additional sites on every bond. Upon squaring, this fermion system corresponds to both the original spins on the

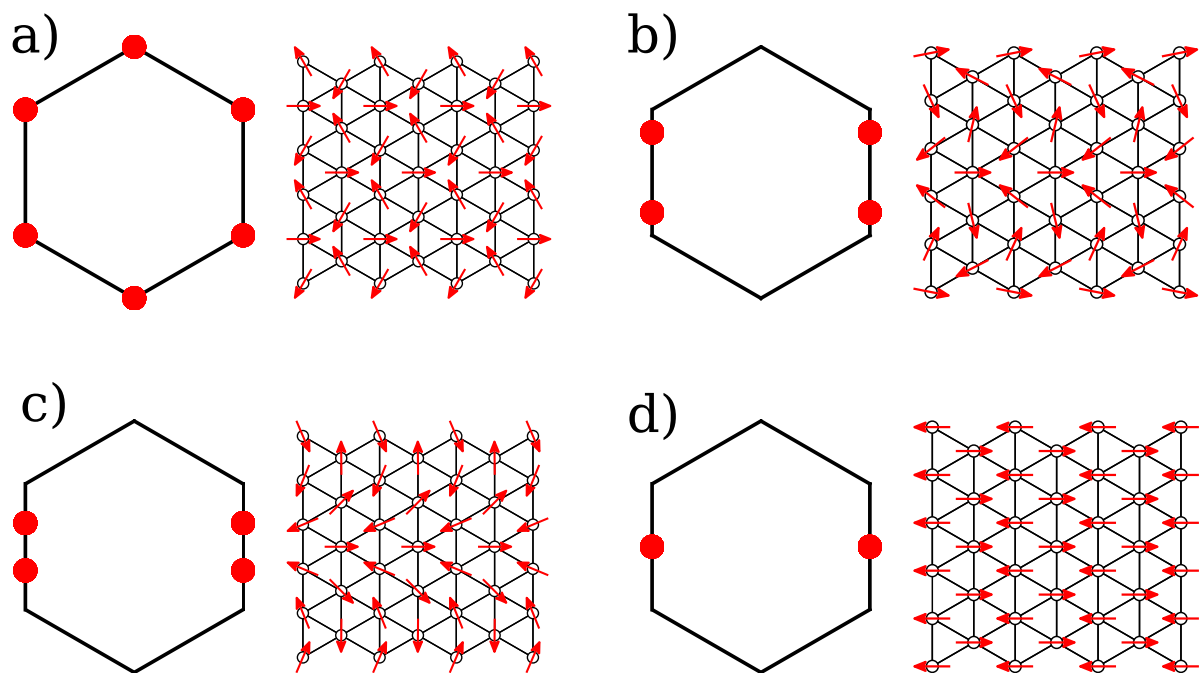


Figure 11.2.: Triangular lattice 120° order – Panels a)-d) show the evolution of the 120° order on the triangular lattice upon decreasing vertical couplings. Momenta describing this tilted order move on the edge of the Brillouin zone and can be linked to the Dirac points merging in the corresponding honeycomb model. Figure adapted from Ref. [P6].

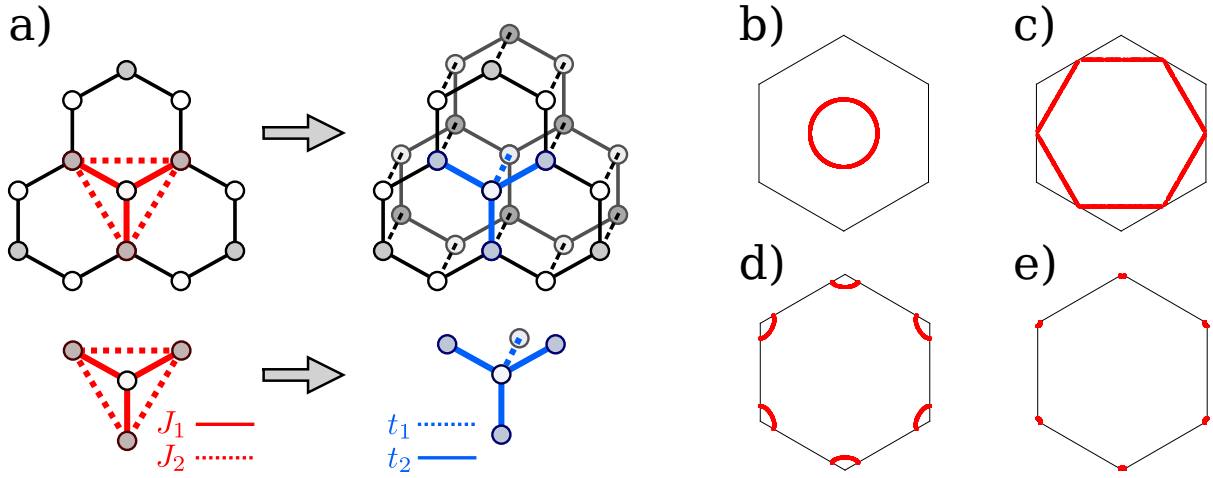


Figure 11.3.: Mapping J_1 - J_2 Heisenberg models to free fermions – Panel a) illustrates the relation of J_1 - J_2 Heisenberg models on bipartite lattices to bilayer free-fermion models on the same lattice. The connection is drawn by replacing plaquettes which are spanned from J_1 and J_2 . Additional sites can be rearranged to form a second layer. Panels b)-e) show the progression of spin-spiral ground state manifolds upon increase of J_2 , emerging from the Γ point in panel b) and merging into the K points in panel e) for large J_2 . Figure adapted from Ref. [P6].

honeycomb as well as additionally spins on the Kagome lattice. The mapping procedure guarantees that the spin models on honeycomb and Kagome are isospectral albeit with an additional flat band in the Kagome which comes from its larger unitcell and is actually physical.

Coming from the perspective of classical spin models, the class of J_1 - J_2 Heisenberg models host many promising candidate systems with already classically degenerate ground state manifolds. Especially the J_1 - J_2 Heisenberg models on honeycomb and diamond lattice have been shown to exhibit spin-spiral manifolds with sub-extensive degeneracies. It can be shown generically with the spin-fermion correspondence, that ground states of any J_1 - J_2 Heisenberg model on a bipartite lattice, where J_2 strictly describes interactions between next-nearest neighbors defined by bond distance, can be mapped on the Fermi surface of a bilayer nearest-neighbor free fermion model, as demonstrated in Fig. 11.3 a). This is in particular interesting as these fermion models can also be rephrased in single-layer spinful fermions with additional spin-flip terms on every site. The spin interaction ratio J_2/J_1 would then be reflected in the ratio between intersite hopping and on-site spin-flip in the fermion model. Such fermion models are also generically expected to show a sub-extensive Fermi surface which might yet be another interesting perspective on why the corresponding spin models exhibit a degenerate ground state manifold.

A final set of examples concerns the precise numerical parameters in spin models. It was already shown in Ref. [P6], that for the case of bipartite J_1 - J_2 Heisenberg models, the

parametric transition from antiferromagnetism to spin-spiral order can be determined only based on properties of the mapping to a fermion bilayer system. Moreover, since the spin-fermion correspondence connects the spin ground state to the fermion Fermi surface, the exact ground state energy of the spin-spiral state can also be explicitly given only based on investigation of the underlying lattice structure.

In other classes of models, some parameter combinations allow for particular choices of plaquettes that could not have been identified for other parameters. This is particularly important for the J_1 - J_2 Heisenberg model on the square lattice where J_2 denotes the diagonals through square plaquettes. Since here J_2 does not describe next-nearest neighbors by bond-distance, the model does not fall in the aforementioned category. However at the parametrical value of $J_2 = J_1/2$, each nearest neighbor bond can be split into two of half the coupling strength and every existing fully connected square plaquette can be replaced entirely. This replacement only works for $J_2 = J_1/2$, thus leading to a qualitative difference in behavior between $J_2 = J_1/2$ and other parameters.

A very similar explanation can also be facilitated for the emerging classical J_1 - J_2 - K model on the fcc lattice in Ref. [P1]. This reference has already been discussed in the context of RIXS for probing the underlying electronic degrees of freedom. However, in the context of spin systems there is yet another aspect worth noting. In this paper, the electronic structure allows for an effective description in pseudospin $j = 1/2$ moments which interact with both Heisenberg and Kitaev terms on the underlying fcc lattice. It was shown that the classical limit of this model in the $K = 0$ limit (i.e. pure Heisenberg interactions), the parameter combination $J_2 = J_1/2$ facilitates an extensive ground state degeneracy which is absent for smaller or larger values of J_2 . From the perspective of the spin-fermion correspondence, this point is again singular. Only for $J_2 = J_1/2$ one can replace checkerboard plaquettes spanned by J_1 and J_2 in the underlying fcc lattice by newly added 4-coordinated sites to form a fermion lattice.

Both these parametrical examples go along to show that even beyond mapping a well-known model to another one, the spin-fermion correspondence can be used to explain certain qualitative changes in model behavior.

12. Summary and discussion

In this part, the role of graph theory in formulating supersymmetry has been discussed. Fundamentally, this was understood as bringing the SUSY concept of relating boson to fermion models in correspondence with the formulation of matrices as adjacency matrices of graphs. Throughout the chapters, various examples of this correspondence have been discussed, including isospectral complex fermion and complex boson lattice models, Majorana fermion models which are isospectral classical mechanical systems as well as connections to other mappings such as spin spirals to fermions. Overall, the impact of graph theory allowed a direct formulation of SUSY through the use of interaction graphs, having a broad range of implications ranging even to the definition of topological invariants for bosonic systems.

In the first part, a complex fermion to complex boson mapping has been discussed. A particular focus was put on the isospectrality between models on sublattices of a bipartite lattice which have been interpreted as boson and fermion models. The bipartite lattice played the role of the supersymmetric charge. Numerous example systems in both two and three spatial dimensions showed the persistence of isospectrality and the reliability of the graph-based construction when defining corresponding models or the SUSY charge.

Furthermore, the concept of the Witten index, known from supersymmetry, was brought into the graph language. Already in basic supersymmetry, the number of flat bands at the bottom of either the fermion or boson spectrum is equal to the Witten index. Brought into the context of graph language, the Witten index can be interpreted as the mismatch between basis sizes in the two sublattices, therefore allowing to determine the number of zero modes in the system from a geometric property alone.

The second example demonstrating the graph-theory assisted SUSY connection concerned Majorana fermion models. These systems could be connected to real boson models which in return could be rephrased as classical mechanical systems. Whereas previously, both the fermion and the boson model were defined on sublattices of the bipartite SUSY charge graph, in this context the Majorana model occupied a bipartite lattice graph and the corresponding mechanical model one of its sublattices.

The first incarnation of a Majorana model being implemented into a classical model was performed on the well-known Kitaev model, famous for hosting an analytically solvable spin liquid ground state. Although being defined as a spin model, Majorana fermions come into play when fractionalizing the spins into Majorana fermion and gauge field, both being defined on a honeycomb lattice. The mechanical version then describes balls and

springs on a triangular lattice with spring constants on-site and between sites. Emerging wavepatterns under periodic drive could be observed when numerically solving the classical equations of motion and were observed to be dependent on the drive frequency. This led to the numerical measurement of mechanical spectra which agree remarkably well with their Majorana fermion counterparts.

A second incarnation mapped the famous quadrupolar insulator of Bernevig and Hughes, a prime example for a second order topological insulator (SOTI), to a mechanical model which again was found to exhibit mechanical spectra agreeing with their Majorana fermion counterpart. Additionally, a zero-frequency mode with topological origin could be observed. This mode showed corner-localization as expected for the topological mode of a SOTI and agreed well to the states predicted by the Majorana model. Moreover, SUSY allowed the definition of a non-trivial topological invariant in the mechanical model, demonstrating its topology and extending conventional definitions of topological invariants by an additional SUSY term.

As a final example showing the impact of graph-theory on supersymmetry, the mapping between spin spiral states and free fermion systems has been discussed. In this case, a lattice construction allowed to relate ground states of spin spirals and Fermi surfaces of free fermion systems. This lattice construction is identical to the one used in the supersymmetric graph construction and therefore could be identified as having connections to supersymmetry. In principle, incarnations of this mapping bear a remarkable similarity to the complex boson systems, however with the change that the SUSY charge is the fermion model and the SUSY partner systems are the two spin models.

All in all, geometric graph language has been proven helpful in discussing supersymmetry through these examples. Many of these examples have only been possible because of the graph interpretation underlying the SUSY language. However, there are also aspects that needed additional discussion. Most prominently, conserving supersymmetry often demands a fine-tuning of couplings in the individual systems, imposing additional constraints on them.

In the case of complex boson, this fine-tuning manifests itself in only mapping between large systems for very fine-tuned cases of hopping parameters. Even small changes in individual hoppings could sometimes render the mapping impossible, therefore making a qualitative change in the SUSY partner system. In particular for the closely related case of spin-spiral states, the qualitative change in behavior could be interpreted as a change in ground state structure, coinciding with a phase-transition in the ground state phase diagram.

For the case of Majorana fermions, fine-tuning meant precise tuning of mechanical spring constants. As this is of course experimentally not possible, one can only conclude that supersymmetry is not present in a true experiment. However, the isospectrality and correspondence between individual (topological) states still was found to be preserved on average, yielding either gapped or unstable features as a result of SUSY-breaking noise.

Through all those examples, a recurring theme of special fine-tuning have been lattice boundaries. Whereas a bulk graph correspondence with SUSY would relate bulk parameters to the bulk connectivity of the lattice, connectivities are usually different at the boundary. Therefore one naturally encounters modified parameters at the boundary to ensure a conservation of supersymmetry, which was particularly important in the case of topological mechanics and finite systems.

In total, many systems have been explored in the context of this chapter. Apart from simply extending this list of examples, there are also some fundamental open questions. For example, it is currently unclear if there is a better incarnation of the real boson systems than the one laid out in the topological mechanics section. Also, the possibility of defining topological invariants hints at the question if one can also *measure* these quantities in an experiment.

Last but not least, it is also unclear if one can extend the graph-based SUSY framework beyond a single particle to interacting systems. A basis for such an analysis would be to identify graph structures that correspond to four-particles terms like $\sum_{ij} \hat{n}_i \hat{n}_j$ where $\hat{n}_i = c_i^\dagger c_j$ or even $\sum_{ijkl} c_i^\dagger c_j^\dagger c_k c_l$. This would naturally lead to fascinating questions regarding the implementations of more than a single Majorana fermion in a classical system with implications not only on a fundamental level but also for practical applications such as quantum computing.

Part III.

Universal Features of Moiré Bandstructures

13. Introduction

In the quest for materials with new and exciting properties, the synthesis of a true isolated *two-dimensional material* was long believed to be most challenging as any buckling in its third dimension would inherently lead to it clumping and collapsing. Naturally, interest in two-dimensional materials exploded upon the first successful isolation of *graphene* by Andre Geim and Konstantin Novoselov, achieved by exfoliating individual layers from bulk graphite [66]. These first samples allowed for experimental confirmation [67] of long-standing theoretical proposals on electronic properties in two-dimensional honeycomb materials, such as a bandstructure exhibiting Dirac cones with linear dispersion in which emergent quasi-particles behave quasi-relativistically [67]. For their advances in the synthesis and investigation of graphene as the first two-dimensional material, Geim and Novoselov were ultimately awarded the 2010 Nobel prize in physics [77].

Following the success of single-layer graphene, honeycomb structures today have become of general interest in other systems like molecular graphene [78], different elemental analogues of graphene [79] as well as optical lattices and cold atoms [80]. Similarly, exfoliation techniques beyond graphene nowadays produced an entire zoo of two-dimensional materials [81]. Alongside the growing number of different materials, more and more mechanical manipulation techniques for two-dimensional materials were established, including straining [82], stacking [83, 84], and twisting [83–86] of individual two-dimensional sheets.

With the invention of scanning tunneling microscopy (STM) it had also been recognized that *Moiré effects* appear in the study of two-dimensional materials. In general such effects arise from a mismatch of two periodic structures leading to an additional periodicity with a large wavelength. A demonstration of the Moiré effect can be seen in Fig. 13.1 a). Moiré effects are quite common in nature and occur naturally in surface science when materials have different lattice constants or a mismatch in orientation. First thought of primarily as cosmetic effects, Moiré patterns were e.g. found on graphite surfaces [87]. In the context of pure graphene, Moiré effects have been known to occur when graphene is grown by chemical vapor decomposition (CVD) on a substrate like Iridium [88]. Since this method yields very clean graphene sheets [89], large-scale Moiré patterns can be observed by STM, forming between the graphene lattice and the underlying Ir[111] surface [90].

Only within the last decade it was realized that twisting and the Moiré effect can substantially alter the electronic properties as well [84]. A first proposal by Bistritzer and MacDonald to find anomalously flat bands in sheets of graphene twisted by a precise angle [91] raised further interest in investigating such twisted materials. The bands can be found at half filling of the band structures and are displayed in Fig. 13.1 b). Flat band systems

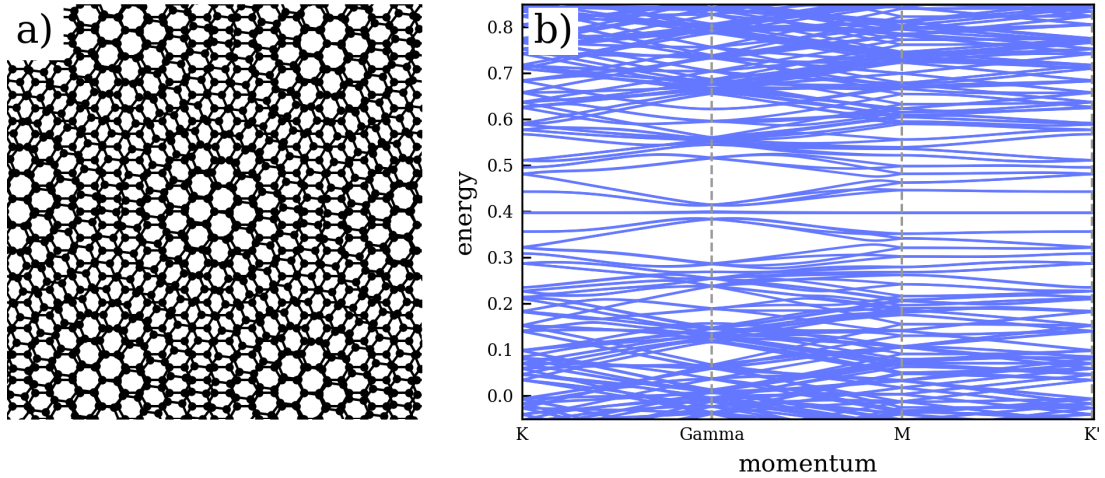


Figure 13.1.: Example of a Moiré system with bandstructure - a) Sketch of twisted bilayer graphene as an example for a Moiré system. Two sheets of graphene are stacked and then rigidly twisted with respect to each other. Panel b) shows the band structure for such a twisted bilayer system tuned to the magic twist angle of $\theta \approx 1.1^\circ$. Note that to better illustrate the Moiré pattern in panel a), the twist angle in the sketch of panel a) is $\theta \approx 7.3^\circ$, which is much larger than the magic angle yielding the bandstructure of panel b).

are of general interest for topics of strongly correlated matter since tuning the narrow bandwidth allows controlling how dominant interaction effects between quasi-particles are compared to the kinetic energy within the bands. Such interaction-dominated or strongly-correlated behavior provides the basis for many modern phenomena in physics like, e.g., the fractional quantum Hall effect [92, 93], Mott insulators and superconductivity. Whereas correlated states generally exhibit a tantalizing complexity [94], *twisted bilayer graphene* seemed to offer an accessible platform for systematically finding and investigating such states.

The interest in twisted bilayer graphene exploded when advances in material fabrication [83] enabled the first experiments [95, 96] revealing a plethora of correlated phases that bear remarkable similarities to high-temperature superconductivity in cuprate systems [97]. Similar to cuprates, a change in doping allows the system to pass through a sequence of exotic phases in which superconducting phases are in close proximity to Mott-like insulating phases. Remarkably, the superconductivity resembles the high- T_C superconductivity found in cuprates as T_C/T_F is close to other high- T_C systems and the superconductivity itself occurs close to the metal-insulator transitions [97]. Furthermore, linear-in-T resistivity measurements suggest the existence of strange metal phases above the superconducting domes, again similar to high- T_C cuprates [98]. While the results are strikingly similar, twisted bilayer graphene offers a much more accessible platform for experiments as no

chemical alteration of the sample is required to measure different doping levels and doping can be achieved by gating.

Altogether, these findings promoted increasing interest in strongly correlated topics from engineering two-dimensional materials with designed band structures [99–105], enabling the observation of various strong correlation effects [106–109]. With this ever-growing interest, more and more materials are currently under investigation, ranging from twisted double bilayer graphene [110–113], via trilayer graphene [114, 115] all the way to hexagonal boron nitride [116, 117] and twisted bilayer transition metal dichalcogenides [118–120] as well as other even more exotic candidates [121, 122].

Within the field of *Moiré materials*, this part, which is based on Ref. [P8], aims at providing a unifying approach to describing flat band Moiré systems. As the Moiré pattern generically covers large regions in real space, bandstructures of such Moiré systems, as shown exemplarily in Fig. 13.1 b), include a plethora of typically $\mathcal{O}(10^3)$ bands. Under close investigation of such bandstructures, one finds both regions of stiff band crossings as well as regions of band avoidances. The statistic of such band avoidances is a quantity often explored in the field of random matrices [123] and quantum chaotic systems. Similar approaches might also be applicable to Moiré systems as the presence of a Moiré potential locally can act as a source of disorder. The complexity of gigantic Moiré band structures might therefore be encapsulated in a statistical approach [124, 125] which can describe the formation of flat bands by inherent band pressure. In contrast to previous approaches describing the flatness of *magic angle flat bands* in twisted bilayer graphene by such a statistical approach [126–130], it is the goal of this part to describe a universal mechanism for generic bands within the bandstructure. The central question is to discuss, *(How) do flat bands generically form in Moiré systems?*

Scales of generic Moiré systems

Before answering the question at length within this part, let us first consider some basic relations in any Moiré system. Since the Moiré effect is not uncommon in nature, all Moiré systems share a common framework on which essential properties can be defined. In the following section, let us consider some generic quantities specific to 2D materials including both a two-dimensional lattice as well as a periodic perturbation. Although examples in this chapter are heavily focused on twisted bilayer graphene, the arguments themselves can be applied in a broader context. Therefore the results not only apply to bilayer systems who form the Moiré perturbation by sliding or twisting of layers, but also to monolayer systems which inherit the Moiré from an interaction with their host materials if they are grown on top of others.

We start the discussion by defining a periodic, two-dimensional lattice consisting of Bravais lattice vectors \vec{a}_1 and \vec{a}_2 as well as a number of basis sites \vec{r}_i . For simplicity, we assume the Bravais lattice to only have one length scale, namely a uni-directional lattice constant a . We will later refer to this lattice as the initial lattice or unperturbed system.

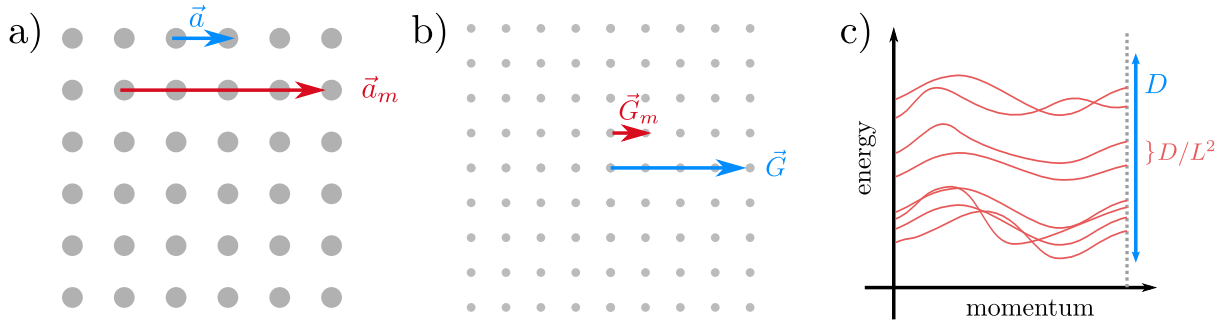


Figure 13.2.: Universal considerations for Moiré systems - a) Sketch of a generic Moiré system with underlying lattice of periodicity a and Moiré lattice with wavevector a_m b) reciprocal space shows Brillouin zone of underlying lattice with reciprocal vectors G being filled with Moiré reciprocal lattice points with distance G_m c) bandstructure gets backfolded so that typical levels are only D/L^2 apart.

The initial lattice is brought into contact with a perturbation V which itself is periodic on length scales $a_M = La$. Generically, a_M is assumed to be much larger than the periodicity of the initial lattice, i.e. $L \gg 1$. The perturbation can be either commensurate or incommensurate with the initial lattice, commensurate meaning that Moiré lattice vectors can be written as

$$\vec{a}_M = m\vec{a}_1 + n\vec{a}_2 \quad (13.1)$$

for some integers m and n , e.g. see an example of $m = 5$ in panel a) of Fig. 13.2. A commensurate perturbation results in a periodic Moiré structure whereas an incommensurate perturbation necessarily leads to a quasi crystal. In the following discussion, most of the calculations are performed in the commensurate case. However, this is mostly a restriction that the numerical tool is imposing as it requires to define unitcells which are strictly periodic in space. In any of these cases, we will from hereon refer to the initial lattice with effects of the perturbation as the Moiré system.

Periodicity allows to Fourier transform into momentum space in which two length scales emerge for this particular situation. The periodicity of the initial Bravais lattice leads to reciprocal lattice with lattice constant $G = 2\pi/a$. In contrast, the Moiré cell yields a denser momentum space lattice with lattice constant $G_M = 2\pi/a_M = G/L$, which is smaller by a factor of L compared to the unperturbed reciprocal lattice constant. In total, there are $\mathcal{O}(L^2)$ momentum points G_M within the first Brillouin zone of the initial lattice. This can again be observed in panel b) of Fig. 13.2 where it is demonstrated schematically.

Considering a tight-binding like model on the initial lattice leads to a band structure with typical bandwidth D , defined on the first Brillouin zone of this lattice. Switching perspective to the Moiré perturbation, one finds momenta $k \bmod G_M$ are conserved which in return means that all $\sim L^2$ momentum points of the reciprocal Moiré lattice within the first Brillouin zone of the initial lattice have to be equivalent. This equivalence leads to

a so-called backfolding of bands into the first Moiré Brillouin zone such that the average bandwidth of the Moiré system is $\sim D/L^2$.

The perturbation acts in real space as a potential V and induces coupling between bands within the bandstructure. Let us assume that the potential V is weak enough to be considered a perturbation but strong enough to couple adjacent bands, i.e. $V \gtrsim D/L^2$. This is well justified for twisted bilayer graphene since V for these systems behaves like $V \sim 1/L$. As the values of V in real space seem locally random due to the Moiré pattern, one might expect that efficient level repulsion within the spectrum takes place, i.e. bands only vary on energy scales $\Delta\varepsilon \sim D/L^2$ upon variation of \vec{k} . Level repulsion in return would imply reduced velocities of the form $\vec{v} \sim \Delta\varepsilon/\Delta\vec{k} \sim v_F(a/L)^\alpha$ where v_F describes the initial group velocity and $1/2 \leq \alpha \leq 1$ is a measure of how much neighboring bands are allowed to be coupled. Independent of the typical values of α , $v \sim 1/L^\alpha$ implies a great reduction of velocities compared to the uncoupled case – an effect that is not observed in typical twisted bilayer graphene systems with experimental parameters.

Momentum space hopping picture

To resolve this puzzle, one has to look beyond the naive picture. The real space potential V can also be understood in terms of an effective hopping in momentum space between neighboring momentum points $\vec{Q}_n = n_1\vec{G}_{m,1} + n_2\vec{G}_{m,2}$. Together with the dispersion of the unperturbed lattice problem on these points, $\varepsilon(\vec{k})$, the whole Moiré problem can then be formulated as an effective Hamiltonian in momentum space, defined on momentum 'sites' \vec{Q}_n containing a quasi-random on-site potential $\varepsilon(\vec{k} + \vec{Q}_n) \equiv \varepsilon_{\vec{Q}_n}$ as well as hopping between these points which is dependent on the Moiré potential V .

Looking at a typical wavefunction in momentum space with energy ε , one can see that for small values of V it will necessarily spread close to regions where its energy matches the initial dispersion $\varepsilon(\vec{k})$. Those regions are generically one-dimensional lines and intersect the momentum sites in a quasi-random pattern. The quasi-random intersection provides a form of randomness on the otherwise normal hopping Hamiltonian that brings it in close relation to the problem of Anderson localization in one-dimensional wires [131]. In this setting, the Moiré potential V acts as a measure of hopping or mobility, whereas the geometry of the underlying dispersion provides the random potential in which wavefunctions can localize or delocalize.

In any case, the relative strength of V compared to other constants determines the behavior of states. Low relative values of V can lead to strong localization in momentum space whereas large values allow wavefunctions spreading out. This in return can facilitate level repulsion and flat bands. The following sections of this chapter are devoted to showing the implications of such an Anderson localization scenario and how it can be probed by numerical calculations.

14. Modeling twisted bilayer graphene

Electronic calculations for twisted bilayer graphene are mostly performed either with a real-space lattice model or a momentum-space continuum model. Whereas the real-space model utilizes explicit hopping terms between different sites within the Moiré unitcell [132–134], thus naturally performing best for large angles and small Moiré cells, the momentum space model makes a continuum approximation and offers an approximate description of the system [91] for small angles. Therefore, both methods can be seen complementary as they offer solutions for two distinct limits of twist angles.

In Ref. [P8], which serves as the basis of this chapter, most data has been calculated with the momentum space model. In the context of this thesis however, let us concentrate on the real-space model, i.e. employing bandstructure calculations for the Moiré unitcell which are in principle similar to those in the previous chapter on supersymmetry. As we will see, the long-ranged connectivity and the large periodicity of the Moiré cell pose additional challenges for the numerics, however in return rewarding the entire band structure including regions inaccessible to the momentum space model.

This section is structured as follows. We will first discuss the geometry of single layer and twisted bilayer graphene. Then, the real-space Hamiltonian is introduced, including all relevant model parameters. Finally, before coming to the results, the continuum model is briefly introduced for comparison.

14.1. Real space geometry

Twisted bilayer graphene consists of two layers of graphene which themselves can be represented as two-dimensional honeycomb lattices twisted by a relative angle θ . The honeycomb lattice consists of a unitcell with two sites located at

$$\begin{aligned} \vec{r}_1 &= (0, 0) \\ \vec{r}_2 &= \left(\frac{a}{\sqrt{3}}, 0 \right) \end{aligned} \tag{14.1}$$

as well as Bravais lattice vectors

$$\begin{aligned}\vec{a}_1 &= a \left(\frac{\sqrt{3}}{2}, -\frac{1}{2} \right) \\ \vec{a}_2 &= a \left(\frac{\sqrt{3}}{2}, +\frac{1}{2} \right)\end{aligned}\tag{14.2}$$

which are defined with the lattice constant a . The honeycomb lattice as well as its unitcell and Bravais lattice vectors are depicted in Fig. 14.1.

Twisting the two graphene sheets leads to the formation of a Moiré pattern. This pattern is visible by the distinct opacity of the lattice in regions of AA stacking and AB stacking as seen in Fig. 14.2. AA regions are those regions where site 1 of the upper layer is on top of site 1 in the lower layer, whereas AB regions are those where site 1 in the upper is on top of site 2 in the lower layer. The Moiré pattern of AA and AB regions forms again a triangular Bravais lattice. The size of the Moiré lattice constant depends on twist angle and typically grows with decreasing angle.

For most twist angles, the Moiré lattice constant will not be commensurate with the underlying honeycomb lattice constant. Therefore, the Moiré cell is not truly periodic on small length scales and exact diagonalization and band structure calculation cannot be applied to generic angles θ . However, angles for which the two lattice constants are commensurate, can be constructed by twisting the site $R_u = m\vec{a}_1 + n\vec{a}_2$ in the upper layer on top of site $R_l = n\vec{a}_1 + m\vec{a}_2$ in the lower layer. These commensurate angles, constructed by pairs of integer numbers m and n , follow the relation

$$\cos(\theta(m, n)) = \frac{1}{2} \frac{m^2 + n^2 + 4mn}{m^2 + n^2 + mn}\tag{14.3}$$

An example of four different commensurate angles can be seen in Fig. 14.2.

From a numerical perspective, dependence of the linear size of the Moiré cell on the twist angle θ implies a dependence of numerical cost on twist angle. Calculating the entire band structure for a certain set of parameters is numerically equivalent to diagonalizing matrices of size $N \times N$ where N is the number of sites within the Moiré cell. However, since the Moiré cell increases with decreasing twist angle, so does the numerical computation time. The extent of this increase should not be underestimated. To compute the bandstructure for a twist angle of 2.3° ($m = 15, n = 14$), one needs to diagonalize matrices of size $\sim 2500 \times 2500$. Upon decreasing the angle to the magic angle of $\sim 1.1^\circ$ ($m = 27, n = 26$), the matrices increase in size to $\sim 8400 \times 8400$ which means an increase in linear size by a factor of 4 and therefore an increase in computation time by a factor of 64. To get a better grasp on scaling, Fig. 14.3 shows the relations between various parameters of the Moiré cell. It is this scaling in particular, which provides the necessity of a fast bandstructure code later on.

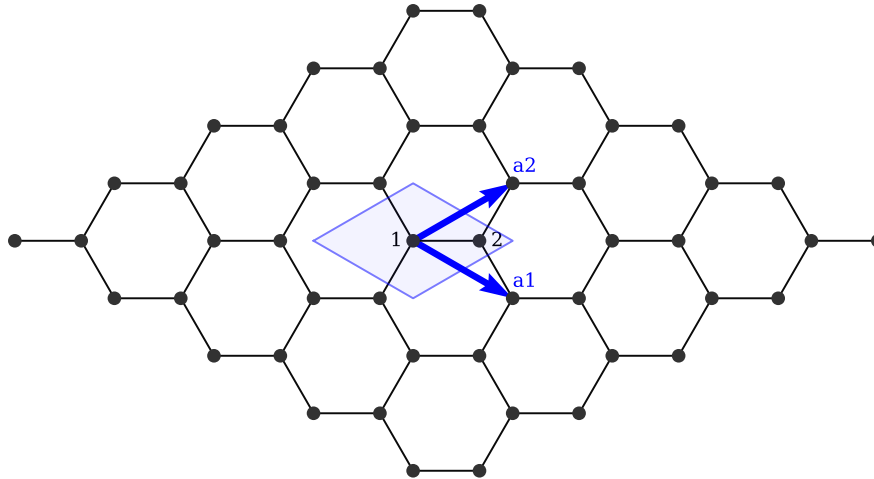


Figure 14.1.: Graphene unitcell - Small patch of honeycomb lattice including the two numbered basis sites / sublattices. Primitive lattice vectors \vec{a}_1 and \vec{a}_2 are shown as well as the primitive unitcell.

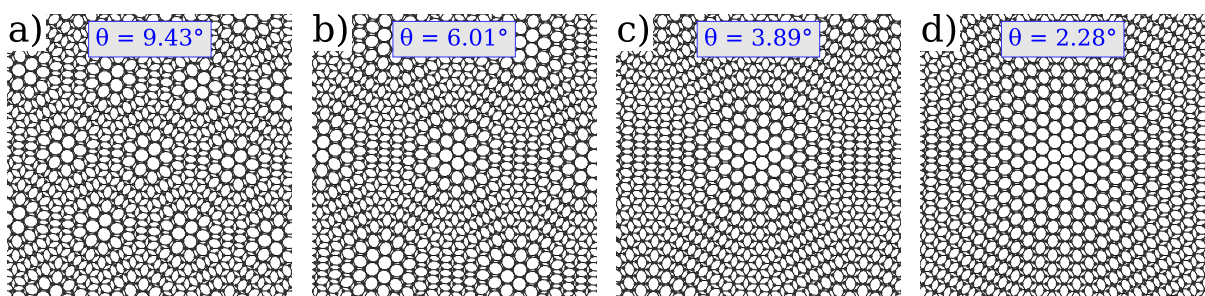


Figure 14.2.: Twisted bilayer graphene - Two twisted layers of graphene on top of each other show a Moiré pattern. Twist angle θ is decreased from left to right. Note that the pattern is centered at the AA region of the Moiré. Examples from left to right correspond to commensurate angles with $m = 4, 6, 9, 15$.

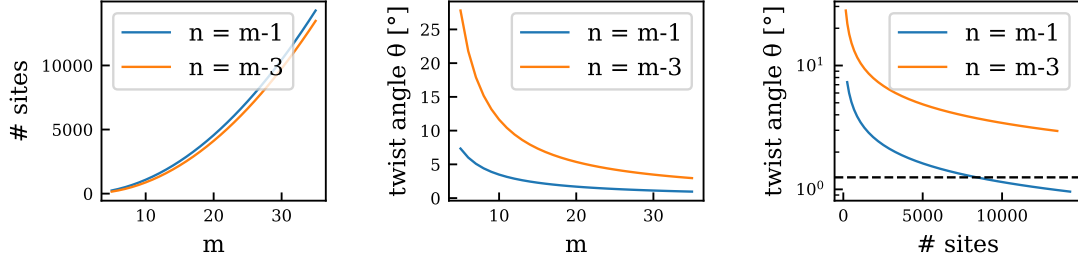


Figure 14.3.: Relations between Moiré unitcell parameters - Twist angle, Moiré unitcell size and parameters m and n shown in functional dependence. Horizontal dashed line denotes the later mentioned *magic angle* in the numerics at $m = 27, n = 26$ corresponding to a twist angle of $\theta = 1.25^\circ$ with a Moiré unitcell of 8428 sites.

Apart from the twisting of the individual honeycomb layers rigidly, real twisted bilayer graphene includes two more geometric effects, corrugation and relaxation. Relaxation describes the effect of carbon atoms relaxing in the in-plane direction to minimize interaction energies between the layers, whereas corrugation describes the buckling of graphene sheets in the out-of-plane direction. Both forms of modulation are spatially correlated with the Moiré structure, however the precise form of relaxation often relies on extensive numerical calculations and only in rare cases can be modeled in a concise analytical fashion [135]. In contrast, corrugation can be approximated more straight forward by a spatially modulated interlayer distance

$$d(\vec{R}) = d_0 + 2d_1 \left[\cos \left(\frac{\vec{R} \cdot \vec{C}_1}{|\vec{C}_1|^2} \cdot 2\pi \right) + \cos \left(\frac{\vec{R} \cdot \vec{C}_2}{|\vec{C}_2|^2} \cdot 2\pi \right) + \cos \left(\frac{\vec{R} \cdot \vec{C}_3}{|\vec{C}_3|^2} \cdot 2\pi \right) \right]. \quad (14.4)$$

Here, the layer distance is expressed in distances d_0 and d_1 which can be written in terms of the AA-region layer distance d_{AA} and the AB-region layer distance d_{AB} as

$$\begin{aligned} d_0 &= \frac{1}{3}(d_{AA} + 2d_{AB}) \\ d_1 &= \frac{1}{9}(d_{AA} - d_{AB}) \end{aligned} \quad (14.5)$$

Also, vectors C_i span the corrugation in different directions. All C_i enclose angles of 60° with each other and C_1 can be written in terms of Moiré Bravais lattice vectors as

$$\vec{C}_1 = \frac{1}{2}(\vec{a}_{1,M} + \vec{a}_{2,M}). \quad (14.6)$$

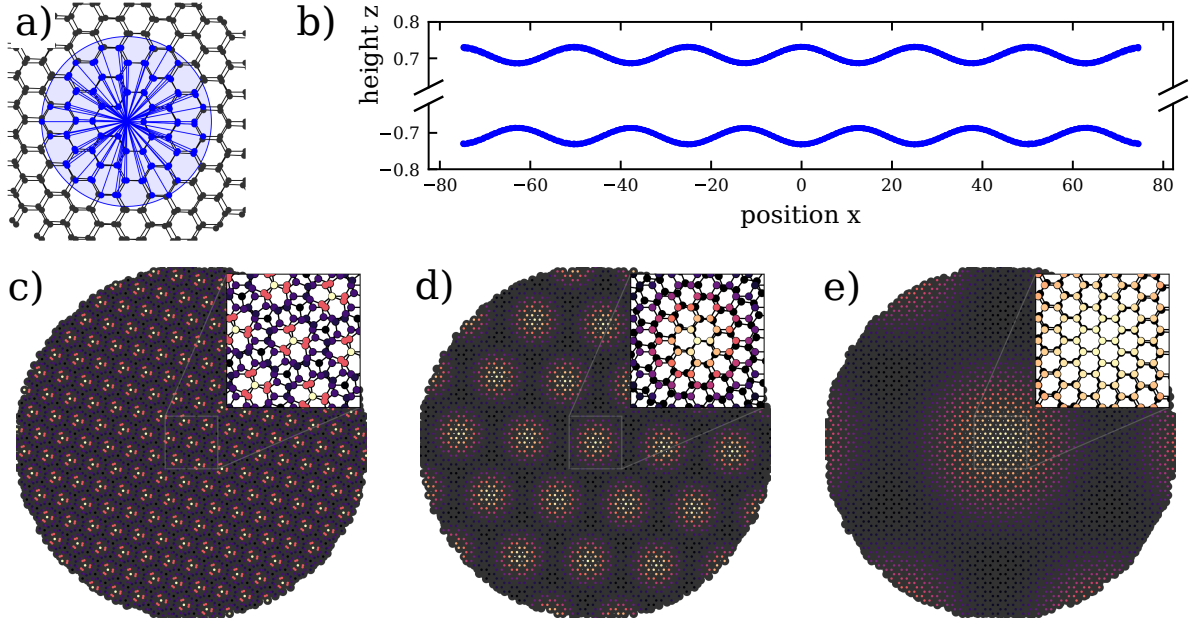


Figure 14.4.: Hopping elements and corrugation - Visualization of the different hopping elements within the two layers shown in panel a). Hopping elements going out from the central site are shown as blue lines, the blue circle denotes the range beyond which hopping elements are numerically cut off. Panel b) shows a side view on the corrugation in twisted bilayer graphene which describes a height modulation within the layers. The modulation is following the Moire structure and shown from a top view as a color map in panels c)-e) for varying twist angle.

14.2. Real space hopping model

Having discussed the geometric aspects of twisted bilayer graphene, this section aims at providing the hopping Hamiltonian of electrons on the lattice. Generically, the problem of electrons hopping on the bilayer structure can be described by a tight-binding Hamiltonian in real space

$$\mathcal{H} = \sum_{i,j} t(\vec{r}_{i,j}) c_j^\dagger c_i \quad (14.7)$$

where i and j denote lattice sites in either the upper or lower layer.

Hopping amplitudes $t(\vec{r}_{i,j})$ are generically formed by atomic overlaps between sites i and j and therefore can be assumed to only depend on distance and direction of the distance vector. For graphitic systems such as twisted bilayer graphene, one can use hopping elements

of the Slater-Koster form which can be written as

$$\begin{aligned}
 t(\vec{r}) &= V_{pp\pi}(r) \left(1 - \left(\frac{\vec{r} \cdot \vec{e}_z}{r} \right)^2 \right) + V_{pp\sigma}(r) \left(\frac{\vec{r} \cdot \vec{e}_z}{r} \right)^2 \\
 V_{pp\pi}(r) &= V_{pp\pi}^0 e^{-(r-a_0)/\delta_0} \\
 V_{pp\sigma}(r) &= V_{pp\sigma}^0 e^{-(r-d_0)/\delta_0}
 \end{aligned} \tag{14.8}$$

Here, the hopping strength is written as the overlap between the out-of-plane p_z -orbitals, which can either take place between layers (called $V_{pp\sigma}$) or within a layer (called $V_{pp\pi}$). The hopping elements are parameterized by nearest-neighbor distance $a_0 = a/\sqrt{3}$, mean layer distance d_0 , decay distance of the orbital overlap δ_0 as well as fundamental overlap integrals $V_{pp\pi}^0$ and $V_{pp\sigma}^0$. For the sake of reducing numerical costs, hopping elements are cut off at a numerical cutoff distance of ~ 5 nearest-neighbor distances.

In total, the hopping Hamiltonian contains the following mix of electronic as well as geometric parameters:

- *Single layer graphene geometry*, especially the lattice constant a and nearest neighbor distance $a_0 = a/\sqrt{3}$. In the following, experimental values of nearest-neighbor distance $a_0 = 0.142$ nm are used.
- *Twist angle* $\theta(m, n)$ given in terms of pairs (m, n) with usually $n = m - 1$. The celebrated magic angle is at 1.1° which corresponds to $m = 27$, however most calculations in the following do not rely on this magic angle condition and are performed at larger angles, corresponding to smaller m .
- *layer distance and corrugation* of the bilayer system. Experimental studies find AA and AB distances as $d_{AA} = 0.360$ nm and $d_{AB} = 0.335$ nm. In the following examples, a parametrization relative to the experimental findings is used, where relative corrugation c and relative interlayer distance d are defined s.t.

$$\begin{aligned}
 d_{AA} &= d \cdot (0.335 \text{ nm}) + c \cdot (0.360 \text{ nm} - 0.335 \text{ nm}) \\
 d_{AB} &= d \cdot (0.335 \text{ nm})
 \end{aligned} \tag{14.9}$$

- *electronic hopping parameters* such as overlaps $V_{pp\pi}^0$ and $V_{pp\sigma}^0$ as well as the decay distance δ_0 . A good agreement to experimental findings can be achieved with $\delta_0 = 0.319$ nm as well as atomic overlaps $V_{pp\pi}^0 = -2.7$ eV and $V_{pp\sigma}^0 = 0.48$ eV. In the following sections of this chapter, the interlayer coupling and changes of it will be of great importance. To vary this coupling, a relative interlayer overlap V is used

$$V_{pp\sigma}^0 = V \cdot 0.48 \text{ eV} \tag{14.10}$$

Upon having defined the hopping Hamiltonian, one can now calculate bandstructures of

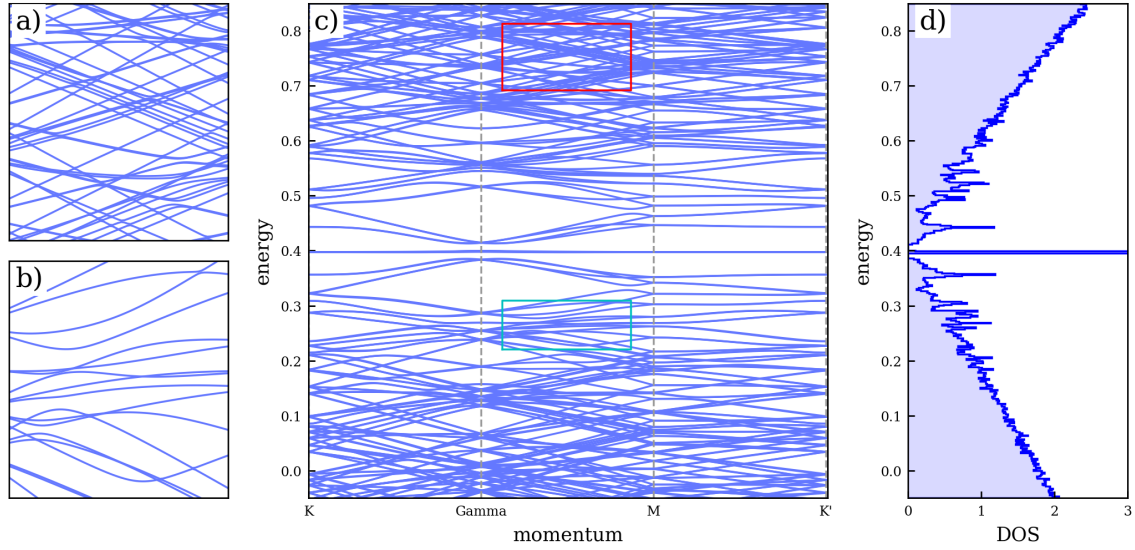


Figure 14.5.: Bandstructure of twisted bilayer graphene - Parameters that match experiments at the flat band condition. Zoom into the bandstructure shown in c) and further highlights in panels a) and b), supplemented by density of states in panel d). Magic angle flat bands are clearly visible in the center of the spectrum and also as a peak in the density of states. Cutouts a) and b) display different regions of the spectrum which feature crossing and repelling levels alike. Figure recreated from [P8].

twisted bilayer graphene like for any other tight-binding model, namely by calculating the k -dependent interaction Hamiltonian in momentum space and diagonalizing it along a path within the first Brillouin zone. The difference compared to a usual tight-binding model lies in the extent of the calculation, more precisely the size of the twisted bilayer unitcell. Whereas normal tight-binding models usually have $\mathcal{O}(1 - 10)$ sites within their unitcell, twisted bilayer graphene can have $\mathcal{O}(1000 - 10000)$ sites within the Moiré cell depending on the twist angle, leading to correspondingly many bands.

Panel c) of 14.5 shows an example bandstructure for twisted bilayer graphene using experimental parameters and an angle of $\theta = 1.1^\circ$. The celebrated flat band can be clearly identified in the center of the spectrum of panel c) and the density of states which is shown in panel d). The flat bands are surrounded by a vast number of conventional bands. The two zooms into the bandstructure, displayed in panels a) and b), show that individual bands among those show both level crossings as well as level avoidances, foreshadowing the relevance of a statistical analysis later on.

Lastly, it is worth mentioning some numerical aspects of the band structure calculations. Since the Moiré cell is much larger than conventional unitcells, the matrices within the calculation also become much larger. These large matrices with many entries are posing an additional challenge on numerical implementations and computing resources

alike. From a software perspective, all calculations have been performed with the package `LatticePhysics.jl` [S3]. This package provides a fast and ready-to-use bandstructure code for Julia, and was developed in the scope of Part II of this thesis. Especially the graphical representation of unitcells and lattices helps in implementing and testing the large Moiré unitcells. From the perspective of computing resources, calculations were performed on the CHEOPS cluster at RRZK Cologne and the JUWELS cluster at the Forschungszentrum Jülich.

14.3. Momentum space continuum model

Before coming to the actual analysis of twisted bilayer graphene bandstructures, let us first consider an alternative approach. Instead of considering real space positions and hopping amplitudes, one can also formulate an effective Hamiltonian entirely in momentum space, the so-called continuum model. This alternative approach uses different model assumptions like approximating the single-layer dispersion by its linear behavior close to Dirac points and thus provides an important reference calculation for the real space results.

The start of the continuum model is the dispersion of single-layer graphene close to the Dirac points where it takes the linear form

$$H(\vec{K} + \vec{p}) = -\frac{\sqrt{3}at}{2} (\vec{\sigma} \cdot \vec{p}). \quad (14.11)$$

Eigenstates of this Hamiltonian are Bloch wavefunctions which are defined with respect to the sublattice $\beta = 1, 2$ as

$$|\Psi_{\vec{k}\beta}\rangle = \frac{1}{\sqrt{N}} \sum_{\vec{R}} e^{i\vec{k}\cdot\vec{R}} |\vec{R} + \tau_{\beta}\rangle. \quad (14.12)$$

Here, N is the total number of lattice sites and τ_{β} is the position of basis site β .

The next step is to form twisted bilayer graphene by twisting two individual sheets of graphene by a relative angle θ . For symmetry reasons this is done by twisting the upper layer by $+\theta/2$ and the lower layer by $-\theta/2$. The twisted wavefunctions can then be written as

$$|\Psi_{\vec{k}\beta}^{U/L}\rangle = \frac{1}{\sqrt{N_{U/L}}} \sum_{\vec{R}^{U/L}} e^{i\vec{k}\cdot\vec{R}^{U/L}} |\vec{R}^{U/L} + \tau_{\beta}^{U/L}\rangle \quad (14.13)$$

with rotated basis vectors $\tau_{\beta}^{U/L} = e^{\pm i\theta\sigma_z/2} \tau_{\beta} e^{\mp i\theta\sigma_z/2}$. Similarly, the single-layer Hamiltonian of the individual layers transforms to

$$H(\vec{K}^{U/L} + \vec{p}) = H_{U/L}^{\vec{K}}(\vec{p}) = -\frac{\sqrt{3}at}{2} (\vec{\sigma}_{\pm\theta/2} \cdot \vec{p}) \quad (14.14)$$

with rotated Pauli matrices $\vec{\sigma}_{\pm\theta/2} = e^{\pm i\theta\sigma_z/4}\vec{\sigma}e^{\mp i\theta\sigma_z/4}$.

Up to this point, the two layers have only been rotated but not brought into contact. Therefore as a necessary next step, interlayer hopping is added to the model, written as a Hamiltonian H_T which describes the tunneling between upper and lower layer. After some simplifications H_T can be written as

$$\langle \Psi_{\vec{p}'}^L | H_T | \Psi_{\vec{p}}^U \rangle = \sum_{i=1,2,3} \delta_{\vec{p}-\vec{p}',\vec{q}_i} \left(t^{AB} \left[\sigma_x \cos\left(\frac{2\pi}{3}(i-1)\right) + \sigma_y \sin\left(\frac{2\pi}{3}(i-1)\right) \right] + t^{AA} \mathbb{1} \right). \quad (14.15)$$

where tunneling between sublattices of different layers is parameterized by t^{AA} and t^{AB} . Also note that in contrast to the single-layer Hamiltonian, the hopping term starts adding interactions between different momenta \vec{p} and \vec{p}' . Under the assumption that the Moiré potential is smooth in real space, which is typically well justified, the hopping in momentum space is dominantly restricted to small momenta \vec{q}_i , equal to the K or K' point of one of the layers. Therefore, momenta \vec{p} and \vec{p}' form a grid in reciprocal space which is consistent with the Brillouin zone of the Moiré cell, i.e. $\vec{p}' = \vec{p} + i_1\vec{G}_{m,1} + i_2\vec{G}_{m,2} - \vec{K}$. Thus all accessible points \vec{p}' in momentum space can be defined from one initial \vec{p} which acts as the origin of the grid.

Another beneficial feature of this particular parametrization of the interlayer hopping is its ability to easily add corrugation effects by mismatching t^{AA} and t^{AB} . One approach to parameterize the entire interlayer coupling is therefore to describe corrugation by a tuning parameter ϕ which regulates the relative ratio between t^{AA} and t^{AB} as well as an overall tunneling strength between the layers called t_{\perp} . Couplings then read

$$t^{AA} = t_{\perp} \sin(\phi) \quad t^{AB} = t_{\perp} \cos(\phi) \quad (14.16)$$

Here, $\phi = \pi/4$ corresponds to the uncorrugated case whereas $\phi = 0$ describes hopping only between different sublattices and therefore the ultra-corrugated case, also called *chiral limit*. In this limit, the continuum model shows remarkable features, such as exactly flat bands at a sequence of magic angles [129]. Furthermore, the chiral limit also allows for identification of magic angle flat bands with Landau levels on a torus [129, 136].

All in all, the continuum model features as similar range of tunability compared to the real space model with regard to tuning interlayer coupling and corrugation. Tuning the twist angle between the graphene sheets is even more straight forward in the continuum model as it does not rely on any commensurability assumptions.

There are however strong differences especially in its numerical applicability. First and foremost, the continuum model is defined for small twist angles θ i.e. it only works for sufficiently large real-space Moiré cells. In this regard, it is complementary to the real-space model which encounters numerical problems when Moiré cells become too large. On the other hand, the real space model can calculate entire band structures in which the number of bands matches the number of sites in the Moiré cell, whereas the continuum

model builds up an approximation to the band structure from the central bands by adding more momenta \vec{p}' and therefore accessing more and more bands, independent on twist angle θ . On hand, this reduces numerical complexity especially for smaller angles compared to the real space model, on the other hand it lacks the features far away from the Dirac points as they are not part of the approximation.

In the following sections of this chapter, the continuum model will therefore only play a minor role. It is mostly used for comparison and to have a second, independent approach to the example of twisted bilayer graphene.

15. Delocalized states in twisted bilayer graphene

Having established means of calculating bandstructure information for twisted bilayer graphene, let us turn our attention to the localization mechanism at play. To measure localization in real and momentum space, different observables have been favored in the context of chaotic systems. First, the observables are presented, after which they are investigated one by one, starting by velocity and energy level statistics and ending with wavefunctions.

The discussion of different observables will reveal the three main regimes of qualitatively different localization behavior, dominant in twisted bilayer graphene. In principle, all bands follow this scheme, however there are some qualitative exceptions which will be discussed at the end of the chapter.

15.1. Measures of localization

Let us start by considering the different observables in which one can find traces of localization-delocalization transitions in general chaotic systems. In the following, these statistical measures are considered:

- *Band velocities*: A first way to observe a localization-delocalization transition is the direct observation of band flattening. Since the slope of a band is related to its group velocity by $\vec{v}_n(\vec{k}) = \vec{\nabla} \varepsilon_n(\vec{k})$, a band flattening can be observed as a reduction of group velocity. Numerically, band velocities can be calculated from the gradient of the dispersion.
- *Energies*: It is known from the study of random matrices and chaotic systems that also the dispersion of a chaotic system shows traces of the underlying physics. In particular it is known that the relative spacing of energy levels, $r_i = \Delta E_{i+1} / \Delta E_i$, will follow different distributions, depending on the amount of localization at play [123, 124, 131]. For a fully localized system, no level repulsion will occur and the distribution of r_n is a Poisson distribution. In contrast, in the delocalized case, the distribution of r_n follows Wigner-Dyson statistics. In practice, the agreement will not be perfect [137]. However, a quantitative statement can still be made by utilizing the so-called Kullback-Leibler divergence [138, 139] which measures the

relative agreement between two distributions. The distribution of r_n is numerically readily available since it can be computed directly from the band structures.

- *Wavefunctions*: The third measure which is discussed in the context of this chapter accounts for the wavefunctions themselves. Here, the delocalization and localization in momentum space can be explicitly investigated graphically when plotted or it can be measured by computing the inverse participation ratio (IPR) [131]. Furthermore, symmetries of these wavefunctions will become important as well.

In general, all of these different measures can show different behavior for different regions of energies. Therefore, the remainder of this section goes through the different observables one by one, analyzing in detail what can be read from different observables.

15.2. Velocity statistics

Let us start by discussing the statistics of band velocities. In general, these velocities can be calculated from the slope of individual bands. A band flattening is then signaled by vanishing of velocities as the slope of the dispersion goes to zero. Therefore in the scenario of quasi-chaotic interlayer couplings, a sufficiently strong coupling on the order of experimental values should be able to efficiently suppress velocities by a factor $1/L$ compared to the uncoupled layers. However, consulting the results obtained with experimental parameters in numerical calculations we will find out that this is not the case.

Numerically, it is feasible to calculate the band velocities by numerical derivatives of the band structure, i.e. for an eigenstate at momentum \vec{k} with index n and dispersion $\varepsilon_n(\vec{k})$ the corresponding velocity \vec{v}_n can be directly obtained from

$$\vec{v}_n(\vec{k}) = \vec{\nabla} \varepsilon_n(\vec{k}). \quad (15.1)$$

To get a better statistical understanding, the velocities $\vec{v}_n(\vec{k})$ are calculated for a set of random momenta $\{\vec{k}\}$ within the first Moiré Brillouin zone and then displayed in one of two ways:

- *histogram*: The most direct way to display velocity data from the band structure is to calculate a histogram $p(v)$ which shows the relative occurrence of a given velocity, averaging over velocity directions, momenta and band index.
- *energy-velocity curves*: Another form of presentation are scatter plots in which band energy and band velocity are put into correspondence. This form of presentation has the advantage that one can access information on different parts of the spectrum separately

In the following, both means will be combined to extract energy-dependent velocity information for twisted bilayer graphene.

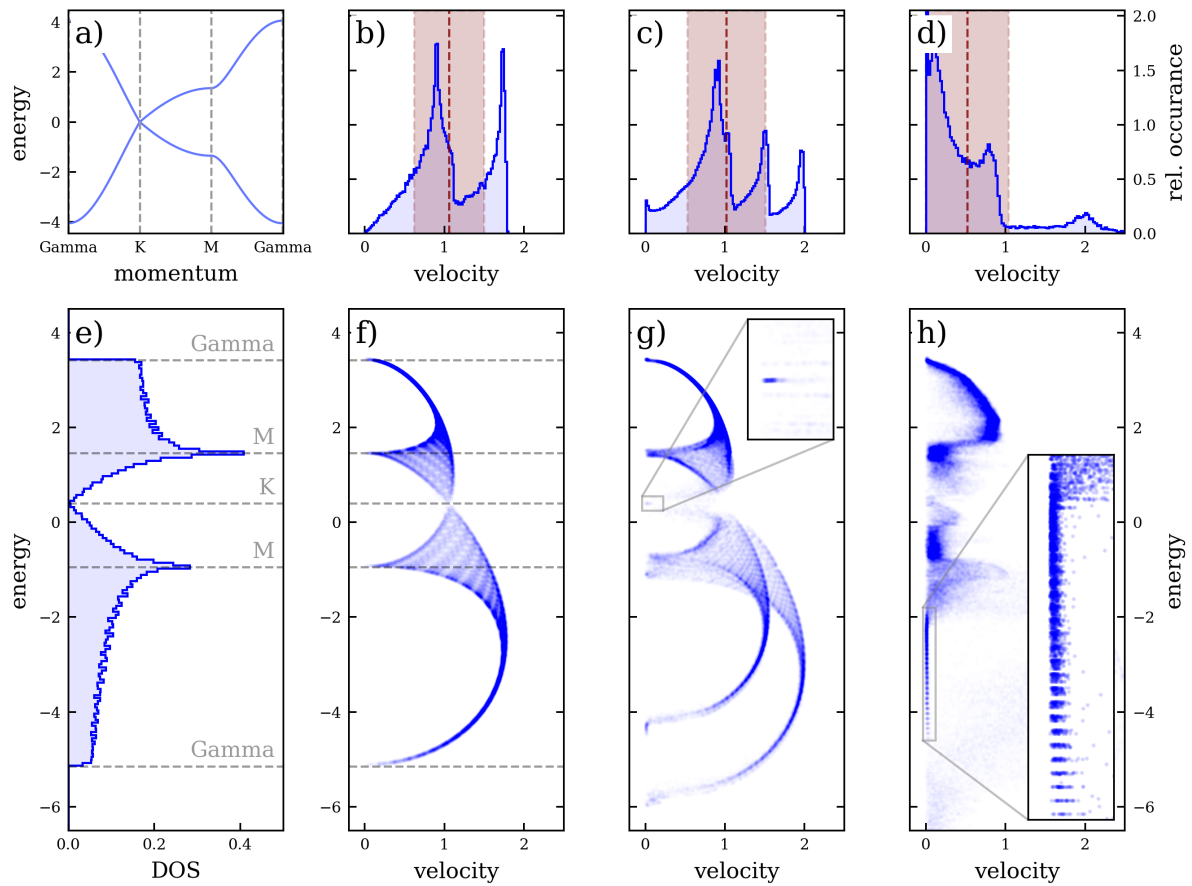


Figure 15.1.: Velocity statistics for experimental parameters - Distribution of velocities in twisted bilayer graphene depending on interlayer overlap V for parameters matching those of an experimental system, i.e. $m = 27$, and flat band conditions. Data can be compared to Fig. 15.2 which shows the same evolution but for a larger twist angle. Magic angle flat bands can be seen to evolve in panel g). Further: Harmonic oscillator ladder states emerge in panel h) for larger values of couplings. Those will be discussed later on in more detail. Figure recreated from [P8].

Let us first answer the most prominent question: Is there a (naively expected) velocity reduction by a factor $1/N$ for experimental parameters in which the interlayer coupling is substantial? To answer this question, results for experimentally relevant parameter regions are displayed in Fig. 15.1 c) and g). Comparing e.g. the velocity histogram obtained for experimental parameters in panel c) with the one obtained for uncoupled layers in panel b), one can observe that the mean velocity did not change drastically at all. Consulting the energy-velocity data for those two cases, the initial observation is confirmed as the two curves seemingly still support strong branches of high velocities, a good indicator of crossing bands.

The argument that interlayer coupling is still too weak to efficiently couple neighboring bands can be neglected if one looks at the lower end of the spectrum and its corresponding velocities in Fig. 15.1 g). The lower branch of high velocities, originating from the parabolic band around the Γ point, is now split due to interlayer coupling into two branches, separated by ~ 2 eV which is about 20% of the entire spectral bandwidth. This splitting is also in accordance with the ratio of bare tunneling strengths or atomic overlaps in-layer (~ 2.7 eV) and between layers (~ 0.5 eV). Therefore, one can conclude that interlayer coupling is indeed very strong for the experimental system, however it seems yet to be unable to efficiently mix neighboring bands.

Still, there seems to be room for vanishing velocities in twisted bilayer graphene as shown in panels d) and h) of 15.1. Here, parameters have been tuned well beyond experimental realizations by doubling the orbital overlap between layers as well as bringing the layers to 55% of their experimental interlayer distance. Velocities in this case are reduced strongly in comparison with the experimental case in panels c) and g) or the uncoupled case in panels b) and f). Especially the energy-velocity data shows that over large regions of the spectrum, velocities mostly vanish.

This general trend of velocities can again be confirmed by the results for a different bilayer graphene system of larger twist angle shown in Fig. 15.2. Again, band velocities tend to decrease substantially for very large interlayer hopping but remain largely unchanged for experimental values that still result in strong energy splits of the lower band. Additionally, the precise form of velocities decrease in interlayer hopping can be observed in the upper heatmap data. Different velocity regions drop to low velocities at different values of couplings in a process that resembles a crossover. Especially at extreme values of interlayer hopping, only infinitesimal velocities can be observed.

The origin of different velocities within the same bandstructure can also be traced back by using energy-velocity data in Fig. 15.1 and Fig. 15.2. Especially for the uncoupled case, certain high-symmetry points and their respective features within the spectrum translate to striking features of the velocity data. In this manner, the band extremes of the graphene dispersion at the Γ point can be seen as branches touching zero velocity. Similarly, the saddle point of the graphene dispersion with its van-Hove singularity around the M point touches zero velocity. Particularly high velocities are observed mostly in the center of the graphene bands and are further split by increased interlayer coupling into a fast and a slow

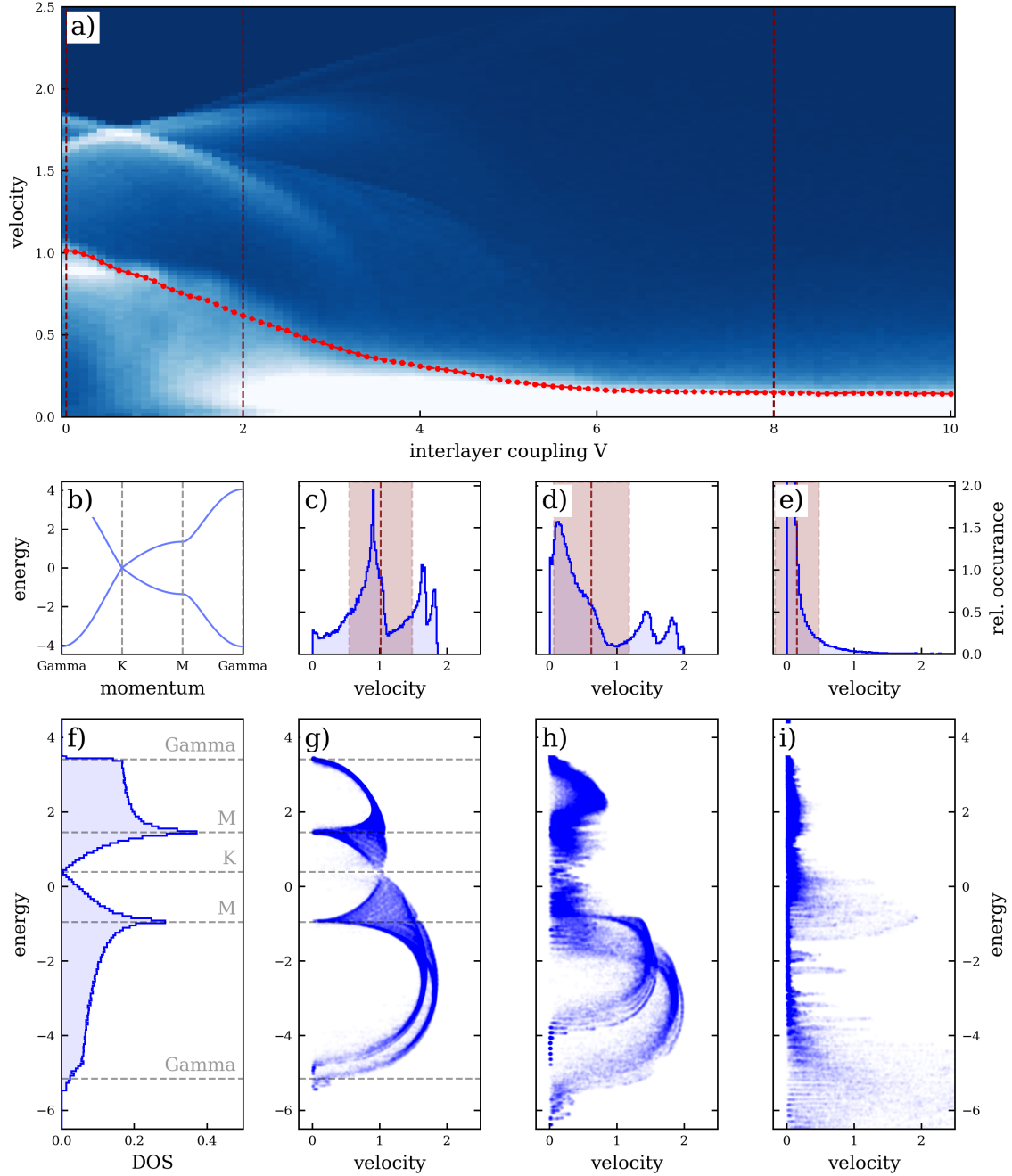


Figure 15.2.: Velocity statistics - Band velocities in twisted bilayer graphene as a function of atomic overlap V for a system of large twist angle $\Theta = 2.2^\circ$. A histogram of velocities as a function of parameters can be seen in panel a), panels c), d) and e) show cutouts with a more detailed view on the velocity statistics for the particular parameters $V = 0, 2, 6$. Further information can be extracted when plotting the band velocities as a function of the corresponding band energies, as seen in panels g), h) and i). These plots should be read in comparison to the density of states in panel f), as well as the generic honeycomb bandstructure in panel b). A general decrease in velocities can be observed upon increasing the overlap V . However, different parts of the spectrum will collapse to flat bands of infinitesimal velocity at different values of V .

branch. The well-known Dirac cone with linear dispersion at the K points can be seen as a single value of velocities in the energy-resolved plots.

In general, the velocity data has shown that suppression of velocities takes place for increased interlayer coupling, just not at the experimental values. This contradicts the naive estimation of simply having some quasi-random interlayer coupling on the order of the band spacing in order to suppress velocities greatly. It remains to be shown that the leading principle behind this delayed suppression is the process of Anderson localization in momentum space.

Apart from the general trend, some special points of anomalously low velocities can be observed in the velocity data. These include

- *magic angle flat bands*: with experimental values of parameters, one obtains flat bands around the center of the spectrum as clearly visible dots at zero velocity, c.f. panel g) of Fig. 15.1. These flat bands only appear for the magic angle but clearly pose an exception to the general trend of band flattening observed in the rest of the velocity data.
- *equally spaced states*: For strong values of interlayer hopping, a ladder-like series of equally spaced dots forms at the lower end of the spectrum at zero velocity, c.f. Fig. 15.1 h). These states will be interpreted as harmonic oscillator states in a later section of this chapter and mark yet another exception from the general trend of velocities.

In the following sections of this chapter, these two exceptions will be mostly excluded as they refer to individual states and do most likely not describe the general behavior prevalent in most Moiré systems. However at the end of this chapter, we will come back to discussing their relevance beyond twisted bilayer graphene.

15.3. Energy level statistics

We now turn our focus to the observables directly related to the energies within the band-structure. It is especially helpful to determine statistically how many levels are crossing or avoiding a crossing by level repulsion. A useful quantity in this context is the relative level spacing

$$\tilde{r}_i = \frac{E_{i+1} - E_i}{E_i - E_{i-1}} \quad (15.2)$$

of some band i in the bulk of the spectrum, or even better the back-folded version

$$r_i = \min(\tilde{r}_i, 1/\tilde{r}_i). \quad (15.3)$$

Despite a single value r_i not giving much information, a large set of r_i can tell a different story. In the case of freely crossing levels, a set of such relative level spacings shows Poisson

statistics, whereas avoided crossings lead to some form of Wigner-Dyson statistics. These differences come from extreme quotients $\Delta E_i/\Delta_{i-1}$ always appearing at the crossing points, in turn leading to an effective accumulation of small r_i values. Therefore, displaying the set of measured r_i values as a histogram can give insights into how much energy levels try to repel each other.

A more quantitative measure of agreement with a certain distribution can be obtained by the so-called Kullback-Leibler divergence. This entropic measure quantifies the distance between two distributions P and Q as

$$D_{\text{KL}}(P|Q) = \sum_i P_i \log \left(\frac{P_i}{Q_i} \right) \quad (15.4)$$

which is minimal if P and Q are the same distribution. Note that $D_{\text{KL}}(P|Q) \neq D_{\text{KL}}(Q|P)$, i.e. the measure is not symmetric.

Results for an initial calculation measuring the dependence of statistics on the interlayer coupling in twisted bilayer graphene are shown in Fig. 15.3. Both the Kullback-Leibler divergence as well as individual histograms show that the ensemble of r_i values resembles a Poisson distribution for $V = 0$, whereas it tends to disagree stronger with Poisson statistics for increased V . For finite V , the shape of the distribution approaches a Wigner Dyson statistics curve for the orthogonal symmetry class (GOE). This behavior is also expected, since the Hamiltonian matrices for fixed momentum \vec{k} are orthogonal matrices.

Overall, the Kullback-Leibler divergence shows good agreement with velocity data which already suggested level flattening in the previous section. Decreases in velocity for moderate interlayer tunneling can be brought into correspondence with decreases in the KL|GOE curve which indicates an increasing agreement with Wigner-Dyson statistics.

However, this agreement with velocity data only holds up for intermediate values of V . Upon increasing the value of the interlayer tunneling further, both Kullback Leibler divergence as well as histograms show a revival of Poisson resemblance and a suppression of the resemblance to GOE. This behavior is in contrast to the unchanged suppressed band velocities, which still indicate flattened bands in a direct way.

A closer inspection of the individual histograms reveals signs of variation beyond a simple change from Poisson to Wigner Dyson. Especially histograms for larger values of V seem to be superimposing different elementary Poisson or Wigner Dyson curves which might originate from different regions of energies.

A possible explanation for the shift back from Wigner-Dyson to Poisson might be the formation of effectively separate sectors within the Hilbert space of wavefunctions. This can e.g. be induced by the onset of (crystalline) symmetries. If those separate sectors build up, different parts of the spectrum are effectively decoupled and can freely cross without level mixing while bands within each sector feel enormous repulsion among themselves. A necessary next step is now to search for possible symmetries within the wavefunctions and

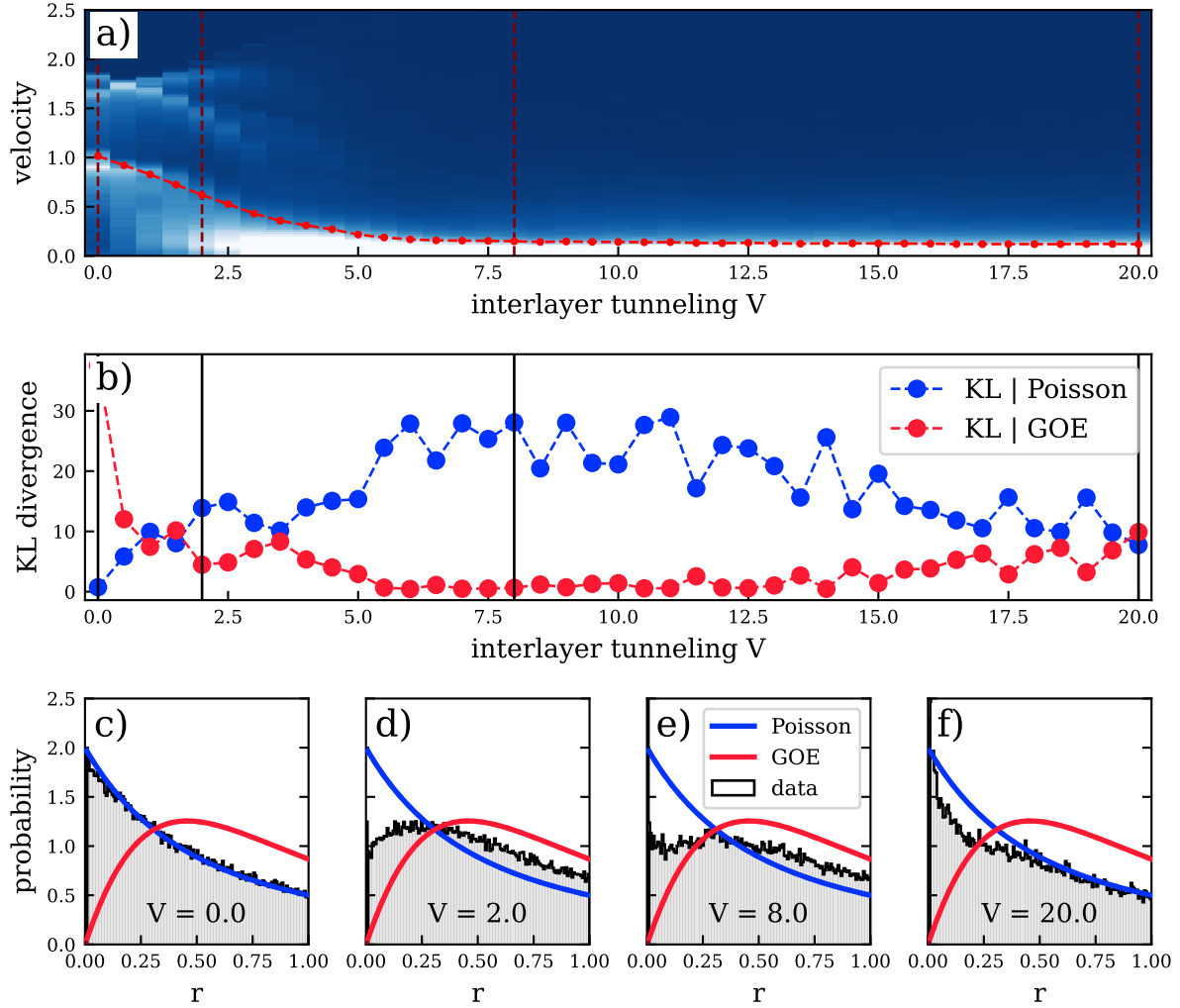


Figure 15.3.: Energy level statistics - Statistics of relative level spacing $r_i = \Delta E_i / \Delta E_{i-1}$ for variation of interlayer tunneling V in comparison to velocity data shown in panel a). A histogram of r values will follow either Poisson or Wigner Dyson statistics, indicating trivially crossing levels or level repulsion respectively. Histograms for various values of overlap V are shown in the lower row in panels c) - f). Panel b) shows the Kullback-Leibler (KL) divergence as a quantitative measure on how well the histograms agree with either distribution. In general, lower values of the KL-divergence signal better agreement. There is a general trend for the levels to show Poisson statistics at low values of V whereas they show more Wigner Dyson statistics for higher values of V , signaling the importance of level repulsion induced by increased interlayer coupling. For very high values of V , this trend seems to reverse.

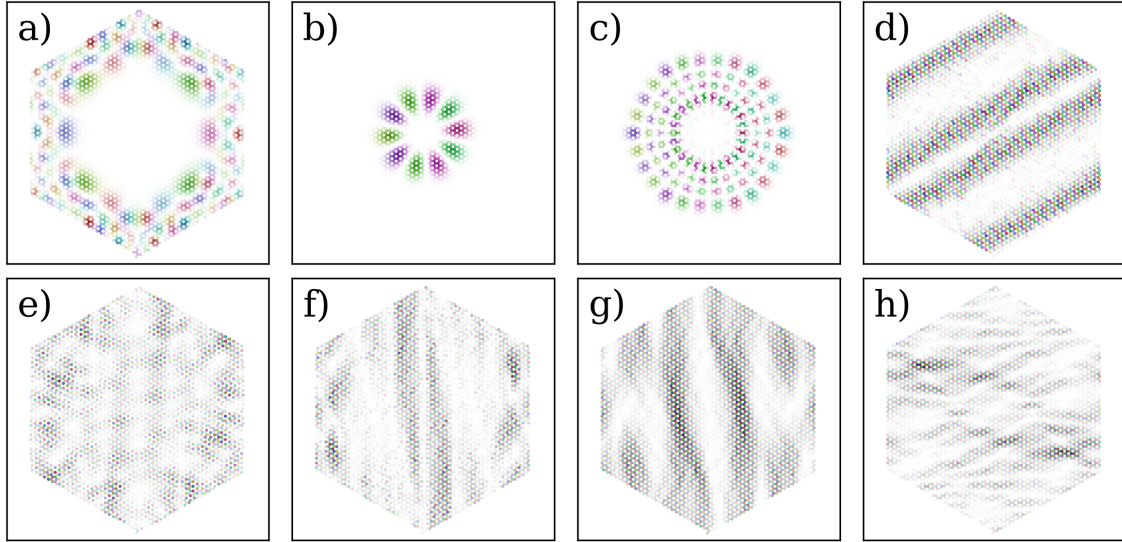


Figure 15.4.: Twisted bilayer wavefunctions in real space - Representative set of wavefunctions for the $m = 27$ system with parameters close to experiment. Wavefunctions are taken for different parts of spectrum, increasing in energy from top left to bottom right. Only the upper layer is plotted for simplicity. Color in the plots indicates the complex phase whereas the transition from white to colorful represents an increase in magnitude. Lower lying states are localized either in the AB or AA regions of the Moire cell with the AB localized states lying even lower in energy since hopping is smaller for those states. AA localized states mostly form very clear patterns which will later be identified as harmonic oscillator states. The rest of wavefunctions is dominated by seemingly random stripes of intensity across the unitcell.

investigate those in greater detail.

15.4. Wavefunction statistics

As a last measurable quantity, let us examine properties of individual wavefunctions in this section, such as qualitative features and / or inverse participation ratio (IPR) in real and momentum space. Wavefunctions in real space are directly obtained from exact diagonalization of the Hamiltonian matrix as the respective eigenvectors. To also obtain wavefunctions in momentum space, one has to perform a Fourier transform on these eigenstates. For the matter of this section, it is helpful to look at the two layers of twisted bilayer graphene separately.

Particular focus is put on two distinct features. For one, emergent symmetries in the parameter region of strong interlayer tunneling are relevant for the contrast between velocity and energy level statistics pointed out in the last section. Secondly, discussing the wave-

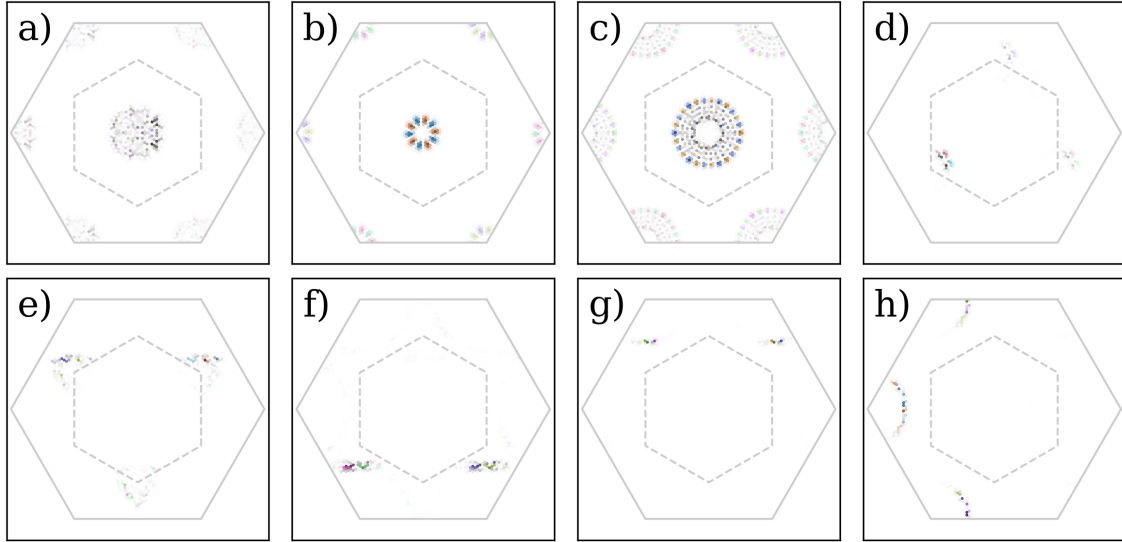


Figure 15.5.: Twisted bilayer wavefunctions in momentum space - Fourier transforms of the wavefunctions in Fig. 15.4. The Fourier transform reveals the connection of the wavefunctions to the original honeycomb dispersion as the wavefunctions trace equal energy contours of this dispersion.

functions themselves is a good opportunity to examine the general trend of delocalization along one-dimensional contours in momentum space that is proposed as an alternative delocalization scenario.

Let us start by discussing typical wavefunctions for experimental parameters which are shown in Fig. 15.4. In this figure, wavefunctions are shown for several different energies within the spectrum. Wavefunctions of lowest energies are slowly varying functions that are localized in AB regions where hopping effects are comparably weaker. The next lower energies show slowly varying wavefunctions in the AA regions. These states have a remarkable resemblance to harmonic oscillator eigenfunctions which will be of importance later on. The rest of states seem to be mostly composed of random stripy patterns.

More structure can be seen if one performs the Fourier transform to momentum space as displayed in Fig. 15.5. Here, the same wavefunctions as shown in Fig. 15.4 are Fourier transformed and plotted. It can be seen that these wavefunctions show a clear tendency to localized along the equal-energy contours of the initial graphene dispersion of that particular energy. For low energies, the wavefunctions localize close to the Γ point. For increasing energy, they spread more outwards but stay localized at one-dimensional contours. Even the random looking real space data for states of higher energies now appears to be consistent in momentum space.

Another feature of individual wavefunctions is their change upon increasing the interlayer tunneling V as shown in Fig. 15.6. Here, representative states are shown in both real

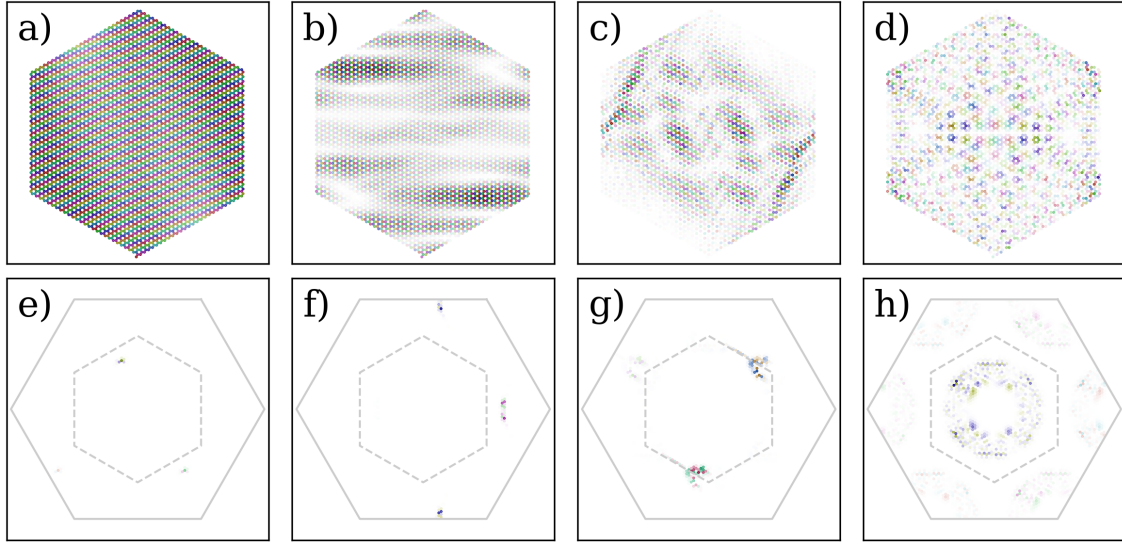


Figure 15.6.: Delocalization of wavefunctions in momentum space - Representative set of wavefunctions for a system of fixed twist angle $\theta = 1.25^\circ$, i.e. $m = 27$, for increasing values of overlap V . Upper row shows the wavefunctions in real space, lower row shows their Fourier transform. V is increased from left to right. A general tendency can be observed for states to become more delocalized in momentum space along the corresponding parts of the honeycomb dispersion. Also symmetries within the real space wavefunctions become more relevant with increasing V .

space (upper row) as well as momentum space (lower row). Note that due to several band crossings it is very difficult to track individual wavefunctions when increasing V . Therefore, for each value of V a representative state is shown which reflects the typical behavior of wavefunctions for this value of interlayer tunneling. The progression of these states shows a continuous evolution from states which are localized in momentum space to states which are completely delocalized in momentum space. In between these two limits, states seem to only delocalize along the one-dimensional equal-energy contours of the single-layer dispersion. Although in Fig. 15.6 only shows four example wavefunctions, this trend can be observed to be quite universal across the entire spectrum and for different tunneling values.

Yet another open question to answer is the discrepancy between velocity and energy level statistics for high interlayer tunneling, specifically why parts of the spectrum seem to be delocalizing but do not show level repulsion in the Kullback-Leibler divergence. In the last section, symmetries of the wavefunctions were proposed to be forming, which could lead to a division of the Hilbert space into sub-blocks.

An initial observation from the data are very symmetric real space wavefunction for high interlayer tunneling V displayed in Fig. 15.6. On the level of individual wavefunctions

one can qualitatively observe that many states show emerging (crystalline) symmetries for high values of interlayer tunneling, strengthening the hypothesis of Hilbert space blocks developing.

The conclusions that can be drawn from this data are quite far reaching. First of all, the data strongly suggests that wavefunctions in momentum space are (de-)localizing along specific equal-energy contours of their initial single-layer dispersion. These contours are chosen by the relative energy of the respective state within the bandstructure. The amount of localization depends on the interlayer tunneling, with no interlayer tunneling leading to fully localized states and high values of interlayer tunneling leading to fully delocalized states that even spread away from the equal-energy contours. Second, for larger values of interlayer tunneling, (crystalline) symmetries can play an important role when the wavefunctions delocalize into the 2d plane.

All in all, the analysis of individual wavefunctions proved to be a crucial piece in describing a concise picture of delocalization in momentum space. Wavefunctions not only strengthened the delocalization trend in momentum space but also showed that different regions of the spectrum have very different eigenfunctions. In the next section, let us therefore discuss all observables together for different regions of the spectrum separately.

15.5. Spectral dependence of observables

Having discussed velocity statistics, energy level statistics as well as individual wavefunctions in the last sections, let us here apply their implications on different parts of the spectrum. The Kullback-Leibler divergence already showed signs of different spectral regions contributing differently to the overall quantities, which is why an energy resolved analysis of all quantities is a necessary endeavor.

Before starting the discussion, let us define more quantitative measurements to describe properties of the individual wavefunctions. As a direct measure of (de-)localization, the inverse participation ratio (IPR) of the wavefunctions has proven to be a useful tool. The IPR quantifies the number of sites over which a wavefunction is spread in real or momentum space [131] and is defined as

$$\text{IPR}(\psi) = \frac{\sum_i |\psi_i|^4}{\sum_i |\psi_i|^2}. \quad (15.5)$$

For a wavefunction that is equally delocalized on N sites, $\psi_i \sim 1/\sqrt{N}$, the IPR can be calculated to be $\text{IPR}(\psi) \sim 1/N$. Therefore, the number of sites that a given wavefunction occupies can be estimated as $N \sim 1/\text{IPR}(\psi)$. In the following, this is used as a quantitative measure of delocalization of individual states in momentum space.

To quantify this emergence of symmetry, let us define a quantitative measure as well. In particular, spatial symmetries will be in the focus of the following discussion. These symmetries are in general defined by a transformation $S : \vec{r}_i \mapsto \vec{r}_j = S(r_i)$. This transformation

defines a symmetry matrix in the basis of the Moiré cell as

$$S_{ij} = \begin{cases} 1 & \vec{r}_j = S(\vec{r}_i) \\ 0 & \text{else} \end{cases} \quad (15.6)$$

i.e. states ψ can be probed to be symmetric under S in terms of checking $S\psi \sim \psi$ or computing $\psi^\dagger S\psi$ as a quantitative measure of the strength of this symmetry. If this number is zero, no symmetry is present as ψ and $S\psi$ remain orthogonal. However if this number is 1, the state is fully symmetric under S .

In the following, we want to focus on the mirror-and-layer-flip symmetry present in twisted bilayer graphene. This symmetry mirrors the lattice around the x -axis as well as exchanges the two layers. Wavefunctions do not necessarily have to fulfill this symmetry but can be probed to what extent they do.

With these definitions in place, observables in three distinct regions of the spectrum have been computed. Data for low-energy bands is shown in Fig. 15.9, data for states around half-filling and the flat bands is shown in Fig. 15.8 and data for states at higher energies is shown in Fig. 15.9. Let us now go through the observables one-by-one, comparing these different spectral regions.

Starting with the analysis of band velocities, depicted in panels b) respectively, one can see that the different branches, already visible in Fig. 15.2 a), can be attributed to different regions of the spectrum. Whereas high energies generally contribute low velocities up to $\mathcal{O}1$, low energy states contribute the two crossing branches at high velocities. Nevertheless, independent of energy, all velocities decrease for increasing value of V , showing a general trend to flatten bands for increasing interlayer couplings.

As a direct measure of delocalization, the data for the IPR depicted in panels c) shows that delocalization in momentum space is in principle present all across the spectrum. This is in agreement with the velocity statistics as the onset of delocalization seen in the IPR is coinciding with a decrease of velocity.

Coming to the Kullback-Leibler divergence depicted in panels e), the three regions seem to behave differently at first glance. Whereas the central and upper parts of the spectrum show Wigner Dyson statistics for intermediate values of tunneling, lower parts of the spectrum seem to host only Poisson statistics for all values of coupling. Furthermore, the trend to fall back to Poisson statistics for strong increase of interlayer tunneling is most pronounced in the upper parts of the spectrum.

However despite these differences, all three regions of the spectrum follow the same general trend. They all show clear Poissonian statistics for no interlayer tunneling, a developing tendency for non-Poissonian behavior when increasing tunneling and finally coming back to Poisson statistics at large values of tunneling. This trend is pronounced differently in all three regions but especially the Kullback-Leibler divergence shows this trend for all

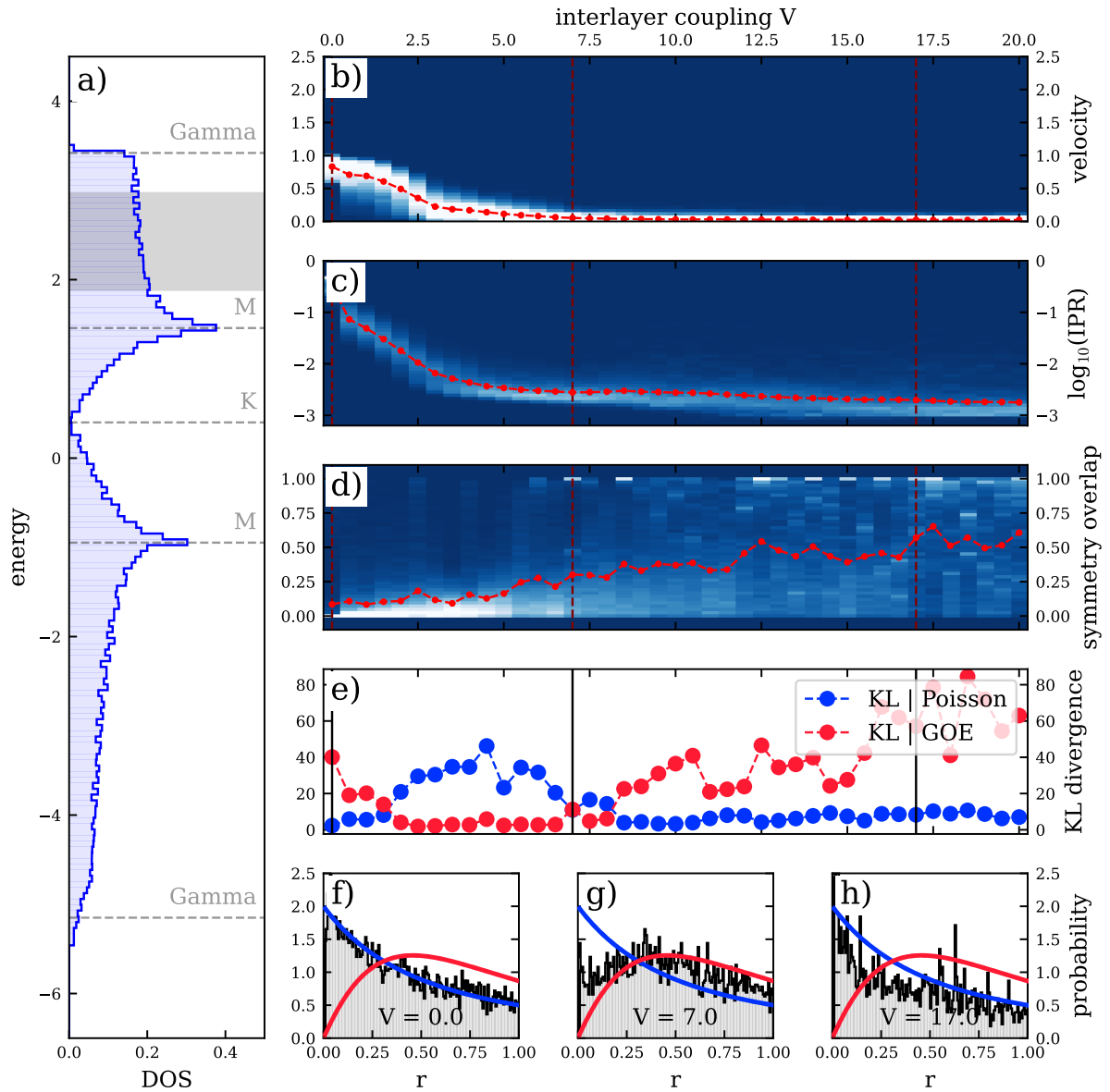


Figure 15.7.: Delocalization at high energies - Panels show statistics for states at high energies, highlighted within the density of states in panel a). Panels b)-d) display statistics of different observables as a function of interlayer coupling V . Histograms of the observables are displayed by color, whereas averages are drawn as a red line. Both velocities (panel b)) and IPR (panel c)) show clear signs of delocalization. This trend is only reflected partly in the Kullback-Leiber divergence of level spacings, displayed in panel e), which finds signatures of Poisson statistics again for larger values of V . However, this trend can be attributed to the role of symmetries which show increased relevance for large V by more finite symmetry overlaps in panel d).

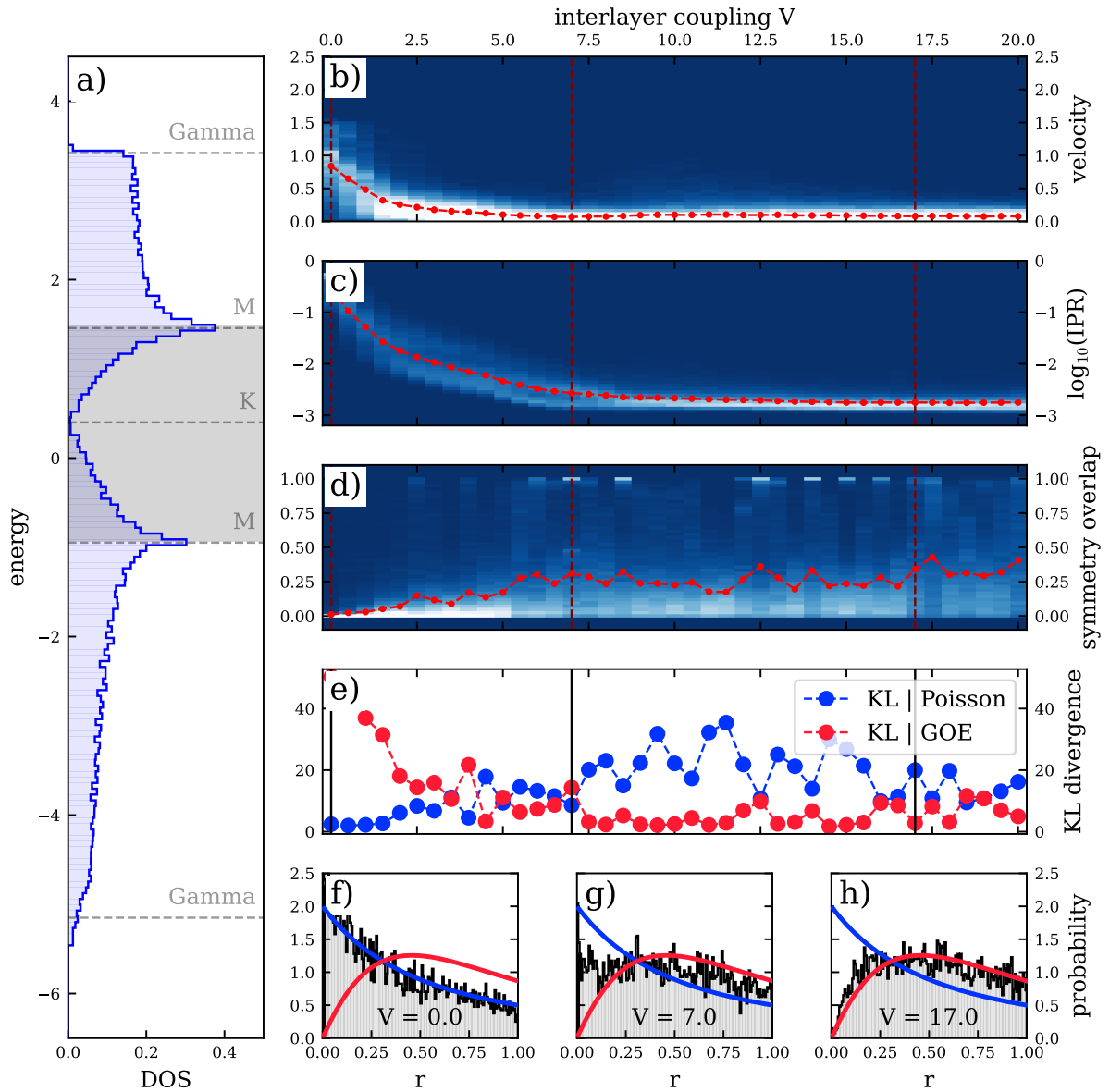


Figure 15.8.: Delocalization around half filling - Panels show statistics for states at medium energies around half filling, highlighted within the density of states in panel a). Panels b)-d) display statistics of different observables as a function of interlayer coupling V . Histograms of the observables are displayed by color, whereas averages are drawn as a red line. Both velocities (panel b)) and IPR (panel c)) show clear signs of delocalization. This trend is mostly reflected in the Kullback-Leiber divergence of level spacings, displayed in panel e). In contrast to the other parts of the spectrum, symmetries play only a reduced role at the investigated values of interlayer coupling V . This is reflected by still retaining the majority of symmetry overlaps near zero in panel d) for large V .

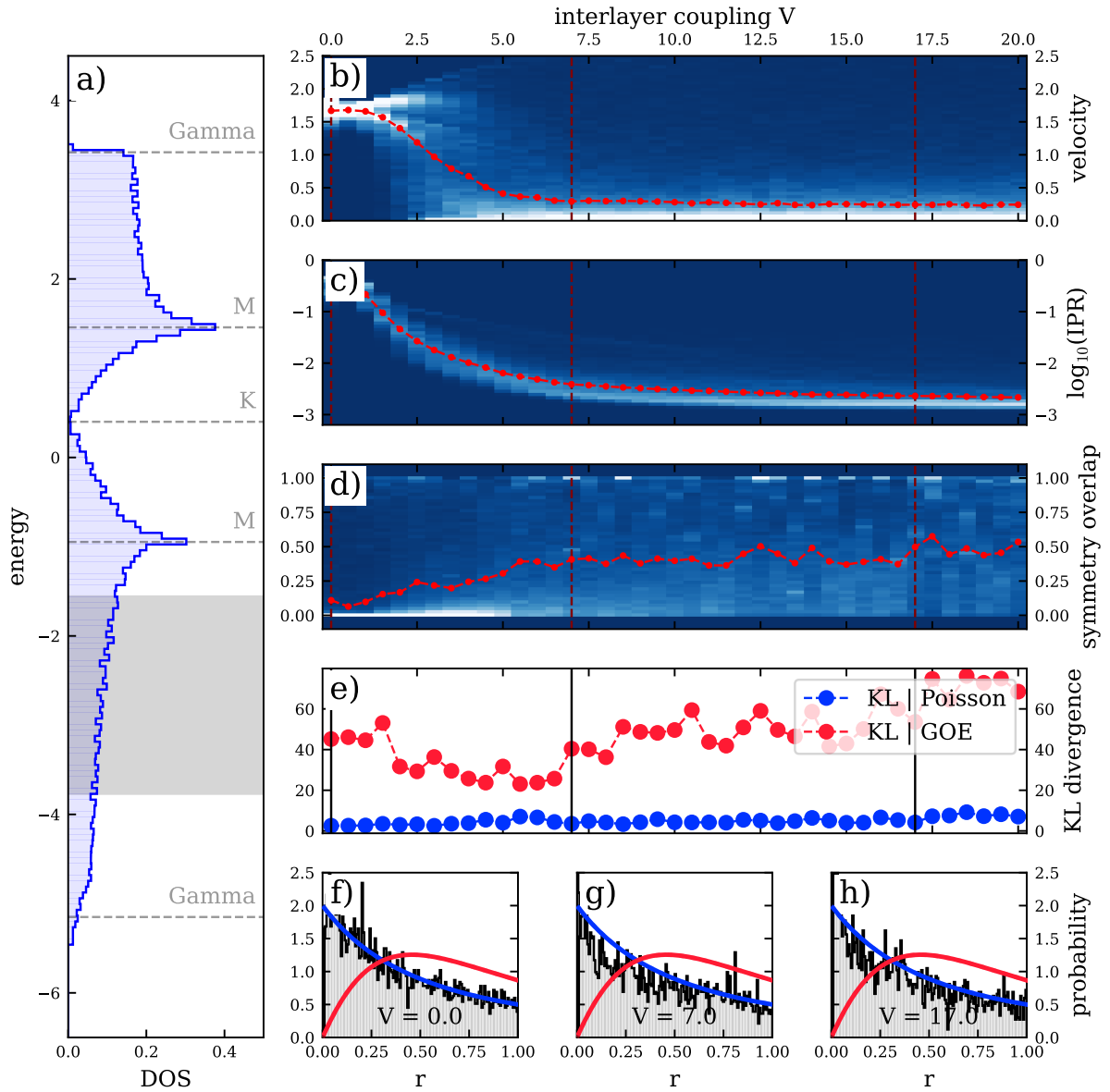


Figure 15.9.: Delocalization at low energies - Panels show statistics for states at low energies, highlighted within the density of states in panel a). Panels b)-d) display statistics of different observables as a function of interlayer coupling V . Histograms of the observables are displayed by color, whereas averages are drawn as a red line. Both velocities (panel b)) and IPR (panel c)) show clear signs of delocalization. This trend is only poorly reflected in the Kullback-Leiber divergence of level spacings which finds signatures of Poisson statistics across all coupling values V . However, it should also be noted that symmetries, depicted in panel d), seem to play a more pronounced role compared to other parts of the spectrum.

regions.

On the level of individual histograms, depicted in panels f) - h) respectively, this trend is reflected. At zero interlayer coupling in panels f) the statistics of level spacings follows a nearly perfect Poisson distribution in all three cases. For higher values of interlayer coupling, the histograms then show partly very clear signs of Wigner-Dyson statistics and partly signs of recovering Poisson statistics, all in agreement with the general KL trend.

Last but not least, let us discuss results for the symmetry overlap $\psi^\dagger S \psi$ which are shown in panels d) respectively. In general, symmetries can be seen to develop consistently for increased interlayer coupling. Although data is not very clean, it becomes apparent that the three regimes show similar behavior while still varying in detail.

In the upper bands of the spectrum, depicted in Fig. 15.7, the Kullback-Leibler divergence previously showed only a narrow window of Wigner Dyson statistics. The fast onset of WD statistics agrees with both IPR falling rapidly as well as symmetry overlaps being mostly zero. However already for $V > 10$, the majority of symmetry overlaps is non-zero which indicate a stronger role of symmetries reflected in Poissonian level statistics.

The central bands of the spectrum, depicted in Fig. 15.8, behave in many ways similar to the upper bands. However, there are two key differences. First of all, the IPR is falling much less rapidly, which is reflected in the Kullback-Leibler divergence transitioning to Wigner Dyson statistics only at intermediate values of V . Secondly, symmetries are much less relevant as the majority of symmetry overlaps stays close to zero even for larger values of V . This agrees nicely with the extended region of WD statistics as shown by the Kullback-Leibler divergence.

Finally, in the lower bands of the spectrum, depicted in Fig. 15.9, symmetries are more relevant as hinted by an increased number of non-zero symmetry overlaps. Also, since the IPR starts dropping slower compared to the other regions, one might conclude that symmetries are more effective at low energies to split the Hilbert space into sub-blocks which effectively prevent the Kullback-Leibler divergence from showing non-Poisson behavior for all coupling values V .

Another helping factor for the lower part of the spectrum might be the presence of harmonic oscillator states which further interfere with level statistics as well as the split of the lower graphene band, which is clearly visible in the velocity statistics. One can therefore conclude that delocalization is also present in the lower bands, but does not show up on the Kullback-Leibler divergence of level statistics due to a number of reasons.

Overall, the data suggests that different regions of the spectrum behave qualitatively the same, however with different signatures in the respective observables. This universal mechanism is layed out in the following section.

15.6. The three regimes of localization

Throughout the previous sections, many observables have contributed to forming a consistent picture of how the transition from a single-layer system to a strongly layer-coupled Moiré system looks like. Initial expectations of interlayer coupling being able to strongly flatten bands already at experimental parameters have been rejected by numerical results and been extended to the picture of Anderson localization in momentum space. Findings through the many observables agree qualitatively very well and follow a generic trend suitable for most Moiré materials that is described in the following as the *three regimes of localization*. In principle, the three regimes of localization describe the tendency of wavefunctions to (de-)localize in momentum space for a certain interlayer coupling which in return leads to a mixing and repulsion of levels.

Regime I, small interlayer coupling – For small interlayer coupling, energy spectra of the Moiré system remain close to their original single-layer dispersion. Energy levels cross because of backfolding into the Moiré (unit) cell but are not mixing. In momentum space, the Moiré system is represented by weak hopping between momentum sites which results in effective localization to a certain momentum.

Regime II, medium interlayer coupling – For intermediate values of interlayer coupling, e.g. close to experimental values in twisted bilayer graphene, the system is stronger exerted to the Moiré potential. Energies are already influenced stronger by the interlayer coupling, e.g. as seen as the split of the lower band in twisted bilayer graphene, however neighboring levels are not yet effectively coupled. The lack of level mixing originates from a momentum space mechanism. Here, hopping between momentum sites grows and leads to a delocalization in momentum space. However, since the momentum on-site potential given by the single-layer dispersion is still relevant, the delocalization only happens along equal-energy contours of the initial single-layer dispersion. Incomplete delocalization along these contours necessarily still retains the finite band velocity of states and also preserves level crossings in the spectrum.

Regime III, strong interlayer coupling – For high values of interlayer coupling, states of the Moiré system become more and more delocalized in momentum space as the hopping between momentum sites is far greater than any quasi-random on-site potential. This reduces band velocities as well as introducing mixing between neighboring levels, leading to an effective level repulsion within the spectrum. While wavefunctions spread out in momentum space, the effect of disorder weakens and crystalline symmetries develop. These symmetries are dividing the Hamiltonian into blocks which prohibits level crossings between levels of different blocks entirely, resulting in Poissonian level statistics despite fully delocalized states with vanishing velocity.

In principle, the behavior in different parts of the spectrum follows the three regimes as shown by all observables. However, quantitative predictions in the different parts might be more nuanced as the regime boundaries depend on many parameters. For high energies (upper bands) a very fast transition through the regimes occurs where symmetries only become relevant for high coupling values and are overall not pronounced strongly compared to other parts of the spectrum. For medium energies (bands close to half filling) one can observe a pronounced transition through the three regimes, especially since symmetries only become relevant for very high coupling values. Thus, an extended delocalized phase can be seen for intermediate interlayer coupling. For low energies (lowest bands) the transition can only be seen in velocities and momentum space occupation. Kullback-Leibler divergence does not show any trace of level repulsion due to a number of reasons. For once, symmetries are more pronounced even at lower interlayer coupling, also other states such as harmonic oscillator ladder states interfere with the spectrum to effectively prohibit the development of Wigner Dyson level statistics.

Apart from this general trend, the remainder of this chapter is used to describe those states within the bandstructure that do not follow this general mechanism. As seen in Fig. 15.10 f), twisted bilayer graphene can in principle host two regions of vanishing velocities. For once, there is the celebrated magic angle flat band in the center of the spectrum, visualized in panels a) and b) of Fig. 15.10. Secondly, the band bottom of the upper split of the lower graphene band gives rise to equally spaced states with zero velocities, seen in panel c) and d) of Fig. 15.10. These states can be identified as harmonic oscillator states whose occurrence is naturally linked to the momentum space picture and the band minimum. The following two sections are dedicated to discuss these two cases of anomalously flat bands in greater detail.

15.7. Anomalously flat bands: Magic angle flat bands

Let us start the discussion of anomalously flat bands with the well-known example of magic angle flat bands, indicated in panels a) and b) of Fig. 15.10. These bands occur in the center of the spectrum at half filling and only turn extremely flat for a specific angle. More precisely, the bandwidth of these central bands has a series of minima close to zero for a set of special angles, so-called magic angles. In experiments, these small bandwidths are observed as well.

In the present calculations, magic angle flat bands only occur at a twist angle of $\sim 1.2^\circ$ which is given by the commensurate pair $m = 27, n = 26$. Fig. 15.11 shows bandstructures and corresponding density of states for a set of angles which decreases from top to bottom beyond the magic angle of $\sim 1.2^\circ$. One can observe that the central bands are only flat and separated from the rest of bands at the magic angle but start to mix with other bands again for larger angles. The separation itself originates from a finite corrugation as without such corrugation, the central bands do not exhibit a band gap to the rest of the spectrum

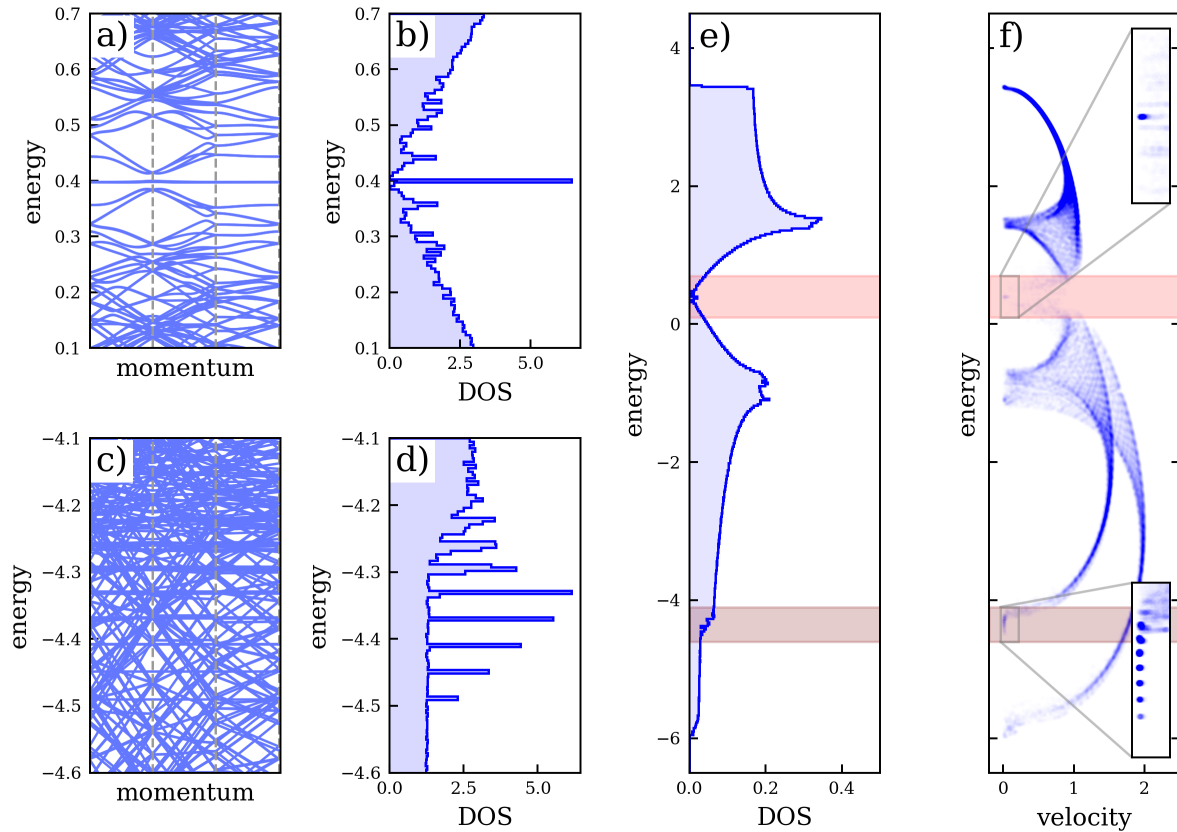


Figure 15.10.: Anomalous flat bands - Data for the experimental parameter set of twisted bilayer graphene, panels a)+c) show parts of the bandstructure, panels b),d) and e) show the density of states, panel f) shows band velocities as function of energy. Two anomalously flat regions emerge in the spectrum: magic angle flat bands (c.f. panels a)+c) which show data from the upper highlighted area of e) and f)) as well as harmonic oscillator ladder states (c.f. panels c)+d) which show data from the lower highlighted part of e) and f)).

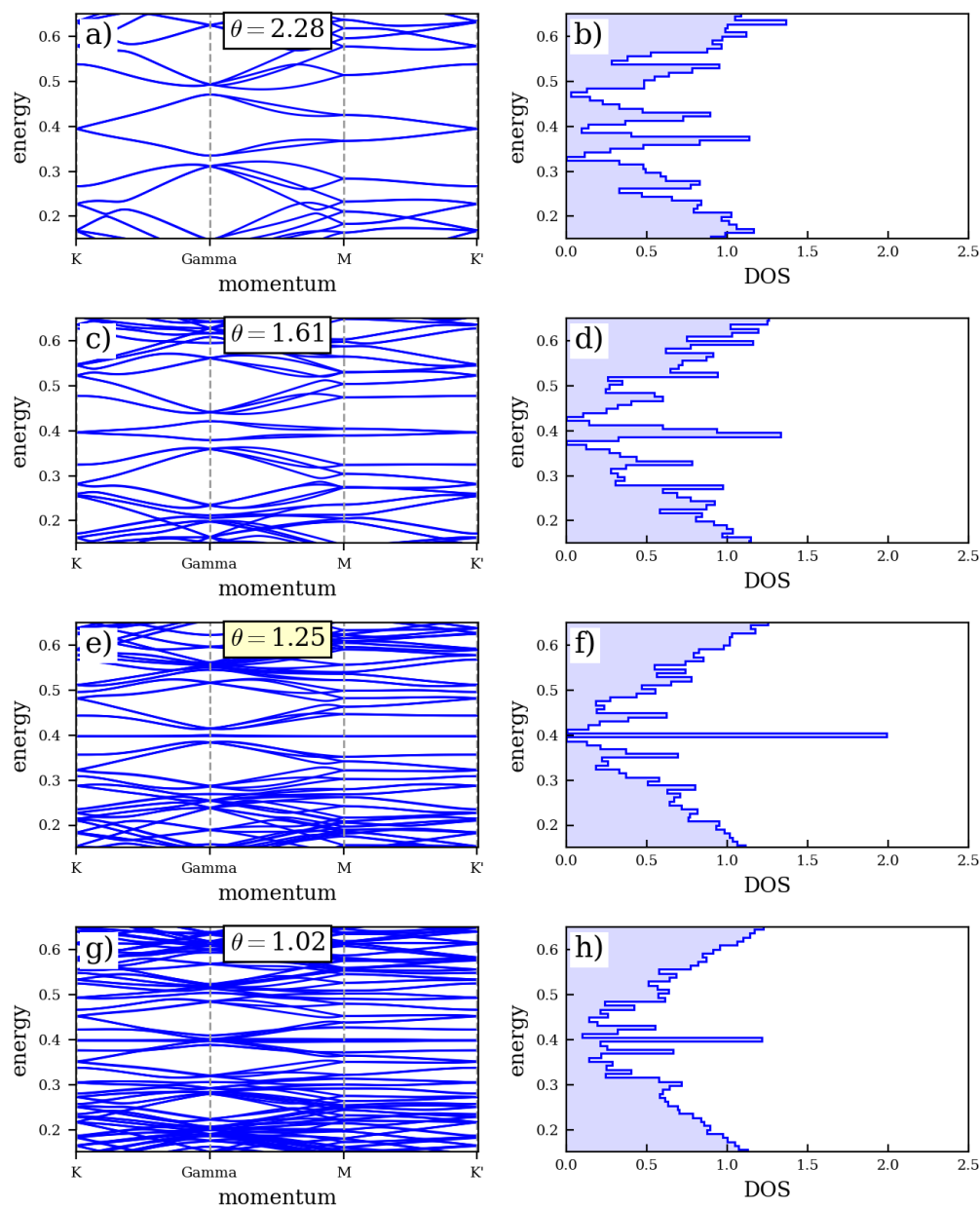


Figure 15.11.: Formation of magic flat bands - Sequence of bandstructures of twisted bilayer graphene with corresponding density of states. The twist angle θ is decreased from top to bottom. At the angle of $\theta = 1.25^\circ$ (corresponding to $m = 27, n = 26$), displayed in panels e) and f), the bandwidth of the flat bands is minimized and starts to increase upon further decrease of angle. This corresponds to the magic angle condition seen in experiments and proceeding studies.

but are still flat at the magic twist angle.

In principle, the magic flat bands can also occur at different angles, however only through fine-tuning of other coupling parameters. In this regard, one can understand the angle of $\sim 1.2^\circ$ as the magic angle for the experimental parameter set. In real experiments, the magic angle is also slightly smaller at around $\sim 1.1^\circ$ which can be traced back to effects of relaxation which are not included into the real space model at hand.

At this point, one might wonder if the magic angle flat bands can also be described in terms of the Anderson localization mechanism in momentum space, discussed in the previous section. The answer to this is both yes and no.

In principle, the flat bands are localized at the K points in momentum space which means that the graphene dispersion of their specific energy is not a 1d contour (which it is for all other energies) but a single point. Therefore, true two-dimensional delocalization in momentum space can already occur for small values of interlayer coupling, i.e. the magic angle flat bands don't have to traverse the three regimes of localization laid out before. One can thus conclude that magic angle flat bands are in general allowed as flat bands within the spectrum.

However, it is well-known that the magic angle flat bands only turn flat at certain magic angles. This cannot be reproduced in terms of the Anderson localization scheme discussed previously. One can argue that from this localization point of view, there is now special reason why the bands should be flat generically or why they should not, i.e. one has to conclude that the magic angle flat bands are indeed flat magically.

15.8. Anomalously flat bands: Harmonic oscillator states

The second region of anomalously flat bands within the spectrum of twisted bilayer graphene can be found at the band bottom of the upper split of the lower graphene band. This region hosts equally spaced states with zero velocity as shown in panels c) and d) of Fig. 15.10. As having noticed in previous sections, these states emerge for an increase in interlayer coupling and appear in various parameter regimes, in contrast to the magic angle flat bands.

Qualitatively these bands are far more abundant than the magic angle flat bands as illustrated in Fig. 15.12. Here, three vastly different parameter sets are compared with respect to the emergence of equally spaced flat bands. One can observe a different spacing between levels as well as a different number of total levels, however the feature of equally spaced states remains the same.

Another observation in numerics is the degeneracy of these bands. If one concentrates on a single value of \vec{k} , the lowest of these levels is not degenerate, the second level is shared between two states, the third level by three and so on. In general one observes that the

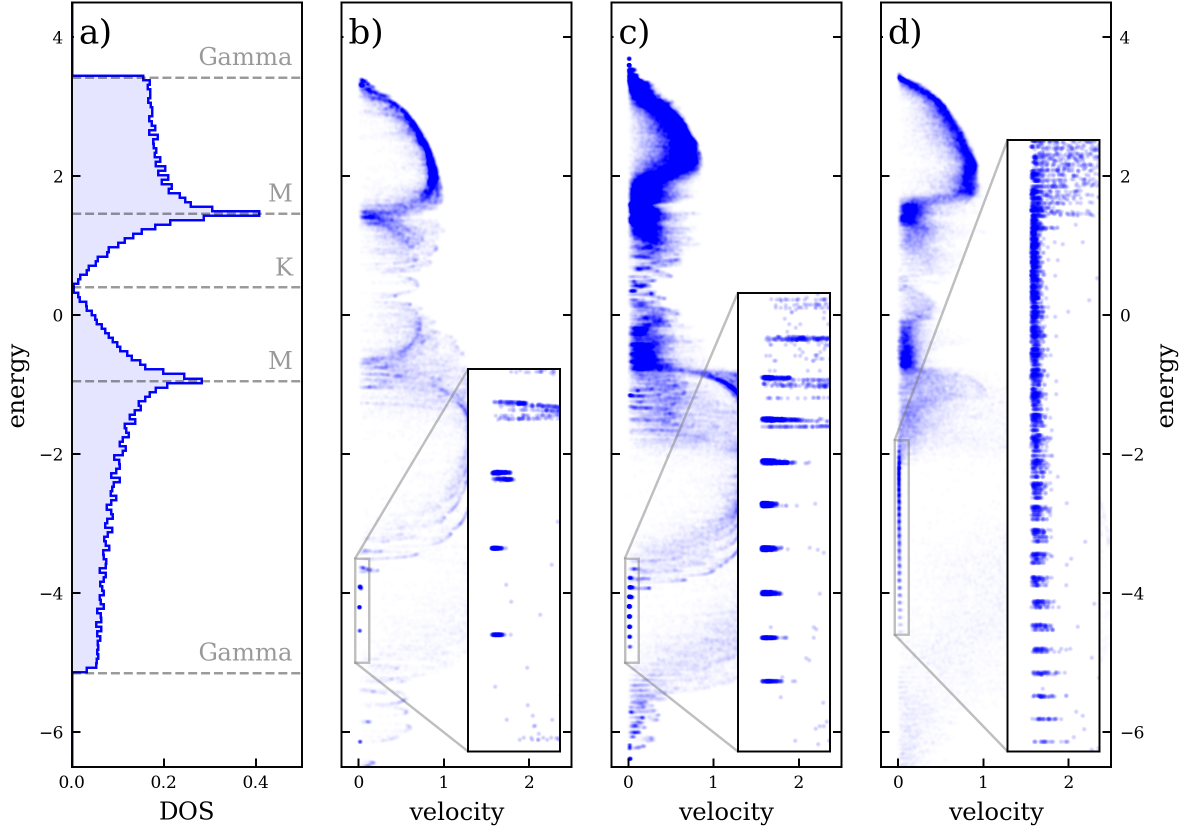


Figure 15.12.: Harmonic oscillator ladders - Velocity statistic data for twisted bilayer graphene systems of different angle, atomic overlap and layer geometry. Each system exhibits the same tendency to form harmonic oscillator states at the upper split of the Γ point. Harmonic oscillator spacing depends on angle as well as on other coupling parameters, therefore varies in between the plots.

n th level is n -fold degenerate.

The degeneracy of levels as well as the equal spacing reveals resemblance to generic harmonic oscillator levels. Upon close inspection, these levels can indeed be understood in terms of eigenstates of a harmonic oscillator in momentum space as the following argument reveals. Previous sections already introduced the core concept of identifying the Moiré problem with those of a hopping Hamiltonian in momentum space where hopping was given by the interlayer coupling V and where the on-site potential was given by the original single-layer dispersion $\varepsilon(\vec{k})$. Applying this argument to the bottom of the graphene bands leads to a hopping problem with a leading-order quadratic potential, i.e. a harmonic oscillator.

More precisely, the potential in momentum space will take the form $\varepsilon(\vec{k}) \sim G_M^2/m$ near the band minimum where m denotes the local curvature. Since hopping in momentum space

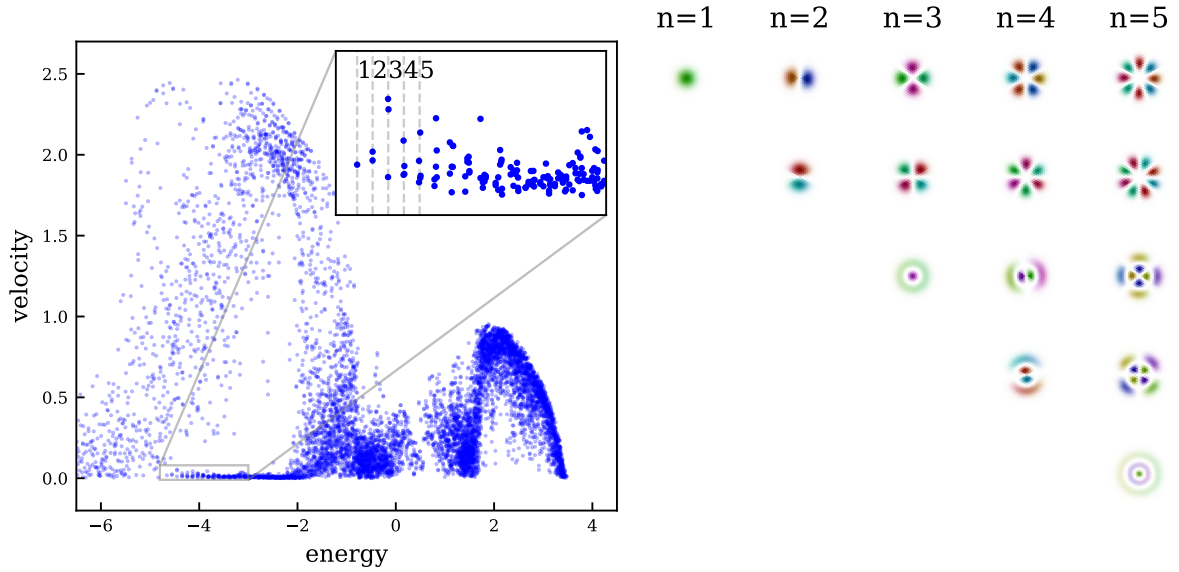


Figure 15.13.: Harmonic oscillator wavefunctions - Eigenstates of the $m = 27$ system show resemblance with harmonic oscillator levels. Their energies are degenerate with degree n in level n . Here, wavefunctions are shown up to $n = 5$ in correspondence to the energy-velocity plot discussed before. Colors in the wavefunctions correspond to their complex phase.

is given by the interlayer coupling denoted by V , the harmonic oscillator frequency can be roughly estimated to be $\omega \sim \sqrt{VG_m^2/m} \sim \sqrt{V}/L$. The dependence $\omega \sim 1/L$ can also be seen qualitatively in Fig. 15.12 where the largest spacing between levels was observed for the largest angle, which corresponds to the smallest value of linear Moiré cell size L .

The last piece of well-fitting resemblance with a true harmonic oscillator are the wavefunctions of the states themselves. In general, these wavefunctions show little to no variation upon change of parameters as well as a striking difference from the usual twisted bilayer wavefunctions. A set of wavefunctions for the levels $n = 1$ up to $n = 5$ can be found in Fig. 15.13.

In terms of universality, the harmonic oscillator states are to some extent generically appearing at the band bottom. The main ingredients, a quadratic band minimum as well as hopping in momentum space, are very likely to be present in most Moiré systems. However, one last key ingredient for the clean appearance of these states is missing. This becomes apparent from the observation that harmonic oscillator states are not developing equally in both the upper and lower band minimum in twisted bilayer graphene.

The difference between the band minima in the upper and lower split of the band is their localization center within the real space unitcell. While the lower band features localization within the AB regions of the Moiré cell, the upper band has states that are localized in

the AA regions. The regions themselves differ in symmetry. Whereas the AA regions are nearly rotationally symmetric, the AB regions have more of a six-fold rotational symmetry. This difference seems to translate to the harmonic oscillator states as well since one finds six-fold degenerate states at the bottom of the spectrum, but harmonic oscillator ladders at the bottom of the other split.

Still approximate rotational symmetry around some center of the Moiré pattern is realized in many materials and as such one can expect the ladder of harmonic oscillator states to appear in other systems beyond twisted bilayer graphene as well.

16. Summary and discussion

In summary, Ref. [P8] as well as this chapter provided a statistical description of bandstructures in twisted bilayer graphene to investigate the localization behavior of states. The investigation was driven by the initial observation that incommensurabilities between the single-layer lattice periodicities of the twisted layers act as an efficient source of disorder and therefore should lead to level repulsion within the bandstructure. Although calculations have been specific to this single system, similarities in modeling suggest that they extend to generic Moiré systems alike.

In total, many different observables have been calculated within the real-space model of twisted bilayer graphene yielding results that allow for the definition of three distinct regimes of localization in momentum space. *Regime I* is characterized by small interlayer coupling and corresponding strong localization in momentum space. Energy spectra within this regime show no sign of level repulsion. In *regime II*, an increase in interlayer coupling leads to effective delocalization of states along the one-dimensional Fermi lines in momentum space. As a consequence, states become correlated and levels in the bandstructures have a tendency to avoid crossings. In *regime III*, the delocalization in momentum space is enhanced by even stronger interlayer coupling. However, the strong coupling also enhances the importance of internal symmetries which divide the Hilbert space into blocks and hamper the development of global level repulsion as individual blocks become independent and do not interact. Nonetheless, levels are still mostly flat and avoid crossings within their respective Hilbert space blocks.

Apart from the general localization-delocalization mechanism, two types of non-generic flat bands have been identified. First, the celebrated magic angle flat bands have been found to be indeed of special origin. On first glance, they do not show a transition through the three regimes. This exception can be explained by the fact that their Fermi surface is given solely by the Dirac point and delocalization in momentum space can therefore immediately occur in two dimensions. The other type of flat bands are harmonic oscillator states which form at the bottom of bands. Increases in interlayer coupling lead to a pronounced developing of these bands, although their experimental relevance is questionable as they lie deep within the bandstructure far away from the Fermi energy.

In comparison to Ref. [P8], this chapter provided a slightly different perspective on the localization mechanism. Whereas Ref. [P8] mainly discussed results obtained by the momentum space continuum model, this chapter aimed at providing results from the real-space perspective. Altogether, both models give similar results while approaching calculations from different limits. Whereas the momentum space model is inherently defined for small

twist angles, the real-space model works best at large twist angles which correspond to small Moiré cells yielding matrices that can still be exactly diagonalized. However, the exact diagonalization also has the benefit of yielding the entire bandstructure in the real-space model, whereas the continuum model only describes the vicinity of the flat bands and therefore can only probe behavior in the center of the spectrum.

Concerning results, both models reach their limits in the scope of this chapter and Ref. [P8]. The momentum space model, discussed in Ref. [P8], captures the transition through the three regimes in the vicinity of the flat bands. In comparison, results utilizing the real-space model are lacking in the number of independent momenta, which are limited by numerical reasons, as well as struggling with interpretations as different regions of the spectra transition through the three regimes at different rates. Still, the three regimes could be resolved in the real-space model through the entire spectrum. All in all, both models complement each other very well and in combination can give much insight into the physics of twisted bilayer graphene and Moiré systems in general.

Coming back to the initial question about how flat bands generically evolve in Moiré systems, one can argue that all Moiré materials should follow the localization transition of the three regimes. Details may vary as the individual single-layer dispersions vary between different compounds, however the sequence of regimes appears to be universal. It is therefore necessary to reach regime III in a material to generally find flat bands. This can either be done by extraordinary high values of interlayer tunneling or by doping to a small Fermi surface and therefore facilitating momentum space delocalization away from the Fermi surface for much lower values of interlayer coupling, similar to the magic angle flat bands in twisted bilayer graphene.

Yet another approach for more level flatness is to implement long-ranged momentum space hopping. Such a hopping could greatly improve the delocalization abilities of wavefunctions in momentum space. To implement this kind of hopping in a material, one had to implement short-ranged real-space structures, like individual atoms that share the periodicity of the Moiré.

All in all, the localization process of the three regimes offers a broadly applicable tool to design new flat-band Moiré materials based on already existing compounds as it offers a qualitative description of how flat bands can form in these systems.

17. General concluding remarks

In summary, this thesis showed the relevance of electronic spectra and their numerical solution. Throughout the chapters, examples from different areas of Condensed Matter Physics have been discussed, including variations to particle number and system size. In total, each example highlighted a different aspect of electronic spectra taking yet another perspective on their solution.

In Part I about RIXS, the focus has been set on measuring electronic spectra of many particles at the example of Iridate materials with partially filled d -shells. To this extent, the electronic structure was calculated numerically first by exact diagonalization techniques. Then in a subsequent step, the numerical eigenstates have been used together with geometrical information to obtain a numerical approximation to the RIXS scattering process and corresponding scattering intensities which were further compared to experimental spectra.

These methods could be applied to a variety of different materials, including systems with a single or more Ir sites per cluster. A general trend in this part was to examine the formation of effective $j = 1/2$ moments under strong spin-orbit coupling and Hubbard interaction as well as their delocalization under hopping on the cluster. Such effective $j = 1/2$ states played an important role in the formation of so-called Kitaev systems, which mark a natural incarnation of a spin system exhibiting a spin-liquid ground state. All in all, the first part demonstrated how a versatile numerical approach to electronic spectrum calculation can be used to probe the building blocks of topological models on a fundamental level.

In Part II, focus shifted towards the application of supersymmetry in electronic spectra. In practice, this shift was accompanied by going from many fully interacting particles on a small cluster to a single non-interacting particle on an infinite periodic lattice. It was then demonstrated that the resulting electronic band structures could be mapped to related bosonic lattice systems by employing supersymmetry. In particular, supersymmetry was shown to be acting as a graph correspondence which greatly simplified the mapping process.

The applicability of such mappings was demonstrated in two examples. For the first example, a lattice model of complex fermions was shown to be corresponding to a lattice model of complex bosons when their two lattices could be casted as the two sublattices of a bipartite lattice. In the second example, a model of Majorana (real) fermions on a bipartite lattice was demonstrated to be connected to a model of real bosons on one of its sublattices. This correspondence also implied a connection to a classical mechanical system, a natural mechanical counterpart of the real boson system. In particular it was

shown that the mechanical system exhibited signs of topological features, previously only present in the Majorana fermion spectrum.

In Part III of this thesis, the investigation of electronic spectra shifted towards Moiré systems which are characterized by a large number of electronic bands stemming from enlarged unitcells. This complexity in the huge number of bands was shown to be encapsulated in a statistical description of the electronic band structure and in particular in the formation of flat bands.

Calculations at the example of twisted bilayer graphene (TBG) were used to investigate the statistics of energy bands, allowing to find an Anderson localization mechanism in momentum space that generically flattens bands by increased Moiré potential. Although the celebrated magic angle flat bands of TBG evade this mechanism, it still presents a basis for other Moiré systems and therefore generically exhibits a broad applicability.

Beyond those three examples, it is worth noting that in the context of this thesis two big code projects have been developed. The first is the Julia package `RIXSCalculator.jl` [S1] which can be utilized to exactly diagonalize multi-particle Hamiltonians for systems on localized clusters. Second, for lattice based calculations the package `LatticePhysics.jl` [S3] has been implemented. This code project focuses on a graph representation of lattices with particular applications in bandstructure calculations, employed both in the context of supersymmetric bandstructures as well as Moiré bandstructures.

Already from looking at the code projects, it becomes apparent that there is a mutual overlap between the different projects. Therefore, one might naturally ask about connections between the chapters which also provide a basis for future work.

Starting with the methods of calculating many-particle electronic spectra, as used in the first part of this thesis about RIXS, those calculations are challenging to extend beyond small clusters as the numerical complexity grows exponentially in the number of single-particle states. For this reason, discussing entire lattice models as done in the second part of the thesis about supersymmetry, on the level of many particles, might not be feasible at all. However, it might be an option to incorporate the single-particle structure underlying the individual Ir sites, into bandstructure calculations. Such an extension could be again rephrased in a graphical way as a multi-layered material and might hold future applications of supersymmetric relations alike. The combination between spin-orbit coupled moments which hop on an infinite lattice might thus be hosting interesting connections to certain bosonic models as well. How these aspects hold up under the presence of strong Hubbard interaction however is yet to be seen.

Concerning a second possible connection between supersymmetry and Moiré systems, one can first acknowledge that in this thesis computations in both parts are carried out utilizing the same optimized code package for band structure calculations, `LatticePhysics.jl`. However, the two projects reside in different limits of calculations: whereas the supersymmetric bandstructures utilize typically few interactions but are explicitly handling individual bonds or plaquettes, Moiré systems are hosting a multitude of different interactions

and rely to a large extent on geometric information of hoppings. Especially the number of interactions in a Moiré system prevents finding suitable plaquette substitution rules which would allow the identification of a graphical SUSY partner system. However, yet another system which is in close relation to Moiré systems might prove more fruitful: quasi-crystals. Such systems are defined by a repetitive tiling of the plane in absence of strict periodicity. The big structural extent can lead naturally to a multitude of different states. As quasi crystals still only have a small local connectivity one might expect them to be the perfect basis for a mix of statistical analysis and supersymmetry. Here, it might be possible to find supersymmetrically related quasi-crystals solely based on the local interaction geometry by just replacing plaquettes or z -coordinated sites. In this context, fascinating questions might arise which connect electronic states in quasi-crystals to bosonic ones.

Lastly, the statistical approach of quantum chaotic systems, discussed in the third part of this thesis about Moiré systems, might pose the potential of further applications to other parts within this thesis. Note that since in principle supersymmetry preserves the energy spectrum (apart from adding flat bands at the bottom), supersymmetry generally preserves the level statistics, yielding direct implications for bosonic systems as a consequence. Moreover, applying these principles to the multitude of many-particle bands in the systems discussed in the RIXS part might be helpful in determining different regimes or hidden transitions. In this case, the level statistics would be rather treated as a numerical tool than a spectroscopic measure but could give insights nonetheless.

All in all, the three parts and their intimate connections hint that there are still various aspects of electronic spectra unexplored today and that exact diagonalization techniques as employed in this thesis can go a long way in providing long sought-after solutions.

Bibliography

- [P1] A. Revelli, C. C. Loo, D. Kiese, P. Becker, T. Fröhlich, T. Lorenz, M. Moretti Sala, G. Monaco, F. L. Buessen, J. Attig, M. Hermanns, S. V. Streltsov, D. I. Khomskii, J. Van Den Brink, M. Braden, P. H. Van Loosdrecht, S. Trebst, A. Paramakanti, and M. Grüninger, “Spin-orbit entangled $j=1/2$ moments in $\text{Ba}_2\text{CeIrO}_6$: A frustrated fcc quantum magnet”, *Physical Review B* **100**, 085139 (2019).
- [P2] A. Revelli, M. M. Sala, G. Monaco, M. Magnaterra, J. Attig, L. Peterlini, T. Dey, A. A. Tsirlin, P. Gegenwart, T. Fröhlich, M. Braden, C. Grams, J. Hemberger, P. Becker, P. H. M. van Loosdrecht, D. I. Khomskii, J. v. d. Brink, M. Hermanns, and M. Grüninger, “Quasi-molecular electronic structure of the spin-liquid candidate $\text{Ba}_3\text{InIr}_2\text{O}_9$ ”, still in preparation during the writing of this thesis, [10.48550/ARXIV.2207.04795](https://arxiv.org/abs/10.48550/ARXIV.2207.04795) (2022).
- [P3] P. Warzanowski, N. Borgwardt, K. Hopfer, J. Attig, T. C. Koethe, P. Becker, V. Tsurkan, A. Loidl, M. Hermanns, P. H. M. van Loosdrecht, and M. Grüninger, “Multiple spin-orbit excitons and the electronic structure of $\alpha\text{-RuCl}_3$ ”, *Physical Review Research* **2**, 042007 (2020).
- [P4] K. Roychowdhury, J. Attig, S. Trebst, and M. J. Lawler, “Supersymmetry on the lattice: Geometry, Topology, and Spin Liquids”, still in preparation during the writing of this thesis, [10.48550/ARXIV.2207.09475](https://arxiv.org/abs/10.48550/ARXIV.2207.09475) (2022).
- [P5] J. Attig, K. Roychowdhury, M. J. Lawler, and S. Trebst, “Topological mechanics from supersymmetry”, *Physical Review Research* **1**, 032047 (2019).
- [P6] J. Attig and S. Trebst, “Classical spin spirals in frustrated magnets from free-fermion band topology”, *Physical Review B* **96**, 085145 (2017).
- [P7] F. Freyer, J. Attig, S. Lee, A. Paramakanti, S. Trebst, and Y. B. Kim, “Two-stage multipolar ordering in $\text{PrT}_2\text{Al}_{20}$ Kondo materials”, *Physical Review B* **97**, 115111 (2018).
- [P8] J. Attig, J. Park, M. M. Scherer, S. Trebst, A. Altland, and A. Rosch, “Universal principles of moiré band structures”, *2D Materials* **8**, 044007 (2021).

- [S1] J. Attig and L. Peterlini, *RIXSCalculator.jl*, GitHub repository, (2021)
<https://github.com/janattig/RIXSCalculator.jl>.
- [S2] J. Attig and L. Peterlini, *RIXSPlotter.jl*, GitHub repository, (2021)
<https://github.com/janattig/RIXSPlotter.jl>.
- [S3] J. Attig, *LatticePhysics.jl*, GitHub repository, (2021)
<https://github.com/janattig/LatticePhysics.jl>.
- [1] J. G. Rau, E. K.-H. H. Lee, and H.-Y. Y. Kee, “Spin-Orbit Physics Giving Rise to Novel Phases in Correlated Systems: Iridates and Related Materials”, *Annual Review of Condensed Matter Physics* **7**, 195–221 (2016).
- [2] W. Witczak-Krempa, G. Chen, Y. B. Kim, and L. Balents, “Correlated quantum phenomena in the strong spin-orbit regime”, *Annual Review of Condensed Matter Physics* **5**, 57–82 (2014).
- [3] A. Kitaev, “Anyons in an exactly solved model and beyond”, *Annals of Physics* **321**, 2–111 (2006).
- [4] G. Jackeli and G. Khaliullin, “Mott insulators in the strong spin-orbit coupling Limit: From Heisenberg to a Quantum Compass and Kitaev Models”, *Physical Review Letters* **102**, 017205 (2009).
- [5] B. J. Kim, H. Jin, S. J. Moon, J. Y. Kim, B. G. Park, C. S. Leem, J. Yu, T. W. Noh, C. Kim, S. J. Oh, J. H. Park, V. Durairaj, G. Cao, and E. Rotenberg, “Novel $j_{\text{eff}}=1/2$ mott state induced by relativistic spin-orbit coupling in Sr₂IrO₄”, *Physical Review Letters* **101**, 10.1103/PhysRevLett.101.076402 (2008).
- [6] B. J. Kim, H. Ohsumi, T. Komesu, S. Sakai, T. Morita, H. Takagi, and T. Arima, “Phase-sensitive observation of a spin-orbital Mott state in Sr₂IrO₄”, *Science* **323**, 1329–1332 (2009).
- [7] G. Khaliullin, “Orbital order and fluctuations in Mott insulators”, in *Progress of Theoretical Physics Supplement*, Vol. 160 (2005), pp. 155–202.
- [8] G. Chen and L. Balents, “Spin-orbit effects in Na₄Ir₃O₈: A hyper-kagome lattice antiferromagnet”, *Physical Review B - Condensed Matter and Materials Physics* **78**, 10.1103/PhysRevB.78.094403 (2008).
- [9] A. Revelli, M. Moretti Sala, G. Monaco, P. Becker, L. Bohatý, M. Hermanns, T. C. Koethe, T. Fröhlich, P. Warzanowski, T. Lorenz, S. V. Streltsov, P. H. van Loosdrecht, D. I. Khomskii, J. van den Brink, and M. Grüninger, “Resonant inelastic

- x-ray incarnation of Young’s double-slit experiment”, *Science Advances* **5**, eaav4020 (2019).
- [10] D. I. Khomskii, *Transition metal compounds* (Cambridge University Press, 2014), pp. 1–485.
- [11] L. J. Ament, G. Khaliullin, and J. Van Den Brink, “Theory of resonant inelastic x-ray scattering in iridium oxide compounds: Probing spin-orbit-entangled ground states and excitations”, *Physical Review B - Condensed Matter and Materials Physics* **84**, 020403 (2011).
- [12] J. G. Rau, E. K. H. Lee, and H. Y. Kee, “Generic spin model for the honeycomb iridates beyond the Kitaev limit”, *Physical Review Letters* **112**, 10.1103/PhysRevLett.112.077204 (2014).
- [13] N. B. Perkins, Y. Sizyuk, and P. Wölfle, “Interplay of many-body and single-particle interactions in iridates and rhodates”, *Physical Review B* **89**, 035143 (2014).
- [14] A. Revelli, M. M. Sala, G. Monaco, P. Becker, M. Hermanns, P. Warzanowski, T. Lorenz, D. Khomskii, P. van Loosdrecht, J. van den Brink, and M. Grüninger, “Role of disorder in the quantum magnet $\text{Ba}_3\text{Ti}_3\text{-xIrxO}_9$ revealed by RIXS”, still in preparation during the writing of this thesis (2020).
- [15] A. Revelli, M. Moretti Sala, G. Monaco, C. Hickey, P. Becker, F. Freund, A. Jesche, P. Gegenwart, T. Eschmann, F. L. Buessen, S. Trebst, P. H. M. van Loosdrecht, J. van den Brink, and M. Grüninger, “Fingerprints of Kitaev physics in the magnetic excitations of honeycomb iridates”, *Physical Review Research* **2**, 10.1103/physrevresearch.2.043094 (2020).
- [16] Y. Doi and Y. Hinatsu, “The structural and magnetic characterization of 6H-perovskite-type oxides $\text{Ba}_3\text{LnIr}_2\text{O}_9$ ($\text{Ln} = \text{Y}$, lanthanides)”, *Journal of Physics Condensed Matter* **16**, 2849–2860 (2004).
- [17] T. Sakamoto, Y. Doi, and Y. Hinatsu, “Crystal structures and magnetic properties of 6H-perovskite-type oxides $\text{Ba}_3\text{M}_2\text{Ir}_2\text{O}_9$ ($\text{M} = \text{Mg}$, Ca , Sc , Ti , Zn , Sr , Zr , Cd and In)”, *Journal of Solid State Chemistry* **179**, 2595–2601 (2006).
- [18] T. Dey, M. Majumder, J. C. Orain, A. Senyshyn, M. Prinz-Zwick, S. Bachus, Y. Tokiwa, F. Bert, P. Khuntia, N. Büttgen, A. A. Tsirlin, and P. Gegenwart, “Persistent low-temperature spin dynamics in the mixed-valence iridate $\text{Ba}_3\text{InIr}_2\text{O}_9$ ”, *Physical Review B* **96**, 174411 (2017).
- [19] A. Nag, S. Middey, S. Bhowal, S. K. Panda, R. Mathieu, J. C. Orain, F. Bert, P. Mendels, P. G. Freeman, M. Mansson, H. M. Ronnow, M. Telling, P. K. Biswas, D. Sheptyakov, S. D. Kaushik, V. Siruguri, C. Meneghini, D. D. Sarma, I. Das-

- gupta, and S. Ray, “Origin of the Spin-Orbital Liquid State in a Nearly $J=0$ Iridate $Ba_3ZnIr_2O_9$ ”, *Physical Review Letters* **116**, 097205 (2016).
- [20] A. Nag, S. Bhowal, M. M. Sala, A. Efimenko, I. Dasgupta, and S. Ray, “Hopping-Induced Ground-State Magnetism in 6H Perovskite Iridates”, *Physical Review Letters* **123**, 017201 (2019).
- [21] M. Majumder, M. Schmidt, H. Rosner, A. A. Tsirlin, H. Yasuoka, and M. Baenitz, “Anisotropic $Ru^{3+} 4d^5$ magnetism in the α - $RuCl_3$ honeycomb system: Susceptibility, specific heat, and zero-field NMR”, *Physical Review B* **91**, 180401 (2015).
- [22] R. D. Johnson, S. C. Williams, A. A. Haghighirad, J. Singleton, V. Zapf, P. Manuel, I. I. Mazin, Y. Li, H. O. Jeschke, R. Valentí, and R. Coldea, “Monoclinic crystal structure of α - $RuCl_3$ and the zigzag antiferromagnetic ground state”, *Physical Review B - Condensed Matter and Materials Physics* **92**, 10.1103/PhysRevB.92.235119 (2015).
- [23] S. M. Winter, K. Riedl, P. A. Maksimov, A. L. Chernyshev, A. Honecker, and R. Valentí, “Breakdown of magnons in a strongly spin-orbital coupled magnet”, *Nature Communications* **8**, 10.1038/s41467-017-01177-0 (2017).
- [24] S. M. Winter, A. A. Tsirlin, M. Daghofer, J. Van Den Brink, Y. Singh, P. Gegenwart, and R. Valentí, *Models and materials for generalized Kitaev magnetism*, 2017.
- [25] A. Banerjee, C. A. Bridges, J. Q. Yan, A. A. Aczel, L. Li, M. B. Stone, G. E. Granroth, M. D. Lumsden, Y. Yiu, J. Knolle, S. Bhattacharjee, D. L. Kovrizhin, R. Moessner, D. A. Tennant, D. G. Mandrus, and S. E. Nagler, “Proximate Kitaev quantum spin liquid behaviour in a honeycomb magnet”, *Nature Materials* **15**, 733–740 (2016).
- [26] A. Banerjee, J. Yan, J. Knolle, C. A. Bridges, M. B. Stone, M. D. Lumsden, D. G. Mandrus, D. A. Tennant, R. Moessner, and S. E. Nagler, “Neutron scattering in the proximate quantum spin liquid α - $RuCl_3$ ”, *Science* **356**, 1055–1059 (2017).
- [27] L. J. Sandilands, Y. Tian, K. W. Plumb, Y. J. Kim, and K. S. Burch, “Scattering Continuum and Possible Fractionalized Excitations in α - $RuCl_3$ ”, *Physical Review Letters* **114**, 10.1103/PhysRevLett.114.147201 (2015).
- [28] A. Glamazda, P. Lemmens, S. H. Do, Y. S. Kwon, and K. Y. Choi, “Relation between Kitaev magnetism and structure in α - $RuCl_3$ ”, *Physical Review B* **95**, 10.1103/PhysRevB.95.174429 (2017).
- [29] Y. Wang, G. B. Osterhoudt, Y. Tian, P. Lampen-Kelley, A. Banerjee, T. Goldstein, J. Yan, J. Knolle, H. Ji, R. J. Cava, J. Nasu, Y. Motome, S. E. Nagler, D. Mandrus, and K. S. Burch, “The range of non-Kitaev terms and fractional particles in α - $RuCl_3$ ”, *npj Quantum Materials* **5**, 10.1038/s41535-020-0216-6 (2020).

-
- [30] A. Little, L. Wu, P. Lampen-Kelley, A. Banerjee, S. Patankar, D. Rees, C. A. Bridges, J. Q. Yan, D. Mandrus, S. E. Nagler, and J. Orenstein, “Antiferromagnetic Resonance and Terahertz Continuum in α - RuCl_3 ”, *Physical Review Letters* **119**, 10.1103/PhysRevLett.119.227201 (2017).
- [31] Z. Wang, S. Reschke, D. Huvonen, S. H. Do, K. Y. Choi, M. Gensch, U. Nagel, T. Rõõm, and A. Loidl, “Magnetic Excitations and Continuum of a Possibly Field-Induced Quantum Spin Liquid in α - RuCl_3 ”, *Physical Review Letters* **119**, 10.1103/PhysRevLett.119.227202 (2017).
- [32] J. Nasu, J. Knolle, D. L. Kovrizhin, Y. Motome, and R. Moessner, “Fermionic response from fractionalization in an insulating two-dimensional magnet”, *Nature Physics* **12**, 912–915 (2016).
- [33] Y. Kasahara, T. Ohnishi, Y. Mizukami, O. Tanaka, S. Ma, K. Sugii, N. Kurita, H. Tanaka, J. Nasu, Y. Motome, T. Shibauchi, and Y. Matsuda, “Majorana quantization and half-integer thermal quantum Hall effect in a Kitaev spin liquid”, *Nature* **559**, 227–231 (2018).
- [34] M. M. Sala, C. Henriquet, L. Simonelli, R. Verbeni, and G. Monaco, “High energy-resolution set-up for ir l3 edge rixs experiments”, *Journal of Electron Spectroscopy and Related Phenomena* **188**, 150–154 (2013).
- [35] M. M. Sala, K. Martel, C. Henriquet, A. Al Zein, L. Simonelli, C. J. Sahle, H. Gonzalez, M. C. Lagier, C. Ponchut, S. Huotari, R. Verbeni, M. Krisch, and G. Monaco, “A high-energy-resolution resonant inelastic X-ray scattering spectrometer at ID20 of the European Synchrotron Radiation Facility”, *Journal of Synchrotron Radiation* **25**, 580–591 (2018).
- [36] S. Trebst, “Kitaev Materials”, (2017).
- [37] J. Chaloupka and G. Khaliullin, “Hidden symmetries of the extended Kitaev-Heisenberg model: Implications for the honeycomb-lattice iridates A_2IrO_3 ”, *Physical Review B - Condensed Matter and Materials Physics* **92**, 10.1103/PhysRevB.92.024413 (2015).
- [38] J. Chaloupka, G. Jackeli, and G. Khaliullin, “Zigzag magnetic order in the iridium oxide Na_2IrO_3 ”, *Physical Review Letters* **110**, 097204 (2013).
- [39] J. Kim, J. Chaloupka, Y. Singh, J. W. Kim, B. J. Kim, D. Casa, A. Said, X. Huang, and T. Gog, “Dynamic Spin Correlations in the Honeycomb Lattice Na_2IrO_3 Measured by Resonant Inelastic x-Ray Scattering”, *Physical Review X* **10**, 021034 (2020).
- [40] S. Hwan Chun, J. W. Kim, J. Kim, H. Zheng, C. C. Stoumpos, C. D. Malliakas, J. F. Mitchell, K. Mehlawat, Y. Singh, Y. Choi, T. Gog, A. Al-Zein, M. M. Sala,

- M. Krisch, J. Chaloupka, G. Jackeli, G. Khaliullin, and B. J. Kim, “Direct evidence for dominant bond-directional interactions in a honeycomb lattice iridate Na_2IrO_3 ”, *Nature Physics* **11**, 462–466 (2015).
- [41] H. Gretarsson, H. Suzuki, H. Kim, K. Ueda, M. Krautloher, B. J. Kim, H. Yavaş, G. Khaliullin, and B. Keimer, “Observation of spin-orbit excitations and Hund’s multiplets in Ca_2RuO_4 ”, *Physical Review B* **100**, 10.1103/PhysRevB.100.045123 (2019).
- [42] B. W. Lebert, S. Kim, V. Bisogni, I. Jarrige, A. M. Barbour, and Y. J. Kim, “Resonant inelastic x-ray scattering study of $\alpha\text{-RuCl}_3$: A progress report”, *Journal of Physics Condensed Matter* **32**, 10.1088/1361-648X/ab5595 (2020).
- [43] J. Kim, D. Casa, M. H. Upton, T. Gog, Y. J. Kim, J. F. Mitchell, M. Van Veenendaal, M. Daghofer, J. Van Den Brink, G. Khaliullin, and B. J. Kim, “Magnetic excitation spectra of Sr_2IrO_4 probed by resonant inelastic X-ray scattering: Establishing links to cuprate superconductors”, *Physical Review Letters* **108**, 10.1103/PhysRevLett.108.177003 (2012).
- [44] J. Kim, M. Daghofer, A. H. Said, T. Gog, J. Van Den Brink, G. Khaliullin, and B. J. Kim, “Excitonic quasiparticles in a spin-orbit Mott insulator”, *Nature Communications* **5**, 10.1038/ncomms5453 (2014).
- [45] H. Gretarsson, J. P. Clancy, X. Liu, J. P. Hill, E. Bozin, Y. Singh, S. Manni, P. Gegenwart, J. Kim, A. H. Said, D. Casa, T. Gog, M. H. Upton, H. S. Kim, J. Yu, V. M. Katukuri, L. Hozoi, J. Van Den Brink, and Y. J. Kim, “Crystal-field splitting and correlation effect on the electronic structure of A_2IrO_3 ”, *Physical Review Letters* **110**, 10.1103/PhysRevLett.110.076402 (2013).
- [46] M. Rossi, M. Retegan, C. Giacobbe, R. Fumagalli, A. Efimenko, T. Kulka, K. Wohlfeld, A. I. Gubanov, and M. Moretti Sala, “Possibility to realize spin-orbit-induced correlated physics in iridium fluorides”, *Physical Review B* **95**, 10.1103/PhysRevB.95.235161 (2017).
- [47] L. J. Sandilands, Y. Tian, A. A. Reijnders, H. S. Kim, K. W. Plumb, Y. J. Kim, H. Y. Kee, and K. S. Burch, “Spin-orbit excitations and electronic structure of the putative Kitaev magnet $\alpha\text{-RuCl}_3$ ”, *Physical Review B* **93**, 10.1103/PhysRevB.93.075144 (2016).
- [48] K. W. Plumb, J. P. Clancy, L. J. Sandilands, V. V. Shankar, Y. F. Hu, K. S. Burch, H. Y. Kee, and Y. J. Kim, “ $\alpha\text{-RuCl}_3$: A spin-orbit assisted Mott insulator on a honeycomb lattice”, *Physical Review B - Condensed Matter and Materials Physics* **90**, 10.1103/PhysRevB.90.041112 (2014).

-
- [49] L. Binotto, I. Pollini, and G. Spinolo, “Optical and transport properties of the magnetic semiconductor α -RuCl₃”, *physica status solidi (b)* **44**, 245–252 (1971).
- [50] G. Guizzetti, E. Reguzzoni, and I. Pollini, “Fundamental optical properties of α -RuCl₃”, *Physics Letters A* **70**, 34–36 (1979).
- [51] S. Reschke, F. Mayr, Z. Wang, S. H. Do, K. Y. Choi, and A. Loidl, “Electronic and phonon excitations in α -RuCl₃”, *Physical Review B* **96**, 10.1103/PhysRevB.96.165120 (2017).
- [52] Y. Hasegawa, T. Aoyama, K. Sasaki, Y. Ikemoto, T. Moriwaki, T. Shirakura, R. Saito, Y. Imai, and K. Ohgushi, “Two-phonon absorption spectra in the layered honeycomb compound α -RuCl₃”, *Journal of the Physical Society of Japan* **86**, 10.7566/JPSJ.86.123709 (2017).
- [53] S. Reschke, F. Mayr, S. Widmann, H. A. K. Von Nidda, V. Tsurkan, M. V. Eremin, S. H. Do, K. Y. Choi, Z. Wang, and A. Loidl, “Sub-gap optical response in the Kitaev spin-liquid candidate α -RuCl₃”, *Journal of Physics Condensed Matter* **30**, 10.1088/1361-648X/aae805 (2018).
- [54] S. Agrestini, C. Y. Kuo, K. T. Ko, Z. Hu, D. Kasinathan, H. B. Vasili, J. Herrero-Martin, S. M. Valvidares, E. Pellegrin, L. Y. Jang, A. Henschel, M. Schmidt, A. Tanaka, and L. H. Tjeng, “Electronically highly cubic conditions for Ru in α -RuCl₃”, *Physical Review B* **96**, 10.1103/PhysRevB.96.161107 (2017).
- [55] R. Yadav, N. A. Bogdanov, V. M. Katukuri, S. Nishimoto, J. Van Den Brink, and L. Hozoi, “Kitaev exchange and field-induced quantum spin-liquid states in honeycomb α -RuCl₃”, *Scientific Reports* **6**, 10.1038/srep37925 (2016).
- [56] A. Altland and M. R. Zirnbauer, “Nonstandard symmetry classes in mesoscopic normal-superconducting hybrid structures”, *Physical Review B - Condensed Matter and Materials Physics* **55**, 1142–1161 (1997).
- [57] Y. A. Gol’Fand and E. P. Likhtman, “Extension of the Algebra of Poincare Group Generators and Violation of P invariance”, *JETPL* **13**, 323 (1971).
- [58] P. Ramond, “Dual theory for free fermions”, *Physical Review D* **3**, 2415–2418 (1971).
- [59] A. Neveu and J. H. Schwarz, “Factorizable dual model of pions”, *Nuclear Physics, Section B* **31**, 86–112 (1971).
- [60] H. Baer and X. Tata, *Weak scale supersymmetry: From superfields to scattering events* (2006).
- [61] K. Efetov, *Supersymmetry in Disorder and Chaos* (Cambridge University Press, 1999).

- [62] S. D. Huber, “Topological mechanics”, *Nature Physics* **12**, 621–623 (2016).
- [63] C. L. Kane and T. C. Lubensky, “Topological boundary modes in isostatic lattices”, *Nature Physics* **10**, 39–45 (2013).
- [64] J. C. Maxwell, “L. On the calculation of the equilibrium and stiffness of frames”, *The London, Edinburgh, and Dublin Philosophical Magazine and Journal of Science* **27**, 294–299 (1864).
- [65] M. J. Lawler, “Supersymmetry protected topological phases of isostatic lattices and kagome antiferromagnets”, *Physical Review B* **94**, 10.1103/PhysRevB.94.165101 (2016).
- [66] K. S. Novoselov, A. K. Geim, S. V. Morozov, D. Jiang, Y. Zhang, S. V. Dubonos, I. V. Grigorieva, and A. A. Firsov, “Electric field in atomically thin carbon films”, *Science* **306**, 666–669 (2004).
- [67] A. H. Castro Neto, F. Guinea, N. M. Peres, K. S. Novoselov, and A. K. Geim, “The electronic properties of graphene”, *Reviews of Modern Physics* **81**, 109–162 (2009).
- [68] C. Rackauckas and Q. Nie, “DifferentialEquations.jl – A Performant and Feature-Rich Ecosystem for Solving Differential Equations in Julia”, *Journal of Open Research Software* **5**, 15 (2017).
- [69] W. A. Benalcazar, B. A. Bernevig, and T. L. Hughes, “Quantized electric multipole insulators”, *Science* **357**, 61–66 (2017).
- [70] W. A. Benalcazar, B. A. Bernevig, and T. L. Hughes, “Electric multipole moments, topological multipole moment pumping, and chiral hinge states in crystalline insulators”, *Physical Review B* **96**, 10.1103/PhysRevB.96.245115 (2017).
- [71] F. Schindler, A. M. Cook, M. G. Vergniory, Z. Wang, S. S. Parkin, B. Andrei Bernevig, and T. Neupert, “Higher-order topological insulators”, *Science Advances* **4**, 10.1126/sciadv.aat0346 (2018).
- [72] M. Serra-Garcia, V. Peri, R. Süsstrunk, O. R. Bilal, T. Larsen, L. G. Villanueva, and S. D. Huber, “Observation of a phononic quadrupole topological insulator”, *Nature* **555**, 342–345 (2018).
- [73] C. W. Peterson, W. A. Benalcazar, T. L. Hughes, and G. Bahl, “A quantized microwave quadrupole insulator with topologically protected corner states”, *Nature* **555**, 346–350 (2018).
- [74] S. Imhof, C. Berger, F. Bayer, J. Brehm, L. W. Molenkamp, T. Kiessling, F. Schindler, C. H. Lee, M. Greiter, T. Neupert, and R. Thomale, “Topoelectrical-circuit realization of topological corner modes”, *Nature Physics* **14**, 925–929 (2018).

-
- [75] F. Schindler, Z. Wang, M. G. Vergniory, A. M. Cook, A. Murani, S. Sengupta, A. Y. Kasumov, R. Deblock, S. Jeon, I. Drozdov, H. Bouchiat, S. Guéron, A. Yazdani, B. A. Bernevig, and T. Neupert, “Higher-order topology in bismuth”, *Nature Physics* **14**, 918–924 (2018).
- [76] V. Dwivedi, C. Hickey, T. Eschmann, and S. Trebst, “Majorana corner modes in a second-order Kitaev spin liquid”, *Physical Review B* **98**, 10.1103/PhysRevB.98.054432 (2018).
- [77] Nobel Media AB, *The Nobel Prize in Physics 2010*. *Nobelprize.org*, (2020) <https://www.nobelprize.org/prizes/physics/2010/summary/> (visited on 10/18/2021).
- [78] K. K. Gomes, W. Mar, W. Ko, F. Guinea, and H. C. Manoharan, “Designer Dirac fermions and topological phases in molecular graphene”, *Nature* **483**, 306–310 (2012).
- [79] S. Balendhran, S. Walia, H. Nili, S. Sriram, and M. Bhaskaran, *Elemental analogues of graphene: Silicene, germanene, stanene, and phosphorene*, 2015.
- [80] L. Tarruell, D. Greif, T. Uehlinger, G. Jotzu, and T. Esslinger, “Creating, moving and merging Dirac points with a Fermi gas in a tunable honeycomb lattice”, *Nature* **483**, 302–305 (2012).
- [81] N. Mounet, M. Gibertini, P. Schwaller, D. Campi, A. Merkys, A. Marrazzo, T. Sohier, I. E. Castelli, A. Cepellotti, G. Pizzi, and N. Marzari, “Two-dimensional materials from high-throughput computational exfoliation of experimentally known compounds”, *Nature Nanotechnology* **13**, 246–252 (2018).
- [82] N. Levy, S. A. Burke, K. L. Meaker, M. Panlasigui, A. Zettl, F. Guinea, A. H. Castro Neto, and M. F. Crommie, “Strain-induced pseudo-magnetic fields greater than 300 tesla in graphene nanobubbles”, *Science* **329**, 544–547 (2010).
- [83] K. Kim, M. Yankowitz, B. Fallahazad, S. Kang, H. C. Movva, S. Huang, S. Larentis, C. M. Corbet, T. Taniguchi, K. Watanabe, S. K. Banerjee, B. J. Leroy, and E. Tutuc, “Van der Waals Heterostructures with High Accuracy Rotational Alignment”, *Nano Letters* **16**, 1989–1995 (2016).
- [84] G. Li, A. Luican, J. M. Lopes Dos Santos, A. H. Castro Neto, A. Reina, J. Kong, and E. Y. Andrei, “Observation of Van Hove singularities in twisted graphene layers”, *Nature Physics* **6**, 109–113 (2010).
- [85] K. Kim, A. DaSilva, S. Huang, B. Fallahazad, S. Larentis, T. Taniguchi, K. Watanabe, B. J. LeRoy, A. H. MacDonald, and E. Tutuc, “Tunable moiré bands and strong correlations in small-twist-angle bilayer graphene”, *Proceedings of the National Academy of Sciences of the United States of America* **114**, 3364–3369 (2017).

- [86] A. Luican, G. Li, A. Reina, J. Kong, R. R. Nair, K. S. Novoselov, A. K. Geim, and E. Y. Andrei, “Single-layer behavior and its breakdown in twisted graphene layers”, *Physical Review Letters* **106**, 126802 (2011).
- [87] T. R. Albrecht, H. A. Mizes, J. Nogami, S. I. Park, and C. F. Quate, “Observation of tilt boundaries in graphite by scanning tunneling microscopy and associated multiple tip effects”, *Applied Physics Letters* **52**, 362–364 (1988).
- [88] J. Coraux, A. T. N’Diaye, M. Engler, C. Busse, D. Wall, N. Buckanie, F. J. Meyer Zu Heringdorf, R. Van Gastel, B. Poelsema, and T. Michely, “Growth of graphene on Ir(111)”, *New Journal of Physics* **11**, 10.1088/1367-2630/11/2/023006 (2009).
- [89] J. Coraux, A. T. N’Diaye, C. Busse, and T. Michely, “Structural coherency of graphene on Ir(111)”, *Nano Letters* **8**, 565–570 (2008).
- [90] A. T. N’Diaye, J. Coraux, T. N. Plasa, C. Busse, and T. Michely, “Structure of epitaxial graphene on Ir(111)”, *New Journal of Physics* **10**, 10.1088/1367-2630/10/4/043033 (2008).
- [91] R. Bistritzer and A. H. MacDonald, “Moiré bands in twisted double-layer graphene”, *Proceedings of the National Academy of Sciences of the United States of America* **108**, 12233–12237 (2011).
- [92] D. C. Tsui, H. L. Stormer, and A. C. Gossard, “Two-dimensional magnetotransport in the extreme quantum limit”, *Physical Review Letters* **48**, 1559–1562 (1982).
- [93] X. G. Wen, “Topological orders and edge excitations in fractional quantum Hall states”, *Advances in Physics* **44**, 405–473 (1995).
- [94] E. Fradkin and S. A. Kivelson, *High-temperature superconductivity: Ineluctable complexity*, 2012.
- [95] Y. Cao, V. Fatemi, S. Fang, K. Watanabe, T. Taniguchi, E. Kaxiras, and P. Jarillo-Herrero, “Unconventional superconductivity in magic-angle graphene superlattices”, *Nature* **556**, 43–50 (2018).
- [96] Y. Cao, V. Fatemi, A. Demir, S. Fang, S. L. Tomarken, J. Y. Luo, J. D. Sanchez-Yamagishi, K. Watanabe, T. Taniguchi, E. Kaxiras, R. C. Ashoori, and P. Jarillo-Herrero, “Correlated insulator behaviour at half-filling in magic-angle graphene superlattices”, *Nature* **556**, 80–84 (2018).
- [97] X. Lu, P. Stepanov, W. Yang, M. Xie, M. A. Aamir, I. Das, C. Urgell, K. Watanabe, T. Taniguchi, G. Zhang, A. Bachtold, A. H. MacDonald, and D. K. Efetov, “Superconductors, orbital magnets and correlated states in magic-angle bilayer graphene”, *Nature* **574**, 653–657 (2019).

-
- [98] Y. Cao, D. Chowdhury, D. Rodan-Legrain, O. Rubies-Bigorda, K. Watanabe, T. Taniguchi, T. Senthil, and P. Jarillo-Herrero, “Strange Metal in Magic-Angle Graphene with near Planckian Dissipation”, *Physical Review Letters* **124**, 076801 (2020).
- [99] A. H. MacDonald and R. Bistritzer, *Graphene moiré mystery solved?*, 2011.
- [100] B. Hunt, J. D. Sanchez-Yamagishi, A. F. Young, M. Yankowitz, B. J. LeRoy, K. Watanabe, T. Taniguchi, P. Moon, M. Koshino, P. Jarillo-Herrero, and R. C. Ashoori, “Massive dirac fermions and hofstadter butterfly in a van der Waals heterostructure”, *Science* **340**, 1427–1430 (2013).
- [101] M. Yankowitz, J. Jung, E. Laksono, N. Leconte, B. L. Chittari, K. Watanabe, T. Taniguchi, S. Adam, D. Graf, and C. R. Dean, “Dynamic band-structure tuning of graphene moiré superlattices with pressure”, *Nature* **557**, 404–408 (2018).
- [102] J. C. Rode, D. Smirnov, C. Belke, H. Schmidt, and R. J. Haug, “Twisted Bilayer Graphene: Interlayer Configuration and Magnetotransport Signatures”, *Annalen der Physik* **529**, 1700025 (2017).
- [103] M. Yankowitz, J. Xue, D. Cormode, J. D. Sanchez-Yamagishi, K. Watanabe, T. Taniguchi, P. Jarillo-Herrero, P. Jacquod, and B. J. Leroy, “Emergence of superlattice Dirac points in graphene on hexagonal boron nitride”, *Nature Physics* **8**, 382–386 (2012).
- [104] L. Balents, C. R. Dean, D. K. Efetov, and A. F. Young, “Superconductivity and strong correlations in moiré flat bands”, *Nature Physics* **16**, 725–733 (2020).
- [105] O. Can, T. Tummuru, R. P. Day, I. Elfimov, A. Damascelli, and M. Franz, “High-temperature topological superconductivity in twisted double-layer copper oxides”, *Nature Physics* **17**, 519–524 (2021).
- [106] M. Yankowitz, S. Chen, H. Polshyn, Y. Zhang, K. Watanabe, T. Taniguchi, D. Graf, A. F. Young, and C. R. Dean, “Tuning superconductivity in twisted bilayer graphene”, *Science* **363**, 1059–1064 (2019).
- [107] Y. Choi, J. Kemmer, Y. Peng, A. Thomson, H. Arora, R. Polski, Y. Zhang, H. Ren, J. Alicea, G. Refael, F. von Oppen, K. Watanabe, T. Taniguchi, and S. Nadj-Perge, “Electronic correlations in twisted bilayer graphene near the magic angle”, *Nature Physics* **15**, 1174–1180 (2019).
- [108] A. Kerelsky, L. J. McGilly, D. M. Kennes, L. Xian, M. Yankowitz, S. Chen, K. Watanabe, T. Taniguchi, J. Hone, C. Dean, A. Rubio, and A. N. Pasupathy, “Maximized electron interactions at the magic angle in twisted bilayer graphene”, *Nature* **572**, 95–100 (2019).

- [109] Y. Jiang, X. Lai, K. Watanabe, T. Taniguchi, K. Haule, J. Mao, and E. Y. Andrei, “Charge order and broken rotational symmetry in magic-angle twisted bilayer graphene”, *Nature* **573**, 91–95 (2019).
- [110] X. Liu, Z. Hao, E. Khalaf, J. Y. Lee, Y. Ronen, H. Yoo, D. Haei Najafabadi, K. Watanabe, T. Taniguchi, A. Vishwanath, and P. Kim, “Tunable spin-polarized correlated states in twisted double bilayer graphene”, *Nature* **583**, 221–225 (2020).
- [111] C. Shen, Y. Chu, Q. S. Wu, N. Li, S. Wang, Y. Zhao, J. Tang, J. Liu, J. Tian, K. Watanabe, T. Taniguchi, R. Yang, Z. Y. Meng, D. Shi, O. V. Yazyev, and G. Zhang, “Correlated states in twisted double bilayer graphene”, *Nature Physics* **16**, 520–525 (2020).
- [112] G. W. Burg, J. Zhu, T. Taniguchi, K. Watanabe, A. H. MacDonald, and E. Tutuc, “Correlated Insulating States in Twisted Double Bilayer Graphene”, *Physical Review Letters* **123**, 197702 (2019).
- [113] M. He, Y. Li, J. Cai, Y. Liu, K. Watanabe, T. Taniguchi, X. Xu, and M. Yankowitz, “Symmetry breaking in twisted double bilayer graphene”, *Nature Physics* **17**, 26–30 (2021).
- [114] G. Chen, A. L. Sharpe, P. Gallagher, I. T. Rosen, E. J. Fox, L. Jiang, B. Lyu, H. Li, K. Watanabe, T. Taniguchi, J. Jung, Z. Shi, D. Goldhaber-Gordon, Y. Zhang, and F. Wang, “Signatures of tunable superconductivity in a trilayer graphene moiré superlattice”, *Nature* **572**, 215–219 (2019).
- [115] G. Chen, L. Jiang, S. Wu, B. Lyu, H. Li, B. L. Chittari, K. Watanabe, T. Taniguchi, Z. Shi, J. Jung, Y. Zhang, and F. Wang, “Evidence of a gate-tunable Mott insulator in a trilayer graphene moiré superlattice”, *Nature Physics* **15**, 237–241 (2019).
- [116] G. X. Ni, H. Wang, B. Y. Jiang, L. X. Chen, Y. Du, Z. Y. Sun, M. D. Goldflam, A. J. Frenzel, X. M. Xie, M. M. Fogler, and D. N. Basov, “Soliton superlattices in twisted hexagonal boron nitride”, *Nature Communications* **10**, 4360 (2019).
- [117] L. Xian, D. M. Kennes, N. Tancogne-Dejean, M. Altarelli, and A. Rubio, “Multiflat Bands and Strong Correlations in Twisted Bilayer Boron Nitride: Doping-Induced Correlated Insulator and Superconductor”, *Nano Letters* **19**, 4934–4940 (2019).
- [118] L. Wang, E. M. Shih, A. Ghiotto, L. Xian, D. A. Rhodes, C. Tan, M. Claassen, D. M. Kennes, Y. Bai, B. Kim, K. Watanabe, T. Taniguchi, X. Zhu, J. Hone, A. Rubio, A. N. Pasupathy, and C. R. Dean, “Correlated electronic phases in twisted bilayer transition metal dichalcogenides”, *Nature Materials* **19**, 861–866 (2020).
- [119] E. C. Regan, D. Wang, C. Jin, M. I. Bakti Utama, B. Gao, X. Wei, S. Zhao, W. Zhao, Z. Zhang, K. Yumigeta, M. Blei, J. D. Carlström, K. Watanabe, T. Taniguchi, S.

- Tongay, M. Crommie, A. Zettl, and F. Wang, “Mott and generalized Wigner crystal states in WSe₂/WS₂ moiré superlattices”, *Nature* **579**, 359–363 (2020).
- [120] Y. Tang, L. Li, T. Li, Y. Xu, S. Liu, K. Barmak, K. Watanabe, T. Taniguchi, A. H. MacDonald, J. Shan, and K. F. Mak, “Simulation of Hubbard model physics in WSe₂/WS₂ moiré superlattices”, *Nature* **579**, 353–358 (2020).
- [121] L. Xian, M. Claassen, D. Kiese, M. M. Scherer, S. Trebst, D. M. Kennes, and A. Rubio, “Realization of nearly dispersionless bands with strong orbital anisotropy from destructive interference in twisted bilayer MoS₂”, *Nature Communications* **12**, 10.1038/s41467-021-25922-8 (2021).
- [122] D. M. Kennes, M. Claassen, L. Xian, A. Georges, A. J. Millis, J. Hone, C. R. Dean, D. N. Basov, A. N. Pasupathy, and A. Rubio, *Moiré heterostructures as a condensed-matter quantum simulator*, 2021.
- [123] M. L. Mehta, *Random Matrices, Volume 142 - 3rd Edition* (2004).
- [124] E. P. Wigner, “Characteristic Vectors of Bordered Matrices With Infinite Dimensions”, *The Annals of Mathematics* **62**, 548 (1955).
- [125] T. Guhr, A. Müller-Groeling, and H. A. Weidenmüller, “Random-matrix theories in quantum physics: Common concepts”, *Physics Report* **299**, 189–425 (1998).
- [126] Y. Fu, E. J. König, J. H. Wilson, Y. Z. Chou, and J. H. Pixley, “Magic-angle semimetals”, *npj Quantum Materials* **5**, 1 (2020).
- [127] J. H. Pixley, J. H. Wilson, D. A. Huse, and S. Gopalakrishnan, “Weyl Semimetal to Metal Phase Transitions Driven by Quasiperiodic Potentials”, *Physical Review Letters* **120**, 207604 (2018).
- [128] Y. Z. Chou, Y. Z. Chou, Y. Fu, J. H. Wilson, E. J. König, and J. H. Pixley, “Magic-angle semimetals with chiral symmetry”, *Physical Review B* **101**, 235121 (2020).
- [129] G. Tarnopolsky, A. J. Kruchkov, and A. Vishwanath, “Origin of Magic Angles in Twisted Bilayer Graphene”, *Physical Review Letters* **122**, 106405 (2019).
- [130] M. Gonçalves, H. Z. Olyaei, B. Amorim, R. Mondaini, P. Ribeiro, and E. V. Castro, “Incommensurability-induced sub-ballistic narrow-band-states in twisted bilayer graphene”, *2D Materials* **9**, 011001 (2022).
- [131] F. Evers and A. D. Mirlin, “Anderson transitions”, *Reviews of Modern Physics* **80**, 1355–1417 (2008).
- [132] J. C. Slater and G. F. Koster, “Simplified LCAO method for the periodic potential problem”, *Physical Review* **94**, 1498–1524 (1954).

- [133] G. Trambly De Laissardière, D. Mayou, and L. Magaud, “Numerical studies of confined states in rotated bilayers of graphene”, *Physical Review B - Condensed Matter and Materials Physics* **86**, 125413 (2012).
- [134] P. Moon and M. Koshino, “Optical absorption in twisted bilayer graphene”, *Physical Review B - Condensed Matter and Materials Physics* **87**, 205404 (2013).
- [135] M. Koshino and N. N. Nam, “Effective continuum model for relaxed twisted bilayer graphene and moiré electron-phonon interaction”, *Physical Review B* **101**, 195425 (2020).
- [136] J. Liu, J. Liu, and X. Dai, “Pseudo Landau level representation of twisted bilayer graphene: Band topology and implications on the correlated insulating phase”, *Physical Review B* **99**, 155415 (2019).
- [137] V. Oganesyan and D. A. Huse, “Localization of interacting fermions at high temperature”, *Physical Review B - Condensed Matter and Materials Physics* **75**, 155111 (2007).
- [138] F. Monteiro, T. Micklitz, M. Tezuka, and A. Altland, “Minimal model of many-body localization”, *Physical Review Research* **3**, 013023 (2021).
- [139] C. Berke, E. Varvelis, S. Trebst, A. Altland, and D. P. DiVincenzo, “Transmon platform for quantum computing challenged by chaotic fluctuations”, (2020).

Acknowledgments

First and foremost, I want to deeply thank my supervisor, Simon Trebst, for enthusiastically mentoring and guiding me through numerous interesting research projects. I am particularly grateful for the many and diverse opportunities he offered to me, not only in physics but also regarding teaching and programming. I am most thankful that he always found time to give helpful advice and provided the best possible environment for me in Cologne. Further, I want to thank Sebastian Diehl and Thomas Michely for kindly agreeing to be my second referee and chairman of the thesis committee.

During the time of my PhD, I particularly enjoyed the numerous collaborations within the different projects I pursued. In this regard, I want to thank all my collaborators who have broadened my horizon and provided me with invaluable advice. I especially want to express my thanks to Markus Grüninger and Maria Hermanns for their inspiring enthusiasm and valuable insights on the topics of RIXS and spin-orbit coupled materials. On the same topic, I would also like to thank Alessandro Revelli, Marco Magnaterra and Luca Peterlini for many fruitful exchanges. Furthermore, I am particularly grateful for the long-standing collaboration with Michael J. Lawler and Krishanu Roychowdhury on the topic of supersymmetry. Our frequent and regular video meetings across the continents provided many stimulating discussions, which I valued a lot. I further want to thank Achim Rosch, Alexander Altland, Michael Scherer and Jinhong Park who provided insightful exchanges about the fascinating topic of Moiré materials in general, and twisted bilayer graphene in particular. Last but not least, I want to express my thanks to Frederic Freyer, SungBin Lee, Arun Paramekanti and Yong Baek Kim, as well as to Martin Gembé and Joel Kunkel, for collaborations on additional projects which were going beyond the topic of this thesis.

All of these collaborations could not have been possible without organizational support. In this regard, I want to thank Andreas Sindermann and Mariela Boevska at the Institute for Theoretical Physics as well as Petra Neubauer-Guenther and the Bonn-Cologne Graduate School of Physics and Astronomy. Further thanks goes to the collaborative research centers CRC1238 and CRC183 for funding my PhD position and my research stay at the University of Stockholm – a trip for which I am very grateful. The numerical simulations were performed on the CHEOPS cluster at RRZK Cologne and the JUWELS cluster at the Forschungszentrum Jülich.

Last but not least, I am deeply grateful for the warm and open work environment of the Rosch and Trebst groups which have uniquely shaped my time at the University of Cologne – thanks to everyone who accompanied me along my journey! Especially, I want to thank Ciarán, Luca, Dominik, Michael, Jinhong and Martin for proofreading parts of my thesis, my office mates and former group members, Finn, Tim, Dominik, Martin, Carsten and Christoph as well as the countless friends and colleagues who may forgive me, for not naming them explicitly. Finally, I want to genuinely thank my girlfriend Lydia as well as my family for their continuous love and encouragement that especially supported me through the last part of my PhD time.

Erklärung zur Dissertation

Ich versichere, dass ich die von mir vorgelegte Dissertation selbständig angefertigt, die benutzten Quellen und Hilfsmittel vollständig angegeben und die Stellen der Arbeit – einschließlich Tabellen, Karten und Abbildungen –, die anderen Werken im Wortlaut oder dem Sinn nach entnommen sind, in jedem Einzelfall als Entlehnung kenntlich gemacht habe; dass diese Dissertation noch keiner anderen Fakultät oder Universität zur Prüfung vorgelegen hat; dass sie – abgesehen von unten angegebenen Teilpublikationen – noch nicht veröffentlicht worden ist, sowie, dass ich eine solche Veröffentlichung vor Abschluss des Promotionsverfahrens nicht vornehmen werde. Die Bestimmungen der Promotionsordnung sind mir bekannt. Die von mir vorgelegte Dissertation ist von Prof. Dr. Simon Trebst betreut worden.

Datum

(Jan Attig)

(Bereits veröffentlichte Teilpublikationen sind auf der Folgeseite aufgeführt.)

Publikationen

(Bereits veröffentlicht)

- [P1] A. Revelli, C. C. Loo, D. Kiese, P. Becker, T. Fröhlich, T. Lorenz, M. Moretti Sala, G. Monaco, F. L. Buessen, J. Attig, M. Hermanns, S. V. Streltsov, D. I. Khomskii, J. Van Den Brink, M. Braden, P. H. Van Loosdrecht, S. Trebst, A. Paramekanti, and M. Grüninger, “Spin-orbit entangled $j=1/2$ moments in $\text{Ba}_2\text{CeIrO}_6$: A frustrated fcc quantum magnet”, *Physical Review B* **100**, 085139 (2019).
- [P3] P. Warzanowski, N. Borgwardt, K. Hopfer, J. Attig, T. C. Koethe, P. Becker, V. Tsurkan, A. Loidl, M. Hermanns, P. H. M. van Loosdrecht, and M. Grüninger, “Multiple spin-orbit excitons and the electronic structure of $\alpha\text{-RuCl}_3$ ”, *Physical Review Research* **2**, 042007 (2020).
- [P5] J. Attig, K. Roychowdhury, M. J. Lawler, and S. Trebst, “Topological mechanics from supersymmetry”, *Physical Review Research* **1**, 032047 (2019).
- [P6] J. Attig and S. Trebst, “Classical spin spirals in frustrated magnets from free-fermion band topology”, *Physical Review B* **96**, 085145 (2017).
- [P7] F. Freyer, J. Attig, S. Lee, A. Paramekanti, S. Trebst, and Y. B. Kim, “Two-stage multipolar ordering in $\text{PrT}_2\text{Al}_{20}$ Kondo materials”, *Physical Review B* **97**, 115111 (2018).
- [P8] J. Attig, J. Park, M. M. Scherer, S. Trebst, A. Altland, and A. Rosch, “Universal principles of moiré band structures”, *2D Materials* **8**, 044007 (2021).

(Noch in Arbeit während des Verfassens der Dissertation)

- [P2] A. Revelli, M. M. Sala, G. Monaco, M. Magnaterra, J. Attig, L. Peterlini, T. Dey, A. A. Tsirlin, P. Gegenwart, T. Fröhlich, M. Braden, C. Grams, J. Hemberger, P. Becker, P. H. M. van Loosdrecht, D. I. Khomskii, J. v. d. Brink, M. Hermanns, and M. Grüninger, “Quasi-molecular electronic structure of the spin-liquid candidate $\text{Ba}_3\text{InIr}_2\text{O}_9$ ”, still in preparation during the writing of this thesis, [10.48550/ARXIV.2207.04795](https://arxiv.org/abs/10.48550/ARXIV.2207.04795) (2022).
- [P4] K. Roychowdhury, J. Attig, S. Trebst, and M. J. Lawler, “Supersymmetry on the lattice: Geometry, Topology, and Spin Liquids”, still in preparation during the writing of this thesis, [10.48550/ARXIV.2207.09475](https://arxiv.org/abs/10.48550/ARXIV.2207.09475) (2022).

Abstract

The description of electronic behavior within solids is a major part of modern Condensed Matter Physics. It is well known that depending on the precise conditions, very diverse phenomena arise from the interacting electrons in the material. To make predictions, it is therefore crucial to understand the electronic structure in a material and to compute its *electronic spectrum*. This thesis discusses three different aspects of electronic spectra including their numerical solution, each highlighting a distinct approach.

Kurzzusammenfassung

Die Beschreibung elektronischen Verhaltens in Materialien ist ein Kernpunkt moderner Festkörperphysik. Es ist bekannt, dass sich abhängig von den genauen Materialparametern sehr unterschiedliche qualitative Eigenschaften aus den wechselwirkenden Elektronen ergeben können. Daher ist es grundsätzlich unumgänglich, für jede Art von Vorhersage das elektronische Verhalten des Materials zu kennen und dessen sogenanntes *elektronisches Spektrum* berechnen zu können. Das Ziel dieser Arbeit ist es, in drei verschiedenen Teilen jeweils verschiedene Aspekte der Berechnung elektronischer Spektren hervorzuheben und zu diskutieren.

